Quantifying the effect of sex-related differences in biomechanical factors on brain deformation response

---

A
Dissertation
Presented to
the faculty of the School of Engineering and Applied Science
University of Virginia

---

in partial fulfillment
of the requirements for the degree

Doctor of Philosophy

by

Kristen A. Reynier

December 2022

APPROVAL SHEET

This

Dissertation

is submitted in partial fulfillment of the requirements
for the degree of

Doctor of Philosophy

Author: Kristen A. Reynier

This Dissertation has been read and approved by the examing committee:

Advisor: Matthew Panzer

Advisor:

Committee Member: Jason Forman

Committee Member: Jeff Crandall

Committee Member: Donna Broshek

Committee Member: Pavel Chernyavskiy

Committee Member:

Committee Member:

Accepted for the School of Engineering and Applied Science:

Jennifer L. West, School of Engineering and Applied Science

December 2022

Abstract

Traumatic brain injuries (TBIs) are complex injuries resulting in a variety of symptoms, disabilities, or even death, with common causes including motor vehicle crashes, sports, or unintentional falls. For belted automotive occupants in frontal crashes, females have a significantly greater risk of sustaining a moderate brain injury after controlling for covariates such as age, height, body mass index, delta-V of the collision, and vehicle model year. There are physical differences between males and females which may influence the biomechanics of the brain during a crash and explain the disparity of brain injury risk between the sexes. Biomechanical factors such as neuroanatomy, material properties, and the resulting head kinematics caused by the event all contribute to the severity of brain deformation, the primary mechanism of diffuse TBI. Computational finite element (FE) brain models are commonly used to predict brain response under potentially injurious loading, but a majority of research has focused on mid-sized adult males, and additional research is required to determine the effect of sex on brain deformation using these FE brain models. Therefore, the goal of this dissertation is to quantify sex-related differences in neuroanatomy, material properties, and head kinematics and their effect on brain deformation response in automotive loading environments using subject-specific FE brain models.

A previously developed registration-based morphing framework was utilized to develop subject-specific FE brain models from magnetic resonance imaging and elastography brain scans to capture unique neuroanatomies and material property features. For each of the subjects, intrinsic biomechanical features were evaluated and included measures of brain volumes, shear stiffnesses, and damping ratios. Sex was a significant predictor for many of these intrinsic biomechanical features, such as intracranial volume (ICV) and mean damping ratio, as estimated the Bayesian linear mixed model. The subject-specific FE models were then simulated using head kinematics from an oblique frontal sled test, and the biomechanical features and sex were

assessed to determine their effect on the brain tissue deformation metrics. Of the neuroanatomical features, ICV had the greatest effect on brain tissue maximum principal strain, and damping ratio had the greatest effect of the material properties; however, sex did not have a significant effect on the deformation metrics tested based on the Bayesian linear mixed model.

Based on differences in mass distribution and engagement with restraint systems, the effect of sex on automotive crash head kinematics needs to be considered. For sex-matched sled tests of post-mortem human surrogates and anthropometric test devices, sex was a significant predictor of peak kinematic metrics; however, the surrogate's sex did not have a significant effect on predicting brain deformation after including these kinematic features. However, the number of sex-matched sled test environments was limited, and there are often differences in experimental restraint systems (e.g., shoulder belt load limiters). Potential differences in head kinematics, as a result of these inconsistent test environment, have not been assessed.

A final sensitivity study assessed which of the biomechanical features within the neuroanatomy study, material properties study, and the head kinematics study had the greatest impact on brain deformation. Overall, biomechanical factors associated with the head kinematics had the overall greatest effect, and sex did not have a statistically significant effect on brain deformation. Additionally, ICV had a statistically significant effect on all deformation metrics.

The research presented in this dissertation provides an analysis of how biomechanical features within a subject's neuroanatomy, material properties, and head kinematics affect brain deformation. Ultimately, the outcomes presented in this dissertation can direct future work to address areas with the greatest impact on brain deformation to reduce injury risk in both male and female automotive occupants.

Table of Contents

Chapter 3: Effect of Material Properties 64

List of Figures

List of Tables

Introduction

Statement of Problem

The Centers for Disease Control (CDC) documented 2.53 million traumatic brain injury (TBI) related emergency department visits (ED) and 56,800 TBI-related deaths in the United States in 2014, with both ED visits and deaths increasing steadily from 2006 (Peterson et al., 2019). Additionally, there are an estimated 5.3 million people living with a TBI-related disability in the United States (Control & Prevention, 2015). The most common sources of TBIs were unintentional falls, unintentionally being struck by an object (including sports), motor vehicle collisions, assault, other (no mechanism specified), and intentional self-harm (Peterson et al., 2019). Emergency department and hospitalization records often report higher incidence of TBI in males compared to females, and a meta-analysis of previous epidemiology studies concluded that males have 2.2 higher odds of sustaining a TBI than females (Faul et al., 2010; Frost et al., 2013). It has been suggested the disparity of TBI incidence is due to the higher propensity of males to be involved in physical altercations, military service, and contact sports (Biegon, 2021). However, due to underreporting of female TBIs from intimate partner violence, recent publications suggest the true disparity in incidence rate of TBIs between males and females may not be captured in current epidemiology (Biegon, 2021; Control & Prevention, 2008; Maas et al., 2017). In addition to the overall TBI frequency between males and females presenting in an emergency department, the injury risk within each of these settings, such as motor vehicle crashes and sports, can vary depending on sex (Antona-Makoshi et al., 2018; J. Forman et al., 2019; Resch et al., 2017).

Across all high school and collegiate sports, male athletes have a higher reported concussion incidence rate per 100,000 athlete exposure, defined as one athlete participating in a single game or practice, compared to female athletes; however, when studying sports with similar participation rates in males and females, female athletes sustain more sports concussions compared to male athletes (Resch et al., 2017). In sex-comparable National Collegiate Athletic Association (NCAA) sports, females had 1.4 times overall the concussion injury rate compared to males, with greater rates in women's baseball/softball, basketball, ice hockey, and soccer (Covassin et al., 2016). Additionally, female athletes suffering from sports concussions report more post-concussion symptoms, greater performance decline in cognitive performance measures compared to baseline measures, and are cognitively impaired about 1.7 times more often than male athletes (Broshek et al., 2005). With increased incidence of female TBI and increasing female participation in sports, women now making up 47% of the 2019 NCAA Division I athletes compared to only 26% in 1983, research into possible explanations of this TBI disparity is necessary (Association, 2020). Do female brains injure easier than male brains? Is there a difference in injury tolerance between male and female brains? Is the injurious loading event the same for both sexes? Or is there an inherent, biological difference that explains this disparity?

To isolate the effect of sex on TBI rates or possible injury risk, knowledge of the injurious loading condition is required to eliminate or control for effects of exposure. Characterization or measurement of the injurious exposure is often not included in large hospital or sports injury databases. However, injury exposure can be controlled using automotive crash databases to better understand sex-differences in injury risk under similar loading conditions. Motor vehicle crashes account for more than one fifth of the 288,000 TBI-related hospitalizations and are the most common TBI-related cause of death for 15- to 34-year-olds and those older than 75 years old (Peterson et al., 2019). When controlling for delta-V, sex, age, height, Body Mass Index (BMI), and vehicle model year, females are at a significantly greater risk for moderate brain injury, with an odds ratio (OR) of 1.76 (J. Forman et al., 2019). Additionally, females are at a significantly greater risk for concussions (OR = 1.51) in frontal crashes when controlling for delta-V, sex, age, model year (Antona-Makoshi et al., 2018). However, while not statistically significant, males are at a greater risk for severe brain injury (OR = 0.44) in frontal crashes when controlling for delta-V, sex, age, height, BMI, and model year (J. Forman et al., 2019). These could imply differences in injury tolerance, biomechanical response of brain tissue, or head kinematics between male and female occupants could affect injury risk, but each require additional research.

During an automotive crash, or any inertial loading of the head, the brain tissue deforms, and the amount of deformation is dependent on the severity of the experienced head kinematics. Current brain injury risk functions relate either the external head kinematics or a predicted metric of brain deformation to the probability of a TBI (Gabler, Crandall, et al., 2018; Takhounts et al., 2013; Wu et al., 2021, 2022). While there is no current deformation threshold to define a brain injury, the risk of brain injury increases for increasing deformation or brain strain. To predict brain deformation based on external impact or inertial loading, the human brain can be modelled as a mechanical structure, with its mechanical response governed by the geometry, material properties, and boundary conditions. For brain biomechanics, these components are represented as the neuroanatomy, material properties, and the external head kinematics or the exposure. To best predict brain injury risk in both males and females, a greater understanding of the effect of these biomechanical factors on brain deformation is required, as well as any sex-specific effects within these biomechanical factors.

Motivation

Due to the complexity of traumatic brain injuries, differences in injury rate or injury tolerance between males and females could be dependent on many different factors, such as physiological factors (e.g., cellular response to trauma), biomechanical factors (e.g., neuroanatomy or material properties), or environmental factors (e.g., exposure). To aid in this investigation, computational finite element (FE) brain models are used to study brain deformation, the biomechanical mechanism of diffuse axonal brain injuries, under a wide range of loading conditions. These tools offer a flexible platform for investigating the effect of various biomechanical parameters (e.g., geometry, material properties, and loading conditions), where each of these parameters can be controlled. The geometry of the state-of-the-art in FE brain models are based on neuroanatomical features captured using magnetic resonance imaging (MRI) scans, and these geometries can be representative of a single subject or a population average. Material properties of the various brain tissues are modeled using complex constitutive material models often derived from experimental testing. However, these material properties are often based on a population average and do not capture subject-specific material behavior. As medical imaging, experimental testing, and computational power improve, the ability of these FE brain models to predict brain strain from various head kinematics can advance the understanding of TBIs. Based on recent innovations, FE models with subject-specific geometrics can be quickly generated based on individual MRI scans (J. S. Giudice et al., 2020, 2021). Furthermore, FE brain models based on subject-specific neuroanatomies have been shown to produce different maximum principal strain and strain distributions throughout various brain regions compared to the response of an average brain geometry (S. Giudice & Panzer, 2020). Therefore, these subject-specific geometries can be used to study the effect of neuroanatomy on brain deformation between the sexes using male- and female-specific brain geometries.

The intrinsic properties of the brain, such as the geometry and material properties, can easily be modified in FE brain models to investigate their effects across a wide range of both individual and average parameter ranges. Using this inherent versatility and varied combinations of intrinsic properties, FE brain models can also be evaluated over a large spread of input kinematics. A global statistical analysis would assist in understanding the relative contributions of geometry, material properties, and boundary conditions to FE brain deformation and corresponding TBI metrics. There is a need for overall improved understanding of female TBI biomechanics, which can ultimately help formulate the criteria used to assess the effectiveness of injury countermeasures across the entire population.

Goal of Dissertation and Structure

The goal of this dissertation is to quantify sex-related differences in neuroanatomy, material properties, and head kinematics and their effect on brain deformation response in automotive loading environments using computational brain models. This goal will be accomplished through four specific aims:

1. Quantify the effect of sex-specific neuroanatomical differences on brain deformation during impact.
2. Quantify the effect of sex-specific brain material properties on brain deformation during impact.
3. Quantify the effect of sex-specific head kinematics resulting from automotive level impact scenarios on brain deformation.
4. Quantify the relative effect of each biomechanical factor on brain deformation.

This Introduction includes the primary background and motivation for the dissertation research, describes the overall goal of the dissertation, and provides the structure for the whole dissertation. Following a review of background research related to the goals of this dissertation (Chapter 1), five additional chapters are included to satisfy these aims. In Chapter 2, different biomechanical factors will be quantified from a sample of male and female brain anatomical MRIs to quantify the effect of neuroanatomy on brain deformation. In Chapter 3, a sample of male and female magnetic resonance elastography brain scans will be implemented into the FE brain models to quantify the effect different material properties have on brain deformation. In Chapter 4, a variety of real-world head kinematics from automotive crash environments will be used to quantify the effect of head kinematics on brain deformation. Finally, in Chapter 5, the relative effect of each of these biomechanical factors will be quantified to determine what intrinsic or extrinsic properties of the human brain have the greatest effect on brain deformation during head impacts. Ultimately, the conclusions, contributions, limitations, assumptions, and future work will be summarized in the final Conclusions (Chapter 6).

Expected Contributions

This dissertation will begin to address gaps in the current understanding of sex-specific biomechanics factors and their effect on brain deformation and is innovative in several aspects.

1. This work is the first to holistically quantify the relative contributions of neuroanatomy, material properties, and head kinematics on brain deformation metrics using finite element brain models.
2. This work is the first to evaluate the effect of sex-specific parameters within these biomechanical factors on brain deformation metrics.
3. The proposed work will investigate the combined effect of subject-specific neuroanatomies and subject-specific material properties on brain deformation using both male and female subject-specific finite element models in automotive crash environments.

Overall, the application of this dissertation will improve our understanding of female TBI, will explain the differences between male and female brain deformation response during head impacts, and will inform future TBI research by identifying the biomechanical factor with the greatest effect on brain deformation within both the male and female populations.

Chapter 1: Background

This chapter offers a literature review of the pertinent background information for the dissertation research and includes a review of brain neuroanatomy, brain material properties, head kinematics relevant to automotive loading environments, advanced neuroimaging analysis techniques, finite element (FE) brain models, brain injury metrics, and the clinical relevance of this dissertation research with special interest in sex-specific considerations.

Brain Neuroanatomy

The brain is arguably the most complex human organ with billions of cells that manage "elaborate molecular, cellular, and neuronal phenomena that together form the physical and biological basis of cognition" (Bassett & Gazzaniga, 2011). The adult human brain weighs between 1070-1767g for males and 1000-1618g for females and is primarily composed of three main parts: the cerebrum, the cerebellum, and the brainstem (Figure 1) (Molina & DiMaio, 2012, 2015; Purves et al., 2011). The cerebrum accounts for more than two-thirds of the total brain weight and is composed of two hemispheres connected by a large bundle of myelinated nerve fibers (Azevedo et al., 2009). Each of the hemispheres is divided into four lobes – frontal, parietal, temporal, and occipital – primarily based on brain function in those regions (Figure 1) (Purves et al., 2011). The frontal lobe is mainly responsible for higher executive function, such as problem solving, planning, and emotional regulation, as well as personality. The parietal lobe is responsible for interpreting some sensory information, such as touch and taste. The temporal lobe is responsible for processing and understanding language, as well as some sensory information, such as interpreting sounds and smells. Finally, the occipital lobe houses the primary visual cortex and is responsible for interpreting visual information (Purves et al., 2011). The cerebellum, which is Latin for "little brain," plays a critical role in motor control, coordination, and balance. Finally, the brainstem connects the brain to the spinal cord and is responsible for regulation of many vital functions, such as breathing, blood pressure, and heart rate (Purves et al., 2011). The outer surface of the cerebrum and cerebellum is folded into gyri (ridges) and sulci (grooves) which increase the surface area of the brain.

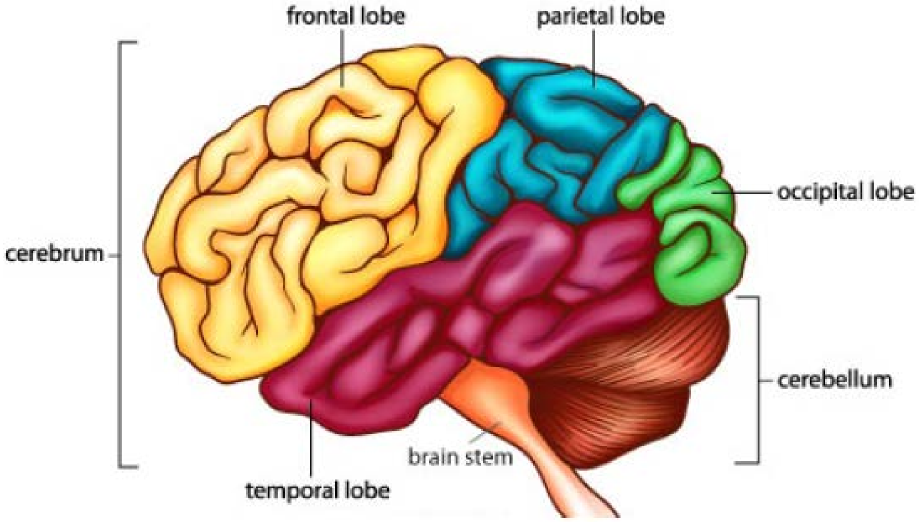

Figure 1: The major macroscopic regions of the human brain (cerebrum, cerebellum, and brain stem) and the lobes of the cerebrum (frontal, parietal, temporal, and occipital). (Source: Idaho Public Television ("The Brain: Facts Science Trek: Idaho Public Television)").

Surrounding the entire brain parenchyma are three membranes (from superficial to deep), the tough dura mater, the middle arachnoid mater, and the thin pia mater, collectively called the meninges (Purves et al., 2011). Cerebral spinal fluid (CSF), a colorless bodily fluid, is housed in the sub-arachnoid space between the pia mater and the arachnoid mater. CSF acts as a mechanical and immunological protection mechanism to the brain. A mechanical function of the meninges and CSF is protection of the brain by tightly coupling the brain tissue to the skull and providing stability and limiting movement (Decimo et al., 2012).

The brain tissue is composed of two major types of cells: neurons and glia cells. Neurons are electrically excitable cells that are responsible for sending and receiving signals via neurotransmitters; these connections form neural pathways and neural circuits to generate brain activity (Purves et al., 2011). A neuron is composed of the soma, dendrites, axon, and axon terminals. The soma, or the body of the neuron, contains the nucleus of the nerve cell. The dendrites are cellular extensions that receive signals sent from other neurons. The axon of the neuron passes signals from the cell body to the axon terminals which then transmit the signal to other neurons, muscles, or glands. The myelin sheath, a lipid-rich substance, wraps around the axon to insulate and increase the rate of electrical signals passing along the axon (Purves et al., 2011). The gray matter regions of the brain are primarily composed of the soma of neurons and is classified as either deep gray matter or superficial gray matter, also known as the brain cortex (Mercadante & Tadi, 2020). The white matter regions of the brain are mainly composed of myelinated axons, and a bundle of these myelinated axons form tracts throughout the brain tissue (Purves et al., 2011). Glia cells act as support cells in the nervous system by maintaining homeostasis and providing support and protection for nerve cells (Jessen & Mirsky, 1980).

To visualize *in vivo* anatomical structures throughout the brain, advanced medical imaging techniques, such as magnetic resonance imaging (MRI), are used by clinicians and scientists. MRIs are created using a strong magnetic field and radio waves to image brain tissue within the skull without any disruption to the tissue or surrounding structures. In summary, the magnetic field first aligns the protons within the body to this known field; the protons are then stimulated and spin out of equilibrium due to the presence of an applied radiofrequency field. The radiofrequency field is removed, and the protons will realign to the magnetic field. The time required for this realignment and the energy released are dependent on different types of tissue. Based on these properties, different tissues can be highlighted in MRI scans (Hashemi et al., 2012). A T_1-weighted anatomical scan highlights the differences in the T_1 relaxation times of different tissues and is a commonly used MRI in defining neuroanatomical structures, where CSF is dark, white matter is light, and gray matter is gray throughout the brain tissue (Figure 2) (Bigler, 2015).

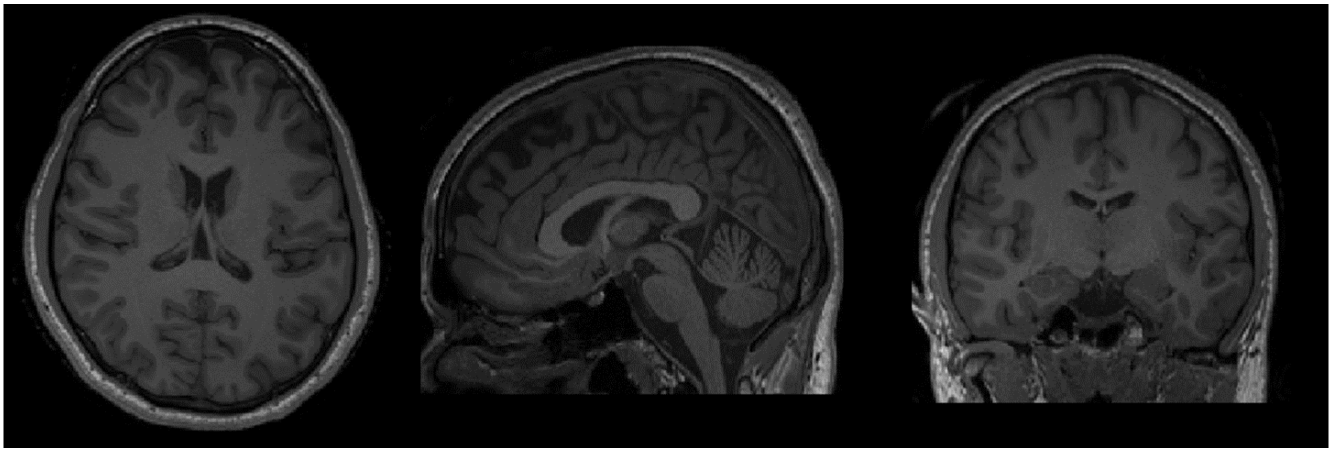

Figure 2: T_1-weighted MRI brain scan for a single subject, including the transverse plane (left), sagittal plane (center), and coronal plane (right).

Sex-Specific Consideration in Neuroanatomy

Multiple imaging studies have identified anatomical differences between male and female brains (Jäncke et al., 2015; Lotze et al., 2019; Ritchie et al., 2018); however, many of these sexual dimorphisms are very small and most are not statistically significant after accounting for total brain volume (Ritchie et al., 2018). Nonetheless, it is widely accepted that both total brain volume (brain parenchyma) and intracranial volume (ICV) (brain parenchyma, cerebrospinal fluid, and meninges) of the male brain are larger than female volumes, on average (Eliot et al., 2021). The male total brain volume and ICV are reported to be 11% and 12% larger, respectively, compared to the female brain (Ritchie et al., 2018; Ruigrok et al., 2014). Additionally, previous studies have shown a higher ratio of gray matter to white matter in females, with the magnitude of this difference ranging from 4% to 7% (Leonard et al., 2008; Pintzka et al., 2015; Ritchie et al., 2018). Once total brain volume was considered a covariate, the significance of this sex difference was greatly reduced (Jäncke et al., 2015; Leonard et al., 2008) and ultimately, larger brains had a larger proportion of white matter, regardless of sex (de Jong et al., 2017). While the gray to white matter ratio might not be sexually dimorphic, it is important to consider the non-linear scaling of white matter when comparing FE brain models that model white and gray matter separately, given different material properties may be assigned to each.

For smaller structures in the brain, such as the subcortical gray matter structures, previous studies have concluded contradictory results regarding volumetric sex differences (Coupé et al., 2017; Lotze et al., 2019; Potvin et al., 2016; Ritchie et al., 2018). As MRI data sets continue to expand, researchers are moving away from the "gold standard" manual tracing and identification of anatomical structures to automated segmentation-based methods (e.g., voxel-based morphometry) (J. S. Giudice et al., 2020; Li et al., 2021; Lotze et al., 2019). These automated processes involve registering each individual brain MRI to a template MRI, which are often created based on a limited population of healthy brains and are often constructed from a sample with unequal numbers of male and female brains (Eliot et al., 2021). Eliot *et al*. reviewed multiple studies to compare the effects of segmentation method on subcortical gray matter volumetric measurements and found volumetric measurements of subcortical gray matter structures varied due to method (manual tracing or automated segmentation) and measured structure, and error was greater for smaller structures (Eliot et al., 2021; Grimm et al., 2015; Makowski et al., 2018). Smaller sex differences were also found when comparing studies using manual traces methods, and these differences "all but disappeared" when using intracranial volume as a covariate (Kennedy et al., 2009; Marwha et al., 2017). When accounting for either total brain volume or intracranial volume, no subcortical gray matter structure was found to be larger in male or females across all studies (Eliot et al., 2021). While it is unknown if these measurement discrepancies affect volumetric sex differences, the range in these findings might contribute to the inconsistency of results for small subcortical gray matter structures (Eliot et al., 2021).

While many geometric differences between male and female neuroanatomies are small, if present at all, using subject-specific geometries based on individual MRI scans can account for these differences seen between the two sexes and across varying brain volumes. Literature suggests difference in total brain volume and intracranial volume are the largest geometry-related sex differences in the brain and should be considered in brain models designed to represent the average male and average female brain response (Ritchie et al., 2018).

Brain Material Properties

In addition to its function and structure, the brain's mechanical properties are also both complex and difficult to characterize. A majority of previous material characterization of brain tissue has been completed using *ex vivo* tissue across a variety of different loading conditions, including tension (Budday, Sommer, Birkl, et al., 2017; Budday et al., 2020; Jin et al., 2013), compression (Budday, Sommer, Birkl, et al., 2017; Budday et al., 2020; Jin et al., 2013), shear (Budday, Sommer, Birkl, et al., 2017; Budday et al., 2020; Darvish & Crandall, 2001; Jin et al., 2013), and indentation testing (Alshareef et al., 2015; Budday et al., 2015, 2020). Due to the complexity of the material, there is not a single set of material properties accepted by the biomechanics field to define brain tissue across different loading conditions. However, it is agreed that brain tissue is a nonlinear (Budday et al., 2015; Darvish & Crandall, 2001), anisotropic (Budday et al., 2015; Jin et al., 2013), nearly incompressible (Libertiaux et al., 2011), viscoelastic material (Darvish & Crandall, 2001). The wide range of material properties of brain tissue could be based on many differences of material testing between previous studies, including the effect of temperature (Arbogast & Margulies, 1998), loading magnitude or rate (Budday et al., 2020; Jin et al., 2013), loading condition (Budday, Sommer, Birkl, et al., 2017; Budday et al., 2020; Jin et al., 2013), or specimen preparation (e.g., storage conditions, post-mortem time of specimen collection) (Fallenstein et al., 1969; Garo et al., 2007).

With advancements in imaging technology, basing brain material characterization solely on *ex vivo* testing, which can be affected by many factors, is no longer necessary. As determining *in vivo* brain material properties using *ex vivo* mechanical testing is impossible without disrupting its biological function and natural environment, recent research has focused on calculating material properties based on magnetic resonance elastography (MRE) of healthy human brain tissue (Arani et al., 2015; Hiscox et al., 2018, 2020; Sack et al., 2009). Using MRE, the viscoelastic properties of the brain are noninvasively quantified by tracking the propagation velocity of micron-level displacements induced in the brain by an external actuator. Using nonlinear inversion, the material properties of the brain tissue are computed, resulting in three-dimensional maps of shear modulus and damping ratios (Hiscox et al., 2020). However, further work is needed to relate the material properties from such small deformations used in MRE to material properties required to capture larger and quicker deformations seen in injurious loading conditions due to the nonlinearity and viscoelasticity of the human brain tissue.

Sex-Specific Considerations in Brain Material Properties

As the number of scanned individuals within MRE datasets increase, the effect of sex on brain stiffness has gained greater attention (Arani et al., 2015; Sack et al., 2009; Wuerfel et al., 2010). Healthy females have been shown to have approximately 10% stiffer brain tissue compared to males across the entire brain parenchyma, and other studies have concluded females have stiffer temporal and occipital lobes (Arani et al., 2015; Wuerfel et al., 2010). Additionally, McIlvain *et al.* concluded females have a higher stiffness and a lower damping ratio in subcortical gray matter structures; however, Hiscox *et al.* found no significant difference in subcortical gray matter damping ratios between males and females, but concluded a significant sex-difference between the damping ratios in white matter (Hiscox et al., 2020; McIlvain et al., 2018). Tissue stiffness and damping ratios captured using MRE for the healthy adult human brain have identified differences for sex-specific material properties, but these MRE material property distributions can also capture subject-specific material features. Further shape analyses can compare these material distributions between the male and female cohorts to determine if sex affects material and strain distributions throughout the brain.

Brain Mechanics and Head Kinematics

Brain deformation mechanics depends on the intrinsic properties of the brain, such as the neuroanatomy and the material properties, as well as the extrinsic loading conditions, such as the head kinematics experienced during an impact. Due to the coupling provided by the meninges, the external kinematics experienced by the skull create deformations within the brain tissue, and it is assumed these tissue deformations cause brain injuries. TBIs caused by these closed-head injuries, or non-penetrating injuries, are often classified as diffuse TBIs and are commonly the result of inertial loading of the head. While the injury mechanism is not currently agreed upon, the most widely accepted hypothesis is the rotational kinematics of the head generate internal brain deformations which strain neurons and either tear or disrupt the physiological function of the axon (Dollé et al., 2018; Holbourn, 1943). Originally hypothesized by Holbourn in 1943, the theory was based on the low shear modulus and near incompressibility of the brain; therefore, the strain induced by the rotation of the skull would be much larger than strain resulting from linear acceleration (Holbourn, 1943). Since this original theory, previous studies have shown poor correlation between brain strain and linear acceleration (Gabler et al., 2016; Kleiven, 2007; Takhounts et al., 2008a, 2013).

The relationship between brain deformation and head kinematics has been a large focus for brain injury biomechanics research (Gabler et al., 2016; Gabler, Crandall, et al., 2018; Gabler et al., 2019; Takhounts et al., 2013). While more recent studies have focused primarily on the rotational kinematics, Gabler et al. investigated the effect of magnitude and duration of angular acceleration on brain deformation using the maximum magnitude of displacement between a single-degree-of-freedom mechanical system and strain-based injury metrics from FE brain models (Gabler, Joodaki, et al., 2018). For long-duration pulses, brain deformation depended primarily on the angular acceleration, while for short-duration pulses, brain deformation depended primarily on the angular velocity (Figure 3). Between these short- and long-durations pulses, near the systems natural period, brain deformation was dependent on a combination of angular velocity and acceleration components (Gabler, Joodaki, et al., 2018).

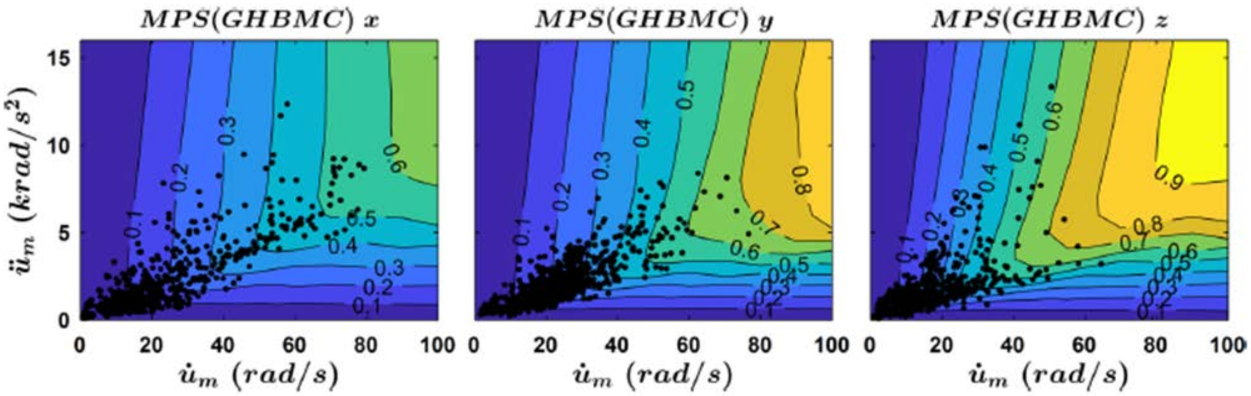

Figure 3: Contour plots showing relationship between velocity, acceleration, and MPS across a range of head kinematics. Contour lines represent constant levels of MPS (Source: Gabler et al. 2018).

However, due to limited well-characterized human brain injury datasets, it is difficult to relate head kinematics, brain strain, and injury risk in order to generate an injury risk function to begin to predict the presence of a brain injury given only information about the loading condition (Sanchez et al., 2017). Recent efforts, such as improvements to wearable sensors, have increased the size and reliability of these injury datasets, but additional attention should be paid to the population variability sampled in these datasets.

Sex-Specific Considerations in Head Kinematics

Potential differences in the extrinsic factors, such as exposure or head kinematics, may contribute to the overall difference in male and female brain deformation and injury. The greatest challenge in investigating the effect of these extrinsic properties is the lack of comparable data between male and female head kinematics under the same loading conditions. Comparable male and female head kinematics have been generated in pseudo-matched injurious cadaveric sled tests, matched volunteer low-severity sled tests, and using full-body computational models in automotive crash loading scenarios.

There are many physiological differences between males and females, which can lead to differences in head kinematics under similar crash or impact conditions, such as mass distribution, cervical vertebrae dimensions, and neck strength (Nikolova & Toshev, 2007; Vasavada et al., 2008; Young et al., 1983). The female neck has 33% more head mass per unit of neck muscle area compared to a height and neck length matched male with more slender necks and less neck cross-sectional area (Vasavada et al., 2008). Additionally, the female neck has only, on average, 68% and 80% of the strength of a size-matched male neck in flexion and extension, respectively (Vasavada et al., 2008). Onset of muscle activation for male and female neck muscles have also been shown to be significantly different during volunteer sled testing (Brault et al., 2000). Neck strength and anticipatory neck muscle activation have been shown to reduce the magnitude of the resulting head kinematics (Eckner et al., 2014; K. A. Reynier et al., 2020); therefore, independent male and female head kinematics are required to further understand the difference in male and female brain deformation and injury.

Brain Imaging Analysis Techniques

To quantify neuroanatomical features across different subject images captured using different MRI scanners, normalization techniques are applied to brain scans to account for some of these differences, such as scanner resolution or image origin location. The Advanced Normalization Tools (ANTs) software package is able to normalize multiple brain images to a single common image space to aid in comparisons between multiple individuals; in addition, ANTs can generate template brain images, subject-specific registration to template image space, multi-tissue segmentation of brain images, and cortical thickness calculations (B. B. Avants et al., 2008; B. Avants & Gee, 2004; Das et al., 2009; Wang et al., 2013).

Image Registration

The foundation of image registration is computing a transformation for each voxel within the “moving” image to geometrically align the moving image with a “fixed” image (Toga & Thompson, 2001). The registration process consists of two steps. First, an affine transformation is computed to align the moving image with the fixed image; this transformation can translate, rotate, scale, and shear the moving image to align with the fixed image (B. B. Avants et al., 2008). Next, a non-linear transformation is applied to the now aligned moving image to deform the moving image's voxel to correspond with the voxels in the fixed image (B. B. Avants et al., 2008). The transformations created by registering an individual subject's brain scan to a template brain scan can then be applied to template finite element brain models to generate subject-specific brain models (J. S. Giudice et al., 2020).

Brain MRI Tissue Segmentations

To quantify tissue shapes, volumes, or thicknesses throughout the brain, image segmentation is often necessary. The true "gold standard" tissue segmentation is manual segmentation of the brain; however, due to the time required for manual segmentation and the increasing number of brain MRI scans, automated processes have dominated recent studies (Klauschen et al., 2009; Wang et al., 2013). Atlas-based segmentation is a widely used technique which applies the segmentation of a previously labeled image, the atlas, (e.g., a segmented template image) to a novel target image (e.g., a single subject image) using the unique one-to-one mapping developed by registering the novel target image to the labeled image space (Rohlfing et al., 2005). The segmentation error associated with atlas-based segmentation is a result of the registration error between the two images; to help reduce this segmentation error, multiple atlases can be included in the segmentation process, referred to as joint label fusion (Wang & Yushkevich, 2013).

Cortical Thickness Calculations

Cortical thickness is often calculated due to its correlation to disease states, such as Parkinson's disease or dementia, and differences in material properties and thickness in some cortical gray matter regions between males and females (Hiscox et al., 2020; Luders et al., 2006; Lyoo et al., 2010). First, the cortical mantle is defined as the tissue between the gray matter-white matter and gray matter-cerebrospinal fluid interfaces (Das et al., 2009). Then, using a Diffeomorphic Registration based Cortical Thickness (DiReCT) measure, the thickness of the cortical mantle is calculated as a distance measure between the two previously defined interfaces (Das et al., 2009; Tustison et al., 2021). Using standard labelled atlases of cortical gray matter regions, such as the Desikian-Killiany-Tourville atlas, thickness and volumes can be reported for different regions throughout the cortical mantle (Klein & Tourville, 2012).

Finite Element Brain Models

Finite element brain models are used to simulate external loads measured during injurious and uninjurious events (often in the form of head kinematics data) to predict the internal brain deformation response resulting from these mechanical loads. A summary of how models are created and formulated for the most widely used FE brain models in injury biomechanics are reviewed in Madhukar et al. 2019 and Giudice et al. 2019, respectively (J. S. Giudice et al., 2019; Madhukar & Ostoja-Starzewski, 2019). The geometries of most FE brain models are based on a single subject's anatomy taken from high resolution medical images, either computer topography (CT) or MRI scans, and often represent the gross anatomy of a mid-sized male. It has been impractical to create new models of different anatomy from another set of medical images owing to the lengthy process of model development. However, recent advancements in image registration and model morphing have allowed for the ability to rapidly generate geometrically subject-specific FE brain models using a template model (J. S. Giudice et al., 2020).

Using MRI anatomical scans and registration-based morphing (RBM), subject-specific FE brain models can be generated to accurately capture size, shape, and local geometry characteristics. The RBM workflow used in this dissertation is based on the methodology developed by Guidice et al. (J. S. Giudice et al., 2020). A template brain image was created from a larger dataset of T1-weight MRI brain images to generate a representative geometry. Based on the template brain image, a template brain model was developed and calibrated using *in situ* brain deformation experimental data (J. S. Giudice et al., 2021). This template brain FE model can then be morphed to a given neuroanatomy using a subject-specific T1-weighted MRI scan (Figure 4).

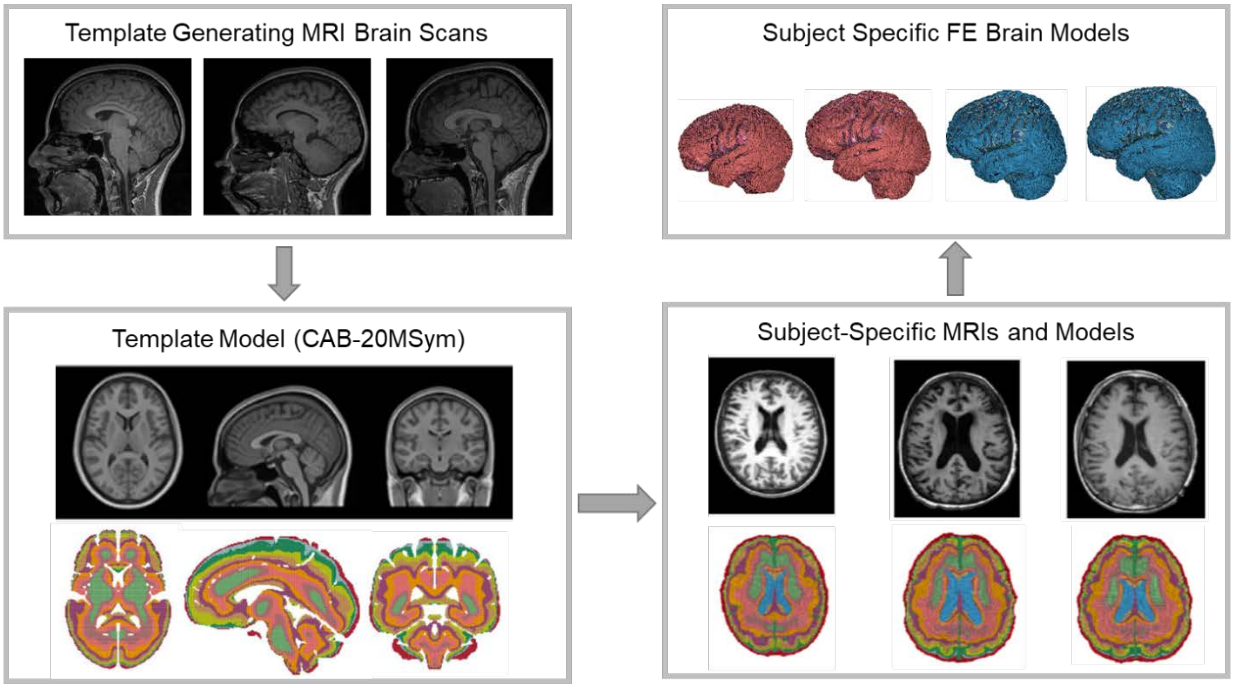

Figure 4: Process for generating subject-specific FE brain models based on individual's MRI brain scans (Figures courtesy of Giudice et al. 2020)

Additionally, most FE brain models use homogenous material definitions throughout a single tissue type within the brain (e.g., all white matter is modeled using the same material parameters) (J. Giudice et al., 2019; Madhukar & Ostoja-Starzewski, 2019). With recent advancements of MRE, the distribution of material properties, such as shear stiffness and damping ratios, can be implemented into the material definitions of certain elements within FE brain models to create heterogeneous brain tissue (Alshareef et al., 2021; J. Giudice et al., 2021). In these heterogenous material defined FE brain models, the number of heterogeneous regions does affect brain deformation metrics, such as MPS; as more information is derived from advanced imaging techniques, FE models will continue to increase in complexity in the attempt to capture brain deformation response more accurately (Figure 5).

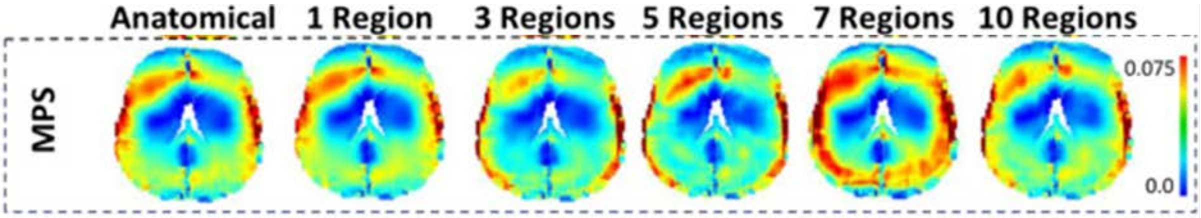

Figure 5: The MPS distributions throughout a single FE brain model using the same input kinematics to highlight the effect of different numbers of heterogenous materials throughout the FE model.

Sex-Specific Considerations in Brain Finite Element Models

One of the largest limitations of the widely used FE brain models is the lack of variability in both geometries and material properties implement. A majority of the FE brain models are based on a variety of different anatomies but are primarily focused on capturing the geometry of a mid-sized adult male (Madhukar & Ostoja-Starzewski, 2019). However, brain anatomies can vary widely across the population in volumes, dimensions, ventricle size, etc., and these differences in neuroanatomy will affect the resulting brain deformation (J. Giudice et al., 2019; K. Reynier et al., 2021). Even FE brain models that were developed based on a female neuroanatomy (e.g., the Global Human Body Models Consortium (GHBMC) 5th percentile female) was formulated using the same material properties as the GHBMC 50th percentile male (Davis, 2017; Mao et al., 2013). The current FE models do not capture the population variance or sex-specific characteristics, in either neuroanatomies or material properties, and more work is needed to explore the effect of this variance on brain deformation response.

Brain Injury Metrics

Injury criteria metrics used to predict brain injury can be categorized as kinematic-based or tissue-level-based. Kinematic-based metrics are dependent on the rigid-body motion of the head, while tissue-level metrics are dependent on the mechanics and deformation of the brain tissue as observed with a brain FE model (Gabler, Joodaki, et al., 2018). These kinematic-based metrics use a combination of linear and/or rotational velocities and/or accelerations, however, more recent brain injury criteria relate these input head kinematics to a strain-based brain response using FE brain models (Gabler, Crandall, et al., 2018; Gabler et al., 2016, 2019). Two commonly used brain strain metrics from brain FE models are the 95th percentile maximum principal strain (MPS-95) and the cumulative strain damage measure (CSDM). If a head impact simulation is performed and the peak maximum principal strain (MPS) of each element is recorded and stored during the simulation, then MPS-95 represents the 95th percentile of all the peak MPS values in the elements of the brain model; the CSDM represents the volume fraction of elements that have a MPS that has exceeded a predefined threshold (often 25% strain). MPS-95 is typically used to avoid the influence of any extreme strain levels that could skew this global deformation metric (Gabler et al., 2016). Ideal brain metrics can predict the tissue-based brain strain response across a variety of loading conditions with the ease and simplicity of a kinematic-based metric.

Additionally, strain-based brain injury metrics, such as the MPS-95 and CSDM, are also often used to determine brain deformation response in FE brain models. A recent study, completed by Wu et al., evaluated the efficacy of a variety of tissue-based brain injury metrics using a brain injury database of human, non-human primate, and pig TBI data (Wu et al., 2021). Overall, 95th percentile maximum principal strain (MPS-95), 95th percentile maximum axonal strain (MAS-95), 95th percentile maximum principal strain rate (MPSR-95), 95th percentile maximum axonal strain rate (MASR-95), products of maximum strains and maximum strain rates for both principal strain and axonal strain, CSDM-25, and CSDM-15 were evaluated to determine which metric was the best predictor for injury. When using multi-species injury data, MAS-95 was the best metric for distinguishing between mild and severe TBIs, and MPS-95 was also a strong predictor of injury (Wu et al., 2021). However, it should be noted that these injury risk functions apply only to the model used for injury risk function development, and a methodology would need to be completed to determine equivalent injury thresholds for additional FE brain models.

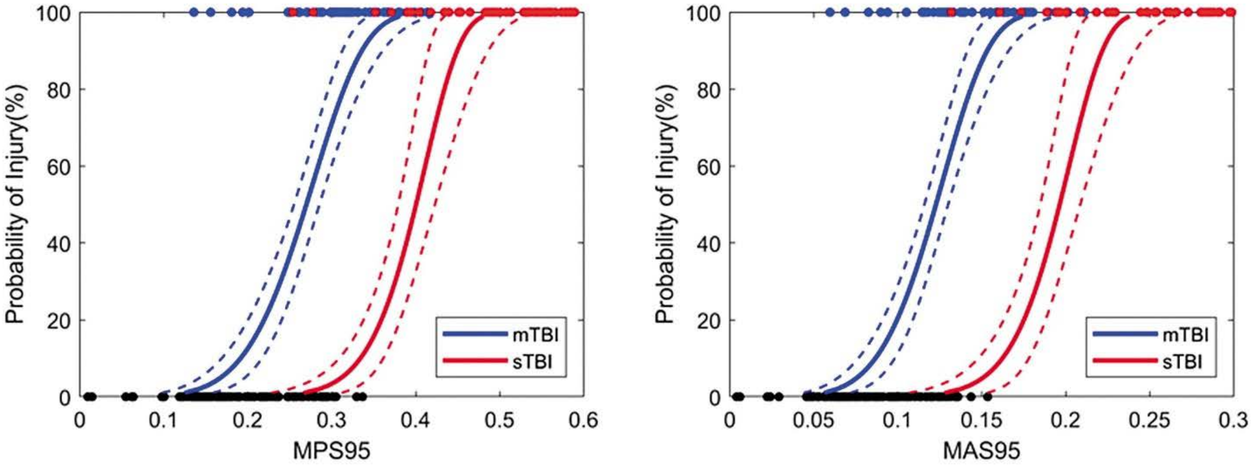

Figure 6: Mild and severe TBI risk function from multi-species dataset using MPS95 and MAS95 as injury predictors (Source: Wu et al. 2021).

Sex-Specific Considerations in Brain Injury Metrics

The previously reviewed brain injury metrics, specifically BrIC, UBrIC, and DAMAGE, relate head kinematics to brain deformation using FE brain models; however, each of these metrics were developed using a 50th percentile male anatomy and have not yet been evaluated for application with female brains or anatomies of other sizes (Gabler, Crandall, et al., 2018; Gabler et al., 2019; Takhounts et al., 2013). Because females, on average, have smaller total brain volumes than males and volume has been shown to affect deformation response of the human brain across multiple kinematic inputs, more research is needed to understand how best to develop female-specific or anthropometric-specific brain injury metrics and interpret tissue-level injury metrics (K. Reynier et al., 2021; Ritchie et al., 2018). Another consideration when creating kinematic-based brain injury metrics are the head kinematics used in the fitting of the metric predictor models. For example, the parameters used for UBrIC and DAMAGE came from databases of more than 1600 real-world head kinematics from volunteer sled testing, postmortem human surrogate (PMHS) sled and crash tests, dummy sled and crash tests, pedestrian sled tests, and helmeted and un-helmeted dummy impact tests (Gabler, Crandall, et al., 2018; Gabler et al., 2019). Of the total head kinematics included in the dataset, 158 of the head kinematics were from either female anthropometric test devices (e.g., Hybrid III 5th percentile female) or female PMHS sled tests. Increasing the variability of surrogates in the head kinematics database can increase applicability of the metrics developed.

Clinical Relevance

The risk of brain injury associated with a patient's sex, age, and cause of injury, as well as the severity of injury, location of injury, and possible symptoms and outcomes from a brain injury could aid clinicians in more accurately diagnosing and treating brain injuries. As FE brain models and imaging techniques advance, the ability to generate subject-specific geometric and material brain models that can be simulated using an individual's injurious head kinematics becomes easier and more realistic in clinical settings. However, the relative importance of these biomechanical factors (e.g., sex, age, or brain volume) under impact loading is currently unknown. While the effect of age on material properties has been studied using MRE data, less is known about the effect of other biomechanical factors, such as sex (Arani et al., 2015; Hiscox et al., 2021; Sack et al., 2009). Clinical studies have investigated the potential neuroprotective effects of female sex hormones, estrogen, and progesterone. Results across studies have not been consistent and results have not translated from animal studies to human clinical trials (Bramlett & Dietrich, 2001; Clevenger et al., 2018; Gupte et al., 2019; Roof et al., 1993; Roof & Hall, 2000; Skolnick et al., 2014). Some studies have concluded a neuroprotective element to these hormones with results showing normally cycling female rats exhibiting improved survival rates, blood-brain barrier integrity, and cortical blood flow, as well as less brain edema than male rats (Gupte et al., 2019; Roof & Hall, 2000). Conversely, when these findings were translated to human TBI clinical care, administering progesterone within 8 hours of a TBI in both male and female patients resulted in no significant improvement in the Glasgow Outcome Scale compared to patients who received a placebo (Skolnick et al., 2014). Therefore, additional work within sex-based biomechanics can attempt to answer further questions about the difference between male and female TBI based on intrinsic factors prior to the injury (e.g., neuroanatomies and material properties) and any sex-specific kinematics experienced during injury. One option to investigate the effect of these sex differences is using FE brain models with varied geometries and material properties.

Current state-of-the-art FE brain models calculate metrics that correlate to injury by predicting strain and spatial distributions of strain; however, the relationship between the model-predicted strains and injury, or the development of thresholds to relate model outcomes to injuries, are still open areas of research. These FE brain models capture the overall deformation of the human brain, but they are not yet validated to predict absolute strain values associated with axonal damage. However, during high rotational accelerations of the brain, studies have shown that microtubules within an axon can mechanically break, creating undulations along the axon and disrupting the transport of sodium and calcium ions (Dollé et al., 2018; Smith et al., 1999; Tang-Schomer et al., 2012; Tang-Schomer et al., 2010). This damage to the axon can cause swelling and activate proteases that begin to break down proteins. These pathological changes can create secondary axonal degeneration (Dollé et al., 2018; Tang-Schomer et al., 2012; Tang-Schomer et al., 2010). Additionally, recent research has shown that female axons are smaller with fewer microtubules, experience greater undulation under the same applied load, and experience greater calcium influx under the same applied load compared to male axons (Dollé et al., 2018). While the axonal damage is closely related to the injury mechanism and potentially differs between males and females, the effect of differences in extrinsic factors (e.g., head kinematics) and global intrinsic factors (e.g., neuroanatomies and material properties) on brain deformation should first be evaluated before concluding a sex-specific injury tolerance.

Finally, high strain may also explain locations of future swelling caused by damage to the axonal cytoskeleton from large inertial loading (Smith & Meaney, 2000). Post injurious swelling can cause further damage to the axon due to activation of proteases, enzymes that break down proteins; however, the current FE brain models used in this dissertation do not account for any post-concussive swelling effect. Future work simulating axonal swelling should consider potential differences in location, pattern, and severity of swelling between males and females (Farin et al., 2003).

Chapter 2: Effect of Neuroanatomy

The differences in male and female brain injury risk in motor vehicle collisions or sports could be a result of variations in brain deformation response, which depend on neuroanatomies, material properties, and impact head kinematics. The effect of neuroanatomy, or brain geometry, on brain deformation has been previously investigated using subject-specific FE brain models, but the effect of sex-specific neuroanatomical differences have not been well characterized (J. S. Giudice et al., 2020; K. Reynier et al., 2021). This chapter will quantify neuroanatomical differences between male and female brains and determine their effect on brain deformation, while keeping material properties and impact head kinematics conditions consistent across multiple neuroanatomies.

Introduction

Traumatic brain injuries (TBI) are a major public health issue in the United States, and based on the Centers for Disease Control, TBI-related hospital visits often occur from unintentional falls, sports injuries, assault, and motor vehicle collisions (Peterson et al., 2019). Within sports injuries and motor vehicle collisions, differences in TBI injury risk present between males and females, but the cause of these differences is unknown (Antona-Makoshi et al., 2018; Covassin et al., 2016; J. Forman et al., 2019). When controlling for factors associated with the occupant, such as age, height, BMI, and sex, and crash parameters, such as delta-V and vehicle model year, female, belted occupants involved in a frontal motor vehicle collision have significantly higher odds of sustaining a moderate brain injury, but male occupants have higher odds of sustaining a severe brain injury (AIS4+) (J. Forman et al., 2019). Similarly, in sex-matched collegiate sports, female athletes had higher concussion injury rates compared to male athletes (Covassin et al., 2016). While there are many possible contributing factors, differences in the brain's biomechanical response may affect these injury risks between the sexes, assuming increased brain deformation increases injury risk.

Brain neuroanatomy has been shown to affect overall brain deformation response in finite element (FE) models, for both subject-specific and single anthropometry (e.g., GHBMC F05 and M50) FE brain models (K. Reynier et al., 2021; K. Reynier et al., 2022; J.S. Giudice et al., 2022). As total brain volume increases, the 95th percentile maximum principal strains (MPS-95) increase linearly, when simulating brain deformation using equal head kinematic input (K. Reynier et al., 2021). The largest and most consistent anatomical difference between male and female brains is the difference in total brain volume; on average, the male brain total brain volume is 11% larger compared to the female brain, and this sex-difference could therefore impact brain deformation between the sexes (Ruigrok et al., 2014). Other global brain tissue metrics have been shown to be different between the sexes, such as females having between 4-7% greater ratios of gray to white matter (Leonard et al., 2008; Pintzka et al., 2015; Ritchie et al., 2018). While sex differences in smaller neuroanatomical features, such as subcortical gray matter regions, have been contradictory, population variance within these smaller regions could still have an effect on overall brain deformation (Coupé et al., 2017; Lotze et al., 2019; Potvin et al., 2016; Ritchie et al., 2018).

Finite element brain models are often used to investigate the effect of intrinsic factors, such as geometric features, on the resulting brain deformation response for a variety of head kinematic inputs while keeping other biomechanical factors (e.g., material properties) constant across multiple models. Subject-specific FE brain models are developed using high resolution medical images, often T_1-weighted magnetic resonance imaging, to capture small details associated with neuroanatomies. Based on the potential of these neuroanatomical differences, subject-specific FE brain models can then be used to capture the population and sex-specific variations in these geometric factors and isolate their effect on brain deformation. Therefore, the goal of this chapter is to quantify differences in neuroanatomic biomechanical factors between males and females using MRI brain scans and determine their effect on brain deformation measured utilizing subject-specific finite element brain models.

Methods

Subjects and MRI Scans

All T_1-weighted anatomical MRI brain scans were acquired from two previously completed imaging studies, Hiscox et al., 2020 and Bayly et al., 2021, and included healthy brain scans from both male and female subjects for a total of 142 scans (mean age = 24.0 years, SD = 5.8, range = 14-57) (Bayly et al., 2021; Hiscox et al., 2020). There were 82 females (mean age = 23.4 years, SD = 5.9, range = 18-57) and 60 males (mean age = 24.8, SD = 5.6, range = 14-54) included in this analysis. Additional details about the subject inclusion and exclusion criteria and imaging acquisition can be found in the original studies (Bayly et al., 2021; Hiscox et al., 2020).

Finite Element Brain Models

For each of the 142 T_1-weighted anatomical scans, a subject-specific FE brain model was generated using the registration-based morphing technique developed and the heterogeneous FE brain model developed by Giudice et al., 2020 and Giudice et al., 2021, respectively (J. S. Giudice et al., 2020, 2021). The CAB-20MSym template, developed from scans of 20 young, healthy male participants with 1 mm^3 isotropic voxels, was used to register all subject scans to a uniform space and create transformations to generate subject-specific models from the template FE brain model (J. S. Giudice et al., 2020; K. A. Reynier et al., 2020). From the CAB-20MSym template image, the CAB-20MSym template FE brain model was then developed and calibrated (J. S. Giudice et al., 2021). The CAB-20MSym FE brain model includes the brain parenchyma, peripheral CSF, internal CSF, and ventricles, where each region's voxels were converted to 1 mm hexahedral elements, as well as, the sagittal sinus, falx cerebri, and tentorium cerebelli modeled using two-dimensional shell elements (J. S. Giudice et al., 2021). Additionally, the dura is modeled using a rigid layer of shell elements surrounding the peripheral CSF, and all 6-DOF head kinematics were applied to the FE brain model via this rigid dura part through the head center of gravity in the local anatomic head coordinate system (Society of Automotive Engineers, 2007).

Additional details on the CAB-20MSym FE brain model development and calibration, including material formulation, can be found in Giudice et al., 2021.

For this study, the Advanced Normalization Tools (ANTs) software package was used to generate the registration transformations between a subject's individual brain scan and the template brain scan. First, each subject's anatomical T_1-weighted MRI scan was registered to the CAB-20MSym template (using "antsRegistrationSyN.sh" in ANTs) (B. B. Avants, Tustison, Song, et al., 2011). These registration transformations were then used to morph the CAB-20MSym template FE brain model into the subject space to create an anatomically subject-specific FE brain model. This process was repeated to generate 142 anatomically subject-specific FE brain models. For all the subject-specific FE brain models, the material properties, boundary conditions, and numerical implementations were kept consistent to isolate the effects of the different neuroanatomies.

All the FE brain models were simulated using the same input head kinematics, which were representative of a moderate automotive loading condition; specifically the head kinematics were of a cadaver in an oblique (60° far-side) sled test with a 32 km/h delta-V with the following brain injury metrics: BrIC = 0.86, UBrIC = 0.44, and DAMAGE = 0.33 (Figure 7) (J. L. Forman et al., 2013; Gabler, Crandall, et al., 2018; Gabler et al., 2019; K. Reynier et al., 2021; Takhounts et al., 2013). The peak absolute linear acceleration was 40.2 g, and the peak absolute angular velocity was 38.7 rad/s. The head anatomical coordinate system is in accordance with SAE J211 standards (SAE, 1995). All simulations were performed using the LS-DYNA explicit solver (mpp971R9.1.0, double precision, LSTC, Livermore, CA, USA), and run on 40 CPUs.

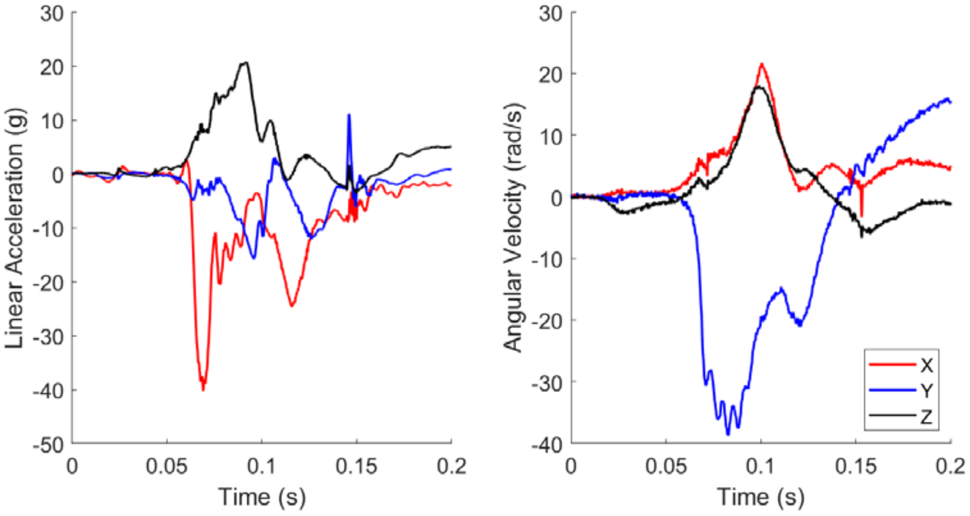

Figure 7: The 6 degree-of-freedom head kinematics applied to all subject-specific FE brain models via the rigid dura part.

Neuroanatomic Biomechanical Factor Definitions

Global volumes, such as total intracranial volume, gray matter volume, and white matter volume, were calculated based on the segmentation of the CAB-20MSym template image (Figure 8) (J. S. Giudice et al., 2020). Using a combination of automated segmentation techniques (using “antsAtroposN4.sh”) and manual segmentation, the CSF, gray matter, and white matter of the CAB-20MSym template were segmented to identify the different tissue regions (B. B. Avants, Tustison, Wu, et al., 2011; J. S. Giudice et al., 2020). The tissue segmentation was then applied (using “antsApplyTransforms.sh”) to each of the subject-specific T_1-weighted scans using the transformations between the subject space and the CAB-20MSym template space previously generated during registration. The ratio of gray matter volume to white matter volume was calculated based on these global volumes derived from the CAB-20MSym template.

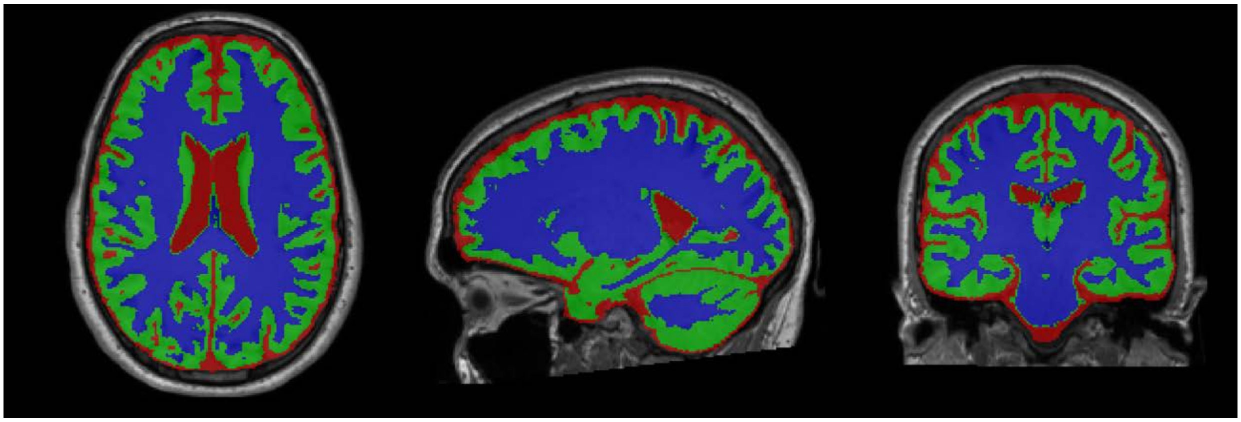

Figure 8: An example of a subject segmentation of the CSF (red), gray matter (green) and white matter (blue) in the axial (left), sagittal (center), and coronal (right) planes.

Cortical gray matter region of interests (ROI) were selected to represent different areas distributed equally throughout the brain and included cortical ROIs which were larger in size due to the spatial resolutions of the images and corresponding regions in the FE brain models (Hiscox et al., 2020). The Desikan-Killiany-Tourville labeling protocol was used to define the cortical regions, and the three ROIs selected in each of the four lobes corresponded to regions analyzed by Hiscox et al. 2020 in their comparison of material properties between male and female brain scans (Hiscox et al., 2020; Klein & Tourville, 2012). The ROIs analyzed were, in the frontal cortical region, the superior frontal cortex (SFC), rostral middle frontal (RMF), and precentral cortex (PRE); in the occipital cortical regions, the lateral occipital (LaO), lingual occipital (LiO), and cuneus (CN); in the parietal cortical regions, the superior parietal (SPC), postcentral (POST), and precuneus (PCN); and in the temporal cortical regions, the superior temporal cortex (STC), inferior temporal cortex (ITC), and fusiform gyrus (FSG) (Figure 9). The average thicknesses and volumes of the cortical gray matter ROIs were calculated for all subjects based on their T_1-weighted brain scans (using “antspynet.cortical_thickness”) (Tustison et al., 2021).

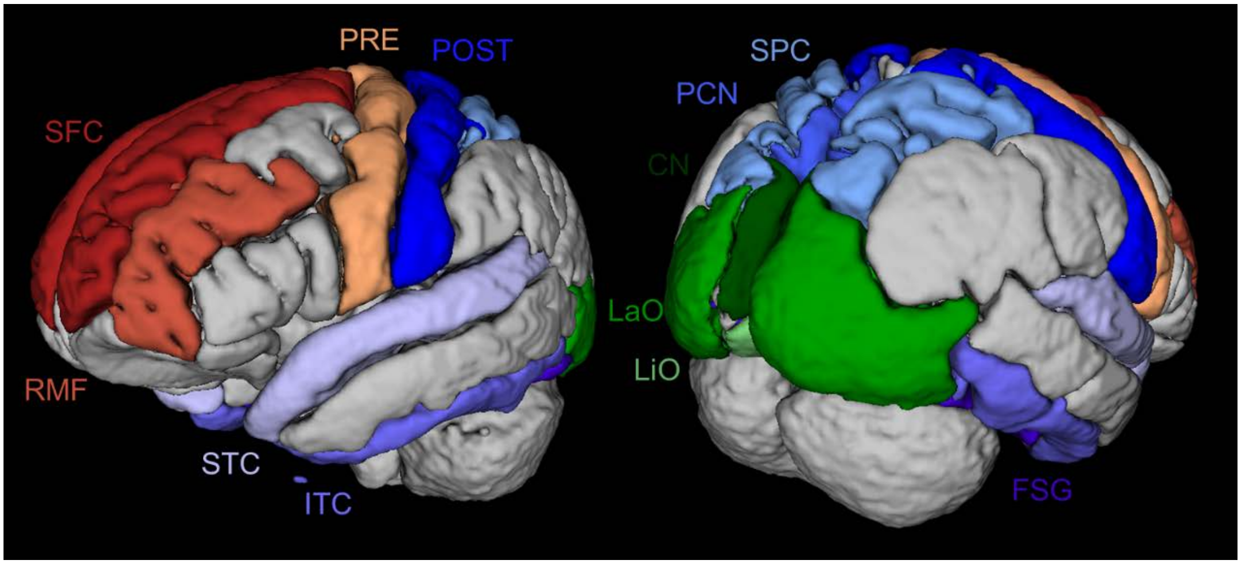

Figure 9: The cortical gray matter ROIs throughout the frontal lobe (red hues), occipital lobe (green hues), parietal lobe (blue hues), and temporal lobe (purple hues) using the DKT labeling on the ANTs-OASIS brain template (B. Avants & Tustison, 2018; Klein, 2016; Klein & Tourville, 2012).

Brain Deformation Metric Definitions

To assess global brain deformation, multiple metrics were calculated and included metrics of strain, strain rate, and the product of strain and strain rate (Wu et al., 2021). To avoid the potential effect of any numerical instabilities associated with the absolute maximum, the 95th percentile of each of these metrics was reported (Gabler et al., 2016; J. S. Giudice et al., 2020; K. Reynier et al., 2021). For clarity, the 95th percentile maximum principal strain (MPS-95) is defined as the 95th percentile of the maximum principal strain experienced by each white and gray matter brain element throughout the simulation; the 95th percentile maximum strain rate (MPSR-95) and the 95th percentile product of MPS and MPSR (MPSxMPSR-95) are defined similarly. Additionally, cumulative strain damage measure (CSDM), which represents the volume fraction of elements greater than a specified threshold, was calculated for two commonly used thresholds (15% and 25%) throughout the white and gray matter elements.

Brain deformation was also assessed within different tissue types of the brain parenchyma, specifically throughout the GM, WM, and cortical GM. For each of these tissues, MPS-95, MPSR-95, MPSxMPSR-95, CSDM15, and CSDM25, were also calculated based on the tissue definitions from the brain tissue segmentations.

Statistical Analysis for Neuroanatomical Factors and Brain Deformation Metrics

For the neuroanatomical biomechanical factors, a multivariate linear mixed model was used to determine if sex and age were statistically significant factors. Because the brain MRI scans were collected from different studies, a random study effect was also included in the linear mixed model (Hiscox et al., 2020). Due to the small number of studies (n = 5), mixed model estimation can be challenging due to a high likelihood of the study effect estimate being zero under a frequentist approach. To avoid this issue, analysis was carried out using a Bayesian linear mixed model where the biomechanical factors (outcome variables) were jointly modelled to take advantage of strong correlations among them. To determine sex effects on the neuroanatomical biomechanical factors, first, the Bayesian multivariate mixed linear model with global absolute and relative volumes had the following structure, with $Y_{ij}^{(k)}$ being the k_{th} outcome associated with the i_{th} brain model in the j_{th} study, with the model equation for ICV provided as an example below:

$$Y_{ij}^{ICV} = \left(\mathrm{β}_0^{ICV} + u_{j0}^{ICV}\right) + \beta_1^{ICV}\left(Age_{ij}\right) + \beta_2^{ICV}\left(Sex_{ij}\right) + \epsilon_{\mathrm{ij}}^{ICV}$$

where β_0 are the population intercepts, u_{j0} are the random intercepts for the j_{th} study, Age is the subject’s age in years (centered and scaled using the mean and standard deviation of the sample), Sex of the subject (reference = female), and $\epsilon_{\mathrm{ij}}^{k}$ are the outcome-specific residuals. The equations for the remaining global and relative volumes are provided in the Supplemental Materials. Due to the limited sample size, the neuroanatomical features were tested for sex effects in groups, with global tissue volumes (e.g., ICV, GM volume, relative WM volume) tested first, followed by absolute cortical thickness, absolute cortical volume, normalized cortical thickness (normalized using ICV), and normalized cortical volume (normalized using cubed root of ICV) with the following structure, with the SFC cortical region model provided as an example below:

$$Y_{ij}^{SFC} = \left(\beta_0^{SFC} + u_{j0}^{SFC}\right) + \beta_1^{SFC}\left(Age_{ij}\right) + \beta_2^{SFC}\left(Sex_{ij}\right) + \epsilon_{\mathrm{ij}}^{SFC}$$

The equations for the remaining cortical regions are provided in the Supplemental Materials.

For each of the individual outcomes (i.e., the biomechanical factors), priors sensitivity analysis was conducted for the intercept, the β terms, and the study random effect standard deviations. Based on this sensitivity, the priors with the largest standard deviation (i.e., least informative) with stable estimates were used in the final model. Estimation took place using the *brms* package in RStudio (R version 4.2.0) (Bürkner, 2017; R Core Team, 2022). Three parallel initially over dispersed Markov Chain Monte Carlo (MCMC) chains were used, where each chain ran for 3,000 iterations after the 2,000 iteration warmup. Effective sample sizes were examined to ensure each parameter’s effective sample size was greater than 1,000 for each parameter. A visual inspection of the MCMC chains and assuring that Rhat values were approximately 1.00 indicated acceptable convergence. Correlation between the material neuroanatomical features were computed, and highly correlated parameters (r > 0.8) were noted. All Credible Intervals (CrI) reported are 95% equal tailed intervals. For each neuroanatomical features, the intraclass correlation (ICC) was computed to report the correlation of observations within one study.

Similar methodology was used to determine significant biomechanical factor predictors of the deformation metrics, the order of importance of these biomechanical factors, and the significance of sex after accounting for these biomechanical factors. Therefore, to determine the effect of the neuroanatomical biomechanical factors and sex on the deformation metrics, the multivariate mixed linear model had the following structure, with $Y_{ij}^{(k)}$ being the k_{th} outcome associated with the i_{th} brain model in the j_{th} study, with the MPS-95 model provided as an example below.

$$
\begin{aligned}
Y_{ij}^{MPS-95} = {} & \left(\beta_0^{MPS-95} + u_{j0}^{MPS-95}\right) + \beta_1^{MPS-95}\left(Age_{ij}\right) + \beta_2^{MPS-95}\left(Sex_{ij}\right) + \beta_3^{MPS-95}\left(ICV_{ij}\right) \\
& + \beta_4^{MPS-95}\left(Rel\ WM_{ij}\right) + \beta_5^{MPS-95}\left(Rel\ GM_{ij}\right) + \beta_6^{MPS-95}\left(SFC\ Vol_{ij}\right) \\
& + \beta_7^{MPS-95}\left(RMF\ Vol_{ij}\right) + \beta_8^{MPS-95}\left(PRE\ Vol_{ij}\right) + \beta_9^{MPS-95}\left(LaO\ Vol_{ij}\right) \\
& + \beta_{10}^{MPS-95}\left(LiO\ Vol_{ij}\right) + \beta_{11}^{MPS-95}\left(CN\ Vol_{ij}\right) + \beta_{12}^{MPS-95}\left(SPC\ Vol_{ij}\right) \\
& + \beta_{13}^{MPS-95}\left(POST\ Vol_{ij}\right) + \beta_{14}^{MPS-95}\left(PCN\ Vol_{ij}\right) + \beta_{15}^{MPS-95}\left(STC\ Vol_{ij}\right) \\
& + \beta_{16}^{MPS-95}\left(ITC\ Vol_{ij}\right) + \beta_{17}^{MPS-95}\left(FSG\ Vol_{ij}\right) + \beta_{18}^{MPS-95}\left(SFC\ Th_{ij}\right) \\
& + \beta_{19}^{MPS-95}\left(RMF\ Th_{ij}\right) + \beta_{20}^{MPS-95}\left(PRE\ Th_{ij}\right) + \beta_{21}^{MPS-95}\left(LaO\ Th_{ij}\right) \\
& + \beta_{22}^{MPS-95}\left(LiO\ Th_{ij}\right) + \beta_{23}^{MPS-95}\left(CN\ Th_{ij}\right) + \beta_{24}^{MPS-95}\left(SPC\ Th_{ij}\right) \\
& + \beta_{25}^{MPS-95}\left(POST\ Th_{ij}\right) + \beta_{26}^{MPS-95}\left(PCN\ Th_{ij}\right) \\
& + \beta_{27}^{MPS-95}\left(STC\ Th_{ij}\right) + \beta_{28}^{MPS-95}\left(ITC\ Th_{ij}\right) + \beta_{29}^{MPS-95}\left(FSG\ Th_{ij}\right) + \epsilon_{\mathrm{ij}}^{MPS-95}
\end{aligned}
$$

The equations for the remaining deformation metrics (MPSR-95, MPSxMPSR-95, and CSDM-25) are provided in the Supplemental Materials. Priors were assigned after a prior sensitivity analysis as previously described. The same model fitting parameters in RStudio were used to estimate the neuroanatomical biomechanical factor and brain deformation metrics model. Correlations between the independent variables were assessed using the biomechanical factors linear mixed model described previously, and for pairs of variables with correlations greater 0.80, a single parameter was kept in the final model. The final linear mixed model included these uncorrelated, independent variables against the deformation metrics. Because all quantitative independent variables were centered and scaled, the relative importance of each biomechanical factor was determined using the absolute value of the estimated coefficient.

Results

Neuroanatomical Features

Overall, the median male brain volumes were larger than median female brain volumes for intracranial volume (ICV), GM volume, WM volume, and CSF volume (Figure 10). However, differences in relative volumes, normalized using ICV, were much smaller between the male and female brains, with the median female GM and WM relative volumes slightly greater than the corresponding male relative volumes (Figure 10). The GM to WM ratio for the males and females was not statistically significant (figure included in Appendix). For both the male and female subjects, there is a strong linear correlation between ICV and absolute GM, WM, and CSF volumes (Figure 11). When comparing the relative volumes of both GM and WM to ICV, the correlations for both the male and female volumes are much weaker (Figure 12). Additionally, as ICV increased, the relative WM volume increased, and the relative GM volume decreases for both sexes; this result has been shown previously in literature (Lüders et al., 2002). Based on the global absolute and relative volume Bayesian linear mixed model, the effect of sex was significant for ICV, WM volume, GM volume; however, after correcting for ICV, sex was not significant for either relative WM or GM volumes. Additionally, age was significant for WM volume, relative WM volume, and relative GM volume. The complete list of estimated parameters from the Bayesian linear mixed model is included in the Supplemental Materials. The ICC for each of the volumetric measurements were less than 0.02.

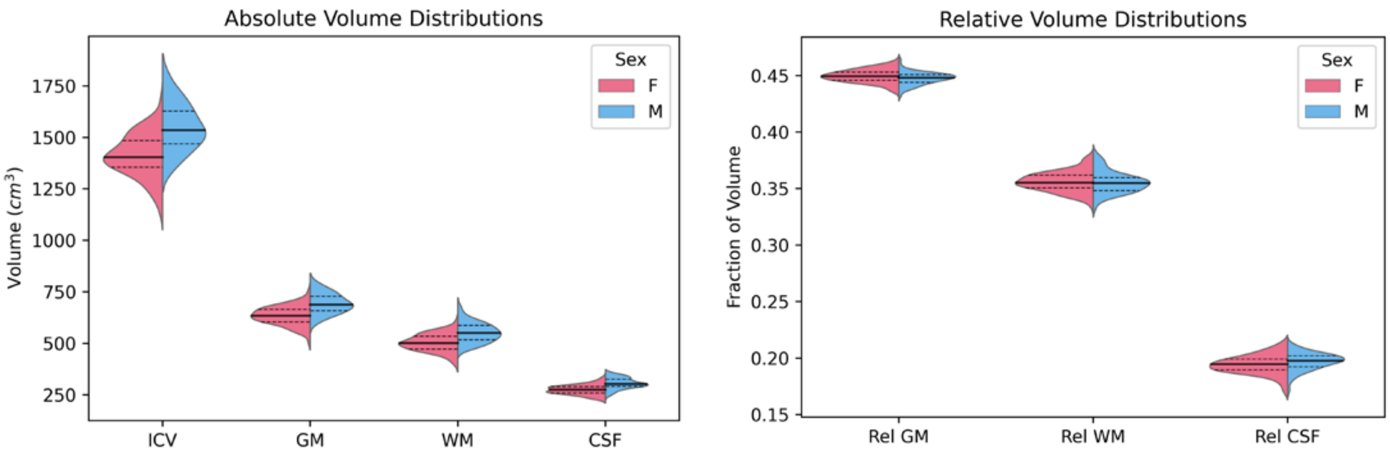

Figure 10: Distributions, based on an estimated probability density function, of the absolute volumes of ICV, gray matter, white matter, and CSF (left) and the relative volumes of gray matter, white matter, and CSF, normalized using ICV (right), for both the female and male subjects. Medians are represented by the solid line, and quartiles one and three are represented by the dashed lines.

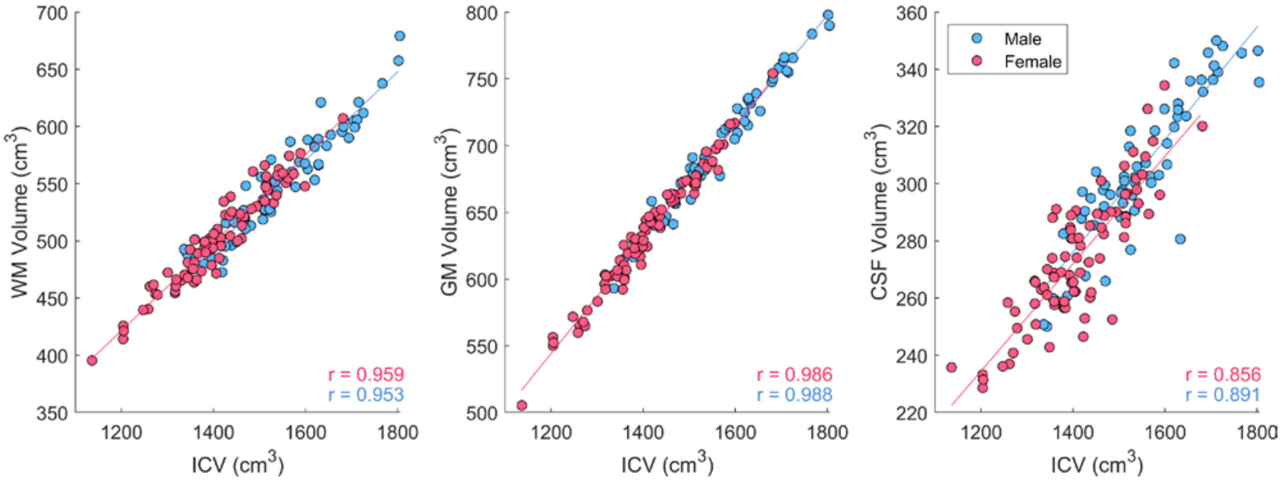

Figure 11: Scatter plots showing linear relationship between ICV and absolute white matter (left), gray matter (center), and intracranial (right) volumes. Correlations between the volumes shown for both male and female subjects. Linear trendlines (solid line) are included for both male and female brains.

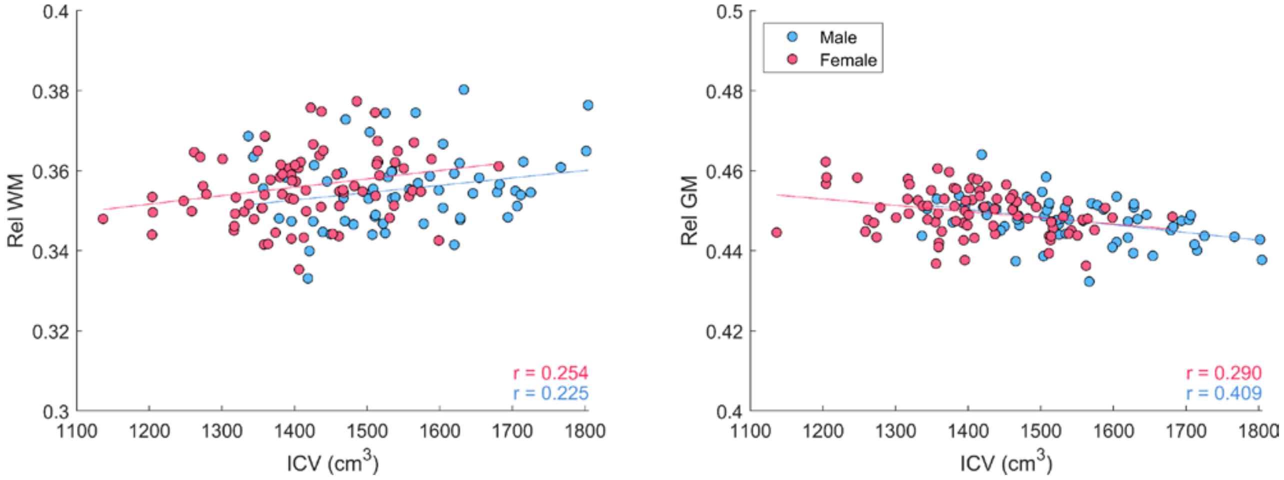

Figure 12: Scatter plots showing relationship between ICV and relative white matter (left) and relative gray matter (right) volumes. Correlations between the volumes shown for both male and female subjects.

For all 12 cortical GM ROIs measured, the median volumes for the male brains were larger than the median volumes for the female brains (Figure 13). Generally, as ICV increased, the cortical volume in each of the ROIs also increased for both male and female brains. For absolute cortical ROI volume, sex was significant for all regions except SPC and POST; however, after normalizing using ICV, sex was only significant for CN and ITC relative cortical volumes. Age was significant for all absolute cortical volumes except SFC, LaO, CN, ITC, and FSG. After correcting for total brain volume, age was significant for all regions except ITC. Both the absolute and relative cortical volumes, the complete list of estimated parameters of the Bayesian linear mixed model are provided in the Appendix. The ICC for each of the cortical volumes were all less than 0.09.

The mean cortical thickness within each ROI was calculated, and the median cortical thickness was not consistently larger for one of the sexes across all ROIs (Figure 13). Compared to the cortical gray matter volumes, the cortical thickness in each ROI were less correlated with ICV. For absolute cortical thickness, sex was significant for RMF, LiO, CN, and STC; however, after cortical thickness was corrected for total ICV, sex was significant only for CN and ITC regions. Age was significant for all cortical ROIs except ITC for absolute cortical thickness and CN for relative cortical thickness, normalized using the cubed root of ICV. For both absolute and relative cortical thickness, the complete list of estimated parameters of the Bayesian linear mixed model is provided in the Appendix. The ICC for each of the cortical ROI’s thickness were less than 0.43.

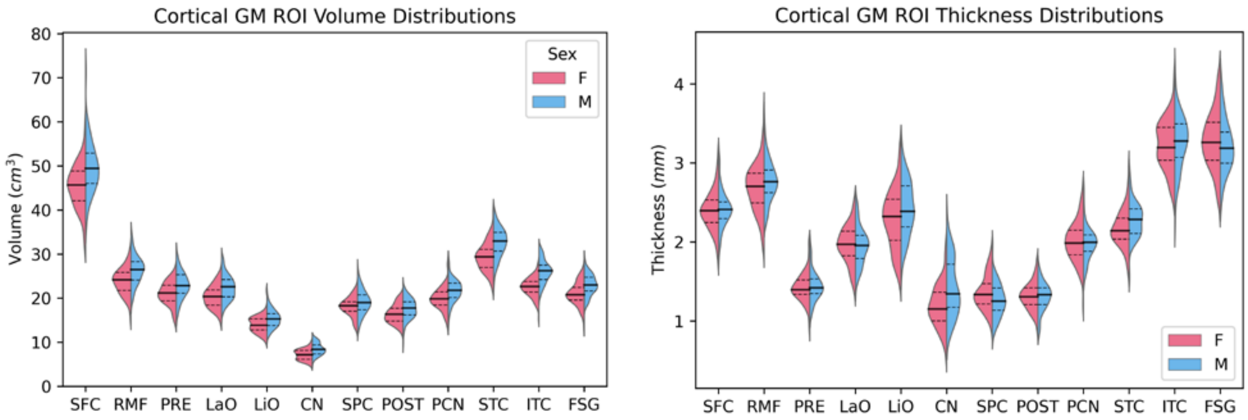

Figure 13: Distributions, based on an estimated probability density function, of the absolute volumes (left) and the mean cortical thicknesses (right) of the 12 cortical GM ROIs for both the female and male subjects. Medians are represented by the solid line, and quartiles one and three are represented by the dashed lines.

Deformation Metrics

Deformation metrics (MPS-95, MPRS-95, and MPSxMPSR-95) were each calculated for the entire brain tissue and additionally within the WM, GM, cortical CM, and cortical GM ROIs. On average, the female brains exhibited smaller MPS-95, MPSR-95, and MPSxMPSR-95 metrics for all tissue types, except CGM MPS-95 (Figure 14). MPS-95, MPSR-95, and MPSxMPSR-95 within the WM tissue were smaller than in the GM tissues for both male and female brains. To highlight the differences in these metrics between a small female brain and a larger male brain, MPS-95 distributions throughout the total brain tissue and specific tissue regions are shown in Figure 15. Additional figures showing MPSR-95 and MPSxMPSR-95 maps are included in the Appendix. The small female had a ICV of 1137 cm^3, and the large male had an ICV of 1802 cm^3. However, without considering the effect of brain volume, sex-differences cannot be concluded from this analysis alone.

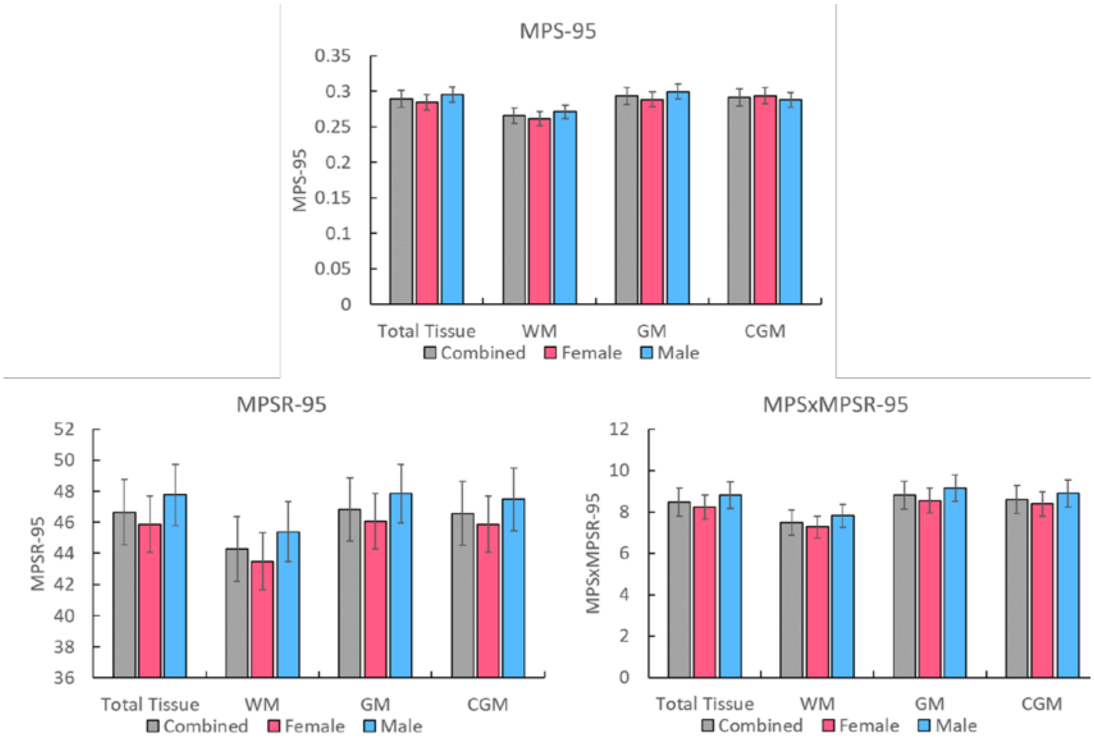

Figure 14: Bar charts for the strain-based deformation metrics (MPS-95, MPSR-95, MPSxMPSR-95) across all brain tissue, WM only, GM only, and CGM only for all brains (male and female), female brains only, and male brains only.

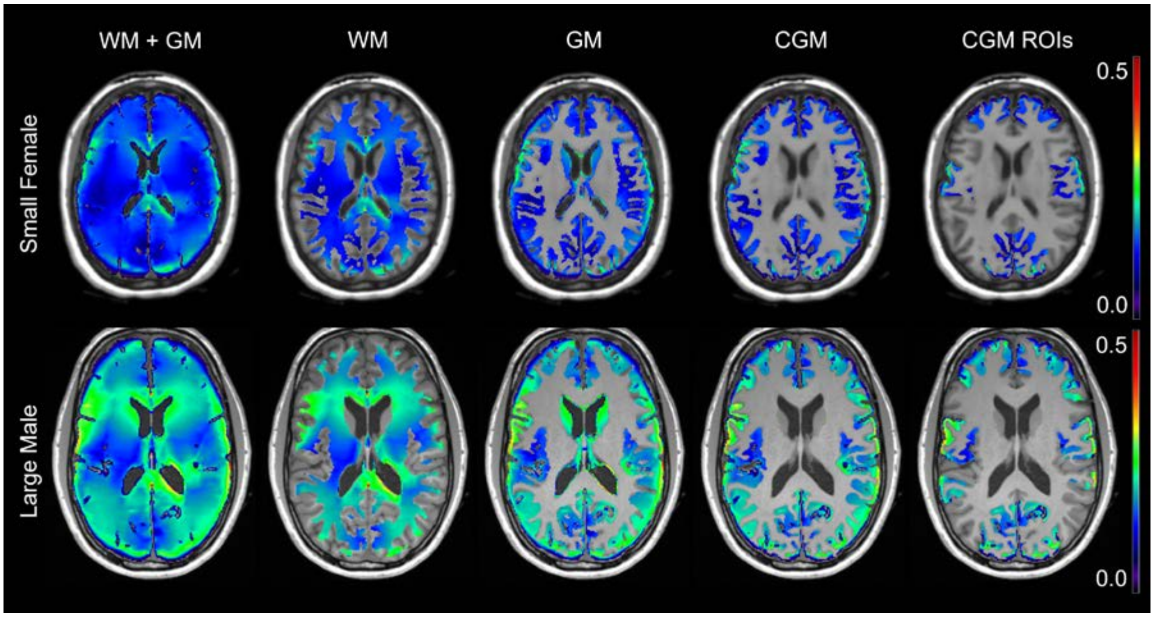

Figure 15: MPS-95 maps for a small female (ICV = 1136 cm^3) and a large male (ICV = 1802 cm^3) across the entire brain tissue, white matter, gray matter, cortical gray matter, and within the CGM regions of interest.

Effect of Neuroanatomical Features on Brain Deformation Metrics

Overall, the deformation metrics increase linearly with measures of brain volume for both male and female brains. The linear correlations between ICV and the deformation metrics (Figure 16) and between WM volume and the deformation metrics (Figure 17) are shown below; the additional neuroanatomical feature correlations are shown in the Appendix. For each of the deformation metrics, WM volume has the highest correlation for both the male and female brain models; additionally, correlations between the deformation metrics and ICV were high, with all correlations greater than r = 0.85. Within the deformation metrics assessed, MPS-95 had the highest correlation to both ICV and WM volume for both males (r = 0.869, r = 0.934, respectively) and females (r = 0.892, r = 0.939, respectively).

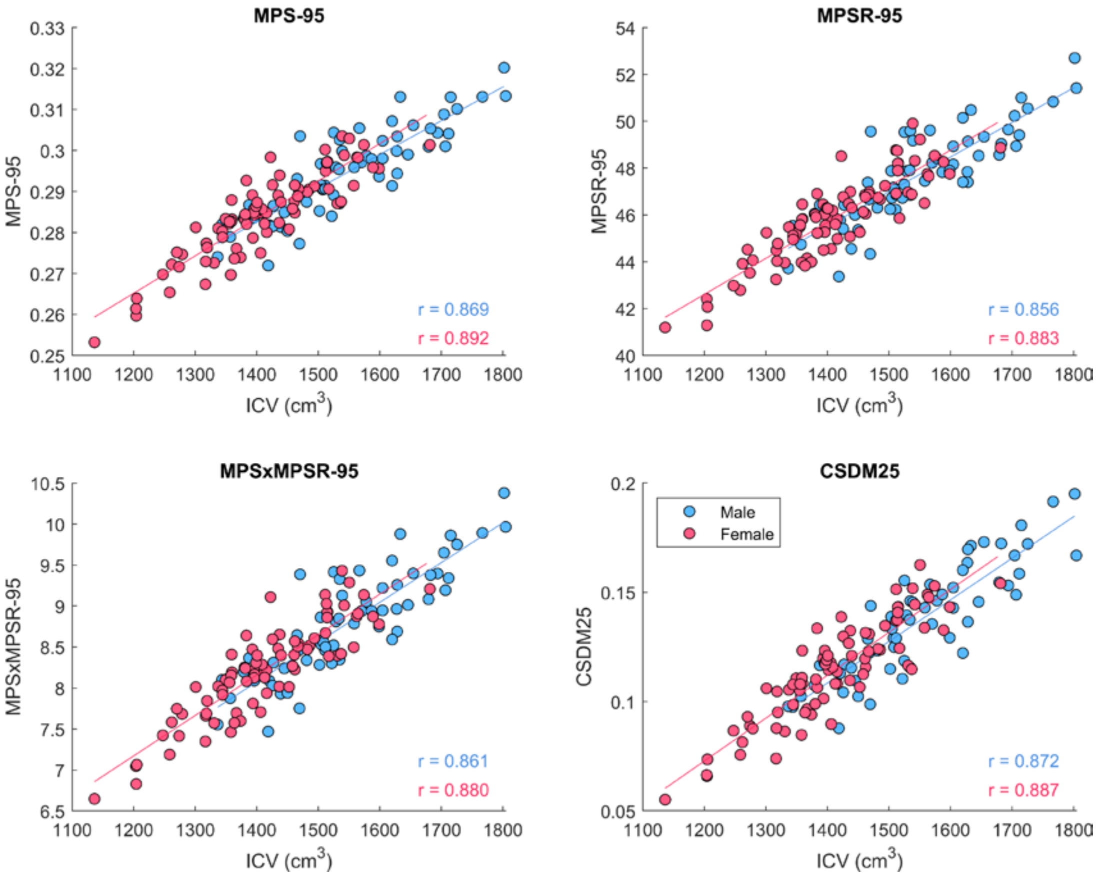

Figure 16: Scatter plots between ICV and each of the global deformation metrics for both male and female brain models. The solid lines show the linear trend lines for each of the sexes. Correlations included for the male and female data.

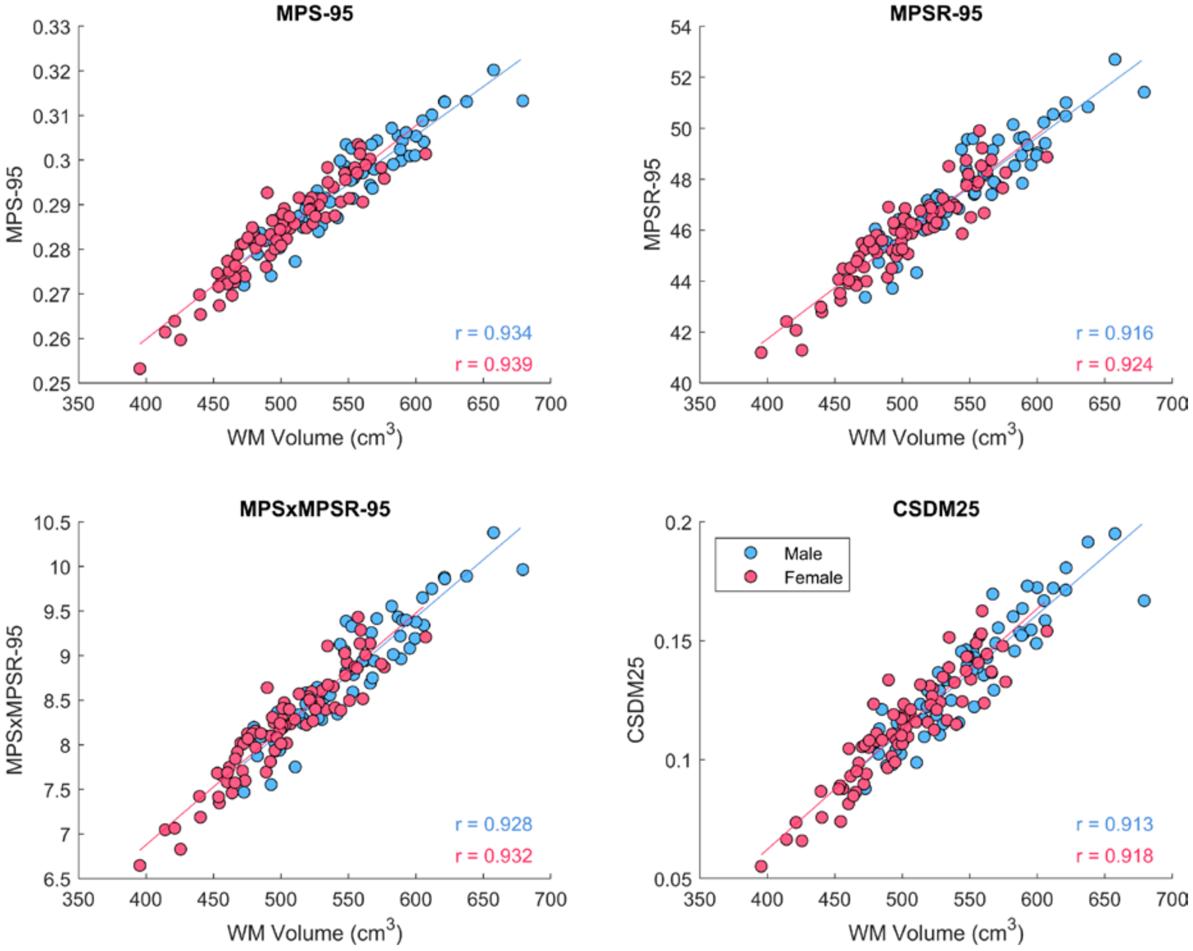

Figure 17: Scatter plots between WM volume and each of the global deformation metrics for both male and female brain models. The solid lines show the linear trend lines for each of the sexes. Correlations included for the male and female data.

Sex was not a statistically significant predictor of deformation after accounting for the neuroanatomical features, with estimates ranging from -0.04 (95% CrI -0.41, 0.33) for MPSR-95 to -0.0005 (-0.002, 0.001) for MPS-95. For all four of the deformation metrics, ICV, relative WM volume, and relative GM volume were significant predictors of deformation, with ICV having the greatest effect on the deformation metrics (ranging from 0.007 (0.005, 0.009) for MPS-95 to 1.03 (0.6, 1.4) for MPSR-95) and relative WM volume having the second highest effect (ranging from 0.003 (0.002, 0.004) for MPS-95 to 0.46 (0.31, 0.60) for MPSR-95). Although sex was not significant, to contextualize the importance of neuroanatomical features over biological sex, ICV had 13.8 times the estimated effect on MPS-95 compared to the effect of sex. The complete list of estimated parameters for the Bayesian linear mixed model are provided in the Appendix. The within-study ICC for each of the deformation metrics were all less than 0.03.

Discussion

One possible explanation for the difference of injury risk between male and female occupants observed in automotive crash field data was sex-specific differences in neuroanatomy. Using a sample of both male and female neuroanatomical brain scans, sex differences were found between each of the absolute volumes: ICV, WM volume, and GM volume. However, when comparing the relative volumes between the male and female samples, normalized with ICV, there were no significant differences. These neuroanatomical differences have been previously discussed in the literature. Several studies have concluded that males have larger volumes of both white matter and gray matter, as well as larger ICV in general, in comparison to female brain volumes (Blatter et al., 1995; Good et al., 2001; Leonard et al., 2008; Luders & Toga, 2010; Ritchie et al., 2018). Additionally, previous studies have shown females have a greater relative WM volume compared to males, which is consistent with the findings from this chapter (Gur et al., 1999; Leonard et al., 2008). For the smaller CGM ROIs, there were significant differences between the male and female volumes for almost all the ROIs in these samples, but there were only a few CGM ROIs with significant differences for cortical thickness. After normalizing the cortical thicknesses using each subject's ICV, the female sample had greater normalized thicknesses for most CGM ROIs compared to the males, which agreed with previous studies (shown in Appendix Figure) (Luders et al., 2006). However, for the absolute measures of CGM thickness, neither males nor females consistently had greater thicknesses.

While there were sex-differences observed between the male and female neuroanatomic features, the primary research question remained, the effect of these sex-differences on brain deformation response. For absolute measures of volume, there was a strong linear correlation between the neuroanatomical features and brain deformation metrics, with WM volume having the highest correlation to each deformation metric followed by ICV volume. In comparison to the neuroanatomical features (e.g., ICV and relative WM volume), sex had very little effect on the deformation metrics shown in the standardized linear regression model. Ultimately, ICV had the highest relative importance on all four deformation metrics, with relative WM having the second greatest effect. Both of these neuroanatomical features had a much greater effect than the nonsignificant predictor of sex.

There are potentially other neuroanatomical sex differences, such as differences in deep gray matter structures of the amygdala or hippocampus, shown throughout the literature which were not included in this study (Ruigrok et al., 2014). While these neuroanatomical features are not explicitly in this analysis or the regression models developed, the FE brain models used to determine the effect of these features included both subject- and sex-specific neuroanatomies; additionally, because the sex variables in these linear mixed models were far away from a level of statistical significance, it is unlikely that these small potential sex differences would be driving any sex-specific deformation response that would help explain the difference in male and female injury risk.

Based on the model selected for this study, there are a few limitations to consider. As with many FE modelling studies, the results and conclusions of this work are based on the model used, specifically the CAB-20MSym. The subject-specific morphing used in this study is based off a template FE brain model, and the resulting subject-specific models all have the same number of elements with varying brain volumes. As a result, the mesh densities between these models vary with volume. A mesh sensitivity study was completed by Giudice *et al.*, comparing the MPS-95 results of a subject-specific registration-based morphed model (method used in this study) and a voxel model developed using the subject-specific brain image, and concluded the difference in MPS-95 was “inconsequential” compared to the level of MPS-95 resulting from the simulated head impact (J. S. Giudice et al., 2020). Therefore, it is assumed the effect of differing mesh densities does not affect the results of this study.

Additionally, it is important to note that there are many areas of brain injury research that could help explain differences in injury patterns between males and females, such as physiological factors (axonal microtubular density, cellular death, hormonal, or biochemical differences), environmental factors (symptomology, injury reporting), or biomechanical factors (neuroanatomy, material properties, impact exposure). This study only addressed the biomechanical response of differences in neuroanatomies, while keeping the material properties and impact exposure consistent. Additional work is needed to better understand the effect of these other biomechanical factors and to determine which has the greatest effect on brain deformation.

Conclusions

- For absolute volumetric measurements of ICV, WM, GM, and CSF volumes, male brains had greater volumes compared to female brains. When these volumes were normalized using ICV, the sex differences were still present, however their effect size was much smaller. For absolute cortical GM ROIs volumetric and thickness measurements, there were sex differences in both neuroanatomical features.
- There was strong correlation for both male and female brains between the global neuroanatomical measurements (e.g., ICV, WM volume) and the deformation metrics (e.g., MPS-95, MPSR-95, MPSxMPSR-95, CSDM25). The correlations between the smaller neuroanatomical measurements (e.g., CGM ROI thickness and volumes) and deformation metrics were smaller than the global measurements.
- A Bayesian linear mixed model between the deformation metrics and neuroanatomical features concluded sex was not statistically significant, but ICV and both relative WM and GM volumes were statistically significant predictors of brain deformation for each of the

four metrics. Of these three neuroanatomical features, ICV had the highest relative importance.

- This analysis of male and female neuroanatomical features effect on brain deformation did not include any potential sex differences in material properties or exposure (i.e., head kinematics). The effect of these biomechanical features needs further research.

Acknowledgements

Publicly available brain MRI scans were analyzed from two previous studies. Data were provided [in part] by the Brain Biomechanics Imaging Repository (http://www.nitrc.org/projects/bbir). Principal Investigators: P. Bayly, D. Pham, C. Johnson, J. Prince, K. Ramesh, through grants U01 NS11212 and R56 NS055951. Additionally, data was also provided [in part] by Hiscox et *al*. 2020 (MRE-134 dataset) at https://github.com/mechneurolab/mre134.

Chapter 3: Effect of Material Properties

Although the effect of volumetric and anatomical sex-differences were not significant on brain deformation response, there are additional biomechanical factors which could affect brain injury risk. The effect of material properties of brain tissue on brain deformation using FE brain models has previously been investigated (Zhao et al., 2018), but the effect of sex-specific material property differences is unknown. Using magnetic resonance elastography (MRE), differences in both tissue stiffness and damping regions between male and female brains have been observed, but the effect of these differences on brain deformation are still unknown. Therefore, this chapter will quantify material property differences between male and female brains using MRE and determine their effect on brain deformation, while keeping the neuroanatomy and impact head kinematics conditions consistent.

Introduction

Human brain tissue material is complex and difficult to characterize, with no single accepted set of material properties to capture its response across different loading conditions. However, it is generally agreed that brain tissue is a nonlinear (Budday et al., 2015; Darvish & Crandall, 2001), anisotropic (Budday et al., 2015; Jin et al., 2013), nearly incompressible (Libertiaux et al., 2011), viscoelastic material (Darvish & Crandall, 2001). Historically, brain material properties have been defined used *ex vivo* mechanical testing of post-mortem human surrogate or animal brain tissue, but advancements in medical imaging technology, such as magnetic resonance elastography (MRE) or tagged magnetic resonance imaging, have improved our understanding of *in vivo* material properties (Arbogast & Margulies, 1998; Bayly et al., 2021; Budday et al., 2020; Budday, Sommer, Haybaeck, et al., 2017; Hiscox et al., 2020; Jin et al., 2013). In particular, MRE imaging techniques allow quantification of viscoelastic properties noninvasively by tracking the propagation velocity of micron-level displacements induced as shear waves in the brain tissue by an external actuator (Hiscox et al., 2020). Three-dimensional maps of both shear stiffness and damping ratios are computed using a nonlinear inversion algorithm to define the material properties throughout the entire tissue (Hiscox et al., 2020). Additional research is required to relate the computed material properties from these small deformation to material properties that can accurately capture the larger and quicker deformations seen in injurious loading conditions due to the nonlinearity and viscoelasticity of brain tissue (Alshareef et al., 2021; J. S. Giudice et al., 2021).

With increased availability of large MRE imaging datasets, research has focused on male and female differences in brain material properties, with results lacking a single conclusive finding potentially due to differences in imaging protocols (Arani et al., 2015; Hiscox et al., 2020; Sack et al., 2009; Wuerfel et al., 2010). Wuerfel et *al.* concluded that female brains were 11% stiffer than age-matched male brains, and Arani et *al.* found female brains to have stiffer temporal and occipital lobes; however, Hiscox et al. found no significant sex differences in stiffness throughout the white matter, cortical gray matter, or subcortical gray matter (Arani et al., 2015; Hiscox et al., 2020; Wuerfel et al., 2010). Additionally, McIlvain et *al.* concluded females had a higher stiffness and a lower damping ratio in subcortical gray matter structures; however, Hiscox *et al.* found no significant sex differences in subcortical gray matter damping ratios, but did find a significant sex difference for white matter damping ratios (Hiscox et al., 2020; McIlvain et al., 2018). Regardless of potential sex differences, the effect of differences in stiffness and damping ratios, implemented from MRE images, needs further investigation to determine their relative importance on brain deformation in FE brain models.

Similar to the methodology used in Chapter 2, the use of subject- and sex-specific MRE images and a consistent neuroanatomy can further the understanding of the relative importance of shear stiffness and damping ratio on brain deformation. Therefore, the goal of this chapter is to develop subject-specific FE brain models, using relative material properties from MRE, to determine sex differences in material properties and determine the relative importance of these material properties and the subject's sex on brain deformation.

Methods

Subjects and MRI/MRE Scans

All T_1-weighted and MRE brain scans were acquired from two previously completed imaging studies, Hiscox et al., 2020 and Bayly et al., 2021, and included healthy brain scans from both male and female subjects for a total of 133 scans (mean age = 26.5 years, SD = 13.0, range = 14-73) (Bayly et al., 2021; Hiscox et al., 2020). There were 88 females (mean age = 25.6 years, SD = 11.5, range = 14-73) and 45 males (mean age = 28.0, SD = 14.7, range = 14-73) included in this analysis. Additional details about the subject inclusion or exclusion criteria and imaging acquisition can be found in the original studies (Bayly et al., 2021; Hiscox et al., 2020).

For each of the subjects, brain imaging scans included a T_1-weighted MRI, a T_2-like anatomical scan in the MRE space, and shear stiffness and damping ratio maps in the MRE space. The Advanced Normalization Tools (ANTs) software package was used to generate the registration transformations required between a subject's individual MRE brain scans and their structural brain scans to generate transformations required to create FE brain models using subject-specific material property definitions. To use the registration-based transformations developed for each subject in Chapter 3, first, each of the subject-specific T_2-like brain scans in MRE space were first registered to their corresponding T_1-weighted structural brain scan image space (using "antsRegistration.sh") (Figure 18). Next, the subject-specific shear stiffness and damping ratio maps were transformed (using "antsApplyTransforms.sh") to the template image space using both the transformation between the T_2-like scan's subject space to the T_1-weighted scan's subject space and the transformation between the T_1-weighted scan's subject space and the template space (Figure 18). With the material property maps in template space, all the subject models will have the same neuroanatomy with unique distributions of material properties.

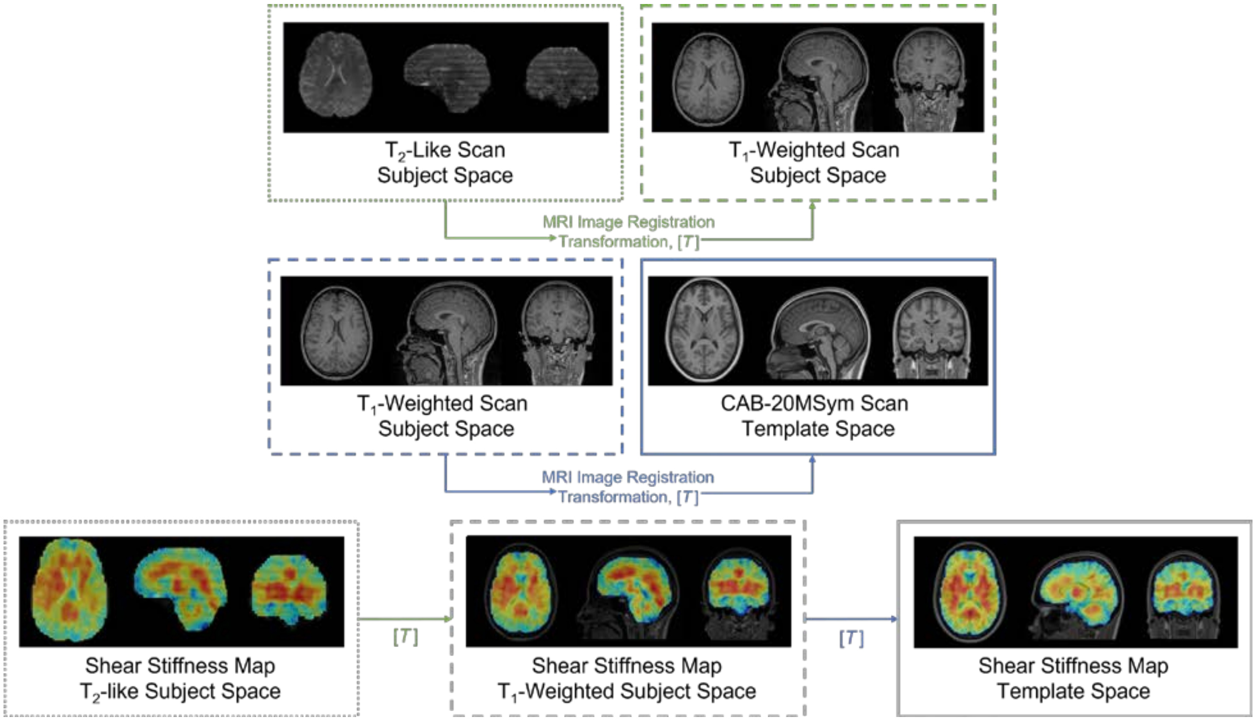

Figure 18: Flowchart showing registrations and transformations used to transform shear stiffness distribution maps into template space. The same process was used to transform damping ratio maps into template space.

Finite Element Brain Models

To keep the effect of material properties isolated, all subject-specific material properties were simulated using a single neuroanatomy, specifically the CAB-20MSym FE brain model (J. S. Giudice et al., 2020, 2021). The neuroanatomy of the CAB-20MSym FE brain model was based on a template MRI image developed using 20 healthy, male brains with 1 mm^3 isotropic voxels (J. S. Giudice et al., 2020). As sex-specific neuroanatomical features did not affect brain deformation response (shown in Chapter 3), the use of a single-sex brain template image is appropriate. The CAB-20MSym FE brain model includes the brain parenchyma, internal CSF, peripheral CSF, and ventricles, each modeled using 1 mm hexahedral elements, as well as the sagittal sinus, falx cerebri, and tentorium cerebri modeled using two-dimensional shell elements, (J. S. Giudice et al., 2020, 2021). The dura is modelled as a rigid layer of shell elements surrounding the peripheral CSF, and all 6-DOF head kinematics are applied to this rigid dura part through the head center of gravity in the local anatomic head coordinate system (Society of Automotive Engineers, 2007). The material properties of the brain parenchyma parts will be adjusted in this chapter to account for variations in subject shear stiffness and damping ratios, but all other features of the CAB-20MSym brain model will be kept consistent with the baseline model (J. S. Giudice et al., 2020, 2021).

Implementation of Material Properties into FE Template Model

Because the material properties determined using MRE are based on small strains, distributions of relative stiffness and relative damping ratios are used in combination with *ex vivo* characterization of brain materials to create the material properties implemented in the FE brain models. Distributions of both shear stiffness and damping ratios throughout the brain tissue were based on the MRE134 template images, which were developed from MRE scans of 134 healthy, young adults (range = 18-35 yr., $N_{female} = 78$, $N_{male} = 56$) (Hiscox et al., 2020). The distribution of shear stiffness of the MRE134 template was truncated to exclude stiffnesses above the 98th percentile shear stiffness and below the 15th percentile shear stiffness to reduce the influence of potential numerical artifacts or edges effects and remove areas associated with the approximate stiffness of CSF (0 - 1.25 kPa), respectively (Figure 19) (J. S. Giudice et al., 2021; Hiscox et al., 2020). The distribution of damping ratios throughout the brain was based on the same voxels used in the shear stiffness assessment (i.e., voxels with stiffness above the 98th percentile and below the 15th percentile shear stiffness were excluded from the damping ratio distribution) (Figure 19). Following a sensitivity study (included in Appendix), the stiffness distribution was separated into 10 bins, and the damping ratio distribution was separated in 10 bins to create ratios between the center of these bins and the median of the truncated shear stiffness ($\mu = 2.67$ kPa) and damping ratio ($\xi = 0.225$) distributions (Figure 20).

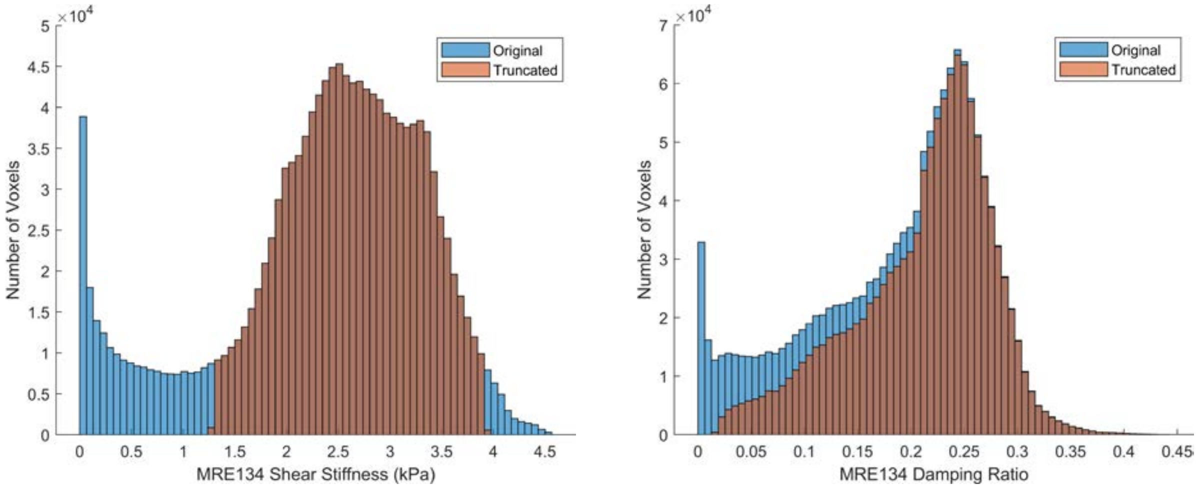

Figure 19: (Left) The original shear stiffness distribution and the truncated distribution of the MRE134 template (distributions shown with equal bin width). (Right) The original damping ratio distribution and the truncated distribution (using the same voxels of the truncated shear stiffness distributions) of the MRE134 template image.

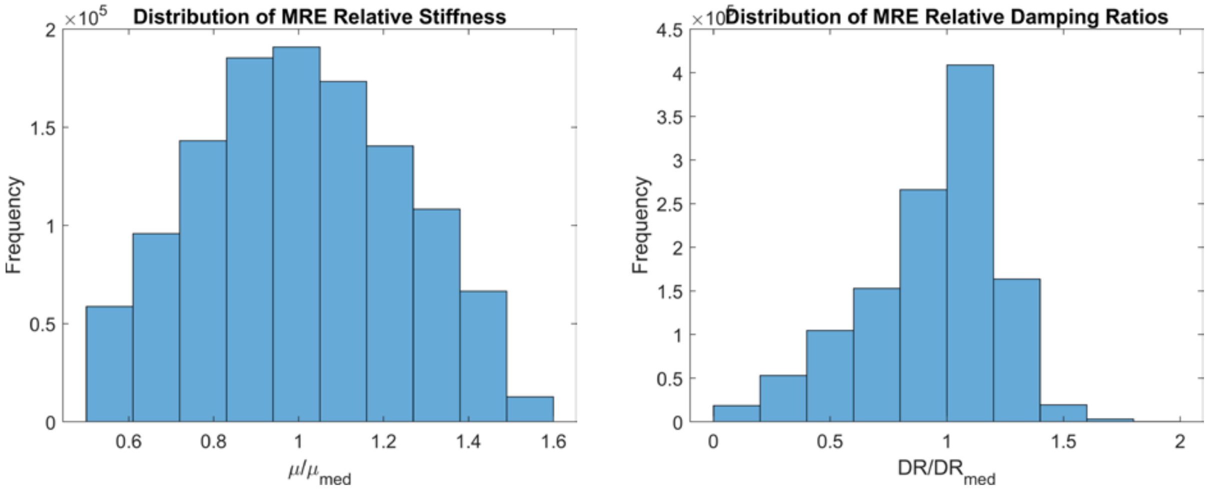

Figure 20: Relative shear stiffness ratios (left) and relative damping ratio ratios (right) used to capture material distributions throughout the brain tissue each using 10 bins and the truncated distributions.

Using the 10 bins to define both the relative stiffness and relative damping ratios based on the MRE134 template images, the material of each element within the subject brain model in the CAB-20MSym template space if assigned to one of these 100 relative material definitions (Figure 21). This binning method allows each subject brain model to include only the number of material definitions required to capture the distribution of relative stiffnesses and damping ratios present in their individual MRE scan.

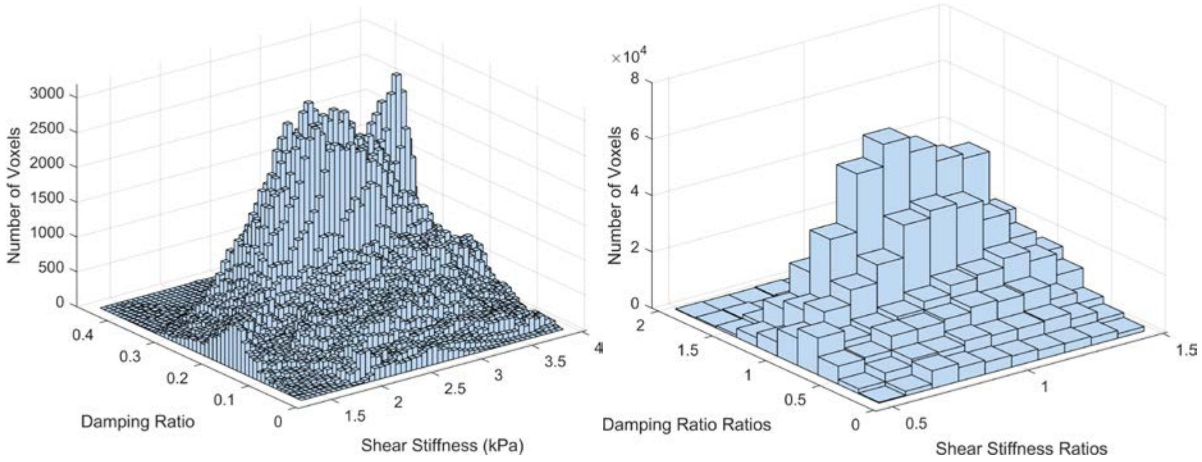

Figure 21: 3-dimensional histograms showing the distributions of absolute material properties (left) and the relative material properties (right) for the MRE134 template.

Material Property Definitions

First, the material of each voxel is defined based on the relative stiffness and damping ratios. These relative material definitions are then used to scale absolute material definitions used in the CAB-20MSym template FE brain model. The brain parenchyma of the baseline CAB-20MSym FE brain model included 10 parts modeled using an Ogden rubber material definition with stiffnesses based on a calibrated median shear stiffness and relative shear stiffness ratios from the MRE134 template image (J. S. Giudice et al., 2021). Both the calibrated median shear stiffness and hyperelastic nonlinearity coefficient were optimized using both *in situ* and *in vivo* experiments and were used to define the absolute shear stiffness for each of the 10 parts throughout the heterogeneous brain model (J. S. Giudice et al., 2021). Therefore, for each of the 10 parts, the i^{th} part had a shear stiffness in the Ogden constitutive model (μ_i) based on the relative shear stiffness ratio (γ_i), the calibrated median stiffness ($\mu_{0,med}$), and the calibrated nonlinearity coefficient (α).

$$\mu_i = \frac{2\gamma_i \mu_{0,med}}{\alpha}$$

A similar process was used to define the absolute stiffness properties for each material within the material-subject-specific models. The calibrated median stiffness of the CAB-20MSym FE brain model (1.125 kPa), the calibrated nonlinearity coefficient (0.667), and the relative ratios of shear stiffness were used to calculated the Ogden material parameters in the material-subject-specific models (Table 1) (J. S. Giudice et al., 2021).

Table 1: Ogden parameters for each relative stiffness part of the brain parenchyma part.

Relative Stiffness Part	**Relative Shear Stiffness Ratio**	**μ_i (kPa)**
1	0.50	0.169
2	0.61	0.205
3	0.71	0.240
4	0.82	0.275
5	0.92	0.311
6	1.03	0.346
7	1.13	0.382
8	1.24	0.417
9	1.34	0.452
10	1.45	0.488

Additionally, the relative damping ratios developed from the MRE134 template were used to capture the heterogeneous distribution of damping throughout the brain parenchyma. The reduced relaxation function of the CAB-20MSym template model is modeled using a four term Prony series:

$$g(t) = g_\infty + \sum_{i=1}^{N} g_i e^{-\beta_i t}$$

$$\beta_i = \frac{1}{\tau_i}$$

$$g_\infty + \sum_{i=1}^{N} g_i = 1$$

where g_∞ and g_i are the normalized coefficients related to the long-term response and each time constant (τ_i), respectively. The reduced relaxation function of the CAB-20MSym template model, which was fit using the tan(δ) response of experimental data, was scaled using the relative damping ratio (ξ) ratios (where ξ = ½ tan(δ)) and refit using a four term Prony series to determine scaled g_∞ and g_i coefficients, with β_1= 10ms, β_2 = 1ms, β_3= 0.1ms, and β_4 = 0.01ms (Figure 22).

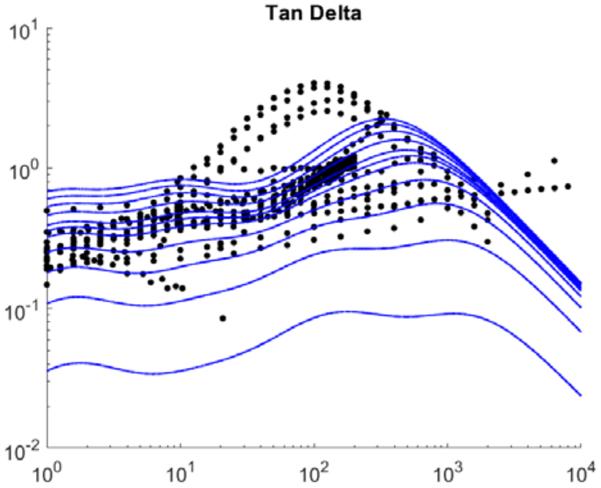

Figure 22: The scaled tan(δ) responses, based on the relative damping ratio raiots, that were used to refit the scaled reduced relaxation functions.

Table 2: Relative damping ratio ratios and reduced relaxation parameters associated with each of the relative damping ratio parts in the material-subject-specific models.

Relative Damping Ratio Part	Relative Damping Ratio Ratios	g_1	g_2	g_3	g_4	g_∞
1	0.099	0.140	0.118	0.022	0.049	0.670
2	0.299	0.415	0.173	0.042	0.068	0.302
3	0.499	0.626	0.131	0.046	0.054	0.143
4	0.699	0.758	0.083	0.045	0.039	0.074
5	0.899	0.835	0.050	0.043	0.029	0.043
6	1.098	0.882	0.029	0.040	0.022	0.027
7	1.297	0.912	0.015	0.037	0.017	0.018
8	1.497	0.933	0.005	0.035	0.014	0.013
9	1.697	0.946	0.001	0.032	0.011	0.009
10	1.896	0.954	0.001	0.029	0.010	0.007

Finally, for all other parts of the material-subject-specific brain models (e.g., ventricle CSF, tentorium, falx, etc.), the material properties were kept consistent with the CAB-20MSym model; additionally, the density of the brain parenchyma material was 1.123 x 10^{-6} kg/mm^3 , and the Poisson's ratio was assumed to be 0.499999 (J. S. Giudice et al., 2021).

Material Property Biomechanical Factor Definitions

Multiple biomechanical features were defined to capture the mechanical properties of each subject's brain and FE brain model. To investigate the effect of shear stiffness, the mean and interquartile range (IQR) of the absolute shear stiffness throughout the entire tissue (gray matter (GM) and white matter (WM)) were calculated for each subject using the MRE brain scans. The mean shear stiffness of just the WM and GM were also calculated. The mean shear stiffness of the FE brain model, using the discretized bins, was also calculated, and compared to the mean shear stiffness of the MRE brain scan. Similarly, to investigate the effect of the damping ratio, the mean and IQR of the damping ratios (throughout the entire GM and WM tissues) were calculated for each subject using the MRE brain scans. The mean damping ratios of the GM and WM were also calculated. Again, the mean damping ratio of the discretized FE brain model was calculated and compared to the mean damping ratio from the MRE brain scan.

Additionally, the effect of the combination of shear stiffness and damping ratios was considered. Using the discretized distributions of both shear stiffness and damping ratios, each with 10 bins (Figure 20), the combination of the two material properties were defined as the following quartiles: quartile one (low stiffness, bins 1-5; low damping, bins 1-5), quartile two (low stiffness, bins 1-5; high damping ratio – bins 6-10), quartile three (high stiffness – bins 6-10, low damping – bins 1-5), and quartile four (high stiffness, bins 6-10, high damping ratio, bins 6-10) (Figure 23). For each subject, the percentage of the brain volume defined in each of these four quartiles was calculated to determine the effect of high and low stiffness and damping ratio regions on brain deformation.

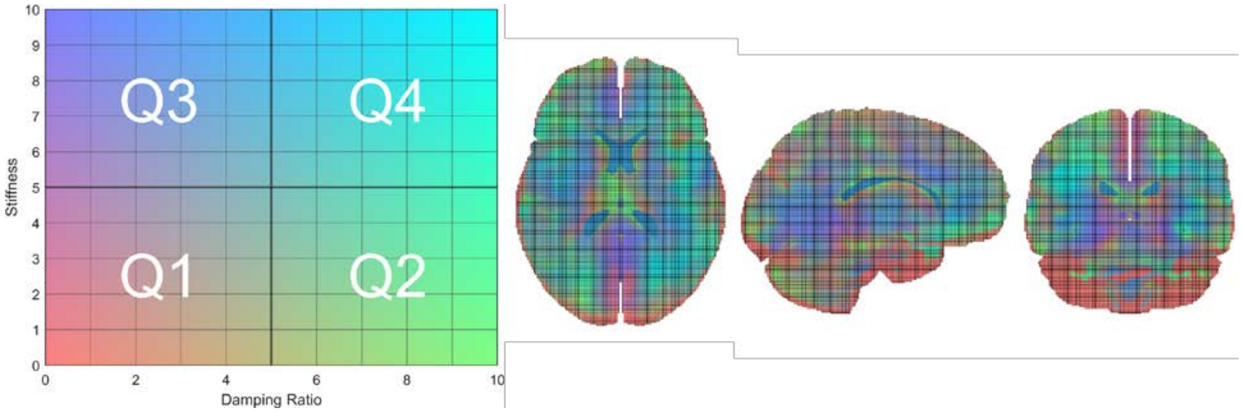

Figure 23: (Left) The 2D color map showing the range of high and low stiffness and damping ratio combinations throughout the brain tissue. (Right) Axial, sagittal, and coronal slices of a single example subject to show distributions of high and low shear stiffness and damping ratios. The ventricles are shown in blue throughout the FE brain model.

Brain Deformation Metric Definitions

To remain consistent with the analysis of neuroanatomical features, the same deformation metrics were used to assess the effect of the material biomechanical factors; these included metrics of strain, strain rate, and the product of strain and strain rate (Wu et al., 2021). To avoid the potential effect of any numerical instabilities associated with the absolute maximum, the 95th percentile of each of these metrics was reported (Gabler et al., 2016; J. S. Giudice et al., 2020; K. Reynier et al., 2021). For clarity, the 95th percentile maximum principal strain (MPS-95) is defined as the 95th percentile of the distribution of maximum principal strains experienced by each white and gray matter brain element throughout the simulation; the 95th percentile maximum strain rate (MPSR-95) and the 95th percentile product of MPS and MPSR (MPSxMPSR-95) are defined similarly. Additionally, cumulative strain damage measure (CSDM), which represents the volume fraction of elements greater than a specified threshold, was calculated for a commonly used threshold (25%) throughout the white and gray matter elements.

Statistical Analysis for Material Biomechanical Factors and Brain Deformation Metrics

For the material property biomechanical factors, a multivariate mixed linear model was used to determine if sex and age were statistically significant factors. Because the brain material properties were collected from different studies, a random study effect was also included in the linear mixed model(Hiscox et al., 2020). Due to the small number of studies (n = 5), mixed model estimation can be challenging due to a high likelihood of the study effect estimate being zero under a frequentist approach. To avoid this issue, analysis was carried out using a Bayesian linear mixed model where the biomechanical factors (outcome variables) were jointly modelled to take advantage of strong correlations among them. To determine sex effects on the material property biomechanical factors, the Bayesian multivariate mixed linear model had the following structure, with $Y_{ij}^{(k)}$ being the k_{th} outcome associated with the i_{th} brain model in the j_{th} study, with the model equation for total tissue mean stiffness provided as an example below:

$$Y_{ij}^{Stiff} = \left(\beta_0^{Stiff} + u_{j0}^{Stiff}\right) + \beta_1^{Stiff}\left(Age_{ij}\right) + \beta_2^{Stiff}\left(Sex_{ij}\right) + \epsilon_{\mathrm{ij}}^{Stiff}$$

where β_0 are the population intercepts, u_{j0} are the random intercepts for the j_{th} study, Age is the age of the subject in years (centered and scaled using the mean and standard deviation of the sample), Sex of the subject (reference = female), and $\epsilon_{\mathrm{ij}}^{k}$ are the outcome-specific residual terms. The equations for the remaining material property features are provided in the Appendix.

For each of the individual outcomes (i.e., the biomechanical factors), priors sensitivity analysis was conducted for the intercept, the β terms, and the study random effect standard deviations. Based on this sensitivity, the priors with the largest standard deviation (i.e., least informative) with stable estimates were used in the final model. Estimation took place using the *brms* package in The RStudio (R version 4.2.0) (Bürkner, 2017; R Core Team, 2022). Three parallel initially over dispersed Markov Chain Monte Carlo (MCMC) chains were used, where each chain ran for 3,000 iterations after the 2,000 iteration warmup. Effective sample sizes were examined to ensure each parameter's effective sample size was greater than 1,000 for each parameter. A visual inspection of the MCMC chains and assuring that Rhat values were approximately 1.00 indicated acceptable convergence. Correlation between the material neuroanatomical features were computed, and highly correlated parameters (r > 0.8) were noted. All Credible Intervals (CrI) reported are 95% equal tailed intervals. For each material property feature, the intraclass correlation (ICC) was computed to report the correlation of observations within one study.

A similar methodology was used to determine significant biomechanical factor predictors of the deformation metrics, the order of importance of these biomechanical factors, and the significance of sex after accounting for these biomechanical factors. Therefore, to determine the effect of the material property biomechanical factors and sex on the deformation metrics, the multivariate mixed linear model had the following structure, with $Y_{ij}^{(k)}$ being the k_{th} outcome associated with the i_{th} brain model in the j_{th} study, with the model for MPS-95 provided as an example below:

$$\begin{aligned}Y_{ij}^{MPS-95} = {} & \left(\beta_0^{MPS-95} + u_{j0}^{MPS-95}\right) + \beta_1^{MPS-95}\left(Age_{ij}\right) + \beta_2^{MPS-95}\left(Sex_{ij}\right) + \beta_3^{MPS-95}\left(Stiff_{ij}\right) \\ & + \beta_4^{MPS-95}\left(Stiff\ WM_{ij}\right) + \beta_5^{MPS-95}\left(Stiff\ GM_{ij}\right) + \beta_6^{MPS-95}\left(Stiff\ IQR_{ij}\right) \\ & + \beta_7^{MPS-95}\left(DR_{ij}\right) + \beta_8^{MPS-95}\left(DR\ WM_{ij}\right) + \beta_9^{MPS-95}\left(DR\ GM_{ij}\right) \\ & + \beta_{10}^{MPS-95}\left(DR\ IQR_{ij}\right) + \beta_{11}^{MPS-95}\left(Quad\ 1_{ij}\right) + \beta_{12}^{MPS-95}\left(Quad\ 2_{ij}\right) \\ & + \beta_{13}^{MPS-95}\left(Quad\ 4_{ij}\right) + \epsilon_{\mathrm{ij}}^{MPS-95}\end{aligned}$$

where β_0 are the population intercepts, u_{j0} are the random intercepts for the j_{th} study, age is the age of the subject in years (scaled using the mean and standard deviation of the sample), sex of the subject, each of the biomechanical features previously justified (scaled using the mean and standard deviation of the variable), and $\epsilon_{\mathrm{ij}}^{k}$ are the outcome-specific residual terms. The equations for the remaining deformation metrics are provided in the Appendix. Priors were assigned after a prior sensitivity analysis as previously described. The same model fitting parameters in RStudio were used to estimate the neuroanatomical biomechanical factor and brain deformation metrics model. Correlations between the independent variables were assessed using the biomechanical factors linear mixed model described previously, and for pairs of variables with correlations greater 0.80, a single parameter was kept in the final model. The final linear mixed model included these uncorrelated, independent variables against the deformation metrics. Because all quantitative independent variables were centered and scaled, the relative importance of each biomechanical factor was determined using the absolute value of the estimated coefficient.

Results

Material Property Biomechanical Features

On average, the male brains had greater total tissue mean stiffness (mean ± std = 2.77 ± 0.21 kPa), mean GM stiffness (2.53 ± 0.20 kPa), and WM stiffness (3.03 ± 0.22 kPa) compared to the female brains (2.71 ± 0.17 kPa, 2.46 ± 0.17 kPa, 2.98 ± 0.18 kPa, respectively); additionally, the male brains individually had a greater spread of stiffness with a greater average stiffness IQR (1.23 ± 0.16 kPa) compared to the females (1.08 ± 0.13 kPa) (Figure 24). However, the average female damping ratio was greater for the mean damping ratio (0.22 ± 0.03), the mean GM damping ratio (0.21 ± 0.03), and the WM damping ratio (0.23 ± 0.03) than the average male damping ratios (0.20 ± 0.03, 0.20 ± 0.03, 0.21 ± 0.03, respectively) (Figure 24). The IQR of the total tissue damping ratio was also greater for the female brains (0.12 ± 0.02) compared to the male brains (0.11 ± 0.02). The difference in female and male damping ratio may be a result of the study parameters, and this is addressed in the statistical model with a study effect parameter.

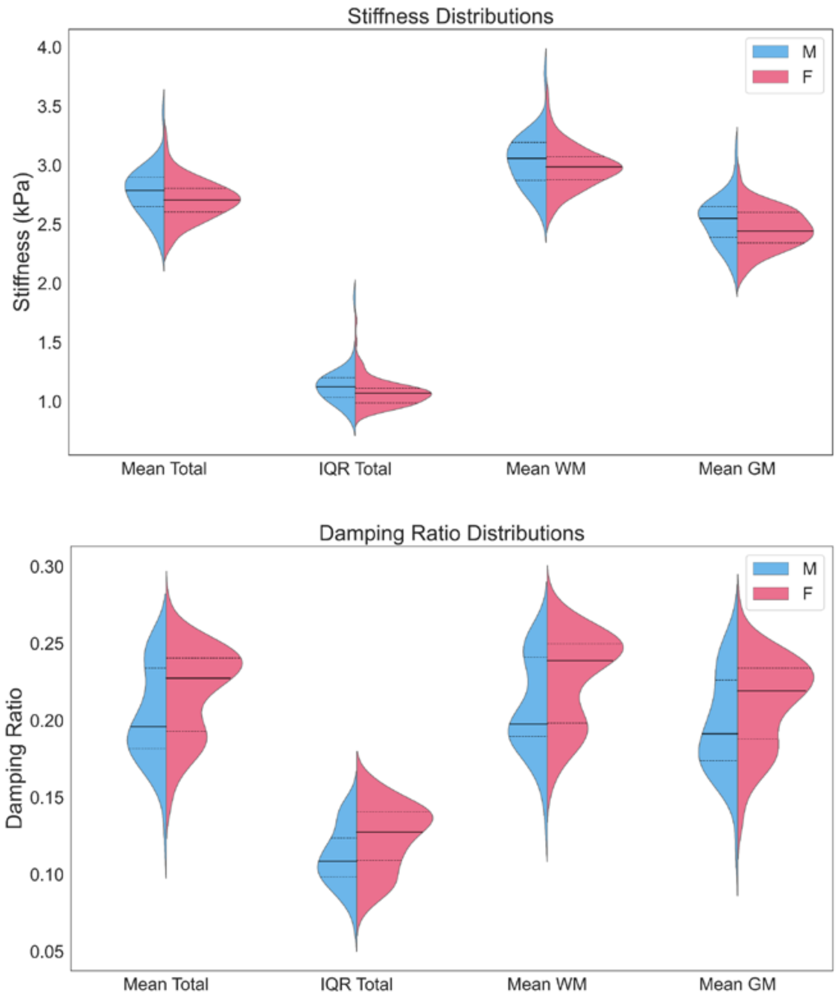

Figure 24: Male and female distributions, based on an estimated probability density function, for mean stiffness (top) and mean damping ratios (bottom) throughout the entire brain tissue, the IQR for the total brain tissue, and the mean stiffness in both the WM and GM. Medians are represented by the solid line, and quartiles one and three are represented by the dashed lines.

The male brains had more percentage volume, on average, in quadrants one (35.3 ± 1.9%) and three (37.6 ± 9.8%) compared to the female brains (32.8 ± 9.0%, 32.1 ± 7.7%, respectively), which were the regions associated with low damping ratios; the female brains had more percentage volume, on average, in quadrants two (19.8 ± 8.2%) and four (15.3 ± 7.0%) compared to the male brains (15.5 ± 8.9% ,11.6 ± 6.7%, respectively), which were areas associated with high damping ratio (Figure 25). For both the male and female brains, there was not a strong correlation between the mean total tissue stiffness and mean total tissue damping ratio (r_{male} = 0.4 and r_{female} = 0.18) (Figure 25).

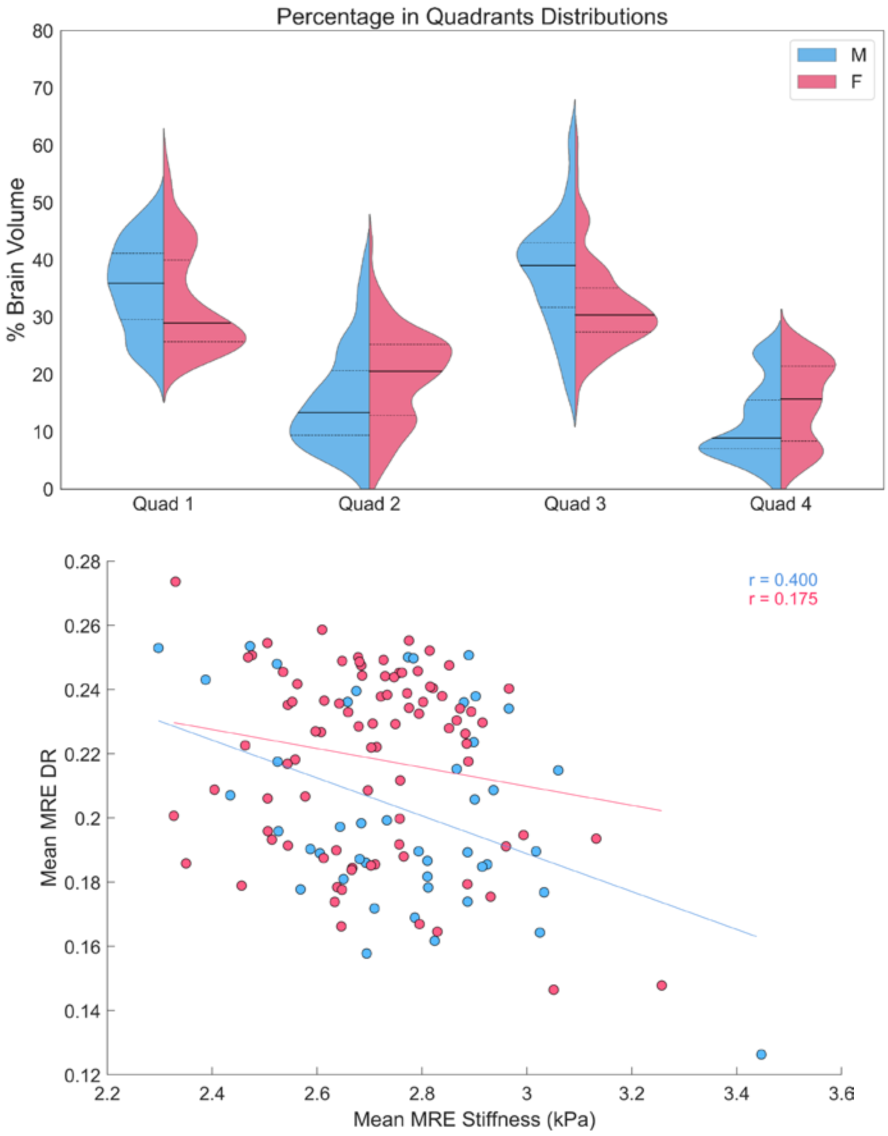

Figure 25: (Top) Male and female distributions, based on an estimated probability density function, for mean percentage of brain volume per quadrants of high and low stiffness and damping ratios. Medians are represented by the solid line, and quartiles one and three are represented by the dashed lines. (Bottom) A scatter plot of both male and female mean stiffness and damping ratios for the entire brain tissue. Correlations between stiffness and damping ratios provided for both sexes.

The Bayesian linear mixed model was used to determine the significance of sex and age, while accounting for study, on each of the material property biomechanical factors (Appendix Table). Age was significant, as determined by the 95% credible interval, for mean total tissue, GM, and WM stiffnesses, total tissue and GM damping ratios, volume percentage in quadrants one, two, and four, and the IQR of the damping ratios. Sex was significant for the mean total tissue, GM, and WM stiffnesses, only the WM DR, only percentage of volume in quadrant two, and the IQR of the damping ratios. The complete list of estimated parameters of the Bayesian linear mixed model are provided in the Appendix. For the mean and IQR stiffness metrics, each tissue has the following ICCs: $ICC_{total} = 0.18$, $ICC_{GM} = 0.38$, $ICC_{WM} = 0.22$, and $ICC_{IQR} = 0.48$. However, the ICC for the metrics of DR were much larger, where the ICC for metrics of both mean DR and IQR were $ICC_{total} = 0.93$, $ICC_{GM} = 0.89$, $ICC_{WM} = 0.94$, $ICC_{IQR} = 0.90$. The ICC for the quadrant percentages were $ICC_{quad1} = 0.91$, $ICC_{quad2} = 0.88$, $ICC_{quad3} = 0.94$. Based on the high ICC for the DR and quadrant percentage metrics, there was an effect of study for the material properties for each of the brains.

Deformation Metrics

For each of the deformation metrics assessed (MPS-95, MPSR-95, MPSxMPSR-95, and CSDM-25), the male models experienced a greater deformation response (0.36 ± 0.02, 65.2 ± 4.9, 14.5 ± 1.7, 0.33 ± 0.10, respectively) compared to the female brains (0.35 ± 0.02, 63.4 ± 5.1, 13.9 ± 1.8, 0.28 ± 0.10, respectively) (Figure 26). The distributions of each deformation metric were bimodal, like the distributions of the damping ratios for both the male and female brains. This was possibly due to differences in the underlying studies.

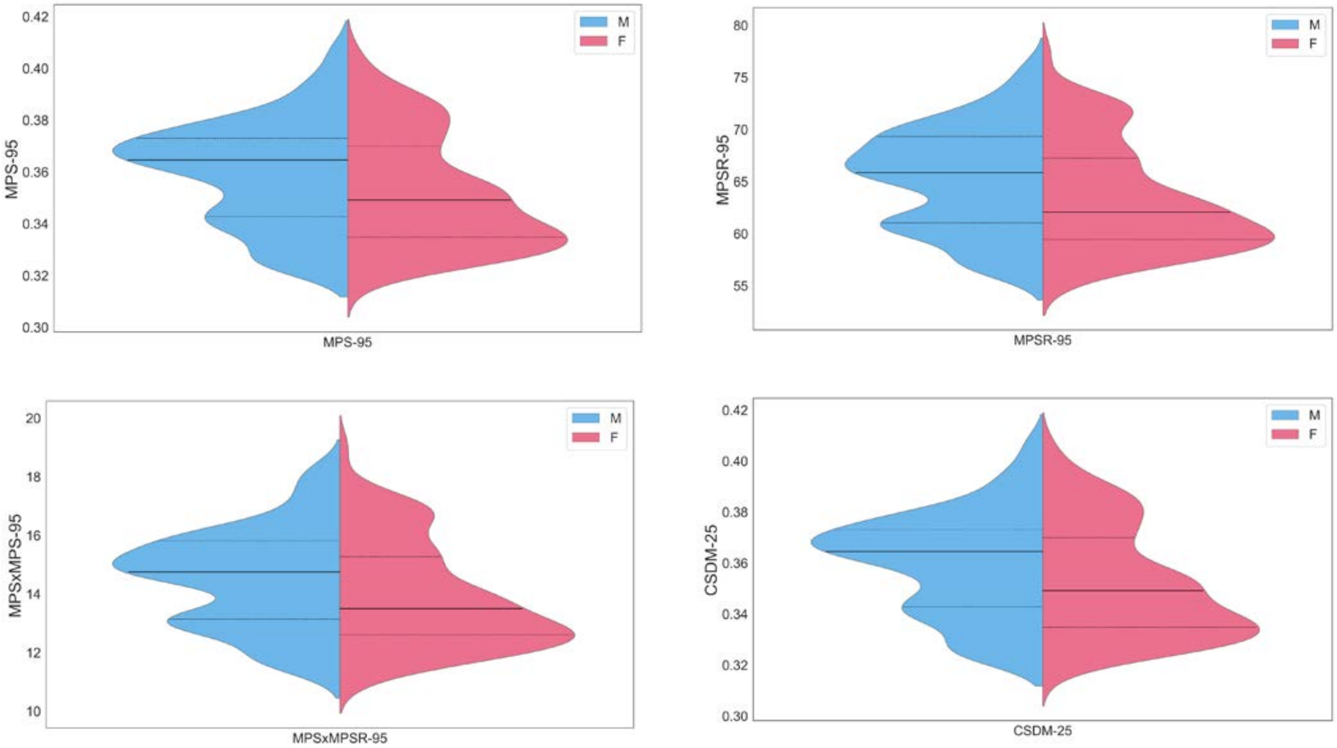

Figure 26: Distributions, based on an estimated probability density function, of male and female deformation metrics, including MPS-95 (top left), MPSR-95 (top right), MPSxMPSR-95 (bottom left) and CSDM-25 (bottom right).

Effect of Material Property Biomechanical Features on Brain Deformation Metrics

Generally, as the mean total tissue stiffness of the subject increased, each of the deformation metrics (MPS-95, MPSR-95, MPSxMPSR-95, and CSDM-25) decreased (Figure 27). The correlations between the deformation metrics and the mean total tissue stiffness were not strong for either the male (all correlations less than 0.1) or the female (all correlations less than 0.27) brain models. It should be noted that the three brain (two female and one male case) with high stiffness and high deformation metrics are the three lowest mean total tissue damping ratio brain models, and the effect of the damping ratio can be seen in their deformation response.

Similar to the relationship between shear stiffness and deformation, as the mean total tissue damping ratio increased, the measured deformation metrics decreased for both the male and female brain models (Figure 28). The correlations between the mean total tissue damping ratio and deformation metrics were high for both males (all correlations greater than 0.86) and females (all correlations greater than 0.83), with the strongest correlation for both sexes CSDM-25 (r_{male} = 0.920 and r_{female} = 0.918).

For quadrant one, the region with both low damping ratio and low shear stiffness, the brain models with greater volume within these regions have greater deformation for each of the metrics, where the correlations between percent brain volume in quadrant one and the deformation metrics are the greatest among the quadrant percentages (Figure 29). The correlation between quadrant one brain volume percentage and MPS-95 was greatest for both male (r = 0.86) and female (r = 0.93) brain models.

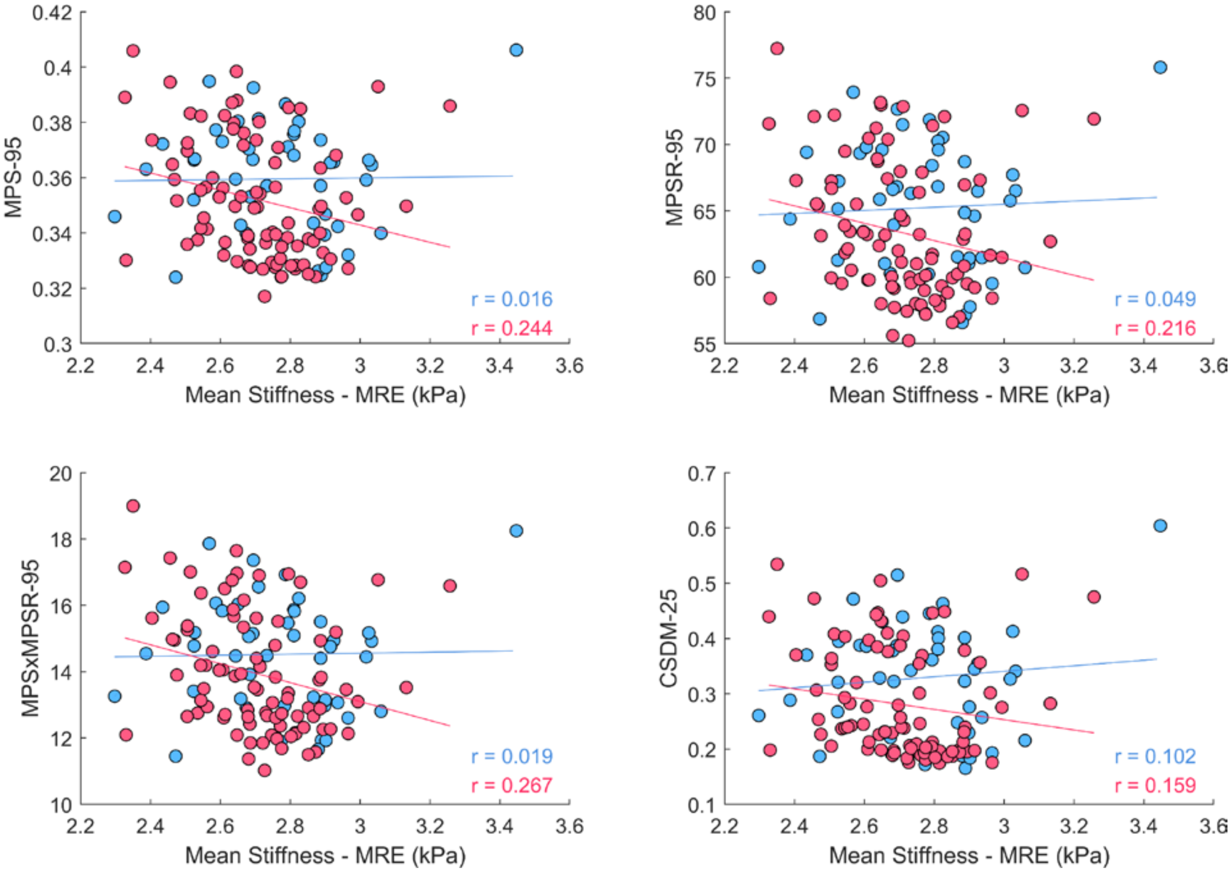

Figure 27: Scatter plots for both male and female for each of the four deformation metrics against the mean stiffness from the MRE scans of each subject. Linear trendlines and correlations also provided for both the male and female subjects.

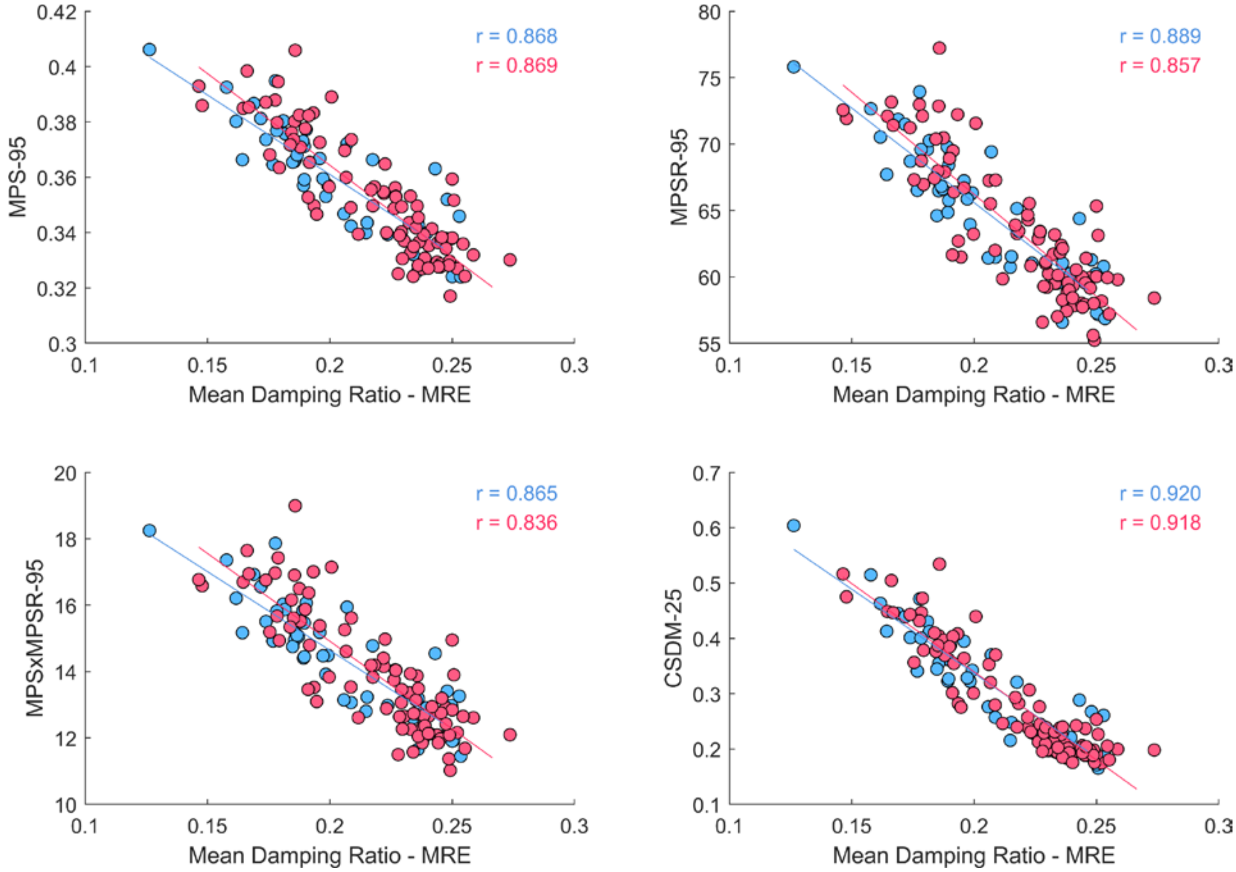

Figure 28: Scatter plots for both male and female for each of the four deformation metrics against the mean damping ratio from the MRE scans of each subject. Linear trendlines and correlations also provided for both the male and female subjects.

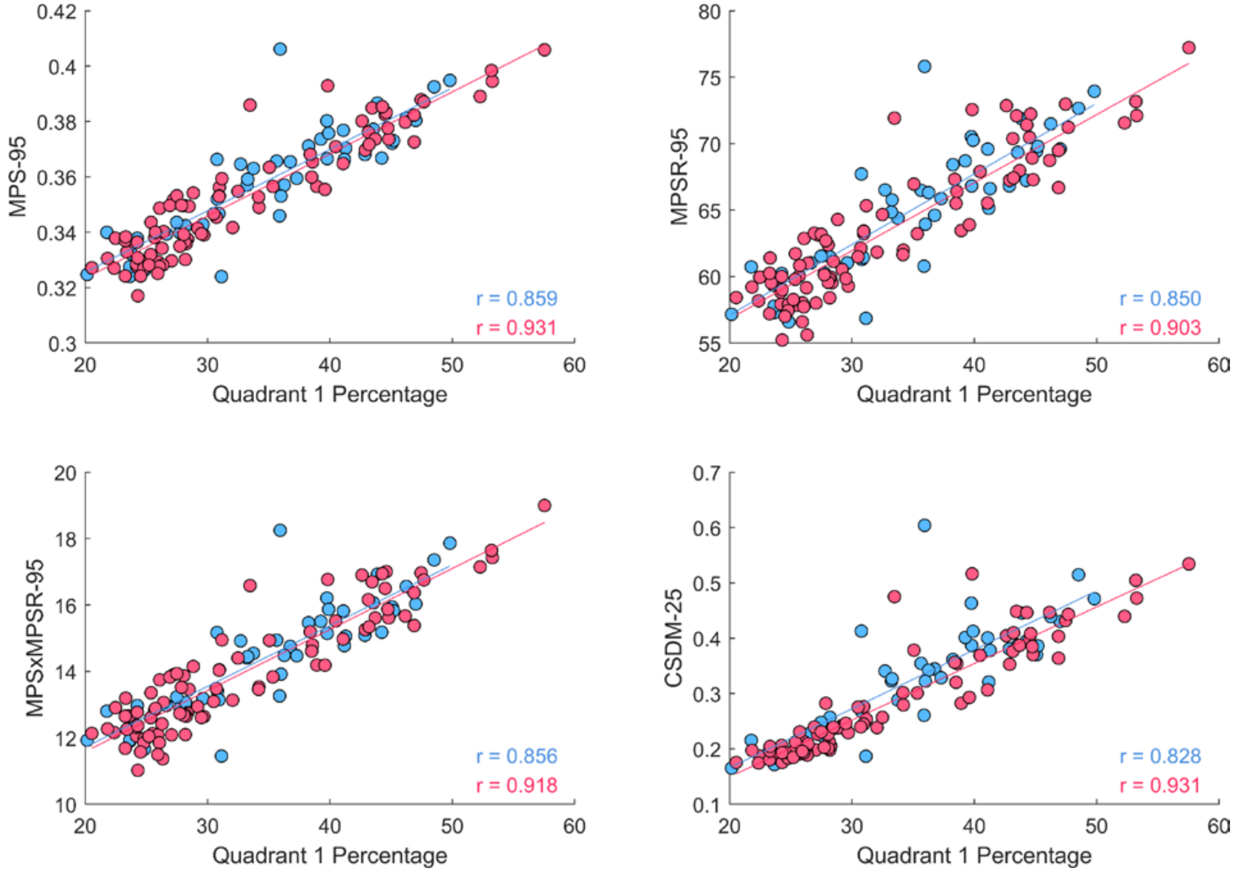

Figure 29: Scatter plots for both male and female for each of the four deformation metrics against the volume percentage in quadrant 1 (low stiffness, low damping ratio) for each subject. Linear trendlines and correlations also provided for both the male and female subjects.

The Bayesian linear mixed model was used to determine the significance of sex, age, and each of the previously described material property biomechanical factors on each brain deformation metric (Table 3). After accounting for differences in material properties, the effect of study was not significant on the deformation metrics; as a result, the effect of study was removed from the analysis of material property biomechanical factors on brain deformation. Additionally, there were high correlations between some of the material property biomechanical factors (e.g., total tissue mean stiffness and GM mean stiffness); GM and WM stiffness and damping ratios were removed from the final model to eliminate collinearities in independent variables.

First, sex was not significant for any of the deformation metrics when additional mechanical property biomechanical features are included in the model, with estimates ranging from -0.001 (95% CrI -0.003, 0.001) for MPS-95 to -0.048 (-0.60, 0.51) for MPSR-95. However, age was significant for both strain-rate independent metrics, MPS-95 and CSDM-25 metrics. Mean total tissue stiffness was not significant for predicting deformation, but the stiffness ICV, or the range of an individual's stiffness, was significant for each of the deformation metrics. In contrast, both mean damping ratio and ICV were significant for each of the deformation metrics. Finally, the percent of brain volume in quadrant one (low stiffness and low damping ratio) was significant for all four deformation metrics, and the volume percentage in quadrant two was significant for CSDM-25.

Based on the value of the estimated parameters, the mean DR had the greatest effect for each of the deformation metrics, except MPSxMPSR-95, with estimates ranging from -0.019 (95% CrI -0.025, -0.122) for MPS-95 to -4.16 (-6.03, -2.30) for MPSR-95. For MPSxMPSR-95, the percentage of brain volume in quadrant one (low stiffness and low DR) had the greatest effect with an estimate of 3.161 (1.76, 4.55). As the mean DR increased, the predicted deformation metrics decreased; while as the percentage of the brain in the low stiffness add damping region increased, the overall deformation metrics also increased. While sex was not a significant predictor of MPS-95, the mean DR of the total tissue had 26.7 times the relative importance of sex on predicting MPS-95.

Table 3: Estimated coefficients for the population-level effects of the multivariate Bayesian linear mixed model and the 95% credible interval (CrI) for the estimated parameter included in square brackets for age, sex, and each material property feature on the deformation metrics. Bolded coefficients are significant based on the CrI. Positive sex coefficients imply male response was greater.

	Intercept	Age	Sex
MPS-95	**0.35** [0.354, 0.36]	**0.002** [0, 0.003]	-0.001 [-0.003, 0.001]
MPSR-95	**64.02** [63.72, 64.31]	0.300 [-0.020 0.612]	-0.048 [-0.60, 0.508]
MPSxMPSR-95	**14.15** [14.05, 14.25]	0.109 [-0.005, 0.221]	-0.046 [-0.236, 0.148]
CSDM 25	**0.30** [0.29, 0.30]	**0.005** [0.001, 0.01]	0.001 [-0.006, 0.008]

	Stiffness Mean	Stiffness IQR	DR Mean	DR IQR
MPS-95	0.000 [-0.004, 0.004]	**0.003** [0.001, 0.004]	**-0.019** [-0.025, -0.122]	**0.007** [0.004, 0.009]
MPSR-95	0.0394 [-1.212, 1.302]	**0.461** [0.0109, 0.929]	**-4.16** [-6.03, -2.30]	**2.2** [1.53, 2.87]
MPSxMPSR-95	0.074 [-0.371, 0.521]	**0.190** [0.032, 0.353]	**-1.281** [-1.953, -0.611]	**0.768** [0.528, 1.005]
CSDM 25	0.015 [-0.002, 0.032]	**0.007** [0.001, 0.013]	**-0.075** [-0.101, -0.050]	**0.013** [0.005, 0.022]

	Quad. 1 Percent.	Quad. 2 Percent.	Quad. 4 Percent.
MPS-95	**0.014** [0.009, 0.019]	0.004 [-0.001, 0.010]	0.002 [-0.002, 0.000]
MPSR-95	**3.161** [1.757, 4.547]	0.2036 [-1.317, 1.716]	0.077 [-1.028, 1.226]
MPSxMPSR-95	**1.332** [0.841, 1.816]	0.121 [-0.417, 0.669]	0.064 [-0.331, 0.467]
CSDM 25	**0.058** [0.040, 0.077]	**0.027** [0.007, 0.047]	-0.007 [-0.022, 0.008]

Discussion

Risk of brain injuries are dependent on both the intrinsic properties, such as a subject's neuroanatomy or material properties, and the head kinematic exposure leading to the injurious event. Based on the result of Chapter 2, after accounting for differences in neuroanatomical features, sex did not have a significant effect on brain deformation, and the effect of sex- and subject-specific material properties needed further analysis. Similar to neuroanatomical features, sex had a statistically significant effect on some material property features, such as mean stiffness and damping ratios, percentage of brain volume in quadrant two (relatively low stiffness and high damping ratio), and IQR of damping ratio within each subject's brain. Additionally, statistically significant age effects were also found for multiple measures of stiffness and damping ratios, which is consistent with previous MRE studies (Hiscox et al., 2021; Sack et al., 2009, 2011). As the subject-specific MRE images were acquired from different studies, the random effect of study was also considered, and for the material property features, there were moderate to excellent ICC for multiple material properties measurements (Cicchetti, 1994). However, similar to the neuroanatomical features analysis, once both the material property features and sex are included in a statistical model to determine their effect on deformation, sex was not a statistically significant predictor of deformation.

Of the material property features, the mean damping ratio of the total brain tissue had the relative highest importance for MPS-95, MPSR-95, and CSDM-25, with increased damping ratio reducing each deformation metric. The damping ratio, defined as the relative viscous-to-elastic behavior, is hypothesized to relate to both the geometric organization of the brain tissue, as well as the network complexity (Guo et al., 2012; Hiscox et al., 2021; Sack et al., 2013). Because previous work has found a strong relationship between hippocampal damping ratios and memory performance, additional research is needed to determine how damping ratio could be affected post-injury and the potential to relate to symptomology (Hiscox et al., 2021). Additionally, as damping ratio relates to the viscosity of the brain tissue, a greater understanding of effect of hydration on damping ratio could offer insights into potential neuroprotective properties. While sex did not have a significant effect on brain deformation after the sex difference seen in the mean damping ratio was accounted for in the model, the statistically significantly lower damping ratio seen in female brains does align with an increased risk of moderate brain injuries seen in Forman et *al.* of belted occupants in frontal automotive crashes (J. Forman et al., 2019).

One major assumption made throughout this study was the implementation of the MRE shear stiffness and damping ratios into the FE brain models by applying a relative scaling metric to *ex vivo* material characterizations. Shown by Hiscox et *al.* with statistically significant differences in shear stiffness between white matter, subcortical gray matter, and cortical gray matter and statistically significant differences in damping ratios between white matter and both cortical and subcortical gray matter, brain tissue is not homogenous through the parenchyma (Hiscox et al., 2020). However, additional research is required to confirm the relative change in both stiffness and damping ratios seen under small deformations during MRE acquisition are equal to the relative changes in stiffness and damping ratios observed at greater levels and higher rates of brain deformation consistent with injurious loading conditions. Additionally, this study investigated the effect of sex and material properties on brain deformation using a single neuroanatomy and a single exposure. There are potentially other head kinematics loading environments which could create a different relative importance of material properties (e.g., very low severity loading environments), but the same analysis could be applied to a greater range of head kinematics.

This study found sex differences within material properties measured in vivo using MRE imaging techniques; however, after accounting for the differences in material properties, sex was not a significant predictor of brain deformation. As the head exposures experienced between male and female occupants may be different for similar automotive crash environments due to differences in mass distribution or engagement with safety equipment (e.g., seat belts), additional work is needed to determine how sex-specific exposures may affect brain deformation and how these differences in exposure could help explain sex differences seen in injury risk between male and female automotive occupants.

Conclusions

- Based on subject specific MRE images, there were statistically significant sex differences between mean total tissue, white matter, and gray matter stiffness, mean total tissue and white matter damping ratios, percentage of brain volume in quadrant two, and the IQR of a subject's damping ratio, after controlling for random study and age effects.
- After accounting for material properties, sex did not have a significant effect on brain deformation; however, the IQR of a subject's stiffness and damping ratio, mean total tissue damping ratio, and percentage of the brain volume in quadrant one were significant predictors of brain deformation for all four metrics, with mean total tissue damping ratio have the greatest relative importance for MPS-95, MPSR-95, and CSDM-25.
- This material properties study did not include any variation or sex differences in neuroanatomical features or head impact kinematics, and additional work is needed to determine the relative importance of intrinsic (e.g., neuroanatomy or material properties) and extrinsic (e.g., head kinematics) factors on brain deformation.

Acknowledgements

Publicly available brain MRI scans were analyzed from two previous studies. Data were provided [in part] by the Brain Biomechanics Imaging Repository (http://www.nitrc.org/projects/bbir). Principal Investigators: P. Bayly, D. Pham, C. Johnson, J. Prince, K. Ramesh, through grants U01 NS11212 and R56 NS055951. Additionally, data was also provided [in part] by Hiscox et *al*. 2020 (MRE-134 dataset) at https://github.com/mechneurolab/mre134.

Chapter 4: Effect of Head Kinematics

Sex had a significant effect on intrinsic neuroanatomical and material property biomechanical features, but after accounting for these biomechanical factors, sex was not significant in predicting brain deformations using intrinsically subject-specific FE brain models. However, these analyses were completed with just one single head kinematic exposure in Chapters 2 and 3. The effect of sex-specific head kinematics must also be considered as a contributing factor to differences in male and female brain injury risks observed in automotive field data (J. Forman et al., 2019). Therefore, this chapter will quantify the differences in male and female head kinematics under matched automotive sled tests and determine their effect on brain deformation using a single neuroanatomy and material property definition.

Introduction

There are some physiological differences between males and females occupants which can lead to differences in head kinematics under similar crash or impact conditions, such as mass distribution, cervical vertebrae dimensions, and neck strength (Nikolova & Toshev, 2007; Vasavada et al., 2008; Young et al., 1983). The female neck has 33% more head mass per unit of neck muscle area compared to a height and neck length matched male with more slender necks and less neck cross-sectional area (Vasavada et al., 2008). Additionally, the female neck has only, on average, 68% and 80% of the strength of a size-matched male neck in flexion and extension, respectively (Vasavada et al., 2008). Neck strength and anticipatory neck muscle activation have been shown to reduce the magnitude of the resulting head kinematics (Eckner et al., 2014; K. A. Reynier et al., 2020); however, injurious head kinematics are often captured with postmortem human surrogates (PMHS), which lack active musculature.

In the past decade, more female anthropometries have been included in automotive crash safety sled testing, with the majority of the female research focusing on the 5th percentile female for continued development of a small female anthropometric test device (ATD). However, the number of sex-matched sled tests is still very limited due to the small number of female PMHS tests. Female PMHS have been tested in the Gold Standard 2 and 3 conditions and recently in both 25° and 45° reclined environments (National Highway Traffic Safety Administration, 2022; Shaw et al., 2017). The Gold Standard 2 (GS2) is a 30 km/h frontal sled test with rigid knee bolsters, a rigid planar seat, and a force limited (3 kN for males, 2 kN for females) three-point shoulder and lap belt (Shaw et al., 2014, 2017). The Gold Standard 3 (GS3) condition is a 30° near-side oblique frontal impact at 30 km/h with a force limited (3 kN for males, 2 kN for females) three-point shoulder and lap belt (Acosta et al., 2016; Humm et al., 2018). Additionally, interest in reclined occupant kinematics has increased with the likelihood of alternate occupant seating options in highly automated vehicles. For both 25° and 45° reclined (relative to vertical) postures, female and male occupants were tested in 15 km/h and 32 km/h frontal sled pulses with a semi-rigid seat, toe pan, knee bolster, and force limited (4.5 kN for males, 2 kN for females) three-point shoulder and lap belt (National Highway Traffic Safety Administration, 2022). While there are differences between the male and female test environments (e.g., load limiters), these conditions are otherwise matched for 50th percentile male and 5th percentile female occupants.

Previous analysis of the effect of head kinematics on brain deformation has been completed, but the effect of sex has not been isolated (Gabler, Crandall, et al., 2018; Gabler et al., 2016, 2019; Takhounts et al., 2013). Gabler et al. investigated the effect of magnitude and duration of angular acceleration on brain deformation using the maximum magnitude of displacement between a single-degree-of-freedom mechanical system and strain-based injury metrics from FE brain models (Gabler, Joodaki, et al., 2018). For long-duration pulses, brain deformation depended primarily on the angular acceleration, while for short-duration pulses, brain deformation depended primarily on the angular velocity (Figure 3). Between these short- and long-durations pulses, near the systems natural period, brain deformation was dependent on a combination of angular velocity and acceleration components (Gabler, Joodaki, et al., 2018). These previous studies primarily investigated male head kinematics using a 50th percentile male FE brain model, and additionally work is needed to determine if sex has a significant effect on both head kinematics and brain deformation.

Using the available sex-matched head kinematics, the first goal of this study was to determine the effect of sex on head kinematic features of PMHS and ATD kinematics, while accounting for surrogate type and BMI; additionally, with an FE brain model with a single representative neuroanatomy and material property definitions, the second goal of this study was to determine if sex was significant on brain deformation and to quantify the relative importance of head kinematic features on the resulting brain deformation metrics.

Methods

Head Kinematics Database

Head kinematics were selected from the National Highway Traffic Safety Administration Biomechanics Test Database (National Highway Traffic Safety Administration, 2022) and included all kinematics with matched male and female conditions. The selected cases included head kinematics from PMHS and ATDs, specifically the 50th percentile male and 5th percentile female Hybrid III and THOR ATDs. The kinematics were considered sex-matched if the loading environment (i.e., crash type, delta-V) was consistent between the male and female occupants. The final 52 selected head kinematics are summarized in Table 4; unless otherwise noted, the male kinematics are associated with a 50th percentile male anthropometry, and the female kinematics are associated with a 5th percentile female anthropometry with normal body mass indices (BMI). For the ATD head kinematics, some test series had more than two repeated tests with the male and female ATDs; to avoid inflating the dataset with repeated test conditions, two traces for each male and female ATD were selected per test condition with ATD traces (i.e., Gold Standard 2 and 3). For these test conditions, the most severe and least severe head kinematic was selected to capture the range of kinematics experienced by the ATD; however, the range of kinematics measured by the ATDs in each of the test conditions was small.

Table 4: The selected head kinematics for male and female matched automotive crash conditions, including the crash condition, sex of occupant, surrogate type, number of cases for each surrogate type, and NHTSA database case numbers. The italicized cases numbers represent obese occupant's head kinematics.

Crash Condition	**Sex**	**Surrogate Type (n)**	**Case Numbers**
Gold Standard 2	Male	PMHS (5)	B11468, B11469, B11509, B11510, B11511
		HIII (2)	B11484, B11508
		THOR (2)	B11473, 11474
	Female	PMHS (10)	B11491, B11492, B11493, B11494, B11495, B12803, B12804, B12805, B12806, B12807
		HIII (2)	S0365, S0366 (internal UVA)
		THOR (2)	B12821, B12822
Gold Standard 3 (Near-Side)	Male	PMHS (3)	B11518, B11519, B11520
		THOR (2)	B11514, B11517
	Female	PMHS (5)	B13162, B13163, B13164, B13167, B13168
		THOR (2)	NSFSD0151, NSFSD0153
Recline 25° - 32 kph	Male	PMHS (2)	B12796, B13109
	Female	PMHS (3)	*B13121*, B13123, B13156
Recline 45° - 15 kph	Male	PMHS (2)	*B13113*, *B13157*
	Female	PMHS (3)	*B13111*, B13115, B13117
Recline 45° - 32 kph	Male	PMHS (4)	B12795, B13110, *B13114*, B13124
	Female	PMHS (3)	*B13112*, B13116, B13118

All signals were debiased using the mean of each signal prior to the beginning of the sled acceleration. The head linear accelerations and angular velocities were then filtered using a CFC180 in accordance with SAE J211. Angular accelerations were computed from debiased, filtered angular velocities using a numerical central difference differentiation. All head kinematics simulated were either transformed to the anatomical center of the head, as is the case for the PMHS data, or measured at the head center of gravity (CG) for the ATDs.

Due to the location of the mounted head kinematic sensor package during PMHS sled testing, often on the top of the head, contact between the PMHS arm and sensor package was common (*Biomechanics Test Database: Test Number 12814*, 2017; National Highway Traffic Safety Administration, 2022). To eliminate these unrelated kinematic spikes, a blended average interpolation scheme was used to correct the head kinematic data (Shaw et al., 2009). The interpolation equation reconstructs the kinematic trace over the disrupted time interval, $f_{gap}(t)$, with uninterrupted data traces, $f_i(t)$, from a similar test condition using the following equation:

$$f_{gap}(t) = \frac{\Delta - (t - t_a)}{\Delta} * \left[\sum_{i}^{n} \frac{[f_i(t) - f_i(t_a)]}{n} + f(t_a)\right] + \frac{(t - t_a)}{\Delta} * \left[\sum_{i}^{n} \frac{[f_i(t) - f_i(t_b)]}{n} + f(t_b)\right]$$

where $\Delta = t_b - t_a$ and n is the number of uninterrupted cases used to inform the disrupted case. Original and corrected signals are included in the Appendix with the time intervals corrected for disrupted signals.

Finite Element Brain Model and Simulations

To keep the effect of head kinematic input condition isolated, all head kinematics were simulated using a single neuroanatomy, specifically the CAB-20MSym FE brain model (used in Chapter 3), with the baseline heterogeneous material properties (used in Chapter 2) (J. S. Giudice et al., 2020, 2021). The neuroanatomy of the CAB-20MSym FE brain model was based on a template MRI image developed using 20 healthy, male brains with 1 mm^3 isotropic voxels (J. S. Giudice et al., 2020). The CAB-20MSym FE brain model includes the brain parenchyma, internal CSF, peripheral CSF, and ventricles, each modeled using 1 mm hexahedral elements, as well as the sagittal sinus, falx cerebri, and tentorium cerebri modeled using two-dimensional shell elements, (J. S. Giudice et al., 2020, 2021). The dura is modelled as a rigid layer of shell elements surrounding the peripheral CSF, and all 6-DOF head kinematics are applied to this rigid dura part through the head center of gravity in the local anatomic head coordinate system (Society of Automotive Engineers, 2007). Each head kinematics simulation was run for 200 ms, and the deformation time history was checked to ensure deformation was not increasing at the end of the simulation.

Head Kinematic Feature Definitions

Multiple head kinematic features were assessed for each of the sex-matched PMHS and ATD sled tests and included measurements of linear acceleration, angular velocity, angular acceleration, and brain injury metrics. For linear acceleration, angular velocity, and angular acceleration, the absolute kinematic in each of the three-anatomic axes and absolute maximum resultant kinematic were computed for each subject. Additionally, brain injury metrics were computed for each of the sex-matched head kinematics, specifically the brain injury criteria (BrIC), the universal brain injury criteria (UBrIC), and the Diffuse Axonal Multi-Axis General Evaluation (DAMAGE) metrics (Gabler, Crandall, et al., 2018; Gabler et al., 2019; Takhounts et al., 2013). Each of these head kinematic biomechanical features were computed using debiased, filter head CG kinematics.

Brain Deformation Metric Definitions

To remain consistent with the analysis of both the neuroanatomical and material property features, the same deformation metrics were used to assess the effect of the head kinematics factors; these included metrics of strain, strain rate, and the product of strain and strain rate (Wu et al., 2021). To avoid the potential effect of any numerical instabilities associated with the absolute maximum, the 95th percentile of each of these metrics was reported (Gabler et al., 2016; J. S. Giudice et al., 2020; K. Reynier et al., 2021). For clarity, the 95th percentile maximum principal strain (MPS-95) is defined as the 95th percentile of the maximum principal strain experienced by each white and gray matter brain element throughout the simulation; the 95th percentile maximum strain rate (MPSR-95) and the 95th percentile product of MPS and MPSR (MPSxMPSR-95) are defined similarly. Additionally, cumulative strain damage measure (CSDM), which represents the volume fraction of elements greater than a specified threshold, was calculated for a commonly used threshold (25%) throughout the white and gray matter elements.

Statistical Analysis of Kinematic Features

For the head kinematics features, a multivariate linear mixed model was used to determine if sex and age were statistically significant factors. To account for differences in study design (e.g., belt pre-tension timing, load limiters, etc.), a random study effect was also included in the linear mixed model. Due to the small number of studies (n = 5), where studies include the differences in delta-V, PDOF, or occupant seat recline angle, mixed model estimation can be challenging due to a high likelihood of the study effect estimate being zero under a frequentist approach. To avoid this issue, analysis was carried out using a Bayesian linear mixed model where the biomechanical factors (outcome variables) were jointly modelled to take advantage of strong correlations among them. To determine sex effects on the head kinematic biomechanical factors, the Bayesian multivariate mixed linear model had the following structure, with $Y_{ij}^{(k)}$ being the k_{th} outcome associated with the i_{th} brain model in the j_{th} study, with linear acceleration in the x-direction provided as an example below:

$$Y_{ij}^{ACC\ X} = \left(\beta_0^{ACC\ X} + u_{j0}^{ACC\ X}\right) + \beta_1^{ACC\ X}(BMI_{ij}) + \beta_2^{ACC\ X}\left(Sex_{ij}\right) + \beta_3^{ACC\ X}\left(Surrogate_{ij}\right) + \epsilon_{\mathrm{ij}}^{ACC\ X}$$

where β_0 are the population intercepts, u_{j0} are the random intercepts for the j_{th} study, BMI is the body mass index of the surrogate, surrogate is either ATD or PMHS (reference = ATD), Sex of the surrogate (reference = female), $\epsilon_{\mathrm{ij}}^{k}$ are the outcome-specific residual terms, and ACC are linear accelerations (g). The remaining equations for the angular velocities (ARS - rad/s) and angular accelerations (Alpha - rad/s^2) are provided in the Appendix.

For each of the individual outcomes (i.e., the biomechanical factors), priors sensitivity analysis was conducted for the intercept, the β terms, and the study random effect standard deviations. Based on this sensitivity, the priors with the largest standard deviation (i.e., least informative) with stable estimates were used in the final model. Estimation took place using the *brms* package in The RStudio (R version 4.2.0) (Bürkner, 2017; R Core Team, 2022). Three parallel initially over dispersed Markov Chain Monte Carlo (MCMC) chains were used, where each chain ran for 3,000 iterations after the 2,000 iteration warmup. Effective sample sizes were examined to ensure each parameter's effective sample size was greater than 1,000 for each parameter. A visual inspection of the MCMC chains and assuring that Rhat values were approximately 1.00 indicated acceptable convergence. Correlation between the material neuroanatomical features were computed, and highly correlated parameters (r > 0.8) were noted. All Credible Intervals (CrI) reported are 95% equal tailed intervals. For each head kinematic feature, the intraclass correlation (ICC) was computed to report the correlation of observations within one study.

A similar methodology was used to determine significant biomechanical factor predictors of the deformation metrics, the order of importance of these biomechanical factors, and the significance of sex after accounting for these biomechanical factors. Therefore, to determine the effect of the head kinematic biomechanical factors and sex on the deformation metrics, the multivariate mixed linear model had the following structure, with $Y_{ij}^{(k)}$ being the k_{th} outcome associated with the i_{th} brain model in the j_{th} study, with the model for MPS-95 provided as an example below:

$$
\begin{aligned}
Y_{ij}^{MPS-95} = {} & \left(\beta_0^{MPS-95} + u_{j0}^{MPS-95}\right) + \beta_1^{MPS-95}\left(BMI_{ij}\right) + \beta_2^{MPS-95}\left(Sex_{ij}\right) + \beta_3^{MPS-95}(Surrogate) \\
& + \beta_4^{MPS-95}\left(ACC\ X_{ij}\right) + \beta_5^{MPS-95}\left(ACC\ Y_{ij}\right) + \beta_6^{MPS-95}\left(ACC\ Z_{ij}\right) \\
& + \beta_7^{MPS-95}\left(ACC_{ij}\right) + \beta_8^{MPS-95}\left(ARS\ X_{ij}\right) + \beta_9^{MPS-95}\left(ARS\ Y_{ij}\right) + \beta_{10}^{MPS-95}\left(ARS\ Z_{ij}\right) \\
& + \beta_{11}^{MPS-95}\left(ARS_{ij}\right) + \beta_{12}^{MPS-95}\left(Alpha\ X_{ij}\right) + \beta_{13}^{MPS-95}\left(Alpha\ Y_{ij}\right) \\
& + \beta_{14}^{MPS-95}\left(Alpha\ Z_{ij}\right) + \beta_{15}^{MPS-95}\left(Alpha_{ij}\right) + \beta_{16}^{MPS-95}\left(BrIC_{ij}\right) + \beta_{17}^{MPS-95}\left(UBrIC_{ij}\right) \\
& + \beta_{18}^{MPS-95}\left(DAMAGE_{ij}\right) + \epsilon_{\mathrm{ij}}^{MPS-95}
\end{aligned}
$$

where β_0 are the population intercepts, u_{j0} are the random intercepts for the j_{th} study, BMI of the surrogate (centered and scaled using the mean and standard deviation of the sample), Surrogate is either ATD or PMHS, Sex of the surrogate, each of the biomechanical features previously justified (centered and scaled using the mean and standard deviation of the sample), and $\epsilon_{\mathrm{ij}}^{k}$ are the outcome-specific residual terms. The equations for the remaining deformation metrics are included in the Appendix. Priors were assigned after a prior sensitivity analysis as previously described. The same model fitting parameters in RStudio were used to estimate the neuroanatomical biomechanical factor and brain deformation metrics model. Correlations between the independent variables were assessed using the biomechanical factors linear mixed model described previously, and for pairs of variables with correlations greater 0.80, a single parameter was kept in the final model. The final linear mixed model included these uncorrelated, independent variables against the deformation metrics. Because all quantitative independent variables were centered and scaled, the relative importance of each biomechanical factor was determined using the absolute value of the estimated coefficient.

Results

Head Kinematics and Biomechanical Features

When comparing distributions of peak kinematics, male and female head kinematic responses are generally similar (Figure 30). For linear accelerations, the mean male peak kinematics were greater than the female kinematics, with a larger male standard deviation for each of the three directional kinematics and peak resultant kinematics. The mean female peak angular rates were greater for the peak resultant and the y- and z-direction, with larger standard deviations, but the male mean peak x-direction angular rate was greater, with a larger standard deviation. The mean z-direction angular acceleration was greater, with a larger standard deviation, than the male z-direction angular acceleration; however, the other three angular acceleration metrics were greater for the male occupants. Of the injury metrics assessed, the mean male UBrIC and DAMAGE were greater with larger standard deviations, but the average female BrIC metric was larger with a larger standard deviation.

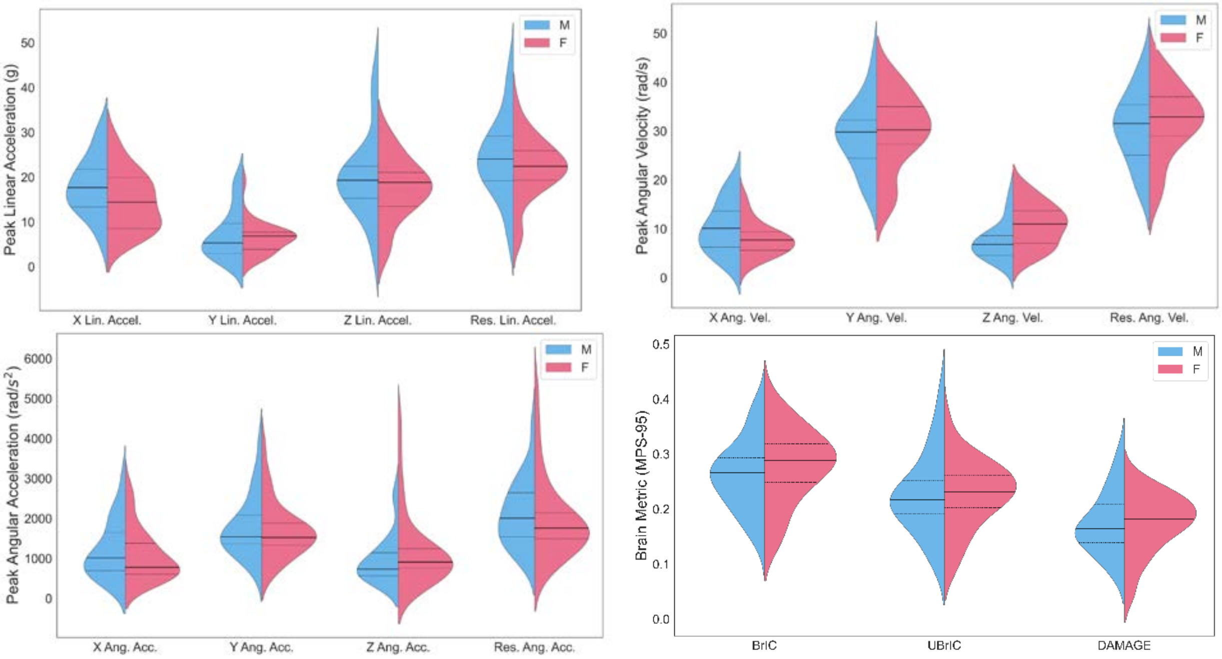

Figure 30: Distributions of the linear acceleration (top left), angular velocity (top right), angular acceleration (bottom left), and kinematic-based brain metrics (bottom right) for the male and

female head kinematics. Medians are represented by the solid line, and quartiles one and three are represented by the dashed lines.

Based on the Bayesian multivariate linear mixed model, sex was significant for the peak x-direction and resultant linear accelerations, and x- and z-direction angular rates. Surrogate type was significant for peak z-direction angular rate and peak y-direction angular acceleration. BMI was significant only for peak z-direction and resultant linear acceleration. The complete list of estimated parameters for the effect of sex, surrogate, and BMI is included in the Appendix. Due to similarities in loading environments, there were high correlations ($r > 0.8$) between the following pairs of head kinematic parameters: peak ARS-Y and resultant ARS, peak ARS-Y and BrIC, peak resultant ARS and BrIC, and peak Alpha-Y and UBrIC. For each of these pairs, a single parameter was included in the final model to determine the effect of head kinematic feature, sex, BMI, and surrogate type on brain deformation. The x-direction angular rate had the largest ICC ($ICC_{ARS\text{-}X} = 0.70$), and all other ICC values for the head kinematics are included in the Appendix.

Effect of Head Kinematics on Brain Deformation

For each of the head kinematic features assessed, as the head kinematic value increases, each of the four metrics of brain deformation increase. The DAMAGE metric (Figure 31) had the highest correlations for both the male and female kinematics for MPS-95 ($r_{male} = 0.98$, $r_{female} = 0.96$), MPSxMPSR-95 ($r_{male} = 0.95$, $r_{female} = 0.95$), and CSDM-25 ($r_{male} = 0.88$, $r_{female} = 0.78$); the UBrIC metric had the highest correlations for the male and female kinematics for MPSR-95 ($r_{male} = 0.93$, $r_{female} = 0.87$). Both of these metrics were developed to predict MPS-95 of the 50th percentile male Global Human Body Models Consortium (GHBMC) FE brain model, so it is unsurprising these two metrics have the highest correlations for the deformation metrics (Gabler, Crandall, et al., 2018; Gabler et al., 2019). Excluding the kinematic-based brain metrics, the y-direction angular acceleration (Figure 32) had the highest correlation for all the MPS-95 ($r_{male} = 0.87$), MPSR-95 ($r_{male} = 0.92$, $r_{female} = 0.83$), and MPSxMPSR-95 ($r_{male} = 0.91$, $r_{female} = 0.82$) metrics for both the male and female kinematics, except the female MPS-95 which had the highest correlation with peak resultant ARS (r_{female} = 0.860).

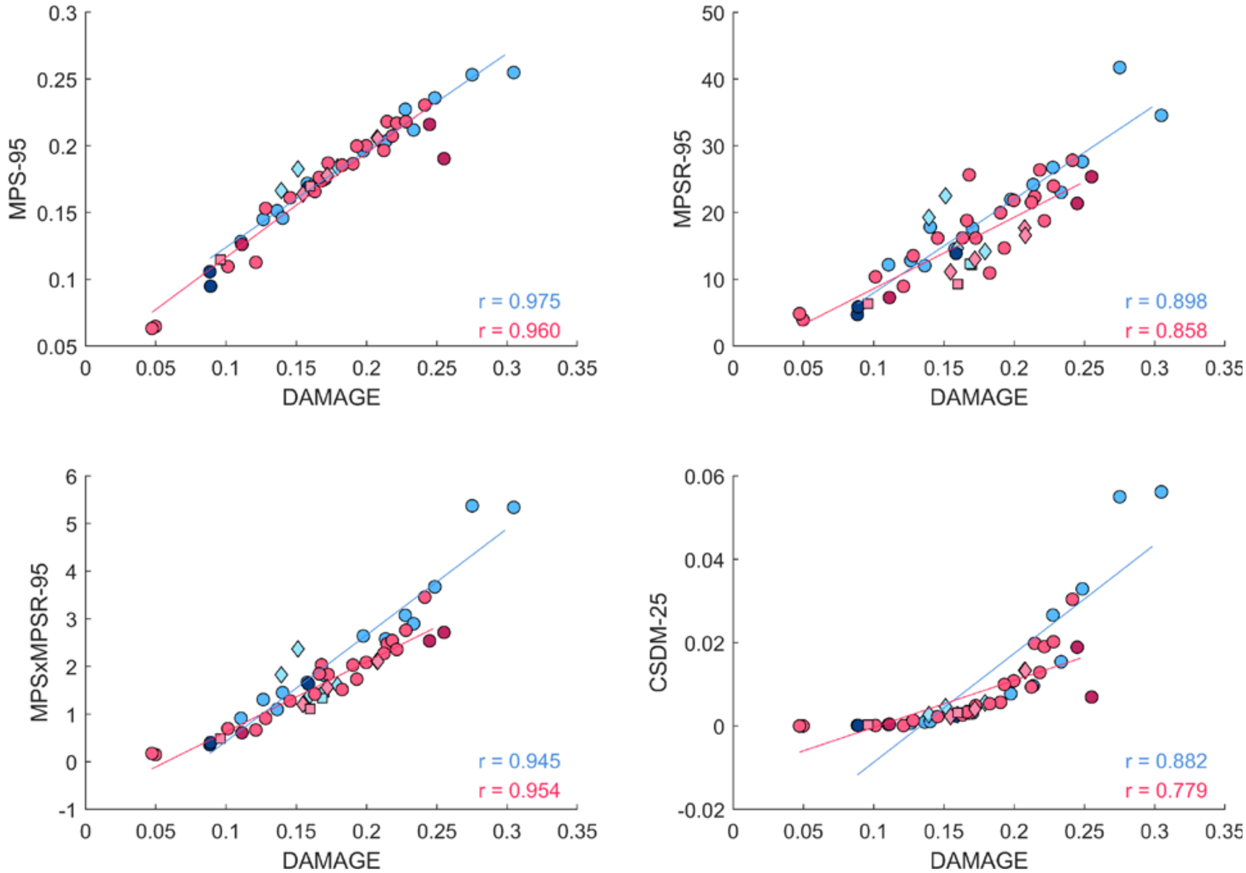

Figure 31: Scatter plots for MPS-95, MPSR-95, MPSxMPSR-95, and CSDM-25 against DAMAGE for the male (blue) and female (pink) kinematics. The circle data points are PMHS kinematics, the diamond data points are THOR kinematics, the square data points are HIII kinematics, and the dark blue and dark pink circles correspond to the obese kinematics for males and females, respectively. Linear trendlines and correlations also provided for both the male and female subjects.

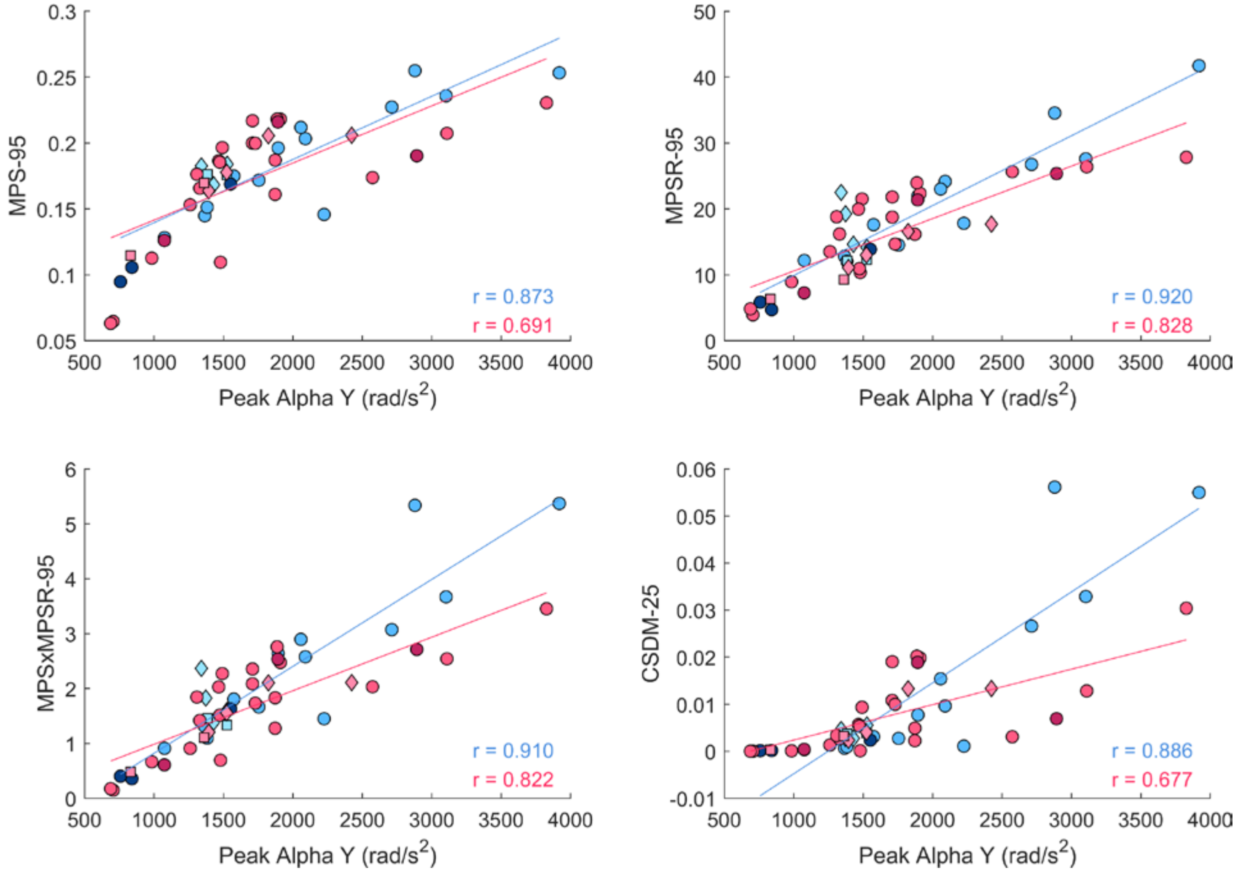

Figure 32: Scatter plots for MPS-95, MPSR-95, MPSxMPSR-95, and CSDM-25 against y-direction angular acceleration for the male (blue) and female (pink) kinematics. The circle data points are PMHS kinematics, the diamond data points are THOR kinematics, the square data points are HIII kinematics, and the dark blue and dark pink circles correspond to the obese kinematics for males and females, respectively. Linear trendlines and correlations also provided for both the male and female subjects.

The deformation metrics linear mixed model revealed no statistically significant sex effects after accounting for the head kinematic features (Table 5), with estimated ranging from 0.003 (95% CrI -0.01, 0.01) for MPS-95 to 1.54 (-0.11, 0.44) for MPSR-95. Surrogate type and BMI were statistically significant predictors of MPSR-95, and surrogate type was also statistically significant for MPSxMPSR-95. Based on the relative size of the estimates, the DAMAGE metric had the greatest effect of each of the deformation metrics. The ICC for the deformation metrics ranged from poor for MPSR-95 and MPSxMPSR-95 ($ICC_{MPSR\text{-}95}$ = 0.15, $ICC_{MPSxMPSR\text{-}95}$ = 0.36), good for MPS-95 ($ICC_{MPS\text{-}95}$ = 0.64), and excellent for CSDM-25 ($ICC_{CSDM\text{-}25}$ = 0.78).

Table 5: Estimated coefficients for the population-level effects of the multivariate Bayesian linear mixed model and the 95% credible interval (CrI) for the estimated parameter included in square brackets for sex, BMI, surrogate, and each head kinematic feature on the deformation metrics. Bolded coefficients are significant based on the CrI. Positive sex, surrogate, and BMI coefficients imply male, cadaver, obese response was greater.

	Intercept	Sex	BMI	Surrogate
MPS-95	**0.17** [0.15, 0.19]	0.003 [-0.005, 0.01]	-0.004 [-0.02, 0.01]	-0.001 [-0.01, 0.01]
MPSR-95	**13.91** [11.52, 16.35]	1.54 [-0.57, 3.62]	**-3.28** [-6.15, -0.30]	**3.89** [1.72, 6.06]
MPSxMPSR-95	**1.58** [1.20, 2.00]	0.16 [-0.11, 0.44]	-0.25 [-0.65, 0.17]	**0.34** [0.03, 0.65]
CSDM-25	0.01 [-0.00, 0.02]	0.0002 [-0.01, 0.01]	-0.004 [-0.01, 0.01]	0.003 [-0.005, 0.01]
	ACC X	ACC Y	ACC Z	ACC
MPS-95	0.005 [-0.004, 0.01]	-0.003 [-0.008, 0.002]	0.001 [-0.008, 0.01]	0.002 [-0.01, 0.01]
MPSR-95	0.28 [-1.74, 2.43]	**2.38** [1.00, 3.76]	1.73 [-0.78, 4.21]	-2.18 [-5.39, 1.04]
MPSxMPSR-95	0.01 [-0.28, 0.30]	0.14 [-0.04, 0.32]	0.22 [-0.12, 0.56]	-0.25 [-0.68, 0.19]
CSDM-25	-0.001 [-0.007, 0.01]	0.0002 [-0.003, 0.003]	0.002 [-0.005, 0.009]	-0.002 [-0.01, 0.007]
	ARS X	ARS Z	ARS	Alpha X
MPS-95	-0.001 [-0.006, 0.004]	-0.001 [-0.009, 0.006]	**0.015** [0.007, 0.02]	-0.001 [-0.005, 0.004]
MPSR-95	-0.09 [-1.36, 1.21]	-0.80 [-2.23, 0.58]	0.98 [-1.17, 3.13]	-1.00 [-2.25, 0.26]
MPSxMPSR-95	0.03 [-0.14, 0.20]	-0.13 [-0.33, 0.07]	-0.14 [-0.43, 0.15]	-0.10 [-0.27, 0.07]
CSDM-25	0.002 [-0.002, 0.005]	-0.0003 [-0.01, 0.005]	-0.005 [-0.01, 0.001]	-0.001 [-0.004, 0.002]
	Alpha Z	Alpha	UBrIC	DAMAGE
MPS-95	-0.001 [-0.008, 0.005]	0.007 [-0.003, 0.017]	-0.009 [-0.026, 0.008]	**0.030** [0.023, 0.036]
MPSR-95	0.22 [-1.52, 1.96]	2.77 [-0.04, 5.62]	0.37 [-3.52, 4.15]	**3.48** [1.58, 5.36]
MPSxMPSR-95	**-0.24** [-0.48, -0.01]	0.33 [-0.05, 0.71]	0.25 [-0.29, 0.79]	**0.84** [0.59, 1.09]
CSDM-25	**-0.005** [-0.01, -0.001]	0.003 [-0.005, 0.01]	0.008 [-0.004, 0.02]	**0.011** [0.006, 0.02]

Discussion

With consistent neuroanatomy and material properties, the effects of the sex-specific extrinsic exposure were investigated in different automotive crash environments. A majority of the head kinematics investigated were associated with either a 50th percentile male anthropometry or a 5th percentile female anthropometry, and as a result, there are potential effects of occupant size associated with any differences in head kinematic features. However, when comparing these two cohorts, there were statistically significant sex differences for peak x- and resultant linear accelerations, and x- and z-angular rates after controlling for BMI and surrogate type of the occupants. In a pure frontal (GS-2 and reclined configurations) and near-side oblique (GS3) and automotive crashes, the primary linear acceleration experienced by the occupant is the x-direction acceleration; however, the primarily local linear acceleration of the head is a positive z-direction, and this significant difference in the x-direction is in the secondary loading direction. Similar trends are seen in the angular rates, with the primary loading in the head local coordinate system about the y-axis, but the significant differences seen in angular rates were in the x- and z-angular rates. Sex did not have a statistically significant effect on the deformation metrics assessed after accounting for the head kinematic features, surrogate type, and occupant BMI in the statistical model. The DAMAGE brain injury metric had the highest relative importance of head kinematic features analyzed. In relative comparison, the effect of the DAMAGE metric is almost nine times as important as sex for MPS-95. In an additional statistical model estimated without the DAMAGE metric, peak resultant angular velocity had the greatest impact on MPS-95, surrogate type had the greatest and peak resultant angular acceleration had the second highest relative effect on MPSR-95, and peak angular acceleration – though not significant – had the highest relative effect on MPSxMPSR-95.

One major limitation of this study is the number of sex-matched head kinematics simulated as a result of the limited sex-matched sled tests available in the automotive safety field. While current and future research is working to better match occupant parameters, such as testing 50th percentile female anthropometries, additionally sled tests are needed to better understand the effect of differing restraint specifications (e.g., load limiters) on resulting head impacts in male and female occupants. For both the Gold Standard 2 (GS2) and GS3 test environments, the 50th percentile male occupants were tested with a 3 kN shoulder belt load limiter, but the smaller 5th percentile female occupants were tested with only a 2 kN load limiter. Additionally, the load limiter in the male reclined tests was 4.5 kN, but the load limiter in the female reclined tests was kept at 2 kN. The difference in these load limiters could affect the head kinematics and max excursions experienced by each of these occupants. For this analysis, the effect of these differing parameters was accounted for with the random study effects to capture the different loading conditions (i.e., GS2, GS3, reclined degree and sled speed).

Similar to the analyses of neuroanatomy and material properties, this assessment of head kinematics does not include variation in the intrinsic brain properties. There is a possibility that different baseline material properties could affect the relative importance of these kinematic features on brain deformation; therefore, an additional analysis investigating the relative importance of each significant intrinsic property and these extrinsic head kinematic features on brain deformation is required. Additionally, this sex-matched analysis is limited to conditions with both male and female head kinematics. There are crash conditions that are more and less severe seen in field data than those included in this small sample of GS2, GS3, and reclined configurations that could affect which kinematic feature has the greatest impact on brain deformation.

Conclusions

- A variety of head kinematic features and brain injury metrics from sex-matched PMHS and ATD sled tests were computed, and there were statistically significant sex differences in peak x- and resultant linear accelerations, and x- and z-axis angular rates, with statistically significant effects of surrogate type and BMI additionally observed.

- A Bayesian linear mixed model predicting brain deformation metrics based on head kinematic features, sex, surrogate type, and BMI concluded sex was not a statistically significant predictor of deformation after accounting for the head kinematic elements.
- The conclusions of this study are based on the limited sample of sex-matched sled tests and resulting head kinematics, which include only GS2, GS3, and reclined configurations. Additional sex-matched kinematics are required to draw larger conclusions about the effects of extrinsic factors (e.g., kinematics features, restraint system features) on brain deformations in both male and female occupants.

Chapter 5: Final Sensitivity of Neuroanatomy, Material Properties, Head Kinematics and Sex

As discussed in previous chapters, sex is correlated with the biomechanical characteristics of anatomy, material properties, and head kinematics. However, sex as an independent covariate was found not to be significant when studying the effects that these factors have on brain deformation. For those previous analyses, each of the biomechanical factors was analyzed independently, making it difficult to identify which feature had the overall largest effect on brain deformation. Furthermore, a holistic analysis incorporating the variability each of these factors and their interactions is needed. Based on the results of the previous chapters, the covariate of sex is expected to remain not statistically significant, but the relative importance of sex to these biomechanical features can offer additional information as to what may be causing differences in injury risk between male and female automotive occupants. Therefore, this chapter will quantify the relative effect of the previously significant biomechanical features and sex on brain deformation from varying head kinematics using subject-specific neuroanatomical and material property-based finite element brain models.

Introduction

Ultimately, the goal of injury biomechanics research is to improve the understanding of a biomechanical response of the human body to a potentially injurious loading environment to reduce the likelihood of injury. In automotive safety, review of epidemiology data provides feedback on the success of this research and highlights areas for possible improvement. For belted female occupants, the odds of sustaining a moderate brain injury (OR = 1.76) in a frontal crash are higher than for male occupants, even after accounting for crash severity (delta-V), age, height, BMI, and model year of vehicle (J. Forman et al., 2019); however, this result does not include intrinsic properties of the human brain, nor direct information about the underlying injury mechanism, brain deformation. Intrinsic properties of the human brain, such as sex, intracranial volume (ICV), or shear stiffness, are factors that cannot be altered, but how these relate to brain deformation needs further analysis, in particular, which of these intrinsic properties has the greatest effect on brain deformation. As finite element (FE) brain models improve, there is growing interest in subject-specific predictive clinical brain models, and a greater understanding of the effect of intrinsic brain properties on brain injury risk would improve applicability of these advanced future models.

Intrinsic brain properties cannot be modified to reduce the risk of injury, but the head kinematic exposure during an automotive crash is affected via active and passive safety features of vehicles, and these features can be tuned to reduce exposure. Passive restraint features, such as belt pre-tensioners, have been shown to reduce head excursion with improved engagement between the shoulder belt and occupant and decreases the time between seat belt engagement by removing any slack in the belt system (R. Kent et al., 2012; R. W. Kent & Forman, 2015). To best improve safety features, the relative importance of exposure metrics on brain deformation is needed to provide a target exposure limit. Additionally, to best protect all occupants, sex-specific passive safety features may be required to best restrain the varying anthropometries or mass distributions present between male and female occupants.

Combined sensitivity of brain deformation to both intrinsic and extrinsic factors is lacking for male and female brain biomechanics. The goal of this chapter is to determine the relative importance of intrinsic (e.g., ICV, stiffness, sex) and extrinsic (e.g., head kinematic features) on brain deformation metrics using FE brain models with subject- and sex-specific neuroanatomies and relative material properties for automotive crash representative loading conditions.

Methods

Final Model Selection

To capture the interactions between neuroanatomic and material property features, a smaller subset of the brain models developed in Chapters 2 and 3 were selected and simulated across a range of head kinematics. Based on the effects of neuroanatomy, 10 brain models were selected to represent the range of intracranial volumes (ICV) and relative white matter (WM) volumes seen within the male and female subjects in Chapter 2. Targets of the minimum, 25th percentile, median, 75th percentile, and maximum ICV for each sex (Table 6) were used to determine 10 brain models (5 male and 5 female brains) which represented the range of neuroanatomical features (Figure 33). The span of these 10 brain models were checked against the spread of the relative WM volume seen within the subject population to assure a distribution of relative WM volumes were also captured. All selected model's ICV were within 1% of their target volume. The correlations between ICV and relative WM for the total male and female populations were 0.44 and 0.37, respectively; for the selected models, the correlation between ICV and relative WM volume were 0.43 and 0.36 for the male and female selected models, respectively.

Table 6: Target ICV measurements, selected model values, and selected subject's age for the final 10 neuroanatomy-based subjects. The percentage difference between the target ICV measurement and the selected model's ICV measurement included in parenthesis.

	ICV Metric	Target ICV (cm^3)	FE Model ICV (cm^3)	Subject Age (yr.)
Female	Minimum	1136.4	1136.4 (0%)	42
	25th Percentile	1337.9	1337.9 (0%)	20
	Median	1397.7	1396.6 (-0.1%)	20
	75th Percentile	1482.3	1467.0 (-1.0%)	39
	Maximum	1681.4	1681.4 (0%)	19
Male	Minimum	1280.5	1280.5 (0%)	69
	25th Percentile	1450.0	1444.8 (-0.4%)	19
	Median	1525.0	1524.9 (-0.0%)	23
	75th Percentile	1627.5	1628.3 (0.1%)	19
	Maximum	1804.5	1801.9 (-0.1%)	19

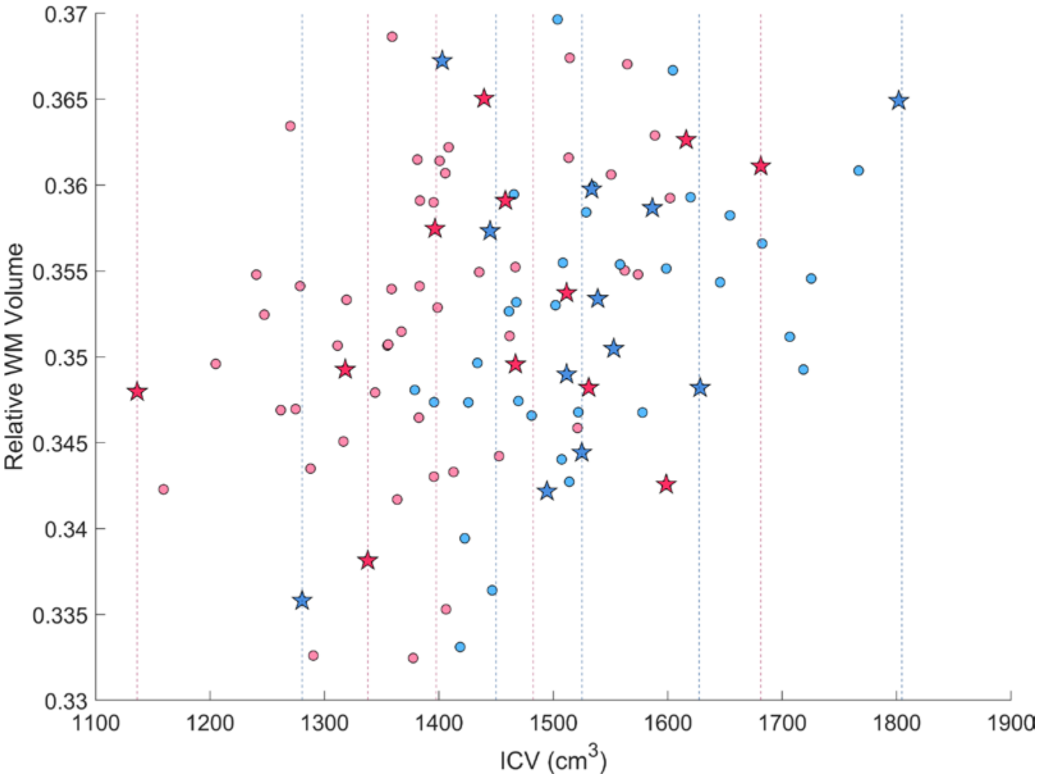

Figure 33: The range of ICV and relative WM volume for all subjects, with all final selected models (including material-based final models) denoted as stars. The dashed lines represent the target ICV measurements for both male (blue) and female (pink) subjects.

Additionally, based on the results of Chapter 3 and the effect of material properties, an additional 14 models (7 male and 7 female models) were selected to capture the spread of the mean shear stiffness and damping ratios seen in the brain MRE scans (Table 6). For each sex separately, nine regions defined the lower, middle, and upper third of both mean shear stiffness and damping ratios; one male and one female model were then selected from the seven regions populated with models (Figure 34). The correlations between mean shear stiffness and mean damping ratio for the total male and female populations were 0.40 and 0.18, respectively; for the selected models, the correlation between mean shear stiffness and mean damping ratio were 0.47 and 0.46 for the male and female selected models, respectively.

These final 24 models (12 male and 12 female) models are based on the subject-specific neuroanatomic meshes, developed in Chapter 2, and the subject-specific material property distributions, developed in Chapter 3, to create subject-specific models from the CAB-20MSym heterogeneous FE brain model (J. S. Giudice et al., 2021).

Table 7: Mean shear stiffness and damping ratio for the 14 final material-based selected subjects and the selected subject's ages.

	Region	Mean Stiffness (kPa)	Mean DR	Subject Age (yr.)
Female	2	2.80	0.17	18
	3	3.05	0.15	21
	4	2.46	0.22	21
	5	2.70	0.21	23
	6	2.99	0.19	22
	7	2.33	0.27	68
	8	2.81	0.25	31
Male	2	2.69	0.16	20
	3	3.45	0.13	20
	4	2.53	0.20	20
	5	2.89	0.19	22
	6	3.06	0.21	20
	7	2.39	0.24	65
	8	2.78	0.25	41

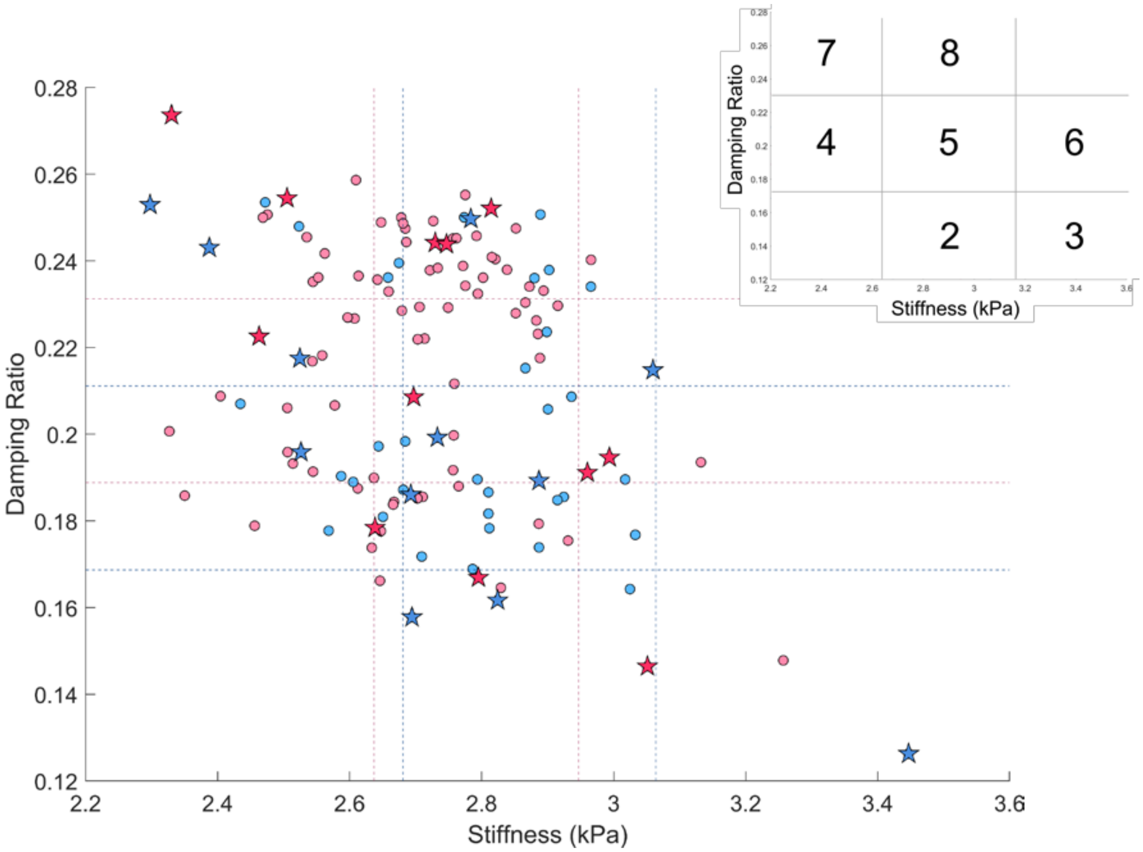

Figure 34: The range of mean stiffness and damping ratios for all subjects, with all final selected models (including ICV-based final models) denoted as stars. The dashed lines represent the target regions for both male (blue) and female (pink) subjects with the region numbers labelled in upper inset.

Final Head Kinematics Selection

Each of these 24 models were then simulated using various head kinematics to understand the relative importance of the intrinsic properties (neuroanatomy and material properties) and the extrinsic properties (head kinematics) on brain deformation. For each of the loading conditions (GS 2, GS 3, Recline 25/45 degrees and 15/32 kph), 6-degree-of-freedom head kinematics was selected to represent the loading environment. The final head kinematics (Figure 35) were selected to capture the spread of head kinematics examined in Chapter 4, and the DAMAGE metric for each kinematic was compared to the total distribution of DAMAGE metrics (Figure 36) to assure a range of loading severities.

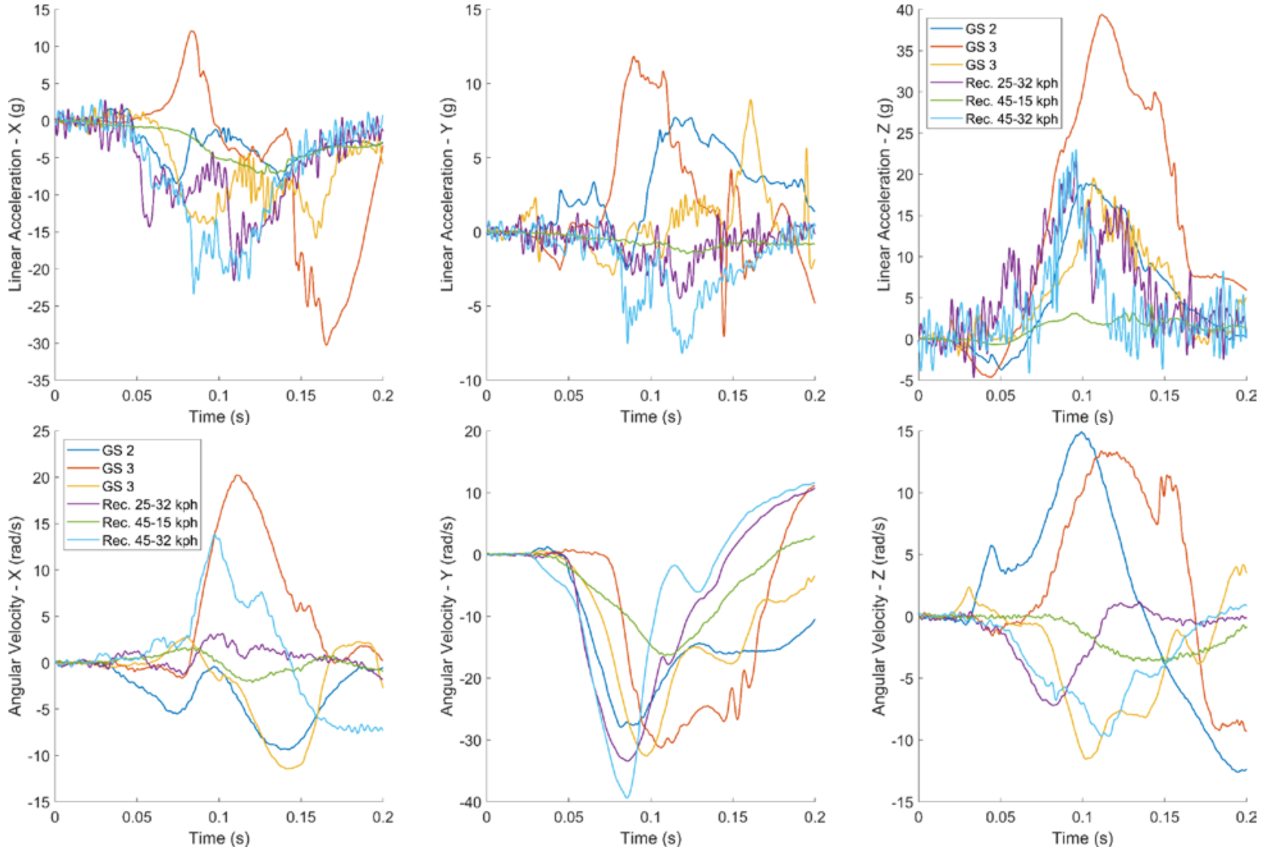

Figure 35: The final selected 6-DOF head kinematics, with the linear acceleration (top) and angular velocity (bottom) time histories for each of the crash conditions investigated in Chapter 4.

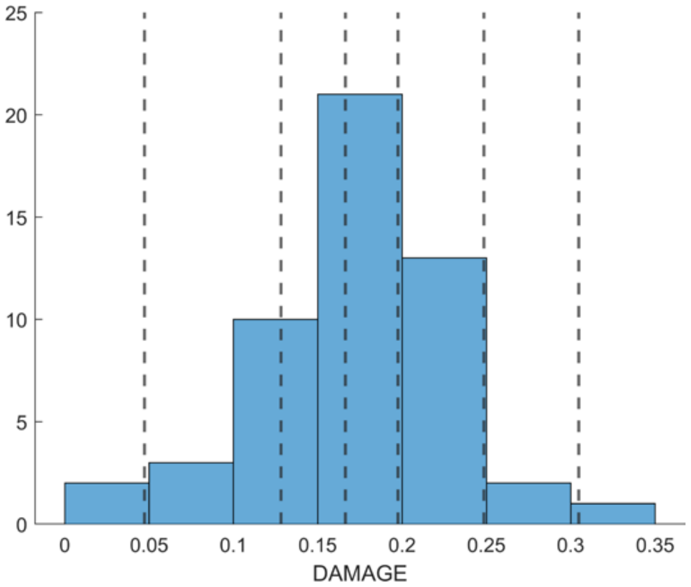

Figure 36: Distribution of DAMAGE metric for the sex-matched head kinematics assessed in Chapter 4 with the DAMAGE metrics of the final selected head kinematics shown as dashed lines.

Biomechanical Features Definitions

To remain consistent with Chapters 2, 3, and 4, the same biomechanical features will be assessed in this study. The total intracranial volume (ICV) and relative white matter (WM) volume percentage were used to assess the effects of the two highest relative importance neuroanatomical features. The mean stiffness and damping ratios of the entire brain tissue, the interquartile ranges of both stiffness and damping ratios, and the percentage of brain volume in quadrants one, two, and four (as defined in Chapter 3) were used to capture the effect of the material properties. For the head kinematic features, all the uncorrelated peak kinematic measurements (linear accelerations: ACC-X, ACC-Y, ACC-Z, resultant ACC; angular velocities: ARS-X, ARS-Z, resultant ARS; angular accelerations: Alpha-X, Alpha-Z, resultant Alpha) and brain injury metrics (UBrIC and DAMAGE) were assessed. Only head kinematics from PMHS sled testing were selected for the final sensitivity assessment, so surrogate type was not included in the final assessment. Additionally, only normal body mass index (BMI) PMHS head kinematics were selected, so BMI also removed from the final assessment.

Brain Deformation Metric Definitions

To remain consistent with the analysis of the previous chapters, the same deformation metrics were used to assess the effect of the material biomechanical factors; these included metrics of strain, strain rate, and the product of strain and strain rate (Wu et al., 2021). To avoid the potential effect of any numerical instabilities associated with the absolute maximum, the 95th percentile of each of these metrics was reported (Gabler et al., 2016; J. S. Giudice et al., 2020; K. Reynier et al., 2021). For clarity, the 95th percentile maximum principal strain (MPS-95) is defined as the 95th percentile of the maximum principal strain experienced by each white and gray matter brain element throughout the simulation; the 95th percentile maximum strain rate (MPSR-95) and the 95th percentile product of MPS and MPSR (MPSxMPSR-95) are defined similarly. Additionally, cumulative strain damage measure (CSDM), which represents the volume fraction of elements greater than a specified threshold, was calculated for a commonly used threshold (25%) throughout the white and gray matter elements.

Statistical Analysis for the Effect of Sex on Biomechanical Features

For each of the biomechanical features, a multivariate linear mixed model was used to determine if sex and age were statistically significant factors in the subset of simulations selected for the final sensitivity. The statistical analysis was carried out using a Bayesian linear mixed model where the biomechanical factors (outcome variables) were jointly modelled to take advantage of any correlations among them. To determine sex effects on the biomechanical factors, the Bayesian multivariate mixed linear model had the following structure, with $Y_i^{(k)}$ being the k_{th} outcome associated with the i_{th} brain model, with ICV provided as an example below:

$$Y_i^{ICV} = \left(\mathrm{\beta}_0^{ICV}\right) + \beta_1^{ICV}(scale(Age_i)) + \beta_2^{ICV}(Sex_i) + \epsilon_{\mathrm{i}}^{ICV}$$

where β_0 are the population intercepts, Age is age in years (centered and scaled using the mean and standard deviation of the sample), Sex is sex of the brain (reference = female), and $\epsilon_{\mathrm{ij}}^{k}$ are the outcome-specific residual terms. The remaining equations for the other biomechanical factors are provided in the Appendix.

For each of the individual outcomes (i.e., the biomechanical factors), priors sensitivity analysis was conducted for the intercept, the β terms, and the study random effect standard deviations. Based on this sensitivity, the priors with the largest standard deviation (i.e., least informative) with stable estimates were used in the final model. Estimation took place using the *brms* package in The RStudio (R version 4.2.0) (Bürkner, 2017; R Core Team, 2022). Three parallel initially over dispersed Markov Chain Monte Carlo (MCMC) chains were used, where each chain ran for 3,000 iterations after the 2,000 iteration warmup. Effective sample sizes were examined to ensure each parameter’s effective sample size was greater than 1,000 for each parameter. A visual inspection of the MCMC chains and assuring that Rhat values were approximately 1.00 indicated acceptable convergence. All Credible Intervals (CrI) reported are 95% equal tailed intervals.

Statistical Analysis for the Effect of Biomechanical Factors on Brain Deformation Metrics

Based on the statistical methodology completed in the previous chapters, a multivariate Bayesian linear model was used to determine significant biomechanical factor predictors of the deformation metrics, the order of importance of these biomechanical factors, and the significance of sex after accounting for these biomechanical factors. Therefore, to determine the effect of biomechanical factors and sex on the deformation metrics, the multivariate linear model had the following structure, with $Y_i^{(k)}$ being the k_{th} outcome associated with the i_{th} brain model, with the model for MPS-95 provided as an example below:

$$\begin{aligned} Y_i^{MPS-95} = {} & \left(\beta_0^{MPS-95}\right) + \beta_1^{MPS-95}(Age_i) + \beta_2^{MPS-95}(Sex_i) + \beta_3^{MPS-95}(ICV) + \beta_4^{MPS-95}(Rel\ WM_i) \\ & + \beta_5^{MPS-95}(Stiff_i) + \beta_6^{MPS-95}(DR_i) + \beta_7^{MPS-95}(Stiff\ IQR_i) + \beta_8^{MPS-95}(DR\ IQR_i) \\ & + \beta_9^{MPS-95}(Quad\ 1_i) + \beta_{10}^{MPS-95}(Quad\ 2_i) + \beta_{11}^{MPS-95}(Quad\ 4_i) \\ & + \beta_{12}^{MPS-95}(DAMAGE_i) + \epsilon_{\mathrm{i}}^{MPS-95} \end{aligned}$$

where β_0 are the population intercepts, Age is the age of the subject in years (centered and scaled using the mean and standard deviation of the sample), Sex of the subject (reference = female), each of the biomechanical features previously justified (centered and scaled using the mean and standard deviation of the sample), and $\epsilon_{\mathrm{ij}}^{k}$ are the outcome-specific residual terms. The equations for the remaining deformation metrics are provided in the Appendix. The correlations between the head kinematic features were computed, and due to the high correlations between them (r > 0.8), a single representative kinematic feature (e.g., DAMAGE, peak resultant angular rate or acceleration) were kept in the model.

The same priors sensitivity analysis was used to determine the final priors used in the model, and the model estimation was the same as previously described.

Results

Sex Effects on Biomechanical Features

Similar to previous chapters, there was a statistically significant sex effect for ICV (70.5, CrI 95% 27.1, 113.0), mean damping ratio (-0.02, CrI 95% -0.03, -0.01), and percentage of brain volume in quadrants one (3.2, CrI 95% 0.9, 5.4), two (-3.7, CrI 95% -5.7, -1.6), and four (-2.8, CrI 95% -4.9, -0.7). The complete list of estimated parameters for both sex and age are included in the Appendix. These statistically significant sex effects were similar to the results of previous chapters; however, it should be noted that there was a significant sex effect on percentage of volume in quadrants one and four that was not present in the previous material properties chapter.

Biomechanical Features on Deformation Metrics

When accounting for biomechanical features, such as neuroanatomical factors, material properties, and head kinematic metrics, the effects of sex (estimates ranging from 0.0002 (CrI 95% -0.008, 0.008) for MPS-95 and 0.03 (-0.40, 0.47) for MPSxMPSR-95) and age (estimates ranging from 0.005 (-0.001, 0.01) for MPS-95 to 0.77 (-0.35, 1.90) for MPSR-95) were not significant on the deformation metrics (Table 8). Even after accounting for head kinematics effects with either DAMAGE, peak resultant angular velocity or acceleration, sex and age did not have statistically significant effects on deformation (additional estimated parameters included in the Appendix).

Of the intrinsic properties assessed and accounting for the extrinsic head kinematics using DAMAGE, ICV had a statistically significant effect on each of the four deformation metrics (Figure 37); additionally, ICV had the greatest relative effect on MPSxMPSR-95 and CSDM-25 of all the intrinsic properties. The mean DR of the total tissue was also statistically significant on MPS-95 and had the greatest relative effect of MPS-95 (Figure 38). The percentage of brain volume in quadrant one also had significant effects on both MPS-95 and MPSR-95, and quadrant one percentage had the greatest relative effect of the intrinsic properties on MPSR-95. However, for each of these deformation metrics, the head kinematic metric, DAMAGE (or peak resultant angular velocity or acceleration) had the absolute largest relative effect.

Table 8: Estimated coefficients for the population-level effects of the multivariate Bayesian linear mixed model and the 95% credible interval (CrI) for the estimated parameter included in square brackets for age, sex, and each biomechanical features on the deformation metrics. Bolded coefficients are significant based on the CrI. Positive sex coefficients imply male response was greater.

	Intercept	Sex	Age	ICV	Rel. WM Volume	Mean Stiffness	Mean DR	Stiffness IQR	DR IQR	Quad. 1 Percent	Quad. 2 Percent	Quad. 4 Percent	DAMAGE
MPS-95	**0.216** [0.211, 0.220]	0.0002 [-0.008, 0.008]	0.005 [-0.001, 0.012]	**0.011** [0.008, 0.015]	0.001 [-0.002, 0.005]	0.005 [-0.0167, 0.0261]	**-0.042** [-0.0769, -0.0061]	0.003 [-0.0067, 0.012]	0.002 [-0.0128, 0.0157]	**0.017** [0.0028, 0.0316]	**0.027** [0.0046, 0.0493]	0.013 [-0.0018, 0.028]	**0.077** [0.0742, 0.0794]
MPSR-95	**28.54** [27.75, 29.35]	0.018 [-1.28, 1.30]	0.770 [-0.35, 1.90]	**1.214** [0.65, 1.78]	0.158 [-0.39, 0.69]	1.881 [-1.49, 5.29]	-4.536 [-9.56, 0.46]	0.118 [-1.44, 1.69]	0.531 [-1.87, 2.92]	**2.849** [0.56, 5.20]	3.243 [-0.25, 6.56]	1.410 [-0.90, 3.74]	**13.181** [12.72, 13.64]
MPSxMPSR-95	**4.21** [3.95, 4.48]	0.032 [-0.40, 0.47]	0.207 [-0.16, 0.58]	**0.363** [0.17, 0.55]	0.030 [-0.15, 0.21]	0.453 [-0.77, 1.65]	-1.288 [-3.20, 0.67]	0.092 [-0.45, 0.64]	0.103 [-0.72, 0.92]	0.792 [-0.01, 1.60]	0.939 [-0.31, 2.16]	0.429 [-0.44, 1.28]	**2.884** [2.73, 3.03]
CSDM-25	**0.061** [0.047, 0.075]	0.002 [-0.02, 0.02]	0.006 [-0.01, 0.03]	**0.011** [0.001, 0.021]	0.001 [-0.009, 0.01]	0.022 [-0.04, 0.09]	-0.042 [-0.14, 0.06]	0.004 [-0.02, 0.03]	0.004 [-0.04, 0.05]	0.030 [-0.01, 0.07]	0.036 [-0.03, 0.10]	0.013 [-0.03, 0.06]	**0.061** [0.05, 0.07]

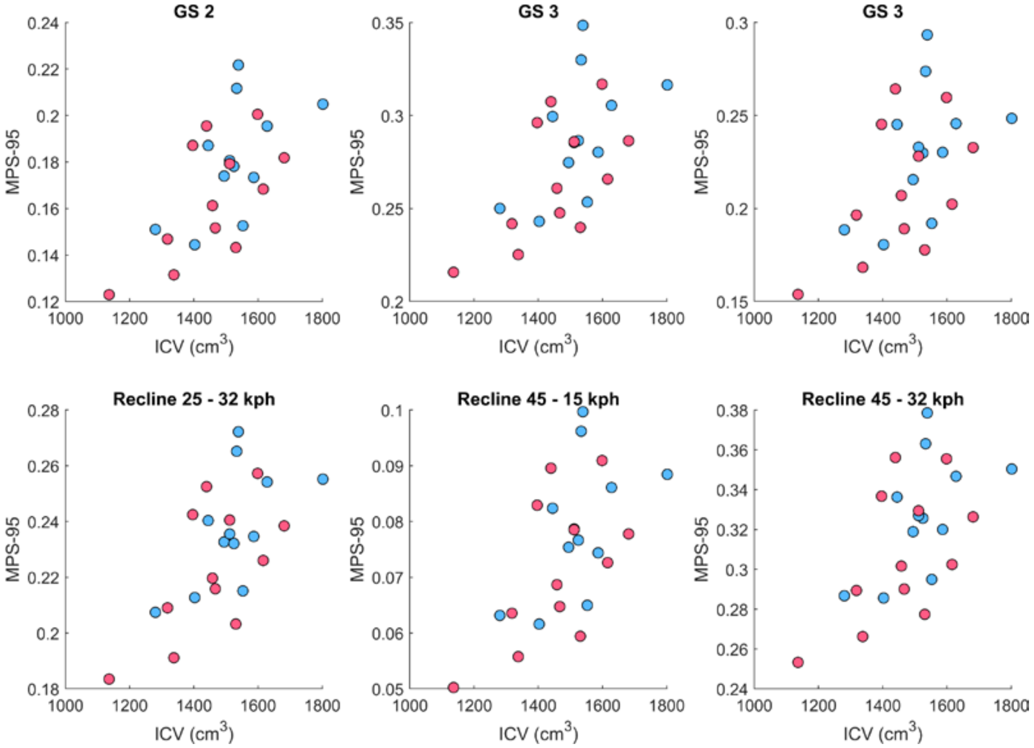

Figure 37: Scatter plots of ICV and MPS-95 for each of the 6 head kinematics simulation for both female (pink) and male (blue) brains.

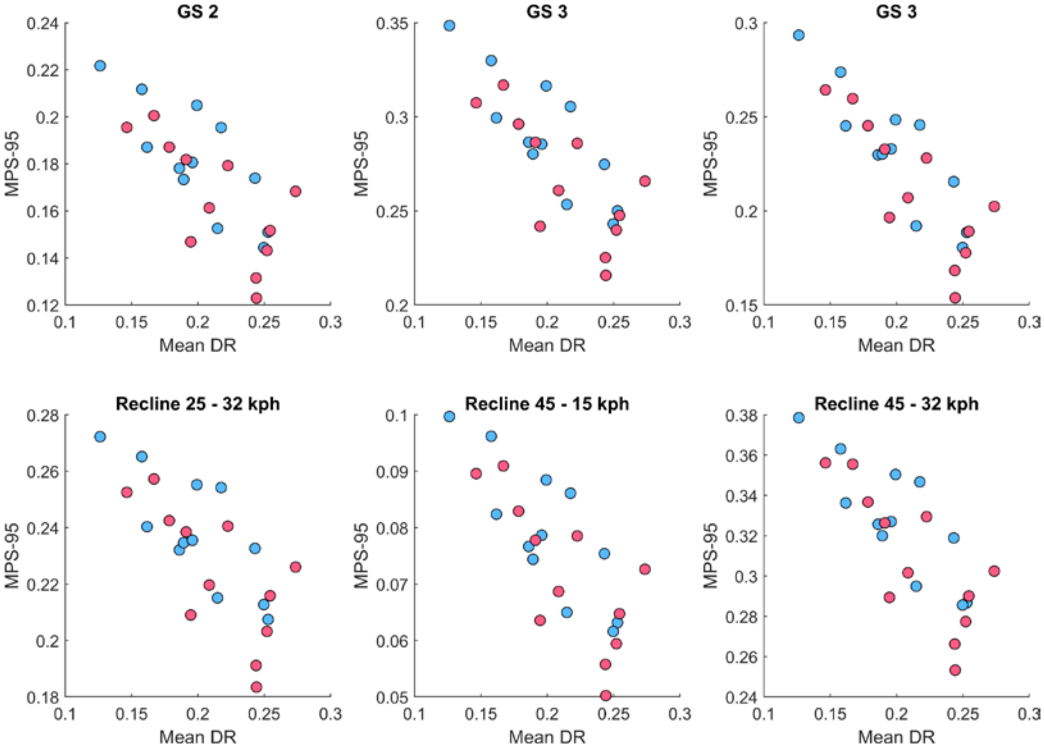

Figure 38: Scatter plots of mean total tissue damping ratio and MPS-95 for each of the 6 head kinematics simulation for both female (pink) and male (blue) brains.

Discussion

A sensitivity analysis was used to determine the relative importance of intrinsic and extrinsic biomechanical factors on brain deformation for male and female brains. Sex was defined as an intrinsic feature of the male and female brain simulations, and each of the FE brain models was simulated across a range of head kinematics seen in automotive crashes. Due to the high correlation between the head kinematic features, and the high correlation between DAMAGE and a majority of the other metrics, DAMAGE was included as a representative factor of extrinsic exposure. For each of the deformation metrics, the head kinematics exposure feature, either DAMAGE, peak resultant angular velocity or acceleration (statistical results included in the Appendix), had the greatest relative importance. Of the intrinsic properties, ICV had a statistically significant effect on all four of the deformation metrics and the greatest effect on MPSxMPSR-95 and CSDM-25. For MPS-95, the mean damping ratio had the greatest effect, and for MPSR-25, the volume percentage in quadrant one (low damping ratio and low stiffness) had the greatest effect. After including the effects of these intrinsic factors and head kinematic features, sex did not have a statistically significant effect on any metric of deformation.

Of the sex-specific intrinsic biomechanical features, a few factors help to explain a possible higher injury risk for female occupants. For MPS-95, ICV, mean damping ratio, and the percentage of brain volume all had significant effects on deformation, with mean damping ratio having the greatest effect. Based on previous analysis, there was a significant sex effect on mean damping ratio, with females having lower mean damping ratio. As mean damping ratio decreases, MPS-95 of the corresponding model increases across all the head kinematics assessed, which would correspond to a higher injury risk seen in females. Additionally, while not statistically significant, a similar effect is seen for percentage of brain volume in quadrant one, which had the second highest relative effect on MPS-95. However, male brains on average have greater ICV, and as ICV increases, MPS-95 also increases. This trend would suggest males have a higher risk of injury due to total brain size, but the importance of ICV is less for MPS-95 than both mean damping ratio and percentage of brain volume in quadrant one. If brain injury risk is assessed using either MPSxMPSR-95 or CSDM-25, additional analysis is needed to explain a higher risk for female occupants seen in epidemiology based on the relative importance of ICV and its effect on these deformation metrics.

After accounting for differences in biomechanical factors, sex did not have a significant effect on brain deformation (the assumed mechanism of diffuse axonal injuries), but field data suggests that sex did have a statistically significant effect on risk of moderate brain injuries ($OR_{sex} = 1.76$) in frontal automotive crashes (J. Forman et al., 2019). One major assumption that could help explain the significant effect seen in field data is the assumption that the injury threshold for male and female brains is equal, which was made in this sensitivity study and throughout previous chapters. Currently, there is no research to support or dispute this assumption. To investigate this assumption, the proposed injury risk functions for MPS-95 mild TBI from Wu et *al.* (2021, 2022) were scaled using the field data odds ratio,

$$Odds\ Ratio(Sex) = \frac{Odds_F}{Odds_M} = 1.76$$

$$Odds_F = \frac{p_F}{1 - p_F} \qquad Odds_M = \frac{p_M}{1 - p_M}$$

$$p_F = \frac{1.76\left(\frac{p_M}{1 - p_M}\right)}{1 + 1.76\left(\frac{p_M}{1 - p_M}\right)}$$

where p_M is the male probability of injury, based on the Wu et al. injury risk functions, and p_F is the scaled female probability of injury (Figure 39). The original Wu et al. injury risk functions were assumed to be male injury risk functions based on the high proportion of male data within the human data sets used in the development, reconstructed impact cases from the National Football League and male volunteer kinematics from the Naval Biodynamics Laboratory (Wu et al., 2021). Based on the axonal model injury risk function, the 50% risk of injury for the male curve was 0.28

MPS-95 and the scaled female curve was 0.25 MPS-95 (Wu et al., 2021). From the GHBMC developed and scaled injury risk function, the 50% risk of injury for male brains was 0.36 MPS-95 and for the scaled female brain was 0.32 MPS-95 (Wu et al., 2022). However, both of these scaled female injury risk functions fall within the 95th percentile confidence interval of the male injury risk functions. This scaled female injury risk is not a proposed injury risk function, but instead is an exercise to highlight how the odds ratio seen in the automotive crash field data would affect the difference between a male and female injury risk function.

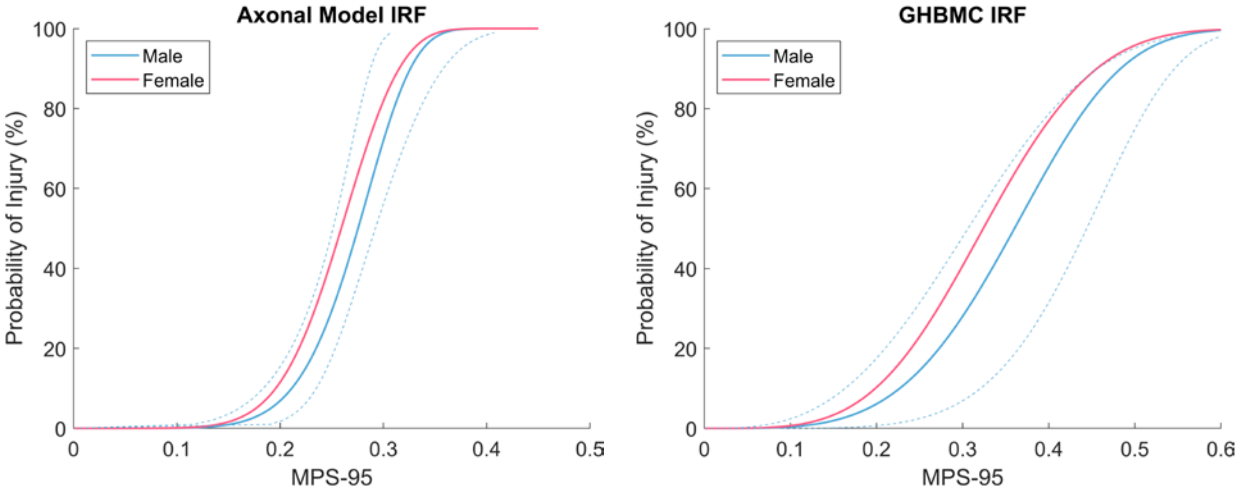

Figure 39: The MPS-95 male (blue) injury risk functions from Wu et al. (2021) axonal brain FE model (left) and Wu et al. (2022) GHBMC brain FE model (right) and the scaled female injury risk function (pink) to capture the odds ratio of sex differences in moderate brain injuries.

With this subtle shift in these injury risk functions, probability of injury risk for male and female brains based on a single head kinematic also changes. When using MPS-95 as a predictor of injury, with equal risk between male and female brains, generally, the male brains had greater MPS-95 and, consequently, greater predicted risk of injury (Figure 40) . However, after applying the Forman et al. odd ratio to the Wu et al. (2022) GHBMC-based injury risk functions, the predicted injury risk of the female brains was greater than the male brains (Figure 41). The expected value (i.e., sum of probabilities of risk) for the males was 0.54, but the female expected value was greater, with an expected value of 0.64, using the GHBMC-based injury risk function.

However, for the axonal FE brain model-based injury risk function, the expected value of the male brains was greater (0.57) than for the female brains (0.53) due to the steeper shape and smaller shift of the axonal-based injury risk function (Figure 39). This difference in injury threshold, or injury risk, is a possible explanation of the differences seen in epidemiology, with females having a higher injury risk, that is not explained in the effect of the biomechanical factors on brain deformation. Overall, additional research is needed to determine sex-specific injury risk functions, as these provide only an initial justification and plausibility of differences in male and female injury thresholds.

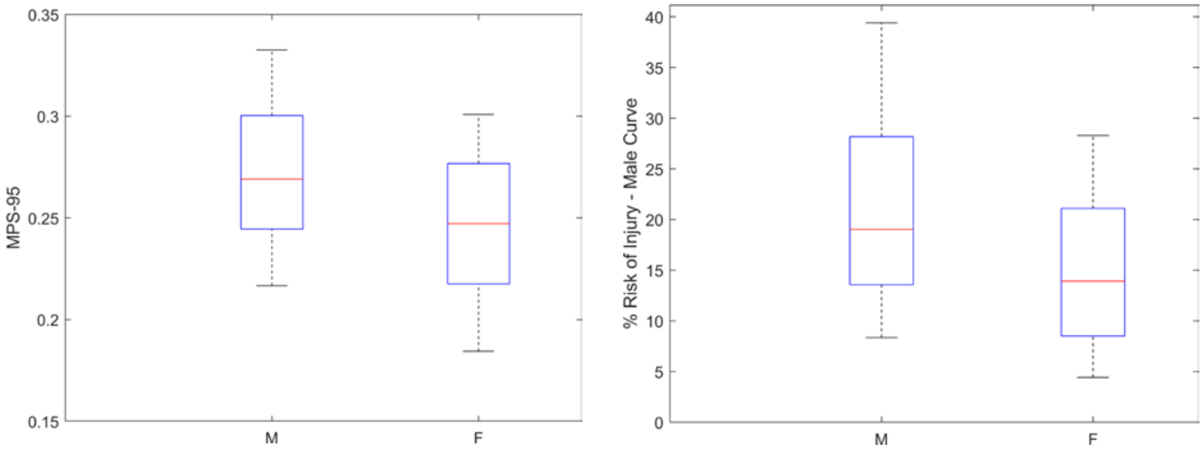

Figure 40: (Left) Boxplots showing the distribution of the male and female MPS-95 results from the sex-specific FE brain models for a single kinematic case. (Right) Boxplots showing the distributions of percent risk of injury using the Wu et al., 2022 derived injury risk function.

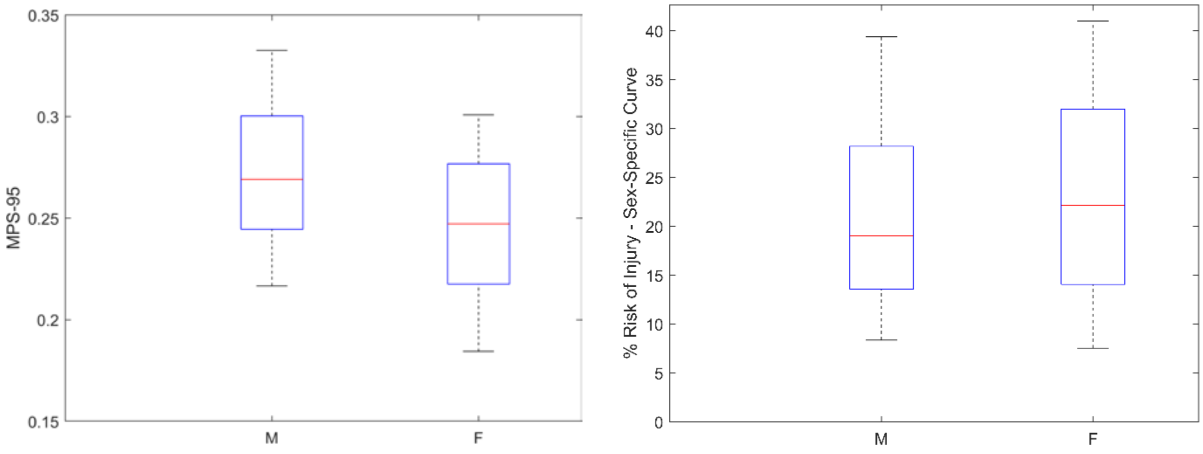

Figure 41: (Left) Boxplots showing the distribution of the male and female MPS-95 results from the sex-specific FE brain models for a single kinematic case. (Right) Boxplots showing the

distributions of percent risk of injury using the scaled, sex-specific injury risk functions based on the Wu et al., 2022 derived injury risk function and the odds ratio from Forman et al., 2019.

There are many assumptions that go along with this analysis, with the first being the male injury risk function was developed based on mild TBI cases and the odds ratio corresponded to moderate brain injuries, defined as AIS2-3 (J. Forman et al., 2019). Additionally, the odds ratio from the field data does not include any intrinsic brain properties, and it only considers height, BMI, age, and sex of the occupant. The injury risk function was developed using the strain resulting from a different brain FE model and does not correspond to the MPS-95 results of this dissertation. Finally, the injury risk functions proposed by Wu et al. are model specific, developed using either the Wu et al. axonal model or the 50th percentile male GHBMC brain FE model, but the augmented MPS-95 values (Figure 40) are produced from the subject-specific models presented in this dissertation and do not directly correspond to deformation levels present in the models used in development. As a result of this analysis and these limitations, the female brain has a higher probability of injury than the male brain for the equal MPS-95. While there has not been any research to explicitly capture a difference in brain injury thresholds between male and female brain tissue, recent research has investigated possible sex differences on axonal structure. Dollé et al. concluded female axons, compared to male axons, were smaller with fewer microtubules, experience greater undulation under the same applied load, and experience greater calcium influx under the same applied load (Dollé et al., 2018).

In addition to potentially different injury thresholds between male and female brains, and as briefly mentioned above, the injury risk model of Forman et al. does not consider the intrinsic brain properties when predicting moderate brain injuries (AIS2-3) (J. Forman et al., 2019). Throughout this dissertation, there have been sex effects in some of these intrinsic factors (e.g., ICV, or mean total tissue stiffness and damping ratio), and it is possible because these intrinsic properties are not included in the Forman et al. statistical model, the sex parameter was significant. It is possible if, for example, total intracranial volume, which has both a statistically significant sex effect and a large effect on brain deformation, was included in the overall moderate brain injury probability model, the sex parameter in the Forman et al. would not have been statistically significant. However, these intrinsic properties are not available with the epidemiology data, and additional research is needed to confirm that these intrinsic properties would affect the significance of the sex parameter.

One final explanation for why differences between male and female brain injury rates and risks observed in epidemiology were not captured in this sensitivity analysis is due to secondary responses following an injurious load. Finite element brain models quantify the amount of deformation based on specific neuroanatomies and material properties given input head kinematics, but the FE brain models used throughout this dissertation did not consider the effects of swelling or axonal damage following the initial injury. While high strain may correspond to locations of injury, future swelling, caused by damage to the axonal cytoskeleton from large inertial loading, can cause further damage to the axon due to activation of proteases, enzymes that break down proteins (Smith & Meaney, 2000). This secondary response could differ between males and females, and additionally could correspond to differences in symptomatology between the sexes. Additional research is needed to relate the swelling response to symptomatology, as well as differing responses between male and female injuries.

While sex was not a statistically significant predictor of brain deformation after accounting for other biomechanical factors, both intrinsic and extrinsic factors have significant effects on brain deformation. The extrinsic head kinematic exposure metric, either DAMAGE or peak resultant angular velocity or acceleration, had the greatest relative effect on brain deformation, but intrinsic factors, such as ICV, should not be ignored in injury assessment or injury risk function development. The difference between male and female injury odds in automotive crash field data was not completely explained with a single justification, but future research into differences in injury tolerance and post-injury response will continue to advance the field to potentially define a sex-specific factor affecting brain injury risk.

Conclusions

- Both intrinsic and extrinsic biomechanical features have statistically significant effects on brain deformation. The extrinsic head kinematic exposure metric had the greatest relative effect of all biomechanical features on all the deformation metrics assessed. For intrinsic brain properties, mean damping ratio had the greatest effect on MPS-95, percentage of brain volume in quadrant one had the greatest effect on MPSR-95, and ICV had the greatest effect on both MPSxMPSR-95 and CSDM-25. Intrinsic properties, and variability of these features, should be included in injury assessments and injury risk function development to between capture the entire population response.
- A lower injury risk threshold for female brains, based on the odds ratio for moderate brain injury (AIS2-3) presented by Forman et al., provides a single justification for the presence of increased odds for brain injuries in belted female occupants; however, depending on the injury risk assessed, either Wu et al. 2021 (axonal model) or Wu et al. 2022 (GHBMC), the scaled female injury threshold does not completely explain injury differences.
- Future research into post-injury response, such as secondary axonal injuries due to swelling, is also needed to investigate the potential microstructural differences seen in male and female axons (Dollé et al., 2018).

Chapter 6: Conclusions

The focus of this dissertation was to, first, identify the effect of sex on brain deformation in automotive crash loading environments and, second, to quantify the relative importance of various biomechanical factors on brain deformation. This goal was achieved through four aims, using subject-specific finite element (FE) models to explore the effect of the intrinsic properties, neuroanatomy and material properties, and extrinsic factors, such as head kinematics, on brain deformation; additionally, when comparing parameters from each of these three main biomechanical components, this work determined which feature had the greatest impact on deformation and, ideally, brain injury risk.

The research presented in this dissertation provides an analysis of how current brain biomechanics research can address sex differences and highlights areas of potential future research to further the understanding of differences in male and female injury rate and risk. The primary contributions are the analyses of which biomechanical factor, across both intrinsic and extrinsic features, had the greatest effect on deformation and how the effect of sex relates to relative changes in these biomechanical features. Ultimately, the outcomes presented in this dissertation can direct future work to address areas with the greatest impact on brain deformation to reduce injury risk in both male and female automotive occupants.

Major Contributions and Impact

Assessment of sex-specific biomechanical factors on brain deformation

The first major contribution of this dissertation was the investigation into the effect of a subject's sex on brain deformation and risk of closed-head diffuse injury, where the assumed mechanism of traumatic brain injury is brain strain. First, the effect of sex on features of neuroanatomy, material properties, and head kinematics in automotive sled tests was assessed. Sex was statistically significant for many of these features, including overall measure of volume (e.g., intracranial volume (ICV)), damping ratio, and distribution of brain volume into areas of high and low stiffness and damping ratios. While a subject cannot alter these intrinsic properties, knowledge of these characteristics (e.g., analysis of pre-season medical imaging) can better inform clinicians and athletic trainers on a specific subject's predisposition to above average brain deformations for a given head kinematic exposure. Additionally, extrinsic factors, such as head kinematics, were assessed for both male and female postmortem human surrogate and anthropometric test device sled tests kinematics, but little to no difference was observed in various peak kinematic metrics. However, the limited data of sex-matched kinematics with repeatable restraint systems did limit the strength of conclusions on differences in male and female exposure levels. This is one major opportunity for future work, to continue to develop male and female matched conditions to understand potential differences in exposure between the occupants and to further understand how differences in anthropometry (e.g., breast tissue, mass distribution) could affect engagement with restraint systems and resulting head kinematics.

After including the effects of the biomechanical factors, sex was not a statistically significant predictor of brain deformation and had a substantially smaller effect on deformation in comparison to any of the significant predictors. For example, ICV had approximately 50 times the relative effect on predicting MPS-95 in comparison to the effect of sex. With the current state of the widely used finite element models in automotive safety, which include can include subject-specific neuroanatomies and representative material properties, sex is not required in prediction of brain deformation but models representing the size of the brains for different sexes are required. As brain models continue to improve and additional aspects of traumatic brain injury (e.g., post-injury response), the effect of sex should again be considered and investigated.

Importance of both intrinsic and extrinsic factors on brain deformation

This dissertation was also the first to address the relative importance of various intrinsic factors on brain deformation using subject-specific brain FE models. While previous work has concluded the effect of neuroanatomical differences on brain deformation, this dissertation also included the effect of subject-specific relative material properties in the FE brain models. Using magnetic resonance elastography (MRE) metrics of shear stiffness and damping ratio, the stiffness and viscoelastic properties of the subject-specific models were augmented to capture the relative distribution of materials throughout the entire brain tissue. These material property features, such as mean damping ratio of interquartile range of both stiffness and damping ratios, did have a statistically significant effect on the brain deformation metrics assessed; however, there were some large assumptions implemented that need further research to verify. Throughout the material implementation, this dissertation assumed that the relative difference in stiffness and damping ratios captured during the small deformations of MRE were equal to the relative change in the material properties under larger deformations, those associated with potentially injurious loading conditions. Under this assumption, these material properties did affect brain deformation, and any ability to augment these properties could reduce injury for both male and female brains.

Of the intrinsic factors, ICV had a consistent statistically significant effect on the four brain injury metrics assessed in this dissertation. A majority of FE brain models are developed based on a single 50th percentile, or mid-sized, male anthropometry. While there may be no sex effect based on the choice of a male anatomy, the size of the 50th percentile male brain has impacted the development of brain injury metrics. When assessing brain size and injury, previous work developed a frequency-based scaling method to create comparable strain metrics given differences in total brain volume (Wu et al., 2020). This work assumed similar strain metrics created similar clinical outcomes, but variation in strain for similar clinical results are required for development of injury risk metrics. Therefore, additional research is needed to include varied brain volumes when developing injury risk metrics, and, at a minimum, when assesses injury risk of specific anthropometrics, using metrics that were developed and tested using the target anthropometry (e.g., a 5th percentile female brain metric based on 5th percentile brain strains).

In addition to the effect of intrinsic features, the head kinematic exposure was also assessed via a representative kinematic feature (i.e., DAMAGE, peak resultant angular velocity or acceleration). In comparison to all of the intrinsic properties, the head kinematic factor had a much larger effect on the deformation metrics. This trend held no matter which of the head kinematic features were included in the final model. While intrinsic brain properties cannot be altered, head kinematics during an automotive crash can be minimized using a combination of occupant safety parameters. Ultimately reducing the angular rates and accelerations of an occupant will reduce the brain deformation and corresponding risk of injury, but any adjustment to the restraint system requires optimization. While there may be different optimal restraint parameters for a male or female occupant, additional research is required to determine how best to restrain different occupants based on anthropometry, age, or sex. Based on the outcomes of this dissertation, reducing head kinematic exposure of an occupant would have the greatest effect on reducing brain deformation of the different biomechanical features considered.

Other Contributions

Implementation of subject-specific material properties

In this dissertation, subject-specific neuroanatomies and material property distributions from high resolution magnetic resonance imaging (MRI) and MRE, respectively, were implemented in FE brain models. Using a previously developed registration-based morphing algorithm, the FE brain models were morphed from a template brain model to each subject's neuroanatomy using MRI brain scans. The same transformations were then used to transform the MRE of each subject-specific scan to the template space to isolate the effects of the material property using a generic neuroanatomy. From this study, the effects of damping ratio were found to have a statistically significant effect on deformation. As the resolution of MRE continues to improve, further research can refine our understanding of the regional effects of damping ratio on regional strain in the FE brain models. This implementation of subject-specific material properties can add variability to the current FE brain models to not only consider the effects of neuroanatomy on brain injury risk, but the material composition as well. With this developed pipeline of neuroanatomically subject-specific brain models with specific material property distributions from MRE, additionally information from MR brain modalities can be added to these FE brain models, including white matter tractography from Diffuse Tensor Imaging (DTI) or chemical composition from magnetic resonance spectroscopy (Kubas et al., 2010).

Assessment of sex-specific biomechanical factors

With advancements in neuroimaging, previous studies have investigated sex differences between male and female brains. This dissertation investigated global sex differences between 142 neuroanatomical scans and 133 MRE scans, as well as a review of 52 sex-matched six degree-of-freedom head kinematics from sled test environments. For each of these biomechanical components, the effect of sex was assessed to study the effects of sex in the human brain. While the effect of sex may not have been statistically significant effect on brain deformation after accounting for these biomechanical effects, the sex differences assessed throughout this dissertation could help explain other potential differences within male and female brain research, such as differences in rate of migraines (Maleki et al., 2012).

Limitations and Future Work

Sex-matched male and female head kinematics

Head kinematics features had the greatest relative impact on brain deformation out of the biomechanical features considered, but the number of sex-matched male and female crash conditions limited the strength of the conclusions within the exposure study. To better understand potentially sex-specific features of head kinematics, additional research is required to capture the effect of crash and restraint parameters on head kinematics. For the final sensitivity in this dissertation, equal head kinematics were applied to the male and female brains. Given the variety of crash conditions present in field data, it is possible different crash conditions (e.g., delta-V, principal direction of force, etc.) and different restraint interactions could result in similar head kinematics for a male and female occupant; however exactly how a male or female occupant would respond given a single set of crash conditions is unknown. Future research could answer the latter question, but this dissertation aimed to understand how any head kinematic feature affected brain deformation in relation to intrinsic factors. To draw the final conclusions on how a single crash condition leads to differences in brain injury risk between male and female occupants, much more work is needed to define all aspects of the occupant interaction and kinematic response within the vehicle body, as well as potentially different post-injury responses.

Relative stiffness and damping ratio definitions

Based on the effect of material properties in this dissertation, the continued work of characterizing human brain tissue *in vivo* has extreme value. However, the implementation of material properties did rely on one major assumption: the relative change in shear stiffness and damping ratios for small levels of deformation is equal to the relative change in the properties for larger and faster deformation modes. Future research can work to determine the validity of this assumption using fresh posthuman human brain tissue, or animal surrogate tissues, using MRE modalities and *ex vivo* and/or *in situ* measurement techniques. As global metrics of material properties did effect brain deformation, the understanding of how to best incorporate the unique *in vivo* MRE material properties of human brain tissue into FE brain models should remain a priority.

Assumption of equality for injury threshold

This dissertation assumes that strain metrics, such as the 95th percentile maximum principal strain, are universal correlates to the injury mechanism. This assumption is founded on previous work relating MPS-95 (or similar measures) to injury risk in both animal surrogates and humans (Fahlstedt et al., 2021; Liu et al., 2020; Takhounts et al., 2008b; Wu et al., 2021, 2022). The threshold of injury is also assumed to vary between individuals, and the variance of injury threshold throughout the population is captured in a probabilistic function (e.g., logistic, Weibull) and is commonly known as an injury criterion. It is not known whether males and females have a difference in injury threshold, and therefore require separate injury criterion to improve the estimation of injury risk in a given impact scenario. Throughout this dissertation, the threshold for male and female injury was assumed to be equal, but the significance of a sex-specific injury criterion is discussed in the final sensitivity analysis (Chapter 5). In sports-related concussions, there are differences in injury rates between male and female athletes (Resch et al., 2017). Additional research is needed using advanced head kinematic measurement devices, such as instrumented mouthguards, to improve our understanding of exposure and the resulting head kinematics in both male and female athletes. Increased numbers of injured and non-injured recorded head kinematics across a range of impact sports will help identify any possible injury threshold difference based on the biomechanical features of the exposure.

Other potential sex dependent features of traumatic brain injury

Finally, traumatic brain injuries are extraordinarily complex, and research from many different disciplines is required to solve these complexities. While brain biomechanics play a large role in the amount of deformation experienced due to an injurious exposure and a smaller role in sex-specific deformation response, findings from other research areas, such as biochemistry, neuropsychology, neuroimaging, or neuroscience, should be combined with the brain biomechanics knowledge to develop the most informed models. Diagnostic steps of linking symptomology to brain deformation may still be years or decades away, but these collaborations are necessary to continue discovering solutions to traumatic brain injury. Incorporating the effect of intrinsic properties, such as age or biological sex, in each of these fields will help understand and reduce brain injury risk across the entire population.

References

Acosta, S. M., Ash, J., Lessley, D., Shaw, G., Heltzel, S., & Crandall, J. (2016). *Comparison of Whole Body Response in Oblique and Full Frontal Sled Tests*. 15.

Alshareef, A., Gabler, L., Stone, J., & Panzer, M. (2015). *Changes in the Mechanical Response of Brain Tissue Following Primary Blast Injury*. 2015 Ohio State University Injury Biomechanics Symposium.

Alshareef, A., Knutsen, A. K., Johnson, C. L., Carass, A., Upadhyay, K., Bayly, P. V., Pham, D. L., Prince, J. L., & Ramesh, K. (2021). Integrating Material Properties from Magnetic Resonance Elastography into Subject-Specific Computational Models for the Human Brain. *Brain Multiphysics*, 100038.

Antona-Makoshi, J., Mikami, K., Lindkvist, M., Davidsson, J., & Schick, S. (2018). Accident analysis to support the development of strategies for the prevention of brain injuries in car crashes. *Accident Analysis & Prevention*, *117*, 98–105. https://doi.org/10.1016/j.aap.2018.04.009

Arani, A., Murphy, M. C., Glaser, K. J., Manduca, A., Lake, D. S., Kruse, S. A., Jack, C. R., Ehman, R. L., & Huston, J. (2015). Measuring the effects of aging and sex on regional brain stiffness with MR elastography in healthy older adults. *NeuroImage*, *111*, 59–64. https://doi.org/10.1016/j.neuroimage.2015.02.016

Arbogast, K. B., & Margulies, S. S. (1998). Material characterization of the brainstem from oscillatory shear tests. *Journal of Biomechanics*, *31*(9), 801–807. https://doi.org/10.1016/S0021-9290(98)00068-2

Association, N. C. A. (2020). *NCAA Sports Sponsorship and Participation Rates Database*.

Avants, B. B., Epstein, C. L., Grossman, M., & Gee, J. C. (2008). Symmetric diffeomorphic image registration with cross-correlation: Evaluating automated labeling of elderly and neurodegenerative brain. *Medical Image Analysis*, *12*(1), 26–41. https://doi.org/10.1016/j.media.2007.06.004

Avants, B. B., Tustison, N. J., Song, G., Cook, P. A., Klein, A., & Gee, J. C. (2011). A reproducible evaluation of ANTs similarity metric performance in brain image registration. *NeuroImage*, *54*(3), 2033–2044. https://doi.org/10.1016/j.neuroimage.2010.09.025

Avants, B. B., Tustison, N. J., Wu, J., Cook, P. A., & Gee, J. C. (2011). An open source multivariate framework for n-tissue segmentation with evaluation on public data. *Neuroinformatics*, *9*(4), 381–400.

Avants, B., & Gee, J. C. (2004). Geodesic estimation for large deformation anatomical shape averaging and interpolation. *NeuroImage*, *23 Suppl 1*, S139-150. https://doi.org/10.1016/j.neuroimage.2004.07.010

Avants, B., & Tustison, N. (2018). *ANTs/ANTsR Brain Templates* (p. 625878567 Bytes) [Data set]. figshare. https://doi.org/10.6084/M9.FIGSHARE.915436.V2

Azevedo, F. A., Carvalho, L. R., Grinberg, L. T., Farfel, J. M., Ferretti, R. E., Leite, R. E., Filho, W. J., Lent, R., & Herculano-Houzel, S. (2009). Equal numbers of neuronal and nonneuronal cells make the human brain an isometrically scaled-up primate brain. *Journal of Comparative Neurology*, *513*(5), 532–541.

Bassett, D. S., & Gazzaniga, M. S. (2011). Understanding complexity in the human brain. *Trends in Cognitive Sciences*, *15*(5), 200–209. https://doi.org/10.1016/j.tics.2011.03.006

Bayly, P. V., Alshareef, A., Knutsen, A. K., Upadhyay, K., Okamoto, R. J., Carass, A., Butman, J. A., Pham, D. L., Prince, J. L., & Ramesh, K. (2021). MR imaging of human brain mechanics in vivo: New measurements to facilitate the development of computational models of brain injury. *Annals of Biomedical Engineering*, 1–16.

Biegon, A. (2021). Considering Biological Sex in Traumatic Brain Injury. *Frontiers in Neurology*, *12*. https://doi.org/10.3389/fneur.2021.576366

Bigler, E. D. (2015). Structural image analysis of the brain in neuropsychology using magnetic resonance imaging (MRI) techniques. *Neuropsychology Review*, *25*(3), 224–249.

Biomechanics Test Database: Test Number 12814 (No. 12814; Small Female/Older Occupant Thoracic Biofidelity: 5th Percentile Female). (2017). University of Virginia/NHTSA. https://www.nhtsa.gov/research-data/research-testing-databases#/biomechanics/12814

Blatter, D. D., Bigler, E. D., Gale, S. D., Johnson, S. C., Anderson, C. V., Burnett, B. M., Parker, N., Kurth, S., & Horn, S. D. (1995). *Quantitative Volumetric Analysis of Brain MR: Normative Database Spanning 5 Decades of Life*. 12.

Bramlett, H. M., & Dietrich, W. D. (2001). Neuropathological protection after traumatic brain injury in intact female rats versus males or ovariectomized females. *Journal of Neurotrauma*, *18*(9), 891–900.

Brault, J. R., Siegmund, G. P., & Wheeler, J. B. (2000). Cervical muscle response during whiplash: Evidence of a lengthening muscle contraction. *Clinical Biomechanics*, *15*(6), 426–435. https://doi.org/10.1016/S0268-0033(99)00097-2

Broshek, D. K., Kaushik, T., Freeman, J., Erlanger, D., Webbe, F., & Barth, J. (2005). Sex differences in outcome following sports-related concussion. *J. Neurosurg.*, *102*, 8.

Budday, S., Nay, R., de Rooij, R., Steinmann, P., Wyrobek, T., Ovaert, T. C., & Kuhl, E. (2015). Mechanical properties of gray and white matter brain tissue by indentation. *Journal of the Mechanical Behavior of Biomedical Materials*, *46*, 318–330.

Budday, S., Ovaert, T. C., Holzapfel, G. A., Steinmann, P., & Kuhl, E. (2020). Fifty Shades of Brain: A Review on the Mechanical Testing and Modeling of Brain Tissue. *Archives of Computational Methods in Engineering*, *27*(4), 1187–1230. https://doi.org/10.1007/s11831-019-09352-w

Budday, S., Sommer, G., Birkl, C., Langkammer, C., Haybaeck, J., Kohnert, J., Bauer, M., Paulsen, F., Steinmann, P., Kuhl, E., & Holzapfel, G. A. (2017). Mechanical characterization of human brain tissue. *Acta Biomaterialia*, *48*, 319–340. https://doi.org/10.1016/j.actbio.2016.10.036

Budday, S., Sommer, G., Haybaeck, J., Steinmann, P., Holzapfel, G. A., & Kuhl, E. (2017). Rheological characterization of human brain tissue. *Acta Biomaterialia*, *60*, 315–329. https://doi.org/10.1016/j.actbio.2017.06.024

Bürkner, P.-C. (2017). brms: An R Package for Bayesian Multilevel Models Using Stan. *Journal of Statistical Software*, *80*, 1–28. https://doi.org/10.18637/jss.v080.i01

Cicchetti, D. V. (1994). Guidelines, criteria, and rules of thumb for evaluating normed and standardized assessment instruments in psychology. *Psychological Assessment*, *6*(4), 284.

Clevenger, A. C., Kim, H., Salcedo, E., Yonchek, J. C., Rodgers, K. M., Orfila, J. E., Dietz, R. M., Quillinan, N., Traystman, R. J., & Herson, P. S. (2018). Endogenous sex steroids dampen neuroinflammation and improve outcome of traumatic brain injury in mice. *Journal of Molecular Neuroscience*, *64*(3), 410–420.

Control, C. for D. & Prevention. (2008). Adverse health conditions and health risk behaviors associated with intimate partner violence—United States, 2005. *MMWR: Morbidity and Mortality Weekly Report*, *57*(5), 113–117.

Control, C. for D. & Prevention. (2015). Report to congress on traumatic brain injury in the United States: Epidemiology and rehabilitation. *National Center for Injury Prevention and Control*, 1–72.

Coupé, P., Catheline, G., Lanuza, E., Manjón, J. V., & Initiative, A. D. N. (2017). Towards a unified analysis of brain maturation and aging across the entire lifespan: A MRI analysis. *Human Brain Mapping*, *38*(11), 5501–5518.

Covassin, T., Moran, R., & Elbin, R. (2016). Sex differences in reported concussion injury rates and time loss from participation: An update of the National Collegiate Athletic Association

Injury Surveillance Program from 2004–2005 through 2008–2009. *Journal of Athletic Training*, *51*(3), 189–194.

Darvish, K. K., & Crandall, J. R. (2001). Nonlinear viscoelastic effects in oscillatory shear deformation of brain tissue. *Medical Engineering & Physics*, *23*(9), 633–645. https://doi.org/10.1016/S1350-4533(01)00101-1

Das, S. R., Avants, B. B., Grossman, M., & Gee, J. C. (2009). Registration based cortical thickness measurement. *NeuroImage*, *45*(3), 867–879. https://doi.org/10.1016/j.neuroimage.2008.12.016

Davis, M. L. (2017). *Development and full body validation of a 5th percentile female finite element model*. Wake Forest University.

de Jong, L. W., Vidal, J., Forsberg, L. E., Zijdenbos, A. P., Haight, T., Initiative, A. D. N., Sigurdsson, S., Gudnason, V., van Buchem, M. A., & Launer, L. J. (2017). Allometric scaling of brain regions to intra-cranial volume: An epidemiological MRI study. *Human Brain Mapping*, *38*(1), 151–164.

Decimo, I., Fumagalli, G., Berton, V., Krampera, M., & Bifari, F. (2012). *Meninges: From protective membrane to stem cell niche*. 14.

Dollé, J.-P., Jaye, A., Anderson, S. A., Ahmadzadeh, H., Shenoy, V. B., & Smith, D. H. (2018). Newfound sex differences in axonal structure underlie differential outcomes from in vitro traumatic axonal injury. *Experimental Neurology*, *300*, 121–134. https://doi.org/10.1016/j.expneurol.2017.11.001

Eckner, J. T., Oh, Y. K., Joshi, M. S., Richardson, J. K., & Ashton-Miller, J. A. (2014). Effect of Neck Muscle Strength and Anticipatory Cervical Muscle Activation on the Kinematic Response of the Head to Impulsive Loads. *The American Journal of Sports Medicine*, *42*(3), 566–576. https://doi.org/10.1177/0363546513517869

Eliot, L., Ahmed, A., Khan, H., & Patel, J. (2021). Dump the “dimorphism”: Comprehensive synthesis of human brain studies reveals few male-female differences beyond size.

Neuroscience & Biobehavioral Reviews, *125*, 667–697. https://doi.org/10.1016/j.neubiorev.2021.02.026

Fahlstedt, M., Abayazid, F., Panzer, M. B., Trotta, A., Zhao, W., Ghajari, M., Gilchrist, M. D., Ji, S., Kleiven, S., & Li, X. (2021). Ranking and rating bicycle helmet safety performance in oblique impacts using eight different brain injury models. *Annals of Biomedical Engineering*, *49*(3), 1097–1109.

Fallenstein, G., Hulce, V. D., & Melvin, J. W. (1969). Dynamic mechanical properties of human brain tissue. *Journal of Biomechanics*, *2*(3), 217–226.

Farin, A., Deutsch, R., Biegon, A., & Marshall, L. F. (2003). Sex-related differences in patients with severe head injury: Greater susceptibility to brain swelling in female patients 50 years of age and younger. *Journal of Neurosurgery*, *98*(1), 32–36.

Faul, M., Wald, M. M., Xu, L., & Coronado, V. G. (2010). *Traumatic brain injury in the United States; emergency department visits, hospitalizations, and deaths, 2002-2006*.

Forman, J. L., Lopez-Valdes, F., Lessley, D. J., Riley, P., Sochor, M., Heltzel, S., Ash, J., Perz, R., Kent, R. W., & Seacrist, T. (2013). *Occupant kinematics and shoulder belt retention in far-side lateral and oblique collisions: A parametric study*. SAE Technical Paper.

Forman, J., Poplin, G. S., Shaw, C. G., McMurry, T. L., Schmidt, K., Ash, J., & Sunnevang, C. (2019). Automobile injury trends in the contemporary fleet: Belted occupants in frontal collisions. *Traffic Injury Prevention*, *20*(6), 607–612. https://doi.org/10.1080/15389588.2019.1630825

Frost, R. B., Farrer, T. J., Primosch, M., & Hedges, D. W. (2013). Prevalence of Traumatic Brain Injury in the General Adult Population: A Meta-Analysis. *Neuroepidemiology*, *40*(3), 154–159. https://doi.org/10.1159/000343275

Gabler, L. F., Crandall, J. R., & Panzer, M. B. (2016). Assessment of Kinematic Brain Injury Metrics for Predicting Strain Responses in Diverse Automotive Impact Conditions. *Annals* *of Biomedical Engineering*, *44*(12), 3705–3718. https://doi.org/10.1007/s10439-016-1697-0

Gabler, L. F., Crandall, J. R., & Panzer, M. B. (2018). Development of a Metric for Predicting Brain Strain Responses Using Head Kinematics. *Annals of Biomedical Engineering*, *46*(7), 972–985. https://doi.org/10.1007/s10439-018-2015-9

Gabler, L. F., Crandall, J. R., & Panzer, M. B. (2019). Development of a Second-Order System for Rapid Estimation of Maximum Brain Strain. *Annals of Biomedical Engineering*, *47*(9), 1971–1981. https://doi.org/10.1007/s10439-018-02179-9

Gabler, L. F., Joodaki, H., Crandall, J. R., & Panzer, M. B. (2018). Development of a Single-Degree-of-Freedom Mechanical Model for Predicting Strain-Based Brain Injury Responses. *Journal of Biomechanical Engineering*, *140*(3). https://doi.org/10.1115/1.4038357

Garo, A., Hrapko, M., Van Dommelen, J., & Peters, G. (2007). Towards a reliable characterisation of the mechanical behaviour of brain tissue: The effects of post-mortem time and sample preparation. *Biorheology*, *44*(1), 51–58.

Giudice, J. S., Alshareef, A., Wu, T., Gancayco, C. A., Reynier, K. A., Tustison, N. J., Druzgal, T. J., & Panzer, M. B. (2020). An Image Registration-Based Morphing Technique for Generating Subject-Specific Brain Finite Element Models. *Annals of Biomedical Engineering*, *48*(10), 2412–2424.

Giudice, J. S., Alshareef, A., Wu, T., Knutsen, A. K., Hiscox, L. V., Johnson, C. L., & Panzer, M. B. (2021). Calibration of a Heterogeneous Brain Model Using a Subject-Specific Inverse Finite Element Approach. *Frontiers in Bioengineering and Biotechnology*, *9*, 354.

Giudice, J. S., Zeng, W., Wu, T., Alshareef, A., Shedd, D. F., & Panzer, M. B. (2019). An analytical review of the numerical methods used for finite element modeling of traumatic brain injury. *Annals of Biomedical Engineering*, *47*(9), 1855–1872.

Giudice, S., & Panzer, M. (advisor). (2020). *Personalized Finite Element Modeling of the Brain: Understanding Subject-Specific Deformation Patterns* [University of Virginia, Mechanical and Aerospace Engineering - School of Engineering and Applied Science, PHD (Doctor of Philosophy), 2020]. https://doi.org/10.18130/v3-9f79-vw06

Good, C. D., Johnsrude, I., Ashburner, J., Henson, R. N. A., Friston, K. J., & Frackowiak, R. S. J. (2001). Cerebral Asymmetry and the Effects of Sex and Handedness on Brain Structure: A Voxel-Based Morphometric Analysis of 465 Normal Adult Human Brains. *NeuroImage*, *14*(3), 685–700. https://doi.org/10.1006/nimg.2001.0857

Grimm, O., Pohlack, S., Cacciaglia, R., Winkelmann, T., Plichta, M. M., Demirakca, T., & Flor, H. (2015). Amygdalar and hippocampal volume: A comparison between manual segmentation, Freesurfer and VBM. *Journal of Neuroscience Methods*, *253*, 254–261.

Guo, J., Posnansky, O., Hirsch, S., Scheel, M., Taupitz, M., Braun, J., & Sack, I. (2012). Fractal network dimension and viscoelastic powerlaw behavior: II. An experimental study of structure-mimicking phantoms by magnetic resonance elastography. *Physics in Medicine & Biology*, *57*(12), 4041.

Gupte, R. P., Brooks, W. M., Vukas, R. R., Pierce, J. D., & Harris, J. L. (2019). Sex Differences in Traumatic Brain Injury: What We Know and What We Should Know. *Journal of Neurotrauma*, *36*(22), 3063–3091. https://doi.org/10.1089/neu.2018.6171

Gur, R. C., Turetsky, B. I., Matsui, M., Yan, M., Bilker, W., Hughett, P., & Gur, R. E. (1999). Sex Differences in Brain Gray and White Matter in Healthy Young Adults: Correlations with Cognitive Performance. *The Journal of Neuroscience*, *19*(10), 4065–4072. https://doi.org/10.1523/JNEUROSCI.19-10-04065.1999

Hashemi, R. H., Bradley, W. G., & Lisanti, C. J. (2012). *MRI: the basics: The Basics*. Lippincott Williams & Wilkins.

Hiscox, L. V., Johnson, C. L., McGarry, M. D. J., Perrins, M., Littlejohn, A., van Beek, E. J. R., Roberts, N., & Starr, J. M. (2018). High-resolution magnetic resonance elastography reveals differences in subcortical gray matter viscoelasticity between young and healthy older adults. *Neurobiology of Aging*, *65*, 158–167. https://doi.org/10.1016/j.neurobiolaging.2018.01.010

Hiscox, L. V., McGarry, M. D. J., Schwarb, H., Van Houten, E. E. W., Pohlig, R. T., Roberts, N., Huesmann, G. R., Burzynska, A. Z., Sutton, B. P., Hillman, C. H., Kramer, A. F., Cohen, N. J., Barbey, A. K., Paulsen, K. D., & Johnson, C. L. (2020). Standard-space atlas of the viscoelastic properties of the human brain. *Human Brain Mapping*, *41*(18), 5282–5300. https://doi.org/10.1002/hbm.25192

Hiscox, L. V., Schwarb, H., McGarry, M. D. J., & Johnson, C. L. (2021). Aging brain mechanics: Progress and promise of magnetic resonance elastography. *NeuroImage*, *232*, 117889. https://doi.org/10.1016/j.neuroimage.2021.117889

Holbourn, A. (1943). Mechanics of head injuries. *The Lancet*, *242*(6267), 438–441.

Humm, J. R., Yoganandan, N., Driesslein, K. G., & Pintar, F. A. (2018). Three-dimensional kinematic corridors of the head, spine, and pelvis for small female driver seat occupants in near- and far-side oblique frontal impacts. *Traffic Injury Prevention*, *19*(sup2), S64–S69. https://doi.org/10.1080/15389588.2018.1498973

Jäncke, L., Mérillat, S., Liem, F., & Hänggi, J. (2015). Brain size, sex, and the aging brain: Brain Size, Sex, and Aging. *Human Brain Mapping*, *36*(1), 150–169. https://doi.org/10.1002/hbm.22619

Jessen, K. R., & Mirsky, R. (1980). Glial cells in the enteric nervous system contain glial fibrillary acidic protein. *Nature*, *286*(5774), 736–737.

Jin, X., Zhu, F., Mao, H., Shen, M., & Yang, K. H. (2013). A comprehensive experimental study on material properties of human brain tissue. *Journal of Biomechanics*, *46*(16), 2795–2801. https://doi.org/10.1016/j.jbiomech.2013.09.001

Kennedy, K. M., Erickson, K. I., Rodrigue, K. M., Voss, M. W., Colcombe, S. J., Kramer, A. F., Acker, J. D., & Raz, N. (2009). Age-related differences in regional brain volumes: A comparison of optimized voxel-based morphometry to manual volumetry. *Neurobiology of Aging*, *30*(10), 1657–1676.

Kent, R., Lopez-Valdes, F., Forman, J., Seacrist, T., Higuchi, K., & Arbogast, K. (2012). PMHS experiments to evaluate shoulder belt retention in oblique impacts. *JSAE Annual Congress. Paper*, *20125172*.

Kent, R. W., & Forman, J. (2015). Restraint System Biomechanics. In N. Yoganandan, A. M. Nahum, & J. W. Melvin (Eds.), *Accidental Injury: Biomechanics and Prevention* (pp. 113–141). Springer. https://doi.org/10.1007/978-1-4939-1732-7_5

Klauschen, F., Goldman, A., Barra, V., Meyer-Lindenberg, A., & Lundervold, A. (2009). Evaluation of automated brain MR image segmentation and volumetry methods. *Human Brain Mapping*, *30*(4), 1310–1327. https://doi.org/10.1002/hbm.20599

Klein, A. (2016). *OASIS-TRT-20_jointfusion_DKT31_CMA_labels_in_OASIS-30_v2.nii.gz* [Data set]. Harvard Dataverse. https://doi.org/10.7910/DVN/XCCE9Q/3YCRGY

Klein, A., & Tourville, J. (2012). 101 labeled brain images and a consistent human cortical labeling protocol. *Frontiers in Neuroscience*, *6*, 171.

Kleiven, S. (2007). Predictors for traumatic brain injuries evaluated through accident reconstructions. *Stapp Car Crash J*, *51*(81), 81–114.

Kubas, B., Łebkowski, W., Łebkowska, U., Kułak, W., Tarasow, E., & Walecki, J. (2010). Proton MR spectroscopy in mild traumatic brain injury. *Polish Journal of Radiology*, *75*(4), 7–10.

Leonard, C. M., Towler, S., Welcome, S., Halderman, L. K., Otto, R., Eckert, M. A., & Chiarello, C. (2008). Size matters: Cerebral volume influences sex differences in neuroanatomy. *Cerebral Cortex*, *18*(12), 2920–2931.

Li, X., Zhou, Z., & Kleiven, S. (2021). An anatomically detailed and personalizable head injury model: Significance of brain and white matter tract morphological variability on strain. *Biomechanics and Modeling in Mechanobiology*, *20*(2), 403–431. https://doi.org/10.1007/s10237-020-01391-8

Libertiaux, V., Pascon, F., & Cescotto, S. (2011). Experimental verification of brain tissue incompressibility using digital image correlation. *Journal of the Mechanical Behavior of Biomedical Materials*, *4*(7), 1177–1185. https://doi.org/10.1016/j.jmbbm.2011.03.028

Liu, Y., Domel, A. G., Yousefsani, S. A., Kondic, J., Grant, G., Zeineh, M., & Camarillo, D. B. (2020). Validation and Comparison of Instrumented Mouthguards for Measuring Head Kinematics and Assessing Brain Deformation in Football Impacts. *Annals of Biomedical Engineering*, *48*(11), 2580–2598. https://doi.org/10.1007/s10439-020-02629-3

Lotze, M., Domin, M., Gerlach, F. H., Gaser, C., Lueders, E., Schmidt, C. O., & Neumann, N. (2019). Novel findings from 2,838 Adult Brains on Sex Differences in Gray Matter Brain Volume. *Scientific Reports*, *9*(1). https://doi.org/10.1038/s41598-018-38239-2

Luders, E., Narr, K. L., Thompson, P. M., Rex, D. E., Woods, R. P., DeLuca, H., Jancke, L., & Toga, A. W. (2006). Gender effects on cortical thickness and the influence of scaling. *Human Brain Mapping*, *27*(4), 314–324. https://doi.org/10.1002/hbm.20187

Lüders, E., Steinmetz, H., & Jäncke, L. (2002). Brain size and grey matter volume in the healthy human brain. *Neuroreport*, *13*(17), 2371–2374.

Luders, E., & Toga, A. W. (2010). Sex differences in brain anatomy. In *Progress in Brain Research* (Vol. 186, pp. 2–12). Elsevier. https://doi.org/10.1016/B978-0-444-53630-3.00001-4

Lyoo, C. H., Ryu, Y. H., & Lee, M. S. (2010). Topographical distribution of cerebral cortical thinning in patients with mild Parkinson’s disease without dementia. *Movement Disorders*, *25*(4), 496–499. https://doi.org/10.1002/mds.22975

Maas, A. I., Menon, D. K., Adelson, P. D., Andelic, N., Bell, M. J., Belli, A., Bragge, P., Brazinova, A., Büki, A., & Chesnut, R. M. (2017). Traumatic brain injury: Integrated approaches to improve prevention, clinical care, and research. *The Lancet Neurology*, *16*(12), 987–1048.

Madhukar, A., & Ostoja-Starzewski, M. (2019). Finite Element Methods in Human Head Impact Simulations: A Review. *Annals of Biomedical Engineering*, *47*(9), 1832–1854. https://doi.org/10.1007/s10439-019-02205-4

Makowski, C., Béland, S., Kostopoulos, P., Bhagwat, N., Devenyi, G. A., Malla, A. K., Joober, R., Lepage, M., & Chakravarty, M. M. (2018). Evaluating accuracy of striatal, pallidal, and thalamic segmentation methods: Comparing automated approaches to manual delineation. *Neuroimage*, *170*, 182–198.

Maleki, N., Linnman, C., Brawn, J., Burstein, R., Becerra, L., & Borsook, D. (2012). Her versus his migraine: Multiple sex differences in brain function and structure. *Brain*, *135*(8), 2546–2559. https://doi.org/10.1093/brain/aws175

Mao, H., Zhang, L., Jiang, B., Genthikatti, V. V., Jin, X., Zhu, F., Makwana, R., Gill, A., Jandir, G., & Singh, A. (2013). Development of a finite element human head model partially validated with thirty five experimental cases. *Journal of Biomechanical Engineering*, *135*(11).

Marwha, D., Halari, M., & Eliot, L. (2017). Meta-analysis reveals a lack of sexual dimorphism in human amygdala volume. *Neuroimage*, *147*, 282–294.

McIlvain, G., Schwarb, H., Cohen, N. J., Telzer, E. H., & Johnson, C. L. (2018). Mechanical properties of the in vivo adolescent human brain. *Developmental Cognitive Neuroscience*, *34*, 27–33. https://doi.org/10.1016/j.dcn.2018.06.001

Mercadante, A. A., & Tadi, P. (2020). *Neuroanatomy, Gray Matter*.

Molina, D. K., & DiMaio, V. J. M. (2012). Normal Organ Weights in Men: Part II—The Brain, Lungs, Liver, Spleen, and Kidneys. *American Journal of Forensic Medicine & Pathology*, *33*(4), 368–372. https://doi.org/10.1097/PAF.0b013e31823d29ad

Molina, D. K., & DiMaio, V. J. M. (2015). Normal Organ Weights in Women: Part II—The Brain, Lungs, Liver, Spleen, and Kidneys. *American Journal of Forensic Medicine & Pathology*, *36*(3), 182–187. https://doi.org/10.1097/PAF.0000000000000175

National Highway Traffic Safety Administration. (2022). *NHTSA Biomechanics Test Database*. National Highway Traffic Safety Administration. https://www.nhtsa.gov/research-data/research-testing-databases#/biomechanics

Nikolova, G. S., & Toshev, Y. E. (2007). Estimation of male and female body segment parameters of the Bulgarian population using a 16-segmental mathematical model. *Journal of Biomechanics*, *40*(16), 3700–3707.

Peterson, A. B., Xu, L., Daugherty, J., & Breiding, M. J. (2019). *Surveillance report of traumatic brain injury-related emergency department visits, hospitalizations, and deaths, United States, 2014*.

Pintzka, C. W. S., Hansen, T. I., Evensmoen, H. R., & Håberg, A. K. (2015). Marked effects of intracranial volume correction methods on sex differences in neuroanatomical structures: A HUNT MRI study. *Frontiers in Neuroscience*, *9*, 238.

Potvin, O., Mouiha, A., Dieumegarde, L., Duchesne, S., & Initiative, A. D. N. (2016). Normative data for subcortical regional volumes over the lifetime of the adult human brain. *NeuroImage*, *137*, 9–20.

Purves, D., Augustine, G. J., Fitzpatrick, D., Hall, W. C., LaMantia, A.-S., & White, L. (2011). *Neuroscience, 5th edn. Sunderland, MA*.

R Core Team. (2022). *R: A language and enviroment for statistical computing*. RStudio. https://www.R-project.org/

Resch, J. E., Rach, A., Walton, S., & Broshek, D. K. (2017). Sport Concussion and the Female Athlete. *Clinics in Sports Medicine*, *36*(4), 717–739. https://doi.org/10.1016/j.csm.2017.05.002

Reynier, K. A., Alshareef, A., Sanchez, E. J., Shedd, D. F., Walton, S. R., Erdman, N. K., Newman, B. T., Giudice, J. S., Higgins, M. J., Funk, J. R., Broshek, D. K., Druzgal, T. J., Resch, J. E., & Panzer, M. B. (2020). The Effect of Muscle Activation on Head Kinematics During Non-injurious Head Impacts in Human Subjects. *Annals of Biomedical Engineering*, *48*(12), 2751–2762. https://doi.org/10.1007/s10439-020-02609-7

Reynier, K., Giudice, J. S., Forman, J., & Panzer, M. (2021). Preliminary investigation of sex-specific geometries and head kinematics on brain response using finite element brain models in automotive crash loading conditions. *IRCOBI Conference Proceedings*, 357–358.

Ritchie, S. J., Cox, S. R., Shen, X., Lombardo, M. V., Reus, L. M., Alloza, C., Harris, M. A., Alderson, H. L., Hunter, S., Neilson, E., Liewald, D. C. M., Auyeung, B., Whalley, H. C., Lawrie, S. M., Gale, C. R., Bastin, M. E., McIntosh, A. M., & Deary, I. J. (2018). Sex Differences in the Adult Human Brain: Evidence from 5216 UK Biobank Participants. *Cerebral Cortex*, *28*(8), 2959–2975. https://doi.org/10.1093/cercor/bhy109

Rohlfing, T., Brandt, R., Menzel, R., Russakoff, D. B., Maurer, C. R., & Jr. (2005). *Quo Vadis, Atlas-based Segmentation?*

Roof, R. L., Duvdevani, R., & Stein, D. G. (1993). Gender influences outcome of brain injury: Progesterone plays a protective role. *Brain Research*, *607*(1–2), 333–336. https://doi.org/10.1016/0006-8993(93)91526-X

Roof, R. L., & Hall, E. D. (2000). Estrogen-related gender difference in survival rate and cortical blood flow after impact-acceleration head injury in rats. *Journal of Neurotrauma*, *17*(12), 1155–1169.

Ruigrok, A. N. V., Salimi-Khorshidi, G., Lai, M.-C., Baron-Cohen, S., Lombardo, M. V., Tait, R. J., & Suckling, J. (2014). A meta-analysis of sex differences in human brain structure. *Neuroscience & Biobehavioral Reviews*, *39*, 34–50. https://doi.org/10.1016/j.neubiorev.2013.12.004

Sack, I., Beierbach, B., Wuerfel, J., Klatt, D., Hamhaber, U., Papazoglou, S., Martus, P., & Braun, J. (2009). The impact of aging and gender on brain viscoelasticity. *NeuroImage*, *46*(3), 652–657. https://doi.org/10.1016/j.neuroimage.2009.02.040

Sack, I., Jöhrens, K., Würfel, J., & Braun, J. (2013). Structure-sensitive elastography: On the viscoelastic powerlaw behavior of in vivo human tissue in health and disease. *Soft Matter*, *9*(24), 5672–5680.

Sack, I., Streitberger, K.-J., Krefting, D., Paul, F., & Braun, J. (2011). The Influence of Physiological Aging and Atrophy on Brain Viscoelastic Properties in Humans. *PLoS ONE*, *6*(9), e23451. https://doi.org/10.1371/journal.pone.0023451

SAE. (1995). Instrumentation for impact test—Part 1: Electronic instrumentation. *SAE Handbook*, 384–392.

Sanchez, E. J., Gabler, L. F., McGhee, J. S., Olszko, A. V., Chancey, V. C., Crandall, J. R., & Panzer, M. B. (2017). Evaluation of Head and Brain Injury Risk Functions Using Sub-Injurious Human Volunteer Data. *Journal of Neurotrauma*, *34*(16), 2410–2424. https://doi.org/10.1089/neu.2016.4681

Shaw, G., David, L., Joseph, A., & Jeff, C. (2014). Development of an Alternative Frontal Impact Condition to Assess Thoracic Response Using the THOR Mod Kit Dummy. *International Journal of Automotive Engineering*, *5*(1), 39–46. https://doi.org/10.20485/jsaeijae.5.1_39

Shaw, G., Lessley, D., Ash, J., Poplin, J., McMurry, T., Sochor, M., & Crandall, J. (2017). Small female rib cage fracture in frontal sled tests. *Traffic Injury Prevention*, *18*(1), 77–82. https://doi.org/10.1080/15389588.2016.1193599

Shaw, G., Parent, D., Purtsezov, S., Lessley, D., Crandall, J., Kent, R., Guillemot, H., Ridella, S., Takhounts, E., & Martin, P. (2009). Impact response of restrained PMHS in frontal sled tests: Skeletal deformation patterns under seat belt loading. *Stapp Car Crash Journal*, *53*, 1–48.

Skolnick, B. E., Maas, A. I., Narayan, R. K., Van Der Hoop, R. G., MacAllister, T., Ward, J. D., Nelson, N. R., & Stocchetti, N. (2014). A clinical trial of progesterone for severe traumatic brain injury. *New England Journal of Medicine*, *371*(26), 2467–2476.

Smith, D. H., & Meaney, D. F. (2000). Axonal Damage in Traumatic Brain Injury. *The Neuroscientist*, *6*(6), 483–495. https://doi.org/10.1177/107385840000600611

Smith, D. H., Wolf, J. A., Lusardi, T. A., Lee, V. M.-Y., & Meaney, D. F. (1999). High Tolerance and Delayed Elastic Response of Cultured Axons to Dynamic Stretch Injury. *The Journal* *of Neuroscience*, *19*(11), 4263–4269. https://doi.org/10.1523/JNEUROSCI.19-11-04263.1999

Society of Automotive Engineers. (2007). *SAE J211-1 Surface Vehicle Recommended Practice: Instrumentation for Impact Test – Part 1 – Electronic Instrumentation.*

Takhounts, E. G., Craig, M. J., Moorhouse, K., McFadden, J., & Hasija, V. (2013, November 11). *Development of Brain Injury Criteria (BrIC)*. 57th Stapp Car Crash Conference. https://doi.org/10.4271/2013-22-0010

Takhounts, E. G., Ridella, S. A., Hasija, V., Tannous, R. E., Campbell, J. Q., Malone, D., Danelson, K., Stitzel, J., Rowson, S., & Duma, S. (2008a). Investigation of traumatic brain injuries using the next generation of simulated injury monitor (SIMon) finite element head model. *Stapp Car Crash Journal*, *52*, 1.

Takhounts, E. G., Ridella, S. A., Hasija, V., Tannous, R. E., Campbell, J. Q., Malone, D., Danelson, K., Stitzel, J., Rowson, S., & Duma, S. (2008b). *Investigation of Traumatic Brain Injuries Using the Next Generation of Simulated Injury Monitor (SIMon) Finite Element Head Model*. 2008-22–0001. https://doi.org/10.4271/2008-22-0001

Tang-Schomer, M. D., Johnson, V. E., Baas, P. W., Stewart, W., & Smith, D. H. (2012). Partial interruption of axonal transport due to microtubule breakage accounts for the formation of periodic varicosities after traumatic axonal injury. *Experimental Neurology*, *233*(1), 364–372. https://doi.org/10.1016/j.expneurol.2011.10.030

Tang-Schomer, M. D., Patel, A. R., Baas, P. W., & Smith, D. H. (2010). Mechanical breaking of microtubules in axons during dynamic stretch injury underlies delayed elasticity, microtubule disassembly, and axon degeneration. *The FASEB Journal*, *24*(5), 1401–1410. https://doi.org/10.1096/fj.09-142844

Toga, A. W., & Thompson, P. M. (2001). The role of image registration in brain mapping. *Image and Vision Computing*, *19*(1–2), 3–24. https://doi.org/10.1016/S0262-8856(00)00055-X

Tustison, N. J., Cook, P. A., Holbrook, A. J., Johnson, H. J., Muschelli, J., Devenyi, G. A., Duda, J. T., Das, S. R., Cullen, N. C., Gillen, D. L., Yassa, M. A., Stone, J. R., Gee, J. C., & Avants, B. B. (2021). The ANTsX ecosystem for quantitative biological and medical imaging. *Scientific Reports*, *11*(1), 9068. https://doi.org/10.1038/s41598-021-87564-6

Vasavada, A. N., Danaraj, J., & Siegmund, G. P. (2008). Head and neck anthropometry, vertebral geometry and neck strength in height-matched men and women. *Journal of Biomechanics*, *41*(1), 114–121. https://doi.org/10.1016/j.jbiomech.2007.07.007

Wang, H., Suh, J. W., Das, S. R., Pluta, J. B., Craige, C., & Yushkevich, P. A. (2013). Multi-Atlas Segmentation with Joint Label Fusion. *IEEE Transactions on Pattern Analysis and Machine Intelligence*, *35*(3), 611–623. https://doi.org/10.1109/TPAMI.2012.143

Wang, H., & Yushkevich, P. (2013). Multi-atlas segmentation with joint label fusion and corrective learning—An open source implementation. *Frontiers in Neuroinformatics*, *7*, 27. https://doi.org/10.3389/fninf.2013.00027

Wu, T., Antona-Makoshi, J., Alshareef, A., Giudice, J. S., & Panzer, M. B. (2020). Investigation of Cross-Species Scaling Methods for Traumatic Brain Injury Using Finite Element Analysis. *Journal of Neurotrauma*, *37*(2), 410–422. https://doi.org/10.1089/neu.2019.6576

Wu, T., Hajiaghamemar, M., Giudice, J. S., Alshareef, A., Margulies, S. S., & Panzer, M. B. (2021). Evaluation of Tissue-Level Brain Injury Metrics Using Species-Specific Simulations. *Journal of Neurotrauma*, *38*(13), 1879–1888. https://doi.org/10.1089/neu.2020.7445

Wu, T., Sato, F., Antona-Makoshi, J., Gabler, L. F., Giudice, J. S., Alshareef, A., Yaguchi, M., Masuda, M., Margulies, S. S., & Panzer, M. B. (2022). Integrating Human and Nonhuman Primate Data to Estimate Human Tolerances for Traumatic Brain Injury. *Journal of Biomechanical Engineering*, *144*(7), 071003. https://doi.org/10.1115/1.4053209

Wuerfel, J., Paul, F., Beierbach, B., Hamhaber, U., Klatt, D., Papazoglou, S., Zipp, F., Martus, P., Braun, J., & Sack, I. (2010). MR-elastography reveals degradation of tissue integrity in multiple sclerosis. *NeuroImage*, *49*(3), 2520–2525. https://doi.org/10.1016/j.neuroimage.2009.06.018

Young, J. W., Chandler, R. F., Snow, C. C., Robinette, K. M., Zehner, G. F., & Loftberg, M. S. (1983). *Anthropometric and mass distribution characteristics of the adult female*. Civil Aerospace Medical Institute.

Zhao, W., Choate, B., & Ji, S. (2018). Material properties of the brain in injury-relevant conditions – Experiments and computational modeling. *Journal of the Mechanical Behavior of Biomedical Materials*, *80*, 222–234. https://doi.org/10.1016/j.jmbbm.2018.02.005

Appendix

A. Neuroanatomy

A.1 Bayesian Statistical Methods

The equations for the multivariate Bayesian linear mixed model to determine the effect of sex and age on each of the neuroanatomical features, accounting for a random study effect.

$$Y_{ij}^{ICV} = \left(\beta_0^{ICV} + u_{j0}^{ICV}\right) + \beta_1^{ICV}\left(scale\left(Age_{ij}\right)\right) + \beta_2^{ICV}\left(Sex_{ij}\right) + \epsilon_{\mathrm{ij}}^{ICV}$$

$$Y_{ij}^{WM} = \left(\beta_0^{WM} + u_{j0}^{WM}\right) + \beta_1^{WM}\left(scale\left(Age_{ij}\right)\right) + \beta_2^{WM}\left(Sex_{ij}\right) + \epsilon_{\mathrm{ij}}^{WM}$$

$$Y_{ij}^{GM} = \left(\beta_0^{GM} + u_{j0}^{GM}\right) + \beta_1^{GM}\left(scale\left(Age_{ij}\right)\right) + \beta_2^{GM}\left(Sex_{ij}\right) + \epsilon_{\mathrm{ij}}^{GM}$$

$$Y_{ij}^{RelWM} = \left(\beta_0^{RelWM} + u_{j0}^{RelWM}\right) + \beta_1^{RelWM}\left(scale\left(Age_{ij}\right)\right) + \beta_2^{RelWM}\left(Sex_{ij}\right) + \epsilon_{\mathrm{ij}}^{RelWM}$$

The equations for the multivariate Bayesian linear mixed model to determine the effect of sex and age on each of the neuroanatomical features, accounting for a random study effect.

$$Y_{ij}^{SFC} = \left(\beta_0^{SFC} + u_{j0}^{SFC}\right) + \beta_1^{SFC}\left(scale\left(Age_{ij}\right)\right) + \beta_2^{SFC}\left(Sex_{ij}\right) + \epsilon_{\mathrm{ij}}^{SFC}$$

$$Y_{ij}^{RMF} = \left(\beta_0^{RMF} + u_{j0}^{RMF}\right) + \beta_1^{RMF}\left(scale\left(Age_{ij}\right)\right) + \beta_2^{RMF}\left(Sex_{ij}\right) + \epsilon_{\mathrm{ij}}^{RMF}$$

$$Y_{ij}^{PRE} = \left(\beta_0^{PRE} + u_{j0}^{PRE}\right) + \beta_1^{PRE}\left(scale\left(Age_{ij}\right)\right) + \beta_2^{PRE}\left(Sex_{ij}\right) + \epsilon_{\mathrm{ij}}^{PRE}$$

$$Y_{ij}^{LaO} = \left(\beta_0^{LaO} + u_{j0}^{LaO}\right) + \beta_1^{LaO}\left(scale\left(Age_{ij}\right)\right) + \beta_2^{LaO}\left(Sex_{ij}\right) + \epsilon_{\mathrm{ij}}^{LaO}$$

$$Y_{ij}^{LiO} = \left(\beta_0^{LiO} + u_{j0}^{LiO}\right) + \beta_1^{LiO}\left(scale\left(Age_{ij}\right)\right) + \beta_2^{LiO}\left(Sex_{ij}\right) + \epsilon_{\mathrm{ij}}^{LiO}$$

$$Y_{ij}^{CN} = \left(\beta_0^{CN} + u_{j0}^{CN}\right) + \beta_1^{CN}\left(scale\left(Age_{ij}\right)\right) + \beta_2^{CN}\left(Sex_{ij}\right) + \epsilon_{\mathrm{ij}}^{CN}$$

$$Y_{ij}^{SPC} = \left(\beta_0^{SPC} + u_{j0}^{SPC}\right) + \beta_1^{SPC}\left(scale\left(Age_{ij}\right)\right) + \beta_2^{SPC}\left(Sex_{ij}\right) + \epsilon_{\mathrm{ij}}^{SPC}$$

$$Y_{ij}^{POST} = \left(\beta_0^{POST} + u_{j0}^{POST}\right) + \beta_1^{POST}\left(scale\left(Age_{ij}\right)\right) + \beta_2^{POST}\left(Sex_{ij}\right) + \epsilon_{\mathrm{ij}}^{POST}$$

$$Y_{ij}^{PCN} = \left(\beta_0^{PCN} + u_{j0}^{PCN}\right) + \beta_1^{PCN}\left(scale\left(Age_{ij}\right)\right) + \beta_2^{PCN}\left(Sex_{ij}\right) + \epsilon_{\mathrm{ij}}^{PCN}$$

$$Y_{ij}^{STC} = \left(\beta_0^{STC} + u_{j0}^{STC}\right) + \beta_1^{STC}\left(scale\left(Age_{ij}\right)\right) + \beta_2^{STC}\left(Sex_{ij}\right) + \epsilon_{\mathrm{ij}}^{STC}$$

$$Y_{ij}^{ITC} = \left(\beta_0^{ITC} + u_{j0}^{ITC}\right) + \beta_1^{ITC}\left(scale\left(Age_{ij}\right)\right) + \beta_2^{ITC}\left(Sex_{ij}\right) + \epsilon_{\mathrm{ij}}^{ITC}$$

$$Y_{ij}^{FSG} = \left(\beta_0^{FSG} + u_{j0}^{FSG}\right) + \beta_1^{FSG}\left(scale\left(Age_{ij}\right)\right) + \beta_2^{FSG}\left(Sex_{ij}\right) + \epsilon_{\mathrm{ij}}^{FSG}$$

The equations for the multivariate Bayesian linear mixed model to predict deformation metrics based on independent neuroanatomical features, age, and sex accounting for a random study effect.

$$\begin{aligned}
Y_{ij}^{MPS-95} = {} & \left(\beta_0^{MPS-95} + u_{j0}^{MPS-95}\right) + \beta_1^{MPS-95}\left(Age_{ij}\right) + \beta_2^{MPS-95}\left(Sex_{ij}\right) + \beta_3^{MPS-95}\left(ICV_{ij}\right) \\
& + \beta_4^{MPS-95}\left(Rel\ WM_{ij}\right) + \beta_5^{MPS-95}\left(Rel\ GM_{ij}\right) + \beta_6^{MPS-95}\left(SFC\ Vol_{ij}\right) \\
& + \beta_7^{MPS-95}\left(RMF\ Vol_{ij}\right) + \beta_8^{MPS-95}\left(PRE\ Vol_{ij}\right) + \beta_9^{MPS-95}\left(LaO\ Vol_{ij}\right) \\
& + \beta_{10}^{MPS-95}\left(LiO\ Vol_{ij}\right) + \beta_{11}^{MPS-95}\left(CN\ Vol_{ij}\right) + \beta_{12}^{MPS-95}\left(SPC\ Vol_{ij}\right) \\
& + \beta_{13}^{MPS-95}\left(POST\ Vol_{ij}\right) + \beta_{14}^{MPS-95}\left(PCN\ Vol_{ij}\right) + \beta_{15}^{MPS-95}\left(STC\ Vol_{ij}\right) \\
& + \beta_{16}^{MPS-95}\left(ITC\ Vol_{ij}\right) + \beta_{17}^{MPS-95}\left(FSG\ Vol_{ij}\right) + \beta_{18}^{MPS-95}\left(SFC\ Th_{ij}\right) \\
& + \beta_{19}^{MPS-95}\left(RMF\ Th_{ij}\right) + \beta_{20}^{MPS-95}\left(PRE\ Th_{ij}\right) + \beta_{21}^{MPS-95}\left(LaO\ Th_{ij}\right) \\
& + \beta_{22}^{MPS-95}\left(LiO\ Th_{ij}\right) + \beta_{23}^{MPS-95}\left(CN\ Th_{ij}\right) + \beta_{24}^{MPS-95}\left(SPC\ Th_{ij}\right) \\
& + \beta_{25}^{MPS-95}\left(POST\ Th_{ij}\right) + \beta_{26}^{MPS-95}\left(PCN\ Th_{ij}\right) \\
& + \beta_{27}^{MPS-95}\left(STC\ Th_{ij}\right) + \beta_{28}^{MPS-95}\left(ITC\ Th_{ij}\right) + \beta_{29}^{MPS-95}\left(FSG\ Th_{ij}\right) + \epsilon_{\mathrm{ij}}^{MPS-95}
\end{aligned}$$

$$\begin{aligned}
Y_{ij}^{MPSR-95} = {} & \left(\beta_0^{MPSR-95} + u_{j0}^{MPSR-95}\right) + \beta_1^{MPSR-95}\left(Age_{ij}\right) + \beta_2^{MPSR-95}\left(Sex_{ij}\right) + \beta_3^{MPSR-95}\left(ICV_{ij}\right) \\
& + \beta_4^{MPSR-95}\left(Rel\ WM_{ij}\right) + \beta_5^{MPSR-95}\left(Rel\ GM_{ij}\right) + \beta_6^{MPSR-95}\left(SFC\ Vol_{ij}\right) \\
& + \beta_7^{MPSR-95}\left(RMF\ Vol_{ij}\right) + \beta_8^{MPSR-95}\left(PRE\ Vol_{ij}\right) + \beta_9^{MPSR-95}\left(LaO\ Vol_{ij}\right) \\
& + \beta_{10}^{MPSR-95}\left(LiO\ Vol_{ij}\right) + \beta_{11}^{MPSR-95}\left(CN\ Vol_{ij}\right) + \beta_{12}^{MPSR-95}\left(SPC\ Vol_{ij}\right) \\
& + \beta_{13}^{MPSR-95}\left(POST\ Vol_{ij}\right) + \beta_{14}^{MPSR-95}\left(PCN\ Vol_{ij}\right) + \beta_{15}^{MPSR-95}\left(STC\ Vol_{ij}\right) \\
& + \beta_{16}^{MPSR-95}\left(ITC\ Vol_{ij}\right) + \beta_{17}^{MPSR-95}\left(FSG\ Vol_{ij}\right) + \beta_{18}^{MPSR-95}\left(SFC\ Th_{ij}\right) \\
& + \beta_{19}^{MPSR-95}\left(RMF\ Th_{ij}\right) + \beta_{20}^{MPSR-95}\left(PRE\ Th_{ij}\right) + \beta_{21}^{MPSR-95}\left(LaO\ Th_{ij}\right) \\
& + \beta_{22}^{MPSR-95}\left(LiO\ Th_{ij}\right) + \beta_{23}^{MPSR-95}\left(CN\ Th_{ij}\right) + \beta_{24}^{MPSR-95}\left(SPC\ Th_{ij}\right) \\
& + \beta_{25}^{MPSR-95}\left(POST\ Th_{ij}\right) + \beta_{26}^{MPSR-95}\left(PCN\ Th_{ij}\right) \\
& + \beta_{27}^{MPSR-95}\left(STC\ Th_{ij}\right) + \beta_{28}^{MPSR-95}\left(ITC\ Th_{ij}\right) + \beta_{29}^{MPSR-95}\left(FSG\ Th_{ij}\right) \\
& + \epsilon_{\mathrm{ij}}^{MPSR-95}
\end{aligned}$$

$$
\begin{aligned}
Y_{ij}^{MPSxMPSR-95} = {} & \left(\mathrm{\beta}_0^{MPSxMPSR-95} + u_{j0}^{MPSxMPSR-95}\right) + \beta_1^{MPSxMPSR-95}\left(Age_{ij}\right) + \beta_2^{MPSxMPSR-95}\left(Sex_{ij}\right) \\
& + \beta_3^{MPSxMPSR-95}\left(ICV_{ij}\right) + \beta_4^{MPSxMPSR-95}\left(Rel\ WM_{ij}\right) + \beta_5^{MPSxMPSR-95}\left(Rel\ GM_{ij}\right) \\
& + \beta_6^{MPSxMPSR-95}\left(SFC\ Vol_{ij}\right) \\
& + \beta_7^{MPSxMPSR-95}\left(RMF\ Vol_{ij}\right) + \beta_8^{MPSxMPSR-95}\left(PRE\ Vol_{ij}\right) \\
& + \beta_9^{MPSxMPSR-95}\left(LaO\ Vol_{ij}\right) + \beta_{10}^{MPSxMPSR-95}\left(LiO\ Vol_{ij}\right) \\
& + \beta_{11}^{MPSxMPSR-95}\left(CN\ Vol_{ij}\right) + \beta_{12}^{MPSxMPSR-95}\left(SPC\ Vol_{ij}\right) \\
& + \beta_{13}^{MPSxMPSR-95}\left(POST\ Vol_{ij}\right) + \beta_{14}^{MPSxMPSR-95}\left(PCN\ Vol_{ij}\right) \\
& + \beta_{15}^{MPSxMPSR-95}\left(STC\ Vol_{ij}\right) + \beta_{16}^{MPSxMPSR-95}\left(ITC\ Vol_{ij}\right) \\
& + \beta_{17}^{MPSxMPSR-95}\left(FSG\ Vol_{ij}\right) + \beta_{18}^{MPSxMPSR-95}\left(SFC\ Th_{ij}\right) \\
& + \beta_{19}^{MPSxMPSR-95}\left(RMF\ Th_{ij}\right) + \beta_{20}^{MPSxMPSR-95}\left(PRE\ Th_{ij}\right) \\
& + \beta_{21}^{MPSxMPSR-95}\left(LaO\ Th_{ij}\right) + \beta_{22}^{MPSxMPSR-95}\left(LiO\ Th_{ij}\right) + \beta_{23}^{MPSxMPSR-95}\left(CN\ Th_{ij}\right) \\
& + \beta_{24}^{MPSxMPSR-95}\left(SPC\ Th_{ij}\right) + \beta_{25}^{MPSxMPSR-95}\left(POST\ Th_{ij}\right) \\
& + \beta_{26}^{MPSxMPSR-95}\left(PCN\ Th_{ij}\right) \\
& + \beta_{27}^{MPSxMPSR-95}\left(STC\ Th_{ij}\right) + \beta_{28}^{MPSxMPSR-95}\left(ITC\ Th_{ij}\right) \\
& + \beta_{29}^{MPSxMPSR-95}\left(FSG\ Th_{ij}\right) + \epsilon_{\mathrm{ij}}^{MPSxMPSR-95}
\end{aligned}
$$

$$
\begin{aligned}
Y_{ij}^{CSDM-25} = {} & \left(\mathrm{\beta}_0^{CSDM-25} + u_{j0}^{CSDM-25}\right) + \beta_1^{CSDM-25}\left(Age_{ij}\right) + \beta_2^{CSDM-25}\left(Sex_{ij}\right) + \beta_3^{CSDM-25}\left(ICV_{ij}\right) \\
& + \beta_4^{CSDM-25}\left(Rel\ WM_{ij}\right) + \beta_5^{CSDM-25}\left(Rel\ GM_{ij}\right) + \beta_6^{CSDM-25}\left(SFC\ Vol_{ij}\right) \\
& + \beta_7^{CSDM-25}\left(RMF\ Vol_{ij}\right) + \beta_8^{CSDM-25}\left(PRE\ Vol_{ij}\right) + \beta_9^{CSDM-25}\left(LaO\ Vol_{ij}\right) \\
& + \beta_{10}^{CSDM-25}\left(LiO\ Vol_{ij}\right) + \beta_{11}^{CSDM-25}\left(CN\ Vol_{ij}\right) + \beta_{12}^{CSDM-25}\left(SPC\ Vol_{ij}\right) \\
& + \beta_{13}^{CSDM-25}\left(POST\ Vol_{ij}\right) + \beta_{14}^{CSDM-25}\left(PCN\ Vol_{ij}\right) + \beta_{15}^{CSDM-25}\left(STC\ Vol_{ij}\right) \\
& + \beta_{16}^{CSDM-25}\left(ITC\ Vol_{ij}\right) + \beta_{17}^{CSDM-25}\left(FSG\ Vol_{ij}\right) + \beta_{18}^{CSDM-25}\left(SFC\ Th_{ij}\right) \\
& + \beta_{19}^{CSDM-25}\left(RMF\ Th_{ij}\right) + \beta_{20}^{CSDM-25}\left(PRE\ Th_{ij}\right) + \beta_{21}^{CSDM-25}\left(LaO\ Th_{ij}\right) \\
& + \beta_{22}^{CSDM-25}\left(LiO\ Th_{ij}\right) + \beta_{23}^{CSDM-25}\left(CN\ Th_{ij}\right) + \beta_{24}^{CSDM-25}\left(SPC\ Th_{ij}\right) \\
& + \beta_{25}^{CSDM-25}\left(POST\ Th_{ij}\right) + \beta_{26}^{CSDM-25}\left(PCN\ Th_{ij}\right) \\
& + \beta_{27}^{CSDM-25}\left(STC\ Th_{ij}\right) + \beta_{28}^{CSDM-25}\left(ITC\ Th_{ij}\right) + \beta_{29}^{CSDM-25}\left(FSG\ Th_{ij}\right) \\
& + \epsilon_{\mathrm{ij}}^{CSDM-25}
\end{aligned}
$$

A.2 Neuroanatomical Features Results

Appendix Table A: Mean (SD) for each of the neuroanatomical features for the male and female brains.

Measure Type	Region or Ratio of Interest	Female [n = 82] Mean (SD)	Male [n = 60] Mean (SD)
Overall Volumes (cm^3)	Total brain volume	1137.4 (84.6)	1245.6 (93.0)
	CSF volume	274.2 (22.7)	308.8 (25.4)
	Gray matter volume	634.5 (44.7)	693.9 (48.5)
	White matter volume	502.9 (41.4)	551.7 (46.6)
Relative Volumes (cm^3/cm^3)	CSF to ICV ratio	0.19 (0.01)	0.20 (0.01)
	GM to ICV ratio	0.45 (0.01)	0.45 (0.01)
	WM to ICV ratio	0.36 (0.01)	0.36 (0.01)
	GM to WM ratio	1.26 (0.04)	1.26 (0.04)
Subcortical Volumes (cm^3)	SFC	45.4 (5.0)	49.8 (5.8)
	RMF	23.8 (3.0)	26.4 (3.2)
	PRE	21.0 (2.6)	22.9 (3.0)
	LaO	20.3 (2.5)	22.4 (2.7)
	LiO	14.1 (1.9)	15.4 (2.0)
	CN	7.2 (1.2)	8.5 (1.4)
	SPC	18.1 (2.2)	19.1 (2.7)
	POST	16.4 (2.0)	17.6 (2.4)
	PCN	19.8 (2.5)	21.7 (2.5)
	STC	29.4 (3.2)	32.6 (3.3)
	ITC	22.5 (2.2)	26.1 (2.5)
	FSG	21.0 (2.6)	23.0 (2.3)
Subcortical Thickness (mm)	SFC	2.2 (0.2)	2.2 (0.2)
	RMF	2.8 (0.3)	2.8 (0.2)
	PRE	1.5 (0.2)	1.5 (0.2)
	LaO	2.0 (0.2)	1.9 (0.3)
	LiO	2.3 (0.4)	2.4 (0.3)
	CN	1.1 (0.3)	1.3 (0.3)
	SPC	1.4 (0.2)	1.3 (0.2)
	POST	1.4 (0.2)	1.4 (0.2)
	PCN	1.9 (0.3)	1.9 (0.3)
	STC	2.7 (0.2)	2.3 (0.3)
	ITC	3.4 (0.3)	3.5 (0.3)
	FSG	3.5 (0.4)	3.5 (0.4)

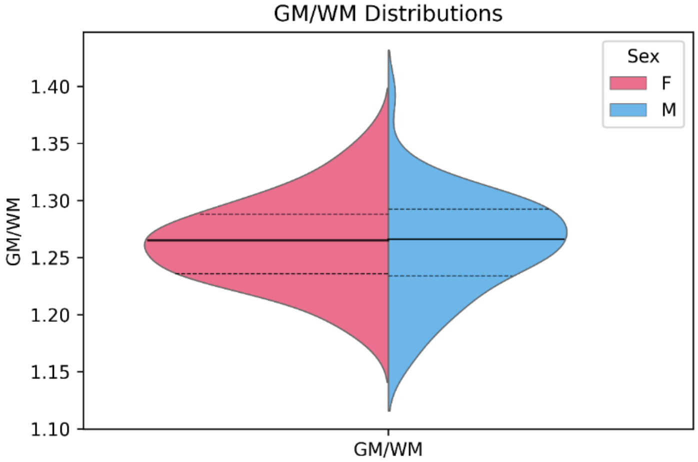

Appendix Figure A: Distributions, based on an estimated probability density function, of gray to white matter ratios for the female and male brains.

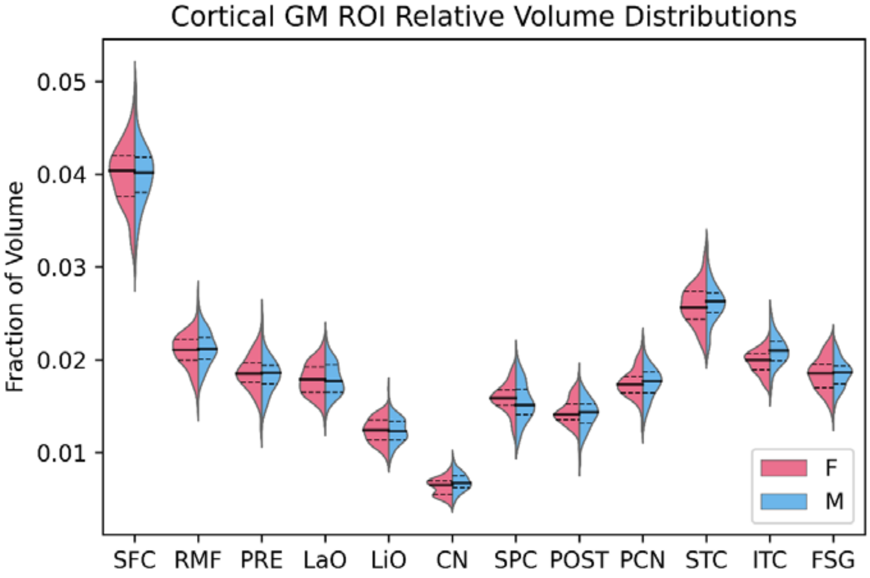

Appendix Figure B: Distributions, based on an estimated probability density function, of the relative volumes of the 12 cortical GM ROIs for both the female and male subjects. Medians are represented by the solid line, and quartiles one and three are represented by the dashed lines.

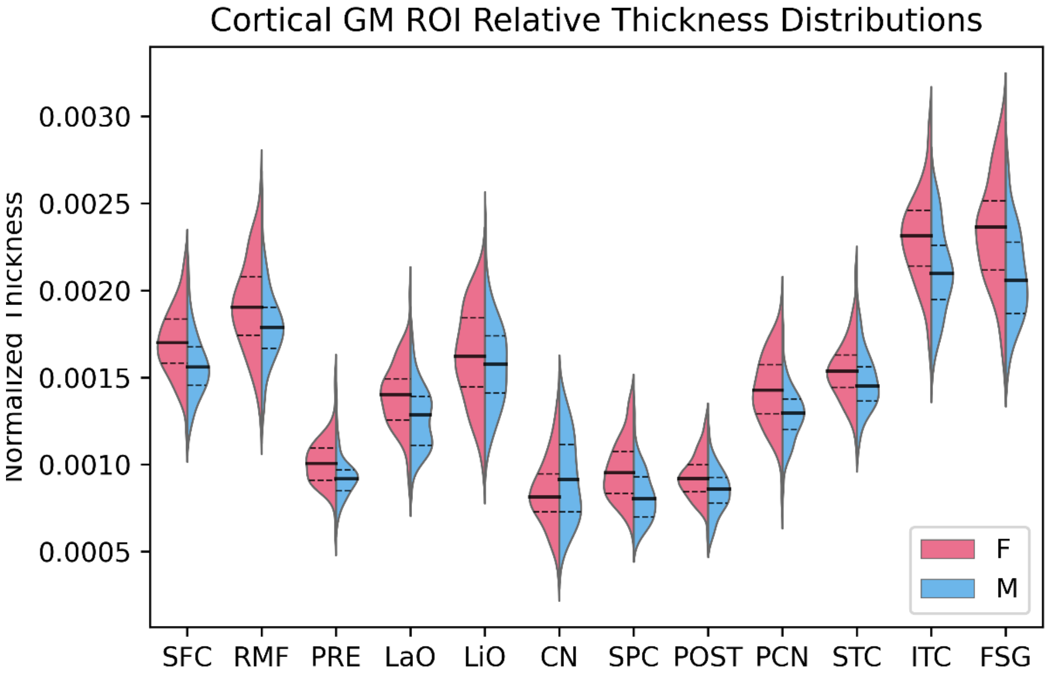

Appendix Figure C: Distributions for relative thickness, normalized using ICV, for both the male and female samples.

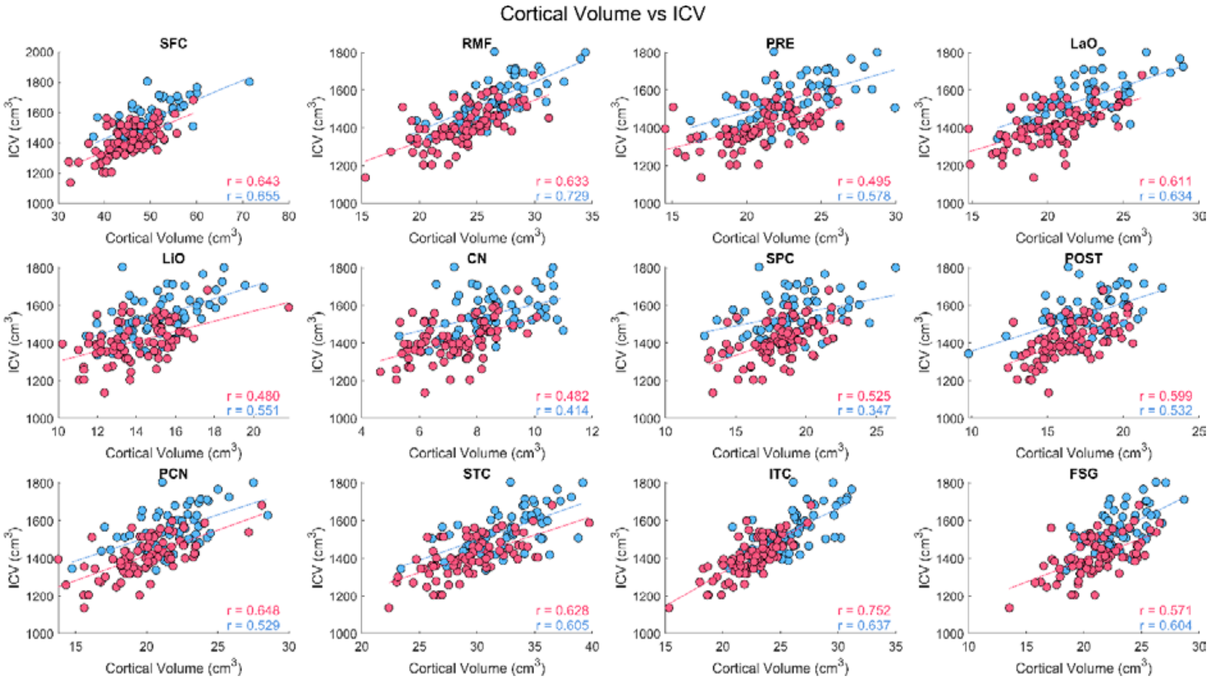

Appendix Figure D: Scatter plots between cortical volume and ICV for each of the 12 CGM ROIs. Solid lines represent linear trendlines for the male and female brains. Correlations between thickness and ICV included for both sexes.

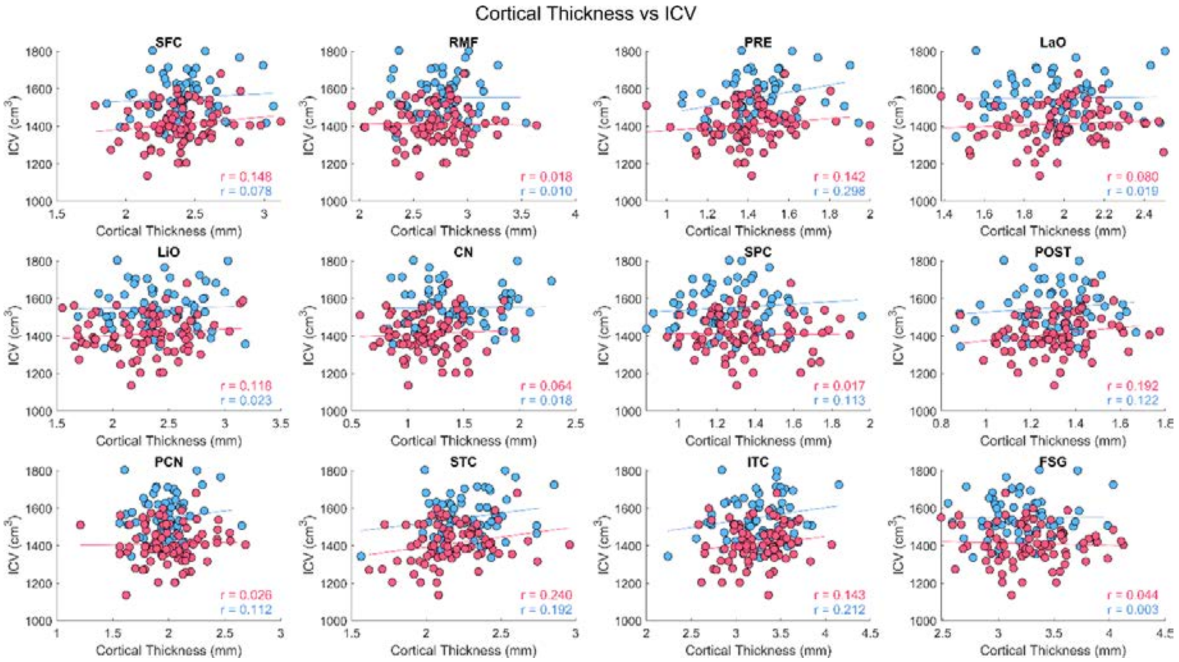

Appendix Figure E: Scatter plots between cortical thickness and ICV for each of the 12 CGM ROIs. Solid lines represent linear trendlines for the male and female brains. Correlations between thickness and ICV included for both sexes.

A.3 Deformation Metrics Results

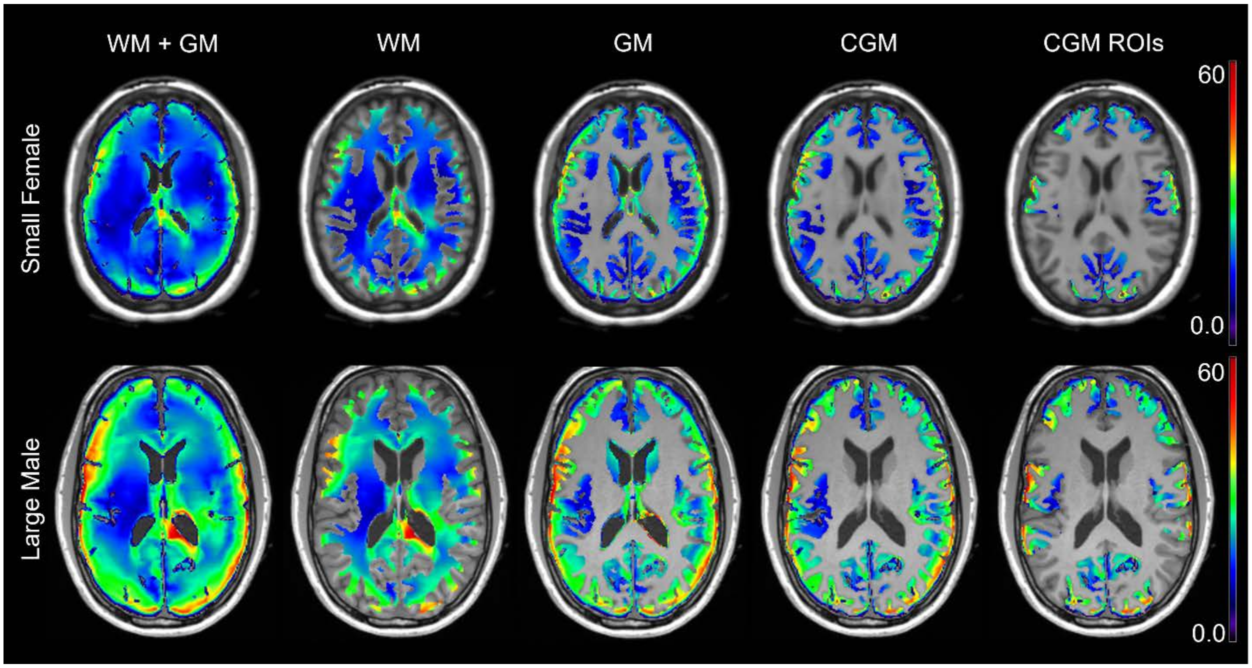

Appendix Figure F: MPSR-95 maps for a small female (ICV = 1136 cm^3) and a large male (ICV = 1802 cm^3) across the entire brain tissue, white matter, gray matter, cortical gray matter, and within the CGM regions of interest.

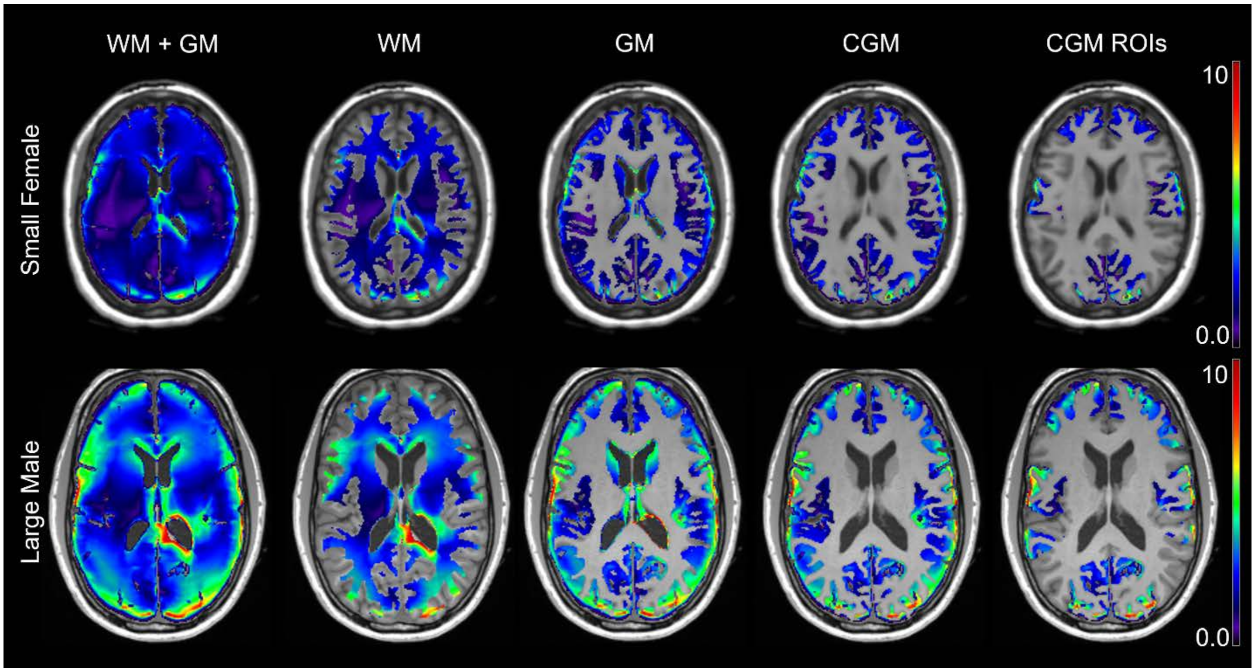

Appendix Figure G: MPSxMPSR-95 maps for a small female (ICV = 1136 cm^3) and a large male (ICV = 1802 cm^3) across the entire brain tissue, white matter, gray matter, cortical gray matter, and within the CGM regions of interest.

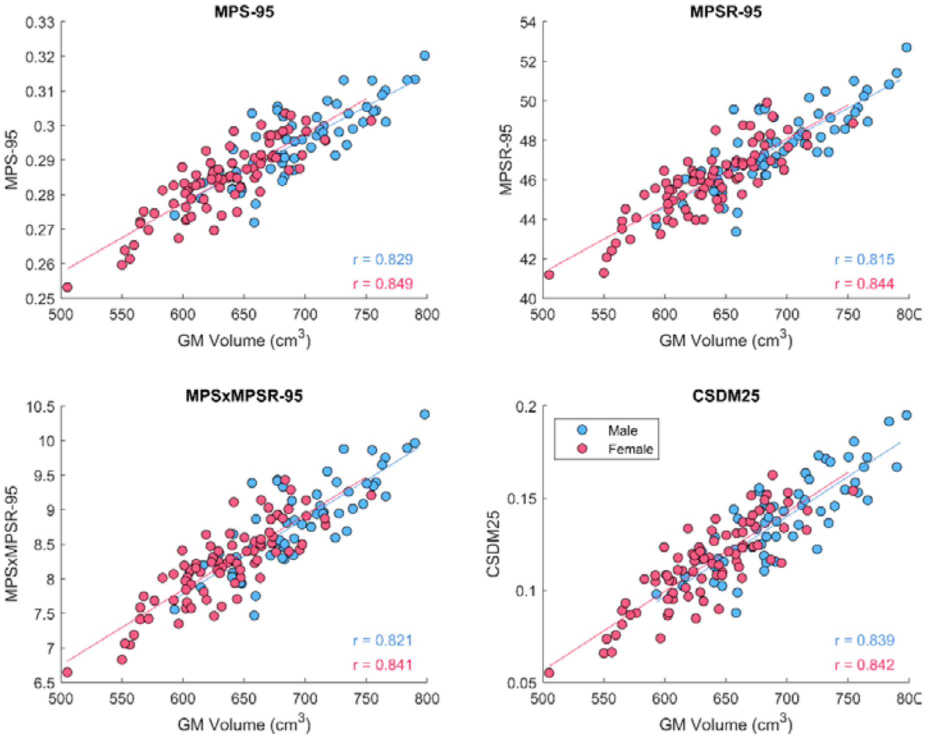

Appendix Figure H: Scatter plots between GM volume and each of the global deformation metrics for both male and female brain models. The solid lines show the linear trend lines for each of the sexes. Correlations included for the male and female data.

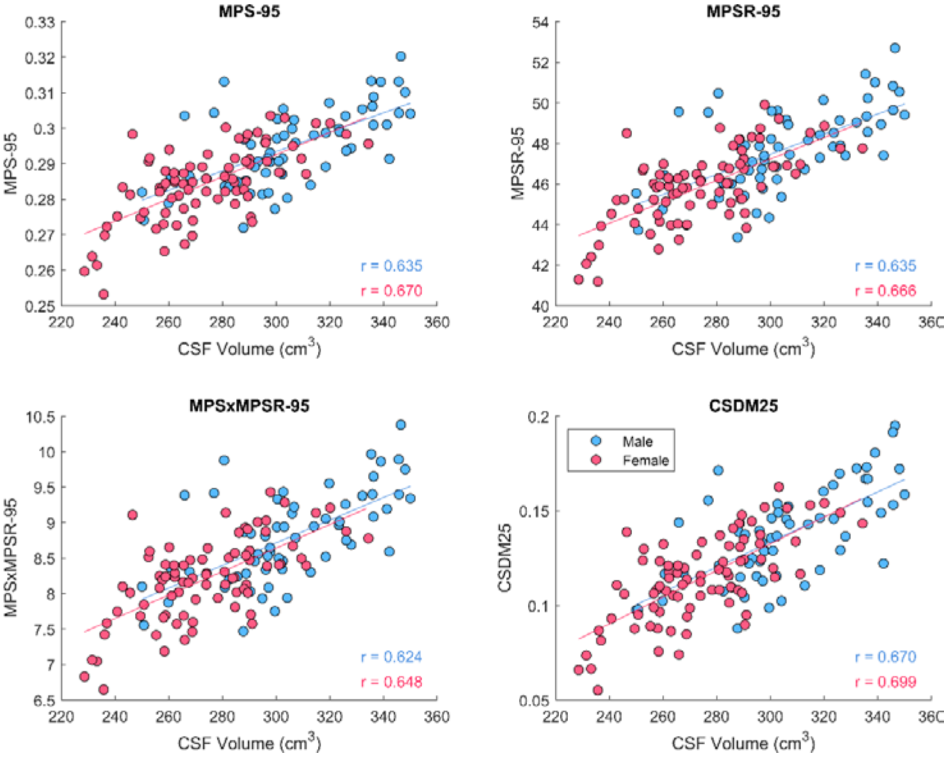

Appendix Figure I: Scatter plots between CSF volume and each of the global deformation metrics for both male and female brain models. The solid lines show the linear trend lines for each of the sexes. Correlations included for the male and female data

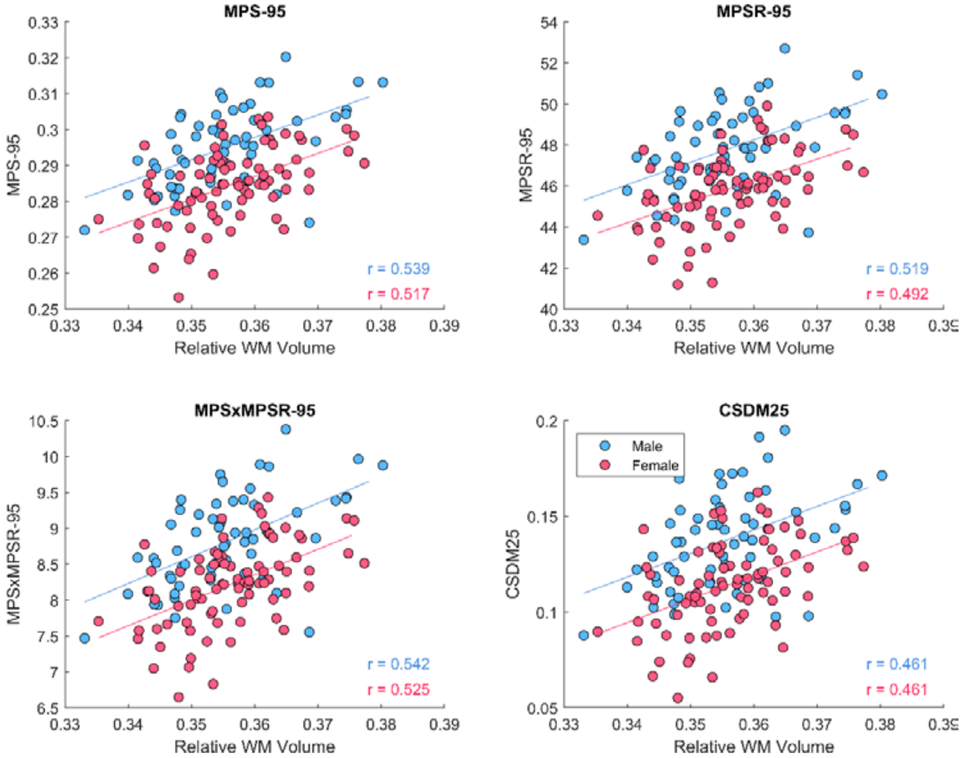

Appendix Figure J: Scatter plots between relative WM volume and each of the global deformation metrics for both male and female brain models. The solid lines show the linear trend lines for each of the sexes. Correlations included for the male and female data.

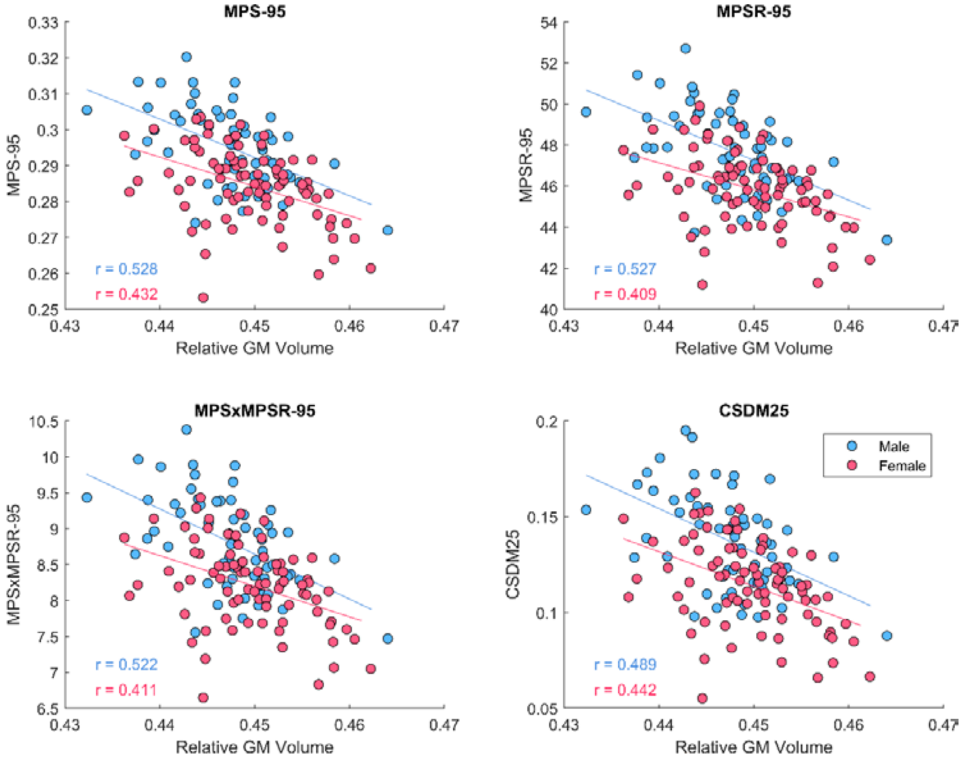

Appendix Figure K: Scatter plots between relative GM volume and each of the global deformation metrics for both male and female brain models. The solid lines show the linear trend lines for each of the sexes. Correlations included for the male and female data.

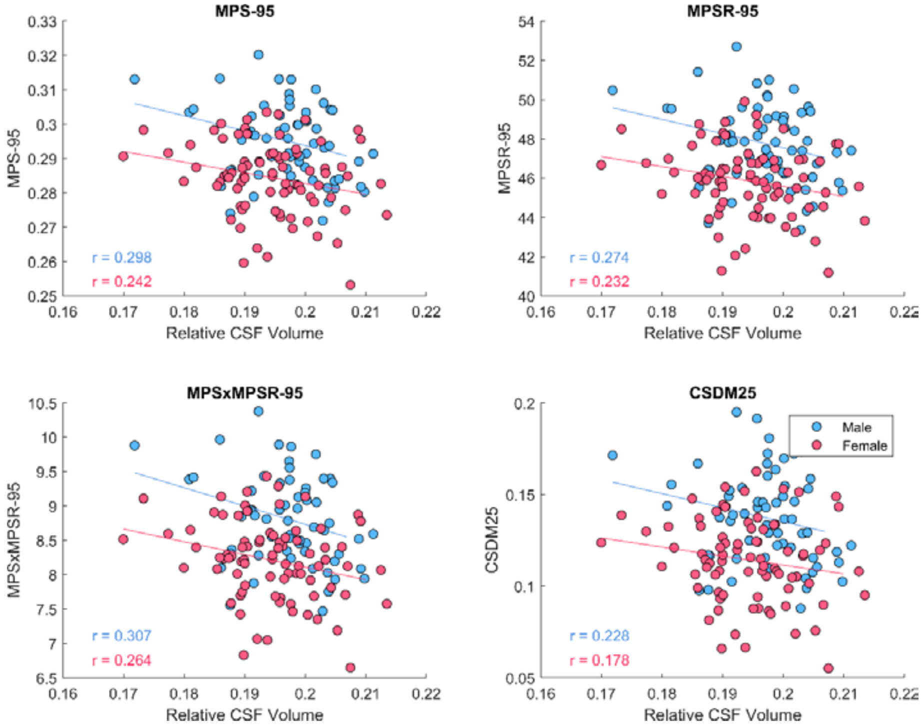

Appendix Figure L: Scatter plots between relative CSF volume and each of the global deformation metrics for both male and female brain models. The solid lines show the linear trend lines for each of the sexes. Correlations included for the male and female data.

A.4 Effect of Neuroanatomical Features on Brain Deformation Metrics Results

Appendix Table B: Estimated coefficients for the population-level effects of the multivariate Bayesian linear mixed model and the 95% credible interval (CrI) for the estimated parameter included in square brackets for each global absolute (cm^3) and relative volumes. Bolded coefficients are significant based on the CrI. Positive sex coefficients imply male response was greater.

	Intercept	Age	Sex
ICV	**1412.84** [1390.42, 1435.48]	8.63 [-8.34, 25.71]	**136.67** [101.89, 170.54]
WM Volume	**503.72** [494.54, 512.98]	**7.08** [0.30, 13.90]	**46.97** [33.14, 60.64]
GM Volume	**634.83** [625.19, 644.58]	-0.43 [-7.74, 6.95]	**58.95** [44.09, 73.76]
WM Relative Volume	**0.36** [0.35, 36]	**0.003** [0.001, 0.004]	-0.001 [-0.004, 0.002]
GM Relative Volume	**0.45** [0.45, 0.45]	**-0.003** [-0.004, -0.002]	-0.002 [-0.003, 0.000]

Appendix Table C: Estimated coefficients for the population-level effects of the multivariate Bayesian linear mixed model and the 95% credible interval (CrI) for the estimated parameter included in square brackets for absolute cortical ROI volumes (cm^3). Bolded coefficients are significant based on the CrI. Positive sex coefficients imply male response was greater.

	Intercept	Age	Sex
SFC Volume	**46.5206** [45.29, 47.77]	-1.2303 [-1.96, 0.50]	**1.61** [0.43, 2.79]
RMF Volume	**24.2168** [23.24, 25.14]	**-0.5476** [-0.98, -0.11]	**1.30** [0.50, 2.12]
PRE Volume	**21.5923** [20.66, 22.55]	**-0.7645** [-1.15, -0.36]	**0.87** [0.16 ,1.57]
LaO Volume	**20.9843** [20.14, 21.86]	-0.1568 [-0.54, 0.23]	**0.96** [0.25, 1.66]
LiO Volume	**14.322** [13.75, 14.85]	**-0.322** [-0.61, -0.03]	**0.71** [0.15, 1.28]
CN Volume	**7.2993** [6.85, 7.70]	-0.075 [-0.28, 0.13]	**0.90** [0.48, 1.31]
SPC Volume	**18.3823** [17.81, 19.03]	**-0.574** [-0.93, -.211]	0.37 [-0.35, 1.05]
POST Volume	**16.7218** [16.20, 17.25]	**-0.3666** [-0.70, -0.04]	0.37 [-0.25, 1.00]
PCN Volume	**20.2284** [19.62, 20.83]	**-0.4307** [-0.79, -0.07]	**0.90** [0.23, 1.56]

STC Volume	**30.2316** [29.18, 31.37]	**-0.6676** [-1.13, -0.21]	**1.23** [0.36, 2.08]
ITC Volume	**23.0373** [22.34, 22.89]	-0.2277 [-0.58, 0.12]	**2.36** [1.65, 3.03]
FSG Volume	**21.4719** [20.85, 22.15]	-0.2527 [-0.63, 0.12]	**0.99** [0.26, 1.68]

Appendix Table D: Estimated coefficients for the population-level effects of the multivariate Bayesian linear mixed model and the 95% credible interval (CrI) for the estimated parameter included in square brackets for relative cortical ROI volumes (cm^3/cm^3). Bolded coefficients are significant based on the CrI. Positive sex coefficients imply male response was greater.

	Intercept	Age	Sex
SFC Volume	**0.022** [0.020, 0.023]	**-0.001** [-0.0014, -0.0008]	-0.0004 [-0.001, 0.0002]
RMF Volume	**0.024** [0.023, 0.026]	**-0.001** [-0.0014, -0.0006]	0.0004 [-0.0004, 0.0013]
PRE Volume	**0.013** [0.011, 0.014]	**-0.001** [-0.0009, -0.0005]	-0.0002 [-0.0007, 0.0003]
LaO Volume	**0.018** [0.017, 0.019]	**-0.001** [-0.0009, -0.0005]	-0.0002 [-0.0009, 0.0005]
LiO Volume	**0.020** [0.019, 0.021]	**-0.001** [-0.001, -0.0001]	0.001 [-0.0002, 0.002]
CN Volume	**0.010** [0.008, 0.012]	**-0.001** [-0.001, -0.0001]	**0.002** [0.001, 0.003]
SPC Volume	**0.012** [0.011, 0.013]	**-0.001** [-0.001, -0.0002]	**-0.001** [-0.0015, -0.0002]
POST Volume	**0.012** [0.011, 0.012]	**-0.001** [-0.0008, -0.0003]	-0.0004 [-0.0009, 0.00013]
PCN Volume	**0.018** [0.017, 0.019]	**-0.001** [-0.0012, -0.0006]	-0.001 [-0.001, 0.00012]
STC Volume	**0.019** [0.019, 0.020]	**-0.0004** [-0.0007, -0.0001]	0.0004 [-0.0003, 0.001]
ITC Volume	**0.029** [0.028, 0.030]	-0.0004 [-0.0009, 0.0000]	-0.001 [-0.0015, 0.0004]
FSG Volume	**0.029** [0.027, 0.032]	**-0.001** [-0.0016, -0.0007]	-0.001 [-0.0015, 0.0005]

Appendix Table E: Estimated coefficients for the population-level effects of the multivariate Bayesian linear mixed model and the 95% credible interval (CrI) for the estimated parameter included in square brackets for absolute cortical ROI thickness (mm). Bolded coefficients are significant based on the CrI. Positive sex coefficients imply male response was greater.

	Intercept	Age	Sex

SFC Thickness	**2.42** [2.28, 2.56]	**-0.12** [-0.15, -0.09]	0.03 [-0.05, 0.10]
RMF Thickness	**2.70** [2.57, 2.84]	**-0.11** [-0.16, -0.07]	**0.13** [0.04, 0.23]
PRE Thickness	**1.42** [1.30, 1.54]	**-0.08** [-0.10, -0.05]	0.03 [-0.03, 0.08]
LaO Thickness	**1.97** [1.85, 2.09]	**-0.07** [-0.10, -0.03]	0.03 [-0.05, 0.11]
LiO Thickness	**2.27** [2.16, 2.37]	**-0.06** [-0.12, -0.00]	**0.17** [0.05,0.30]
CN Thickness	**1.15** [0.94, 1.36]	**-0.06** [-0.12, -0.01]	**0.25** [0.14, 0.36]
SPC Thickness	**1.35** [1.25, 1.43]	**-0.06** [-0.09, -0.03]	-0.06 [-0.13, 0.01]
POST Thickness	**1.31** [1.26, 1.36]	**-0.06** [-0.08, -0.03]	-0.00 [-0.06, 0.05]
PCN Thickness	**2.00** [1.92, 2.07]	**-0.10** [-0.14, -0.07]	0.00 [-0.07, 0.08]
STC Thickness	**2.17** [2.11, 2.24]	**-0.04** [-0.08, -0.01]	**0.11** [0.04, 0.19]
ITC Thickness	**3.23** [3.14, 3.32]	-0.05 [-0.10, 0.01]	0.04 [-0.07, 0.15]
FSG Thickness	**3.30** [3.05, 3.05]	**-0.12** [-0.18, -0.08]	0.039 [-0.07, 0.15]

Appendix Table F: Estimated coefficients for the population-level effects of the multivariate Bayesian linear mixed model and the 95% credible interval (CrI) for the estimated parameter included in square brackets for relative cortical ROI thickness (mm/$\sqrt[3]{ICV\ (mm^3)}$*). Bolded coefficients are significant based on the CrI. Positive sex coefficients imply male response was greater.*

	Intercept	Age	Sex
SFC Thickness	**0.0321** [0.031, 0.033]	**-0.0014** [-0.002, -0.001]	0.0002 [-0.001, 0.001]
RMF Thickness	**0.0168** [0.016, 0.017]	**-0.0007** [-0.001, -0.0004]	0.0003 [-0.0002, 0.001]
PRE Thickness	**0.0150** [0.014, 0.016]	**-0.0008** [-0.001, -0.0005]	0.00007 [-0.0004, 0.001]
LaO Thickness	**0.0145** [0.014, 0.015]	**-0.0003** [-0.001, -0.0001]	0.0002 [-0.0003, 0.0007]
LiO Thickness	**0.0099** [0.009, 0.01]	**-0.0004** [-0.0005, -0.0002]	0.0001 [-0.0003, 0.0005]
CN Thickness	**0.0050** [0.005, 0.005]	-0.0001 [-0.003, 0.00001]	**0.0005** [0.0002, 0.0008]

SPC Thickness	**0.0128** [0.012, 0.013]	**-0.0006** [-0.001, -0.0003]	-0.0003 [-0.0008, 0.0002]
POST Thickness	**0.0116** [0.011, 0.012]	**-0.0004** [-0.0006, -0.0002]	-0.0002 [-0.0006, 0.0002]
PCN Thickness	**0.0140** [0.014, 0.014]	**-0.0005** [-0.0007, -0.0003]	0.0001 [-0.0003, 0.0006]
STC Thickness	**0.0209** [0.020, 0.022]	**-0.0008** [-0.001, -0.0005]	0.0001 [-0.0005, 0.0007]
ITC Thickness	**0.0160** [0.016, 0.016]	**-0.0004** [-0.001, -0.0002]	**0.0009** [0.0005, 0.001]
FSG Thickness	**0.0149** [0.014, 0.015]	**-0.0004** [-0.0007, -0.0002]	0.00006 [-0.0004, 0.0006]

Appendix Table G: Estimated coefficients for the population-level effects of the multivariate Bayesian linear mixed model and the 95% credible interval (CrI) for the estimated parameter included in square brackets for age, sex, and each neuroanatomical features on the deformation metrics. Bolded coefficients are significant based on the CrI. Positive sex coefficients imply male response was greater.

	Intercept	Age	Sex
MPS-95	**0.289** [0.288, 0.290]	-0.0003 [-0.0011, 0.0005]	-0.0005 [-0.0024, 0.0014]
MPSR-95	**46.687** [46.483, 46.900]	0.0068 [-0.153, 0.164]	-0.043 [-0.408, 0.331]
MPSxMPSR-95	**8.471** [8.408, 8.533]	-0.0042 [-0.0526, 0.0441]	-0.0136 [-0.127, 0.098]
CSDM 25	**0.125** [0.122, 0.128]	-0.002 [-0.004, 0.0004]	-0.002 [-0.007, 0.003]

	ICV	Relative WM Volume	Relative GM Volume
MPS-95	**0.007** [0.0047, 0.0091]	**0.003** [0.002, 0.0037]	**-0.002** [-0.0027, -0.0006]
MPSR-95	**1.028** [0.604, 1.436]	**0.455** [0.310, 0.604]	**-0.359** [-0.561, -0.162]
MPSxMPSR-95	**0.364** [0.237, 0.488]	**0.172** [0.128, 0.216]	**-0.089** [-0.150, -0.028]
CSDM 25	**0.017** [0.012, 0.023]	**0.005** [0.003, 0.007]	**-0.004** [-0.006, -0.001]

	SFC Volume	RMF Volume	PRE Volume	LaO Volume
MPS-95	0.0009 [-0.0004, 0.0022]	**0.002** [0.0004, 0.0029]	0.0003 [-0.001, 0.0017]	-0.0001 [-0.0014, 0.0012]
MPSR-95	0.148 [-0.109, 0.400]	**0.280** [0.039, 0.514]	0.073 [-0.188, 0.331]	0.087 [-0.164, 0.339]

MPSxMPSR-95	0.055 [-0.024, 0.131]	**0.103** [0.0317, 0.175]	0.013 [-0.065, 0.092]	0.016 [-0.06, 0.0916]
CSDM 25	0.003 [-0.0002, 0.006]	**0.004** [0.0007, 0.007]	-0.0001 [-0.004, 0.003]	-0.0005 [-0.004, 0.003]
	LiO Volume	CN Volume	SPC Volume	POST Volume
MPS-95	0.0002 [-0.001, 0.0014]	0.0001 [-0.0012, 0.0013]	-0.0003 [-0.0013, 0.0006]	-0.0003 [-0.0013, 0.0007]
MPSR-95	0.187 [-0.0417, 0.415]	0.061 [-0.183, 0.304]	-0.125 [-0.311, 0.057]	-0.087 [-0.288, 0.116]
MPSxMPSR-95	0.031 [-0.038, 0.102]	0.005 [-0.070, 0.079]	-0.037 [-0.095, 0.019]	-0.028 [-0.088, 0.034]
CSDM 25	-0.0015 [-0.004, 0.002]	-0.0005 [-0.004, 0.003]	0.0005 [-0.002, 0.003]	-0.0019 [-0.005, 0.001]
	PCN Volume	STC Volume	ITC Volume	FSG Volume
MPS-95	**0.0016** [0.0004, 0.0028]	**-0.0017** [-0.0031, -0.0002]	0.001 [-0.0004, 0.0024]	**0.0011** [0.0001, 0.0021]
MPSR-95	**0.377** [0.147, 0.609]	**-0.329** [-0.603, -0.047]	0.115 [-0.162, 0.392]	**0.240** [0.0477, 0.431]
MPSxMPSR-95	**0.111** [0.042, 0.181]	**-0.097** [-0.180, -0.012]	0.042 [-0.040, 0.126]	**0.066** [0.008, 0.125]
CSDM 25	**0.0043** [0.001, 0.007]	-0.0036 [-0.007, 0.0001]	0.002 [-0.002, 0.006]	0.0014 [-0.001, 0.004]
	SFC Thickness	RMF Thickness	PRE Thickness	LaO Thickness
MPS-95	0.0000 [-0.0012, 0.0012]	0.0001 [-0.0009, 0.0012]	**-0.0013** [-0.0025, -0.0001]	0.0003 [-0.0007, 0.0013]
MPSR-95	-0.044 [-0.277, 0.194]	0.013 [-0.186, 0.217]	-0.127 [-0.353, 0.105]	-0.086 [-0.279, 0.110]
MPSxMPSR-95	-0.009 [-0.079, 0.063]	0.006 [-0.055, 0.067]	-0.059 [-0.128, 0.011]	-0.005 [-0.063, 0.054]
CSDM 25	-0.0011 [-0.004, 0.002]	0.0010 [-0.002, 0.004]	-0.0033 [-0.006, 0.0003]	0.0010 [-0.002, 0.004]
	LiO Thickness	CN Thickness	SPC Thickness	POST Thickness
MPS-95	0.0000 [-0.0009, 0.0009]	-0.0007 [-0.0018, 0.0004]	0.0003 [-0.0006, 0.0013]	**0.0009** [0, 0.0018]
MPSR-95	-0.008 [-0.187, 0.172]	-0.098 [-0.298, 0.105]	0.135 [-0.0494, 0.328]	0.140 [-0.040, 0.318]
MPSxMPSR-95	0.0000 [-0.056, 0.055]	-0.038 [-0.099, 0.025]	0.041 [-0.015, 0.100]	0.050 [-0.005, 0.103]
CSDM 25	0.0002 [-0.002, 0.003]	-0.0016 [-0.004, 0.001]	0.0004 [-0.002, 0.003]	**0.003** [0.001, 0.005]

	PCN Thickness	STC Thickness	ITC Thickness	FSG Thickness
MPS-95	-0.0012 [-0.0023, 0.000]	0.0000 [-0.001, 0.001]	-0.0003 [-0.0013, 0.0007]	0.0001 [-0.0009, 0.0011]
MPSR-95	**-0.228** [-0.447, -0.007]	0.046 [-0.162, 0.245]	-0.187 [-0.372, 0.004]	0.064 [-0.131, 0.258]
MPSxMPSR-95	**-0.074** [-0.140, -0.006]	0.002 [-0.060, 0.063]	0.031 [-0.089, 0.027]	0.011 [-0.047, 0.070]
CSDM 25	-0.0018 [-0.005, 0.001]	-0.003 [-0.003, 0.002]	0.0005 [-0.002, 0.003]	-0.0014 [-0.004, 0.001]

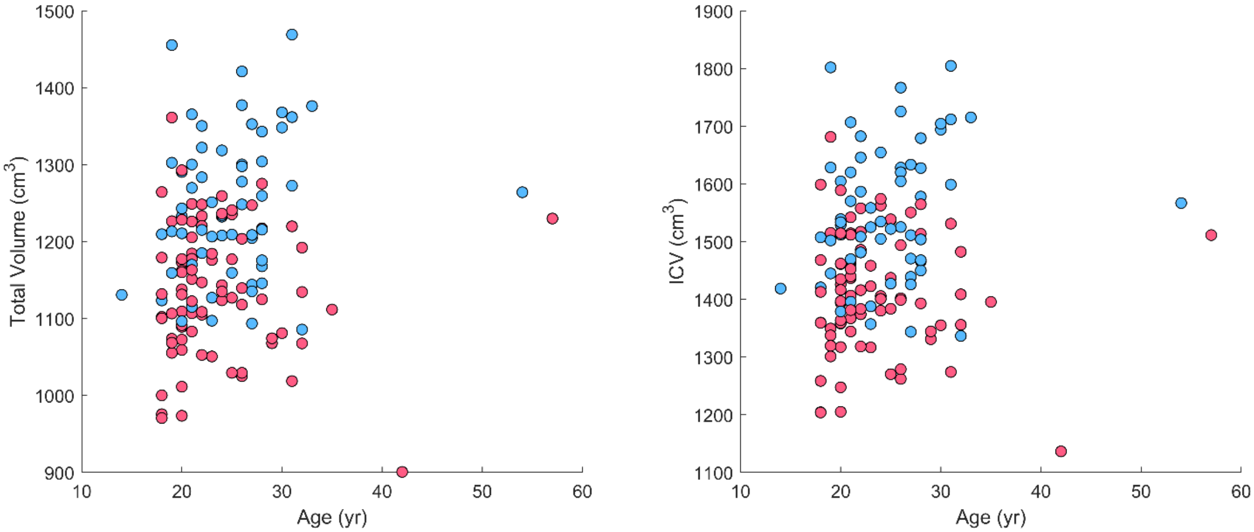

Appendix Figure M: Scatter plots for male and female total brain volume (left) and ICV (right) against age showing no correlation between volumes and subject age.

B. Material Properties

B.1 Stiffness Sensitivity

A sensitivity study was conducted to determine the effect of the number of bins used to define relative stiffnesses on the deformation response of the CAB-20MSym brain model. The original CAB-20MSym model used 10 bins to define relative stiffnesses, and the model was updated based on 1, 5, 10, 15, 20, 35, and 50 bins for relative stiffness. Using the MRE134 template shear stiffness image, the distribution of the truncated data (excluding stiffness less than the 15th percentile and greater than the 98th percentile) was divided into these updated bin numbers and normalized to the median stiffness of the MRE134 template. The CAB-20MSym calibrated median stiffness was scaled by the bin centers of these different distributions to update the heterogenous material properties throughout the brain tissue. Using a consistent neuroanatomy (CAB-20MSym template model) and the remaining material properties of the baseline CAB-20MSym model, the models with varied bin numbers were exercised using the same head kinematic input as Chapter 3 and Chapter 4.

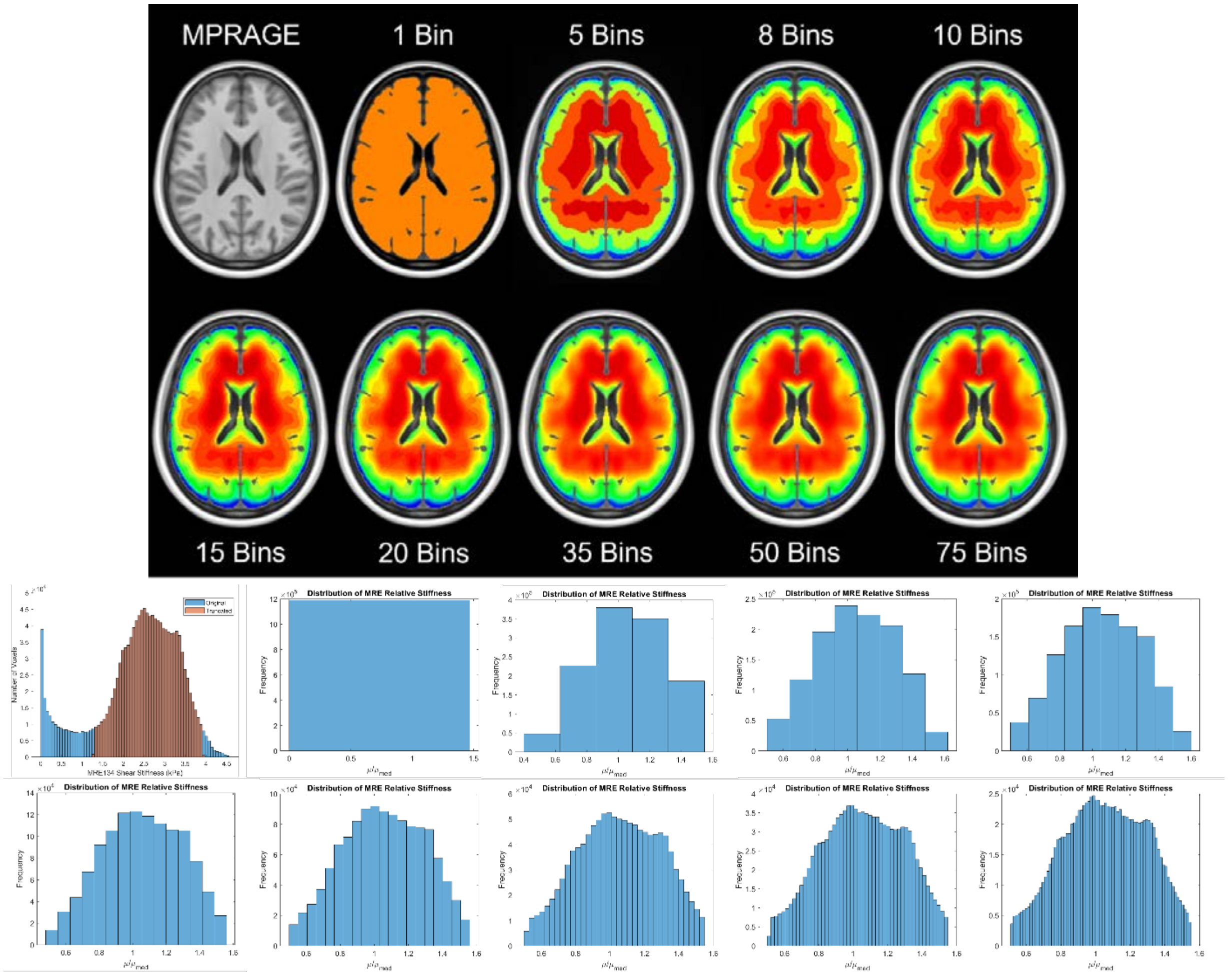

Appendix Figure N: (Top) Relative shear stiffness maps of the MRE134 template using different numbers of bins. (Bottom) Distributions of relative shear stiffnesses using different number of bins.

To determine convergence, first, the absolute change of MPS across all elements in neighboring bin-numbered models (e.g., percent change between 1 bin model and 5 bin model, then 5 bin model and 10 bin model, etc.) was calculated between the 7 simulated models. Next, the volume of elements with less than a 1% change in MPS (strain = 0.01) compared to the previous (e.g., less detailed) model was calculated. A threshold of 99% (i.e., 99% of the elements between two models did not have a change of MPS greater than 1%) was used to define convergence. The difference between the 10 bin model and the 15 bin model produced 93.4% of the elements with less than a 1% absolute difference between MPS (Appendix Figure O). The 10 bin model was the least complex model needed to converge to consistent MPS values (Appendix Figure P).

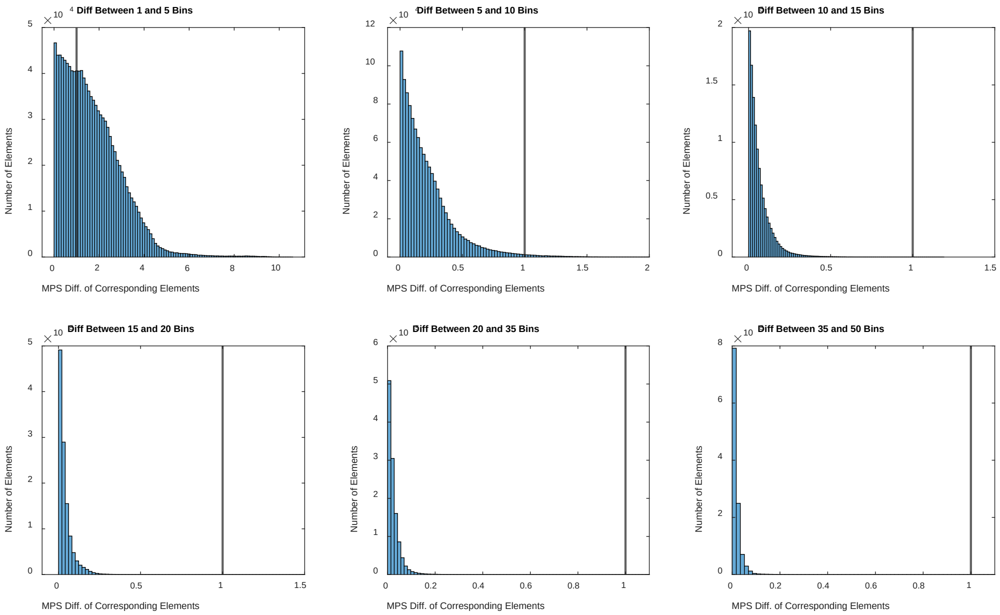

Appendix Figure O: Distributions of percent difference between corresponding elements between two neighboring models of increasing stiffness complexities. The solid line at 1% difference highlights the volume of element above and below this threshold.

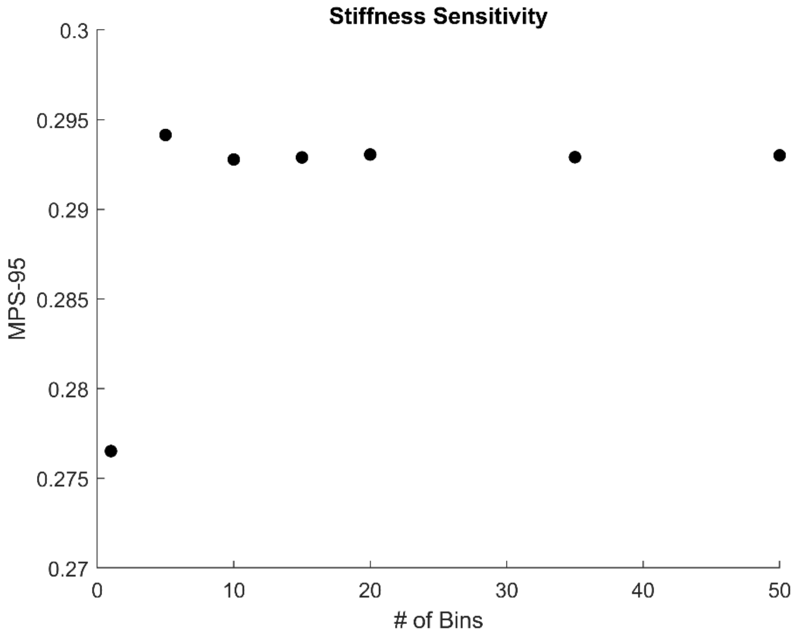

Models	% Elements Less than 1% Different
1 MU – 5 MU	34.6%
5 MU – 10 MU	98.8%
10 MU – 15 MU	**99.99%**
15 MU – 20 MU	99.99%
20 MU – 35 MU	99.99%
35 MU – 50 MU	99.99%

Appendix Figure P: (Left) MPS-95 of each of the 7 models against the number of bins used to define relative shear stiffness materials in the model. (Right) Percentage of elements with change in MPS less than 1% for increasing complexities of models.

B.2 Damping Ratio Sensitivity

A sensitivity study was conducted to determine the effect of the number of bins used to define relative damping ratio on the deformation response of the CAB-20MSym brain model. The original CAB-20MSym model used one set of relaxation parameters to define the damping response throughout the entire brain tissue. For this sensitivity, the model was updated based on 1, 5, 10, 15, 20, 35, and 50 bins for relative damping ratios. Using the MRE134 template damping ratio image, the distribution of the truncated data (excluding voxels with stiffness less than the 15th percentile and greater than the 98th percentile) was divided into these updated bin numbers and normalized to the median damping ratio of the MRE134 template (Appendix Figure Q). To define the CAB-20MSym damping response, a four-term Prony series was fit to *ex vivo* brain tissue mechanical data. Using the bin centers of these relative damping ratios, the tan(delta) response of the *ex vivo* mechanical response across multiple frequencies was scaled, and new relaxation parameters were fit to these scaled tan(delta) curves (Appendix Figure R). Using a consistent neuroanatomy (CAB-20MSym template model) and the remaining material properties of the baseline CAB-20MSym model, the models with varied bin numbers were exercised using the same head kinematic input as Chapter 3 and Chapter 4.

The same convergence thresholds were applied as above in the stiffness sensitivity study. The percent of elements with less than a 1% absolute MPS difference between the 10 bin and 15 bin models was greater than 99%, so the 10 bin damping ratio model was selected (Appendix Figure S).

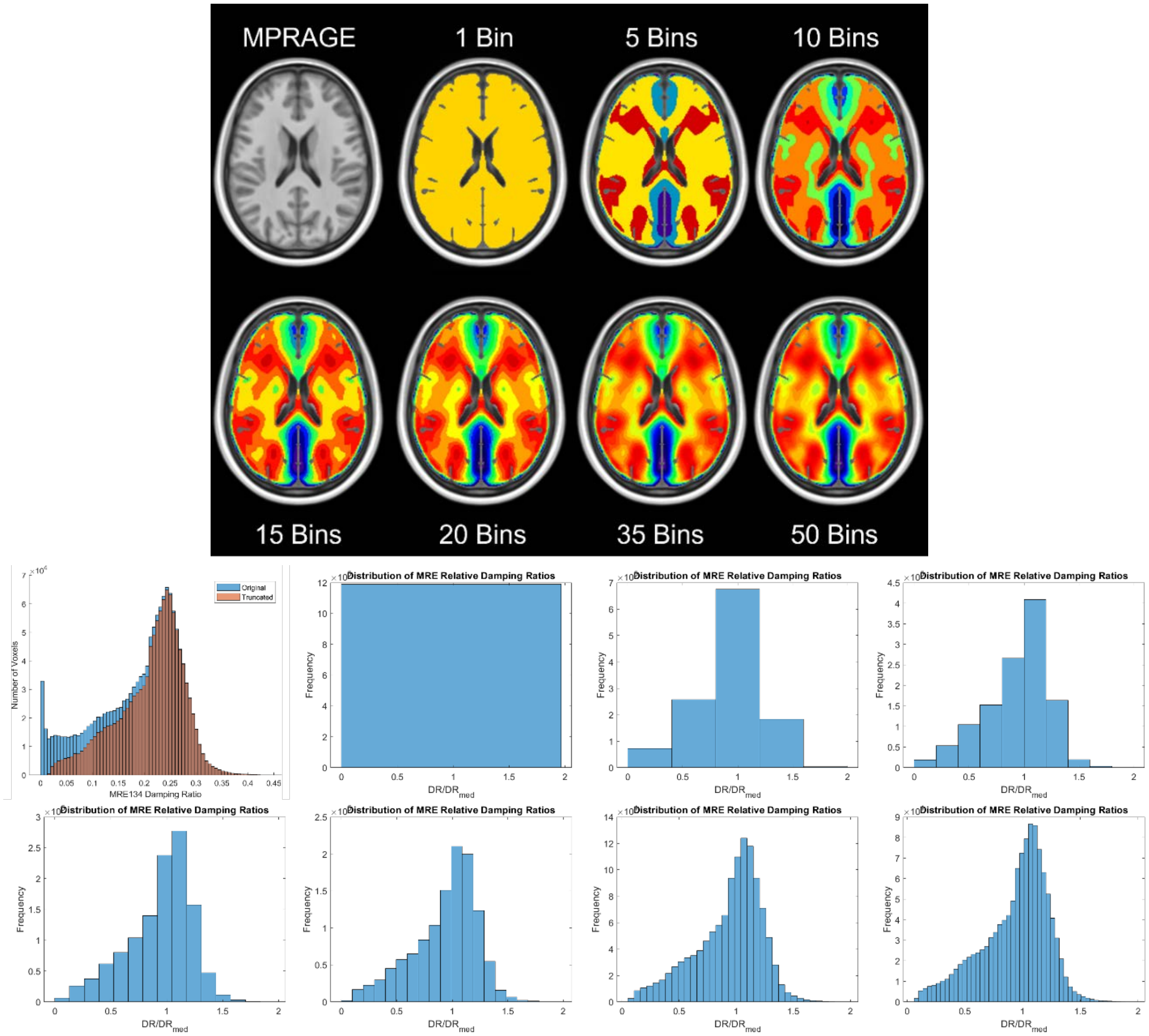

Appendix Figure Q: (Top) Relative damping ratios maps of the MRE134 template using different numbers of bins. (Bottom) Distributions of relative damping ratios using different number of bins.

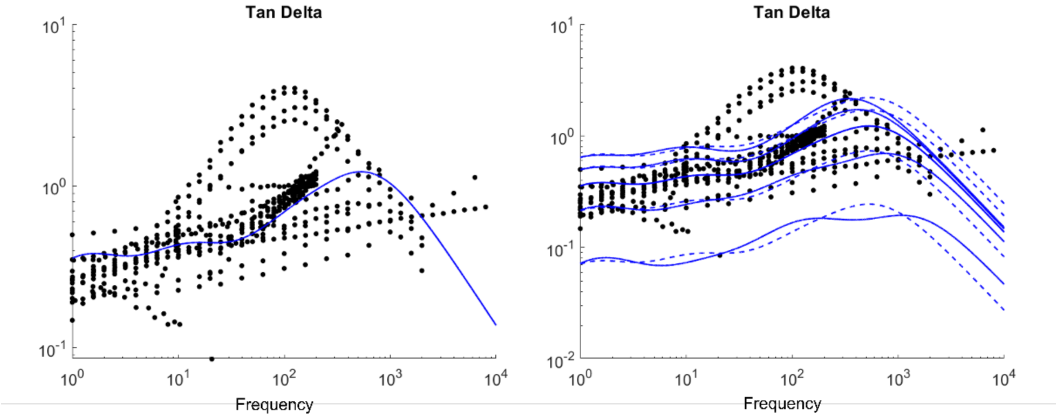

Appendix Figure R: Scaled (dashed lines) and refit tan(delta) responses (solid lines) for one bin (left) and 5 bins (right) used to define damping ratios throughout the FE brain model.

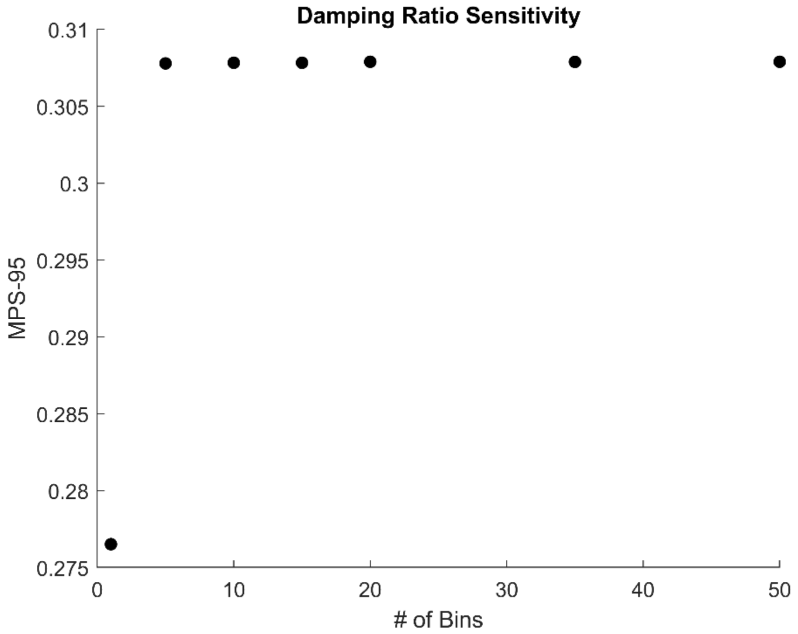

Models	**% Elements Less than 1% Different**
1 DR – 5 DR	45.8%
5 DR – 10 DR	93.4%
10 DR – 15 DR	**99.6%**
15 DR – 20 DR	99.99%
20 DR – 35 DR	99.99%
35 DR – 50 DR	100%

Appendix Figure S: (Left) MPS-95 of each of the 9 models against the number of bins used to define relative damping ratio materials in the model. (Right) Percentage of elements with less than 1% MPS change for increasing complexities of models.

B.3 Additional Methods Figures

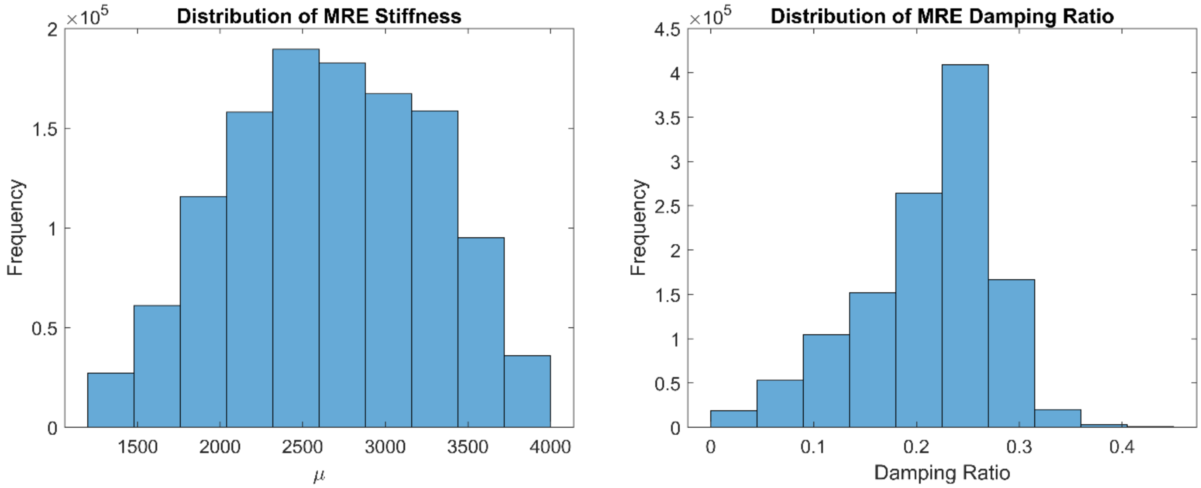

Appendix Figure T: Absolute measures of shear stiffness (left) and damping ratio (right) distributions for the MRE134 template in the 10 bins used to define relative properties.

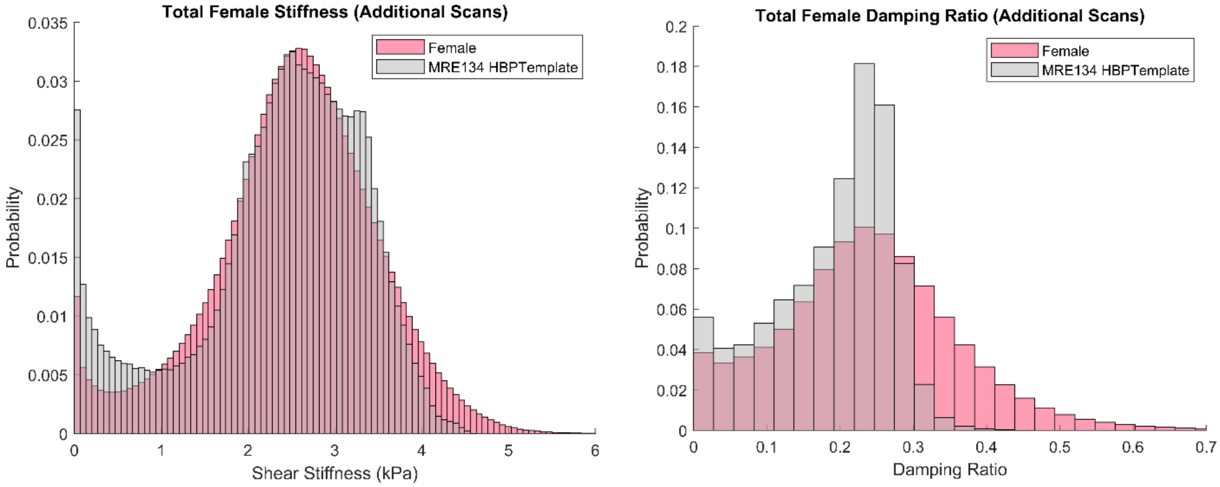

Appendix Figure U: Stiffness (left) and damping ratio (right) distributions for the MRE134 template (gray) compared to the distribution of all the voxels in the female subject scans (pink) not included in the development in the MRE134 template but included in this cohort (i.e., Bayly and Johnson 2021 subjects). Distributions are normalized to represent the probability of a single voxel falling within one bin, and bin widths are consistent between the population distribution and the MRE134 template distribution.

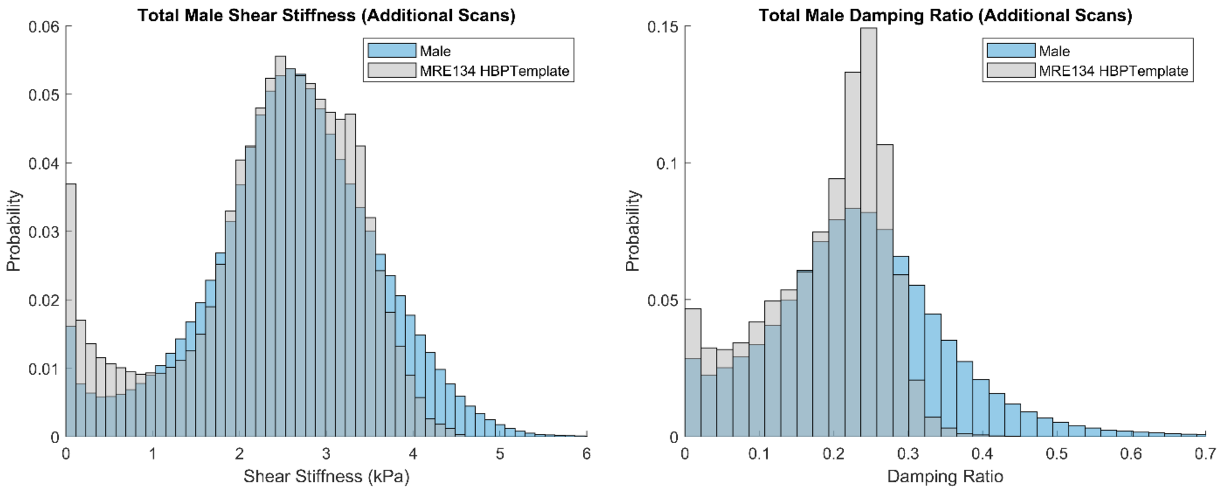

Appendix Figure V: Stiffness (left) and damping ratio (right) distributions for the MRE134 template (gray) compared to the distribution of all the voxels in the male subject scans (blue) not included in the development in the MRE134 template but included in this cohort (i.e., Bayly and Johnson 2021 subjects). Distributions are normalized to represent the probability of a single voxel falling within one bin, and bin widths are consistent between the population distribution and the MRE134 template distribution.

B.4 Statistical Models

The equations for the multivariate Bayesian linear mixed model to determine the effect of sex and age on each of the material property features, accounting for a random study effect.

$$Y_{ij}^{Stiff} = \left(\beta_0^{Stiff} + u_{j0}^{Stiff}\right) + \beta_1^{Stiff}\left(scale\left(Age_{ij}\right)\right) + \beta_2^{Stiff}\left(Sex_{ij}\right) + \epsilon_{\mathrm{ij}}^{Stiff}$$

$$Y_{ij}^{Stiff\ WM} = \left(\beta_0^{Stiff\ WM} + u_{j0}^{Stiff\ WM}\right) + \beta_1^{Stiff\ WM}\left(scale\left(Age_{ij}\right)\right) + \beta_2^{Stiff\ WM}\left(Sex_{ij}\right) + \epsilon_{\mathrm{ij}}^{Stiff\ WM}$$

$$Y_{ij}^{Stiff\ GM} = \left(\beta_0^{Stiff\ GM} + u_{j0}^{Stiff\ GM}\right) + \beta_1^{Stiff\ GM}\left(scale\left(Age_{ij}\right)\right) + \beta_2^{Stiff\ GM}\left(Sex_{ij}\right) + \epsilon_{\mathrm{ij}}^{Stiff\ GM}$$

$$Y_{ij}^{Stiff\ IQR} = \left(\beta_0^{Stiff\ IQR} + u_{j0}^{Stiff\ IQR}\right) + \beta_1^{Stiff\ IQR}\left(scale\left(Age_{ij}\right)\right) + \beta_2^{Stiff\ IQR}\left(Sex_{ij}\right) + \epsilon_{\mathrm{ij}}^{Stiff\ IQR}$$

$$Y_{ij}^{DR} = \left(\beta_0^{DR} + u_{j0}^{DR}\right) + \beta_1^{DR}\left(scale\left(Age_{ij}\right)\right) + \beta_2^{DR}\left(Sex_{ij}\right) + \epsilon_{\mathrm{ij}}^{DR}$$

$$Y_{ij}^{DR\ WM} = \left(\beta_0^{DR\ WM} + u_{j0}^{DR\ WM}\right) + \beta_1^{DR\ WM}\left(scale\left(Age_{ij}\right)\right) + \beta_2^{DR\ WM}\left(Sex_{ij}\right) + \epsilon_{\mathrm{ij}}^{DR\ WM}$$

$$Y_{ij}^{DR\ GM} = \left(\beta_0^{DR\ GM} + u_{j0}^{DR\ GM}\right) + \beta_1^{DR\ GM}\left(scale\left(Age_{ij}\right)\right) + \beta_2^{DR\ GM}\left(Sex_{ij}\right) + \epsilon_{\mathrm{ij}}^{DR\ GM}$$

$$Y_{ij}^{DR\ IQR} = \left(\beta_0^{DR\ IQR} + u_{j0}^{DR\ IQR}\right) + \beta_1^{DR\ IQR}\left(scale\left(Age_{ij}\right)\right) + \beta_2^{DR\ IQR}\left(Sex_{ij}\right) + \epsilon_{\mathrm{ij}}^{DR\ IQR}$$

$$Y_{ij}^{Quad\ 1} = \left(\beta_0^{Quad\ 1} + u_{j0}^{Quad\ 1}\right) + \beta_1^{Quad\ 1}\left(scale\left(Age_{ij}\right)\right) + \beta_2^{Quad\ 1}\left(Sex_{ij}\right) + \epsilon_{\mathrm{ij}}^{Quad\ 1}$$

$$Y_{ij}^{Quad\ 2} = \left(\beta_0^{Quad\ 2} + u_{j0}^{Quad\ 2}\right) + \beta_1^{Quad\ 2}\left(scale\left(Age_{ij}\right)\right) + \beta_2^{Quad\ 2}\left(Sex_{ij}\right) + \epsilon_{\mathrm{ij}}^{Quad\ 2}$$

$$Y_{ij}^{Quad\ 4} = \left(\beta_0^{Quad\ 4} + u_{j0}^{Quad\ 4}\right) + \beta_1^{Quad\ 4}\left(scale\left(Age_{ij}\right)\right) + \beta_2^{Quad\ 4}\left(Sex_{ij}\right) + \epsilon_{\mathrm{ij}}^{Quad\ 4}$$

The equations for the multivariate Bayesian linear mixed model to predict deformation metrics based on independent material property features, age, and sex accounting for a random study effect.

$$
\begin{aligned}
Y_{ij}^{MPS-95} = {} & \left(\beta_0^{MPS-95} + u_{j0}^{MPS-95}\right) + \beta_1^{MPS-95}\left(Age_{ij}\right) + \beta_2^{MPS-95}\left(Sex_{ij}\right) + \beta_3^{MPS-95}\left(Stiff_{ij}\right) \\
& + \beta_4^{MPS-95}\left(Stiff\ WM_{ij}\right) + \beta_5^{MPS-95}\left(Stiff\ GM_{ij}\right) + \beta_6^{MPS-95}\left(Stiff\ IQR_{ij}\right) \\
& + \beta_7^{MPS-95}\left(DR_{ij}\right) + \beta_8^{MPS-95}\left(DR\ WM_{ij}\right) + \beta_9^{MPS-95}\left(DR\ GM_{ij}\right) \\
& + \beta_{10}^{MPS-95}\left(DR\ IQR_{ij}\right) + \beta_{11}^{MPS-95}\left(Quad\ 1_{ij}\right) + \beta_{12}^{MPS-95}\left(Quad\ 2_{ij}\right) \\
& + \beta_{13}^{MPS-95}\left(Quad\ 4_{ij}\right) + \epsilon_{\mathrm{ij}}^{MPS-95}
\end{aligned}
$$

$$
\begin{aligned}
Y_{ij}^{MPSR-95} = {} & \left(\beta_0^{MPSR-95} + u_{j0}^{MPSR-95}\right) + \beta_1^{MPSR-95}\left(Age_{ij}\right) + \beta_2^{MPSR-95}\left(Sex_{ij}\right) + \beta_3^{MPSR-95}\left(Stiff_{ij}\right) \\
& + \beta_4^{MPSR-95}\left(Stiff\ WM_{ij}\right) + \beta_5^{MPSR-95}\left(Stiff\ GM_{ij}\right) + \beta_6^{MPSR-95}\left(Stiff\ IQR_{ij}\right) \\
& + \beta_7^{MPSR-95}\left(DR_{ij}\right) + \beta_8^{MPSR-95}\left(DR\ WM_{ij}\right) + \beta_9^{MPSR-95}\left(DR\ GM_{ij}\right) \\
& + \beta_{10}^{MPSR-95}\left(DR\ IQR_{ij}\right) + \beta_{11}^{MPSR-95}\left(Quad\ 1_{ij}\right) + \beta_{12}^{MPSR-95}\left(Quad\ 2_{ij}\right) \\
& + \beta_{13}^{MPSR-95}\left(Quad\ 4_{ij}\right) + \epsilon_{\mathrm{ij}}^{MPSR-95}
\end{aligned}
$$

$$
\begin{aligned}
Y_{ij}^{MPSxMPSR-95} = {} & \left(\beta_0^{MPSxMPSR-95} + u_{j0}^{MPSxMPSR-95}\right) + \beta_1^{MPSxMPSR-95}\left(Age_{ij}\right) + \beta_2^{MPSxMPSR-95}\left(Sex_{ij}\right) \\
& + \beta_3^{MPSxMPSR-95}\left(Stiff_{ij}\right) + \beta_4^{MPSxMPSR-95}\left(Stiff\ WM_{ij}\right) \\
& + \beta_5^{MPSxMPSR-95}\left(Stiff\ GM_{ij}\right) + \beta_6^{MPSxMPSR-95}\left(Stiff\ IQR_{ij}\right) \\
& + \beta_7^{MPSxMPSR-95}\left(DR_{ij}\right) + \beta_8^{MPSxMPSR-95}\left(DR\ WM_{ij}\right) + \beta_9^{MPSxMPSR-95}\left(DR\ GM_{ij}\right) \\
& + \beta_{10}^{MPSxMPSR-95}\left(DR\ IQR_{ij}\right) + \beta_{11}^{MPSxMPSR-95}\left(Quad\ 1_{ij}\right) \\
& + \beta_{12}^{MPSxMPSR-95}\left(Quad\ 2_{ij}\right) + \beta_{13}^{MPSxMPSR-95}\left(Quad\ 4_{ij}\right) + \epsilon_{\mathrm{ij}}^{MPSxMPSR-95}
\end{aligned}
$$

$$
\begin{aligned}
Y_{ij}^{CSDM-25} = {} & \left(\beta_0^{CSDM-25} + u_{j0}^{CSDM-25}\right) + \beta_1^{CSDM-25}\left(Age_{ij}\right) + \beta_2^{CSDM-25}\left(Sex_{ij}\right) + \beta_3^{CSDM-25}\left(Stiff_{ij}\right) \\
& + \beta_4^{CSDM-25}\left(Stiff\ WM_{ij}\right) + \beta_5^{CSDM-25}\left(Stiff\ GM_{ij}\right) + \beta_6^{CSDM-25}\left(Stiff\ IQR_{ij}\right) \\
& + \beta_7^{CSDM-25}\left(DR_{ij}\right) + \beta_8^{CSDM-25}\left(DR\ WM_{ij}\right) + \beta_9^{CSDM-25}\left(DR\ GM_{ij}\right) \\
& + \beta_{10}^{CSDM-25}\left(DR\ IQR_{ij}\right) + \beta_{11}^{CSDM-25}\left(Quad\ 1_{ij}\right) + \beta_{12}^{CSDM-25}\left(Quad\ 2_{ij}\right) \\
& + \beta_{13}^{CSDM-25}\left(Quad\ 4_{ij}\right) + \epsilon_{\mathrm{ij}}^{CSDM-25}
\end{aligned}
$$

B.5 Biomechanical Factors Analysis

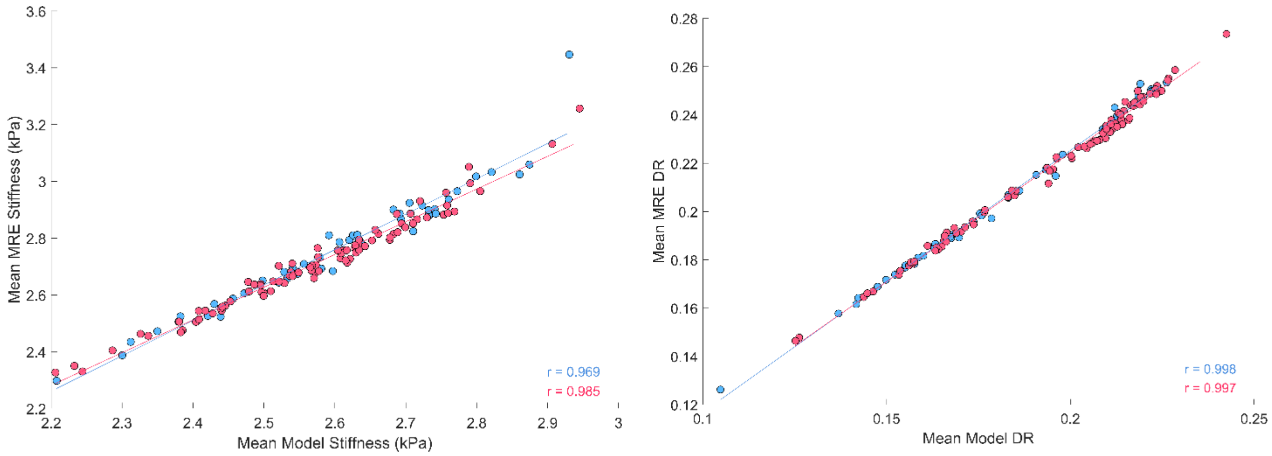

Appendix Figure W: Scatter plots showing relationships between the mean MRE stiffness and mean model stiffness (left) and the mean MRE damping ratio and mean model damping ratio (right) for both male (blue) and female (pink) models.

Appendix Table H: Estimated coefficients for the population-level effects of the multivariate Bayesian linear mixed model and the 95% credible interval (CrI) for the estimated parameter included in square brackets for each material property biomechanical factor. Bolded coefficients are significant based on the CrI. Positive sex coefficients imply male response was greater.

Biomechanical Factor	Intercept	Age	Sex
Mean Stiffness	**2.707** [2.6, 2.8]	**-0.073** [-0.1, -0.05]	**0.082** [0.03, 0.14]
Mean Stiffness (GM)	**2.462** [2.3, 2.6]	**-0.082** [-0.11, -0.05]	**0.086** [0.03, 0.14]
Mean Stiffness (WM)	**2.975** [2.8, 3.1]	**-0.064** [-0.1, -0.04]	**0.071** [0.01, 0.13]
Mean DR	**0.222** [0.16, 0.28]	**0.002** [0.0, 0.004]	**-0.006** [-0.01, -0.002]
Mean DR (GM)	**0.215** [0.16, 0.27]	**0.004** [0.001, 0.01]	-0.005 [-0.01, 0.00]
Mean DR (WM)	**0.231** [0.17, 0.29]	0.000 [-0.002, 0.002]	**-0.007** [-0.01, -0.003]
Quad. 1 Percentage	**31.95** [17.3, 47.0]	**1.248** [0.35, 2.13]	-1.105 [-2.8, 0.62]
Quad. 2 Percentage	**20.824** [7.3, 34.2]	**2.435** [1.5, 3.3]	**-2.31** [-4.01, -0.61]

Quad. 4 Percentage	**16.05** [2.8, 29.5]	**-1.704** [-2.4, -1.0]	-0.363 [-1.62, 0.91]
IQR Stiffness	**1.068** [0.88, 1.2]	-0.006 [-0.03, 0.02]	0.028 [-0.02, 0.07]
IQR DR	**0.126** [0.08, 0.17]	**0.003** [0.001, 0.01]	**-0.005** [-0.01, -0.001]

Appendix Table I: Estimated coefficients for the group-level (study) effects of the multivariate Bayesian linear mixed model and the 95% credible interval (CrI) included in square brackets for each material property.

Biomechanical Factor	Study Standard Deviation Estimate
Mean Stiffness	**0.068** [0.002, 0.3]
Mean Stiffness (GM)	**0.115** [0.03, 0.4]
Mean Stiffness (WM)	**0.085** [0.01, 0.33]
Mean DR	**0.044** [0.02, 0.1]
Mean DR (GM)	**0.042** [0.02, 0.1]
Mean DR (WM)	**0.045** [0.02, 0.1]
Quad. 1 Percentage	**14.326** [4.8, 37.1]
Quad. 2 Percentage	**11.994** [3.8, 33.7]
Quad. 4 Percentage	**13.027** [4.2, 35.6]
IQR Stiffness	**0.117** [0.03, 0.4]
IQR DR	**0.034** [0.01, 0.09]

B.6 Biomechanical Factors and Deformation Analysis

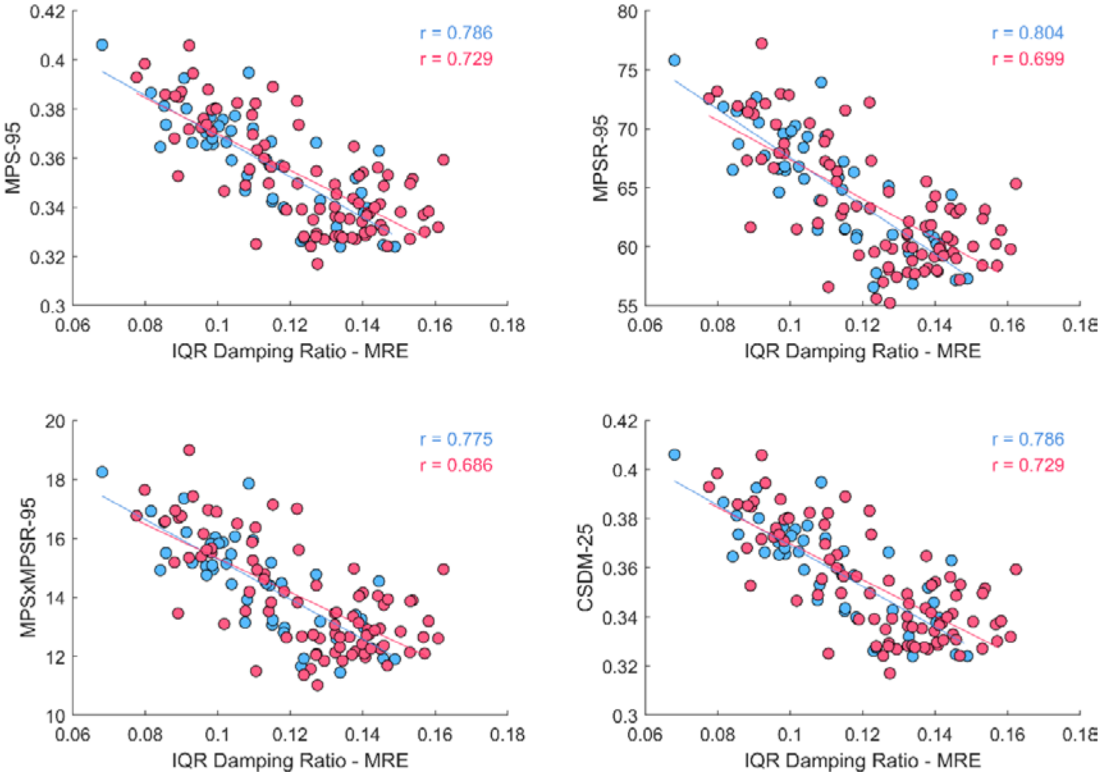

Appendix Figure X: Scatter plots for the deformation metrics against the IQR damping ratio for male (blue) and female (pink) models. Linear regression for both male and female models shown, with correlations provided.

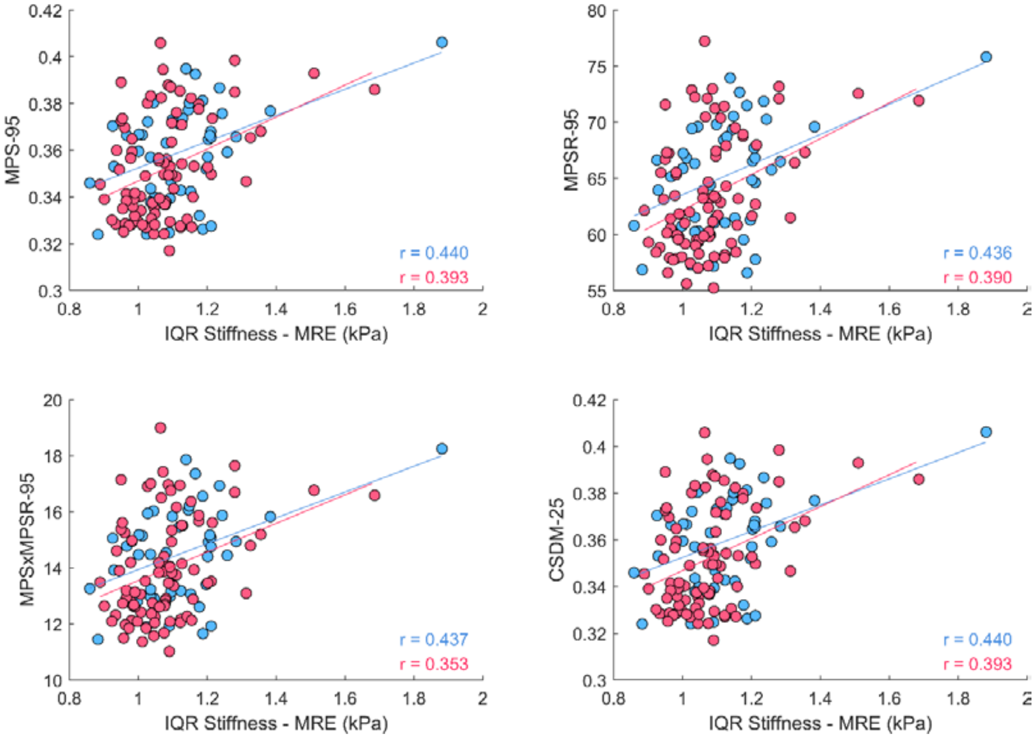

Appendix Figure Y: Scatter plots for the deformation metrics against the IQR stiffness for male (blue) and female (pink) models. Linear regression for both male and female models shown, with correlations provided.

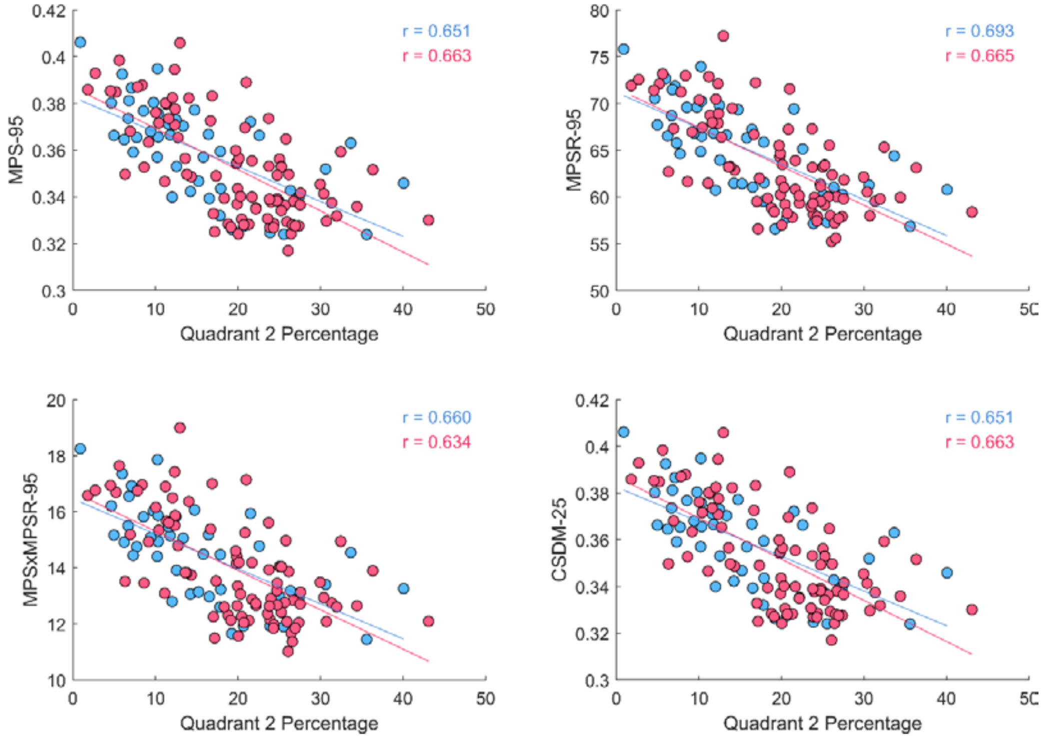

Appendix Figure Z: Scatter plots for the deformation metrics against the percentage of brain volume in quadrant 2 for male (blue) and female (pink) models. Linear regression for both male and female models shown, with correlations provided.

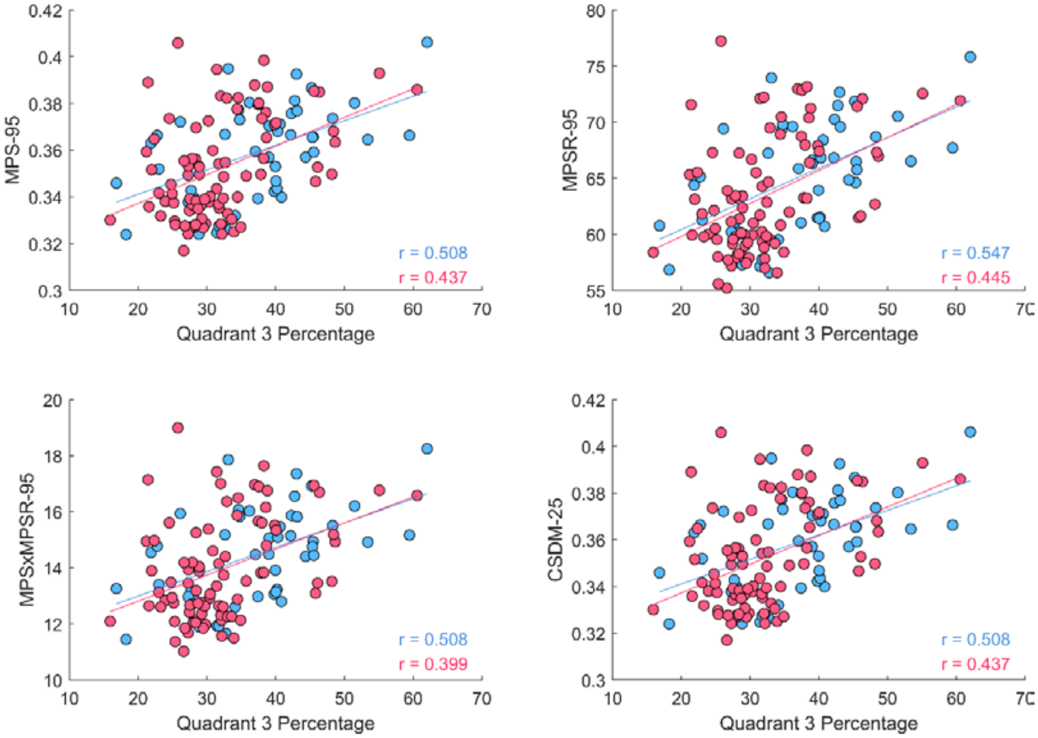

Appendix Figure AA: Scatter plots for the deformation metrics against the percentage of brain volume in quadrant 3 for male (blue) and female (pink) models. Linear regression for both male and female models shown, with correlations provided.

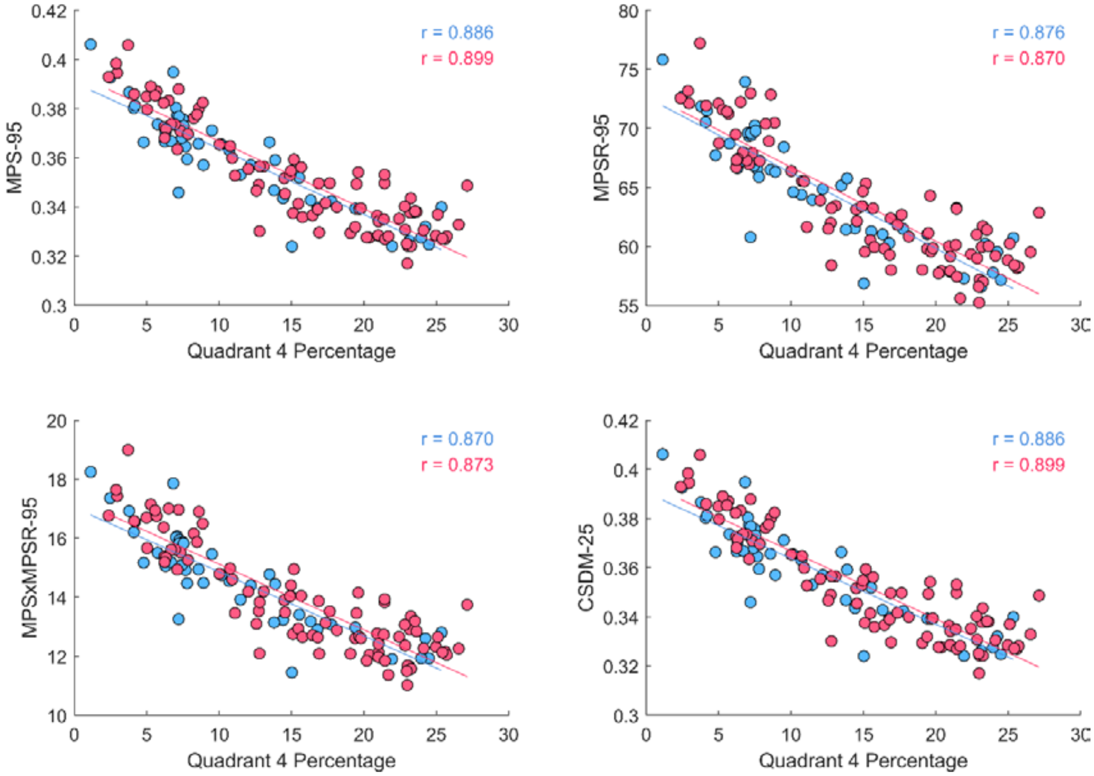

Appendix Figure BB: Scatter plots for the deformation metrics against the percentage of brain volume in quadrant 4 for male (blue) and female (pink) models. Linear regression for both male and female models shown, with correlations provided.

Appendix Table J: Estimated coefficients for the population-level effects of the multivariate Bayesian linear mixed model and the 95% credible interval (CrI) for the estimated parameter included in square brackets for age, sex, and each material property feature on the deformation metrics. Bolded coefficients are significant based on the CrI. Positive sex coefficients imply male response was greater.

	Intercept	Age	Sex
MPS-95	**0.36** [0.349, 0.36]	**0.002** [0, 0.003]	-0.001 [-0.002, 0.001]
MPSR-95	**64.05** [62.62, 65.35]	**0.308** [0.008, 0.618]	-0.124 [-0.66, 0.412]
MPSxMPSR-95	**14.17** [13.43, 14.87]	0.105 [-0.002, 0.212]	-0.074 [-0.262, 0.114]
CSDM 25	**0.30** [0.23, 0.39]	**0.005** [0.001, 0.008]	-0.003 [-0.009, 0.003]

	Stiffness Mean	Stiffness GM	Stiffness WM	Stiffness ICV
MPS-95	**-0.049** [-0.088, -0.01]	**0.028** [0.007, 0.049]	**0.022** [0.003, 0.042]	**0.003** [0.002, 0.005]
MPSR-95	-6.58 [-13.32, 0.052]	**4.32** [0.698, 7.912]	2.41 [-0.996, 5.83]	**0.744** [0.23, 1.25]
MPSxMPSR-95	**-3.681** [-6.51, -0.89]	**2.239** [0.722, 3.78]	**1.602** [0.185, 3.017]	**0.269** [0.089, 0.448]

CSDM 25	-0.032 [-0.196,0.132]	0.044 [-0.042,0.131]	0.003 [-0.078,0.083]	**0.013** [0.007, 0.019]

	DR Mean	DR GM	DR WM	DR ICV
MPS-95	0.017 [-0.072, 0.103]	-0.02 [-0.066, 0.027]	-0.017 [-0.06, 0.026]	**0.007** [0.005, 0.009]
MPSR-95	-2.601 [-10.29, 5.05]	-0.877 [-5.049, 3.287]	-1.22 [-5.13, 2.70]	**2.141** [1.47,2.78]
MPSxMPSR-95	0.479 [-4.42, 5.42]	-0.899 [-3.57, 1.699]	-1.17 [-3.66, 1.23]	**0.744** [0.546, 0.994]
CSDM 25	-0.204 [0.165, -0.525]	0.072 [-0.098, 0.243]	0.042 [-0.115, 0.201]	**0.012** [0.005, 0.019]

	Quad. 1 Percent.	Quad. 2 Percent.	Quad. 4 Percent.
MPS-95	**0.015** [0.01, 0.02]	0.004 [-0.001, 0.009]	0.002 [-0.002, 0.007]
MPSR-95	**3.506** [2.106, 4.855]	0.396 [-1.12, 1.92]	0.453 [-0.85, 1.74]
MPSxMPSR-95	**1.464** [0.979, 1.927]	0.17 [-0.358, 0.698]	0.22 [-0.229, 0.673]
CSDM 25	**0.068** [0.053, 0.084]	**0.031** [0.014, 0.049]	0.003 [-0.012, 0.018]

C. Head Kinematics

C.1 Corrected Head Kinematic Data Traces

C.1.1 Gold Standard 2 Traces

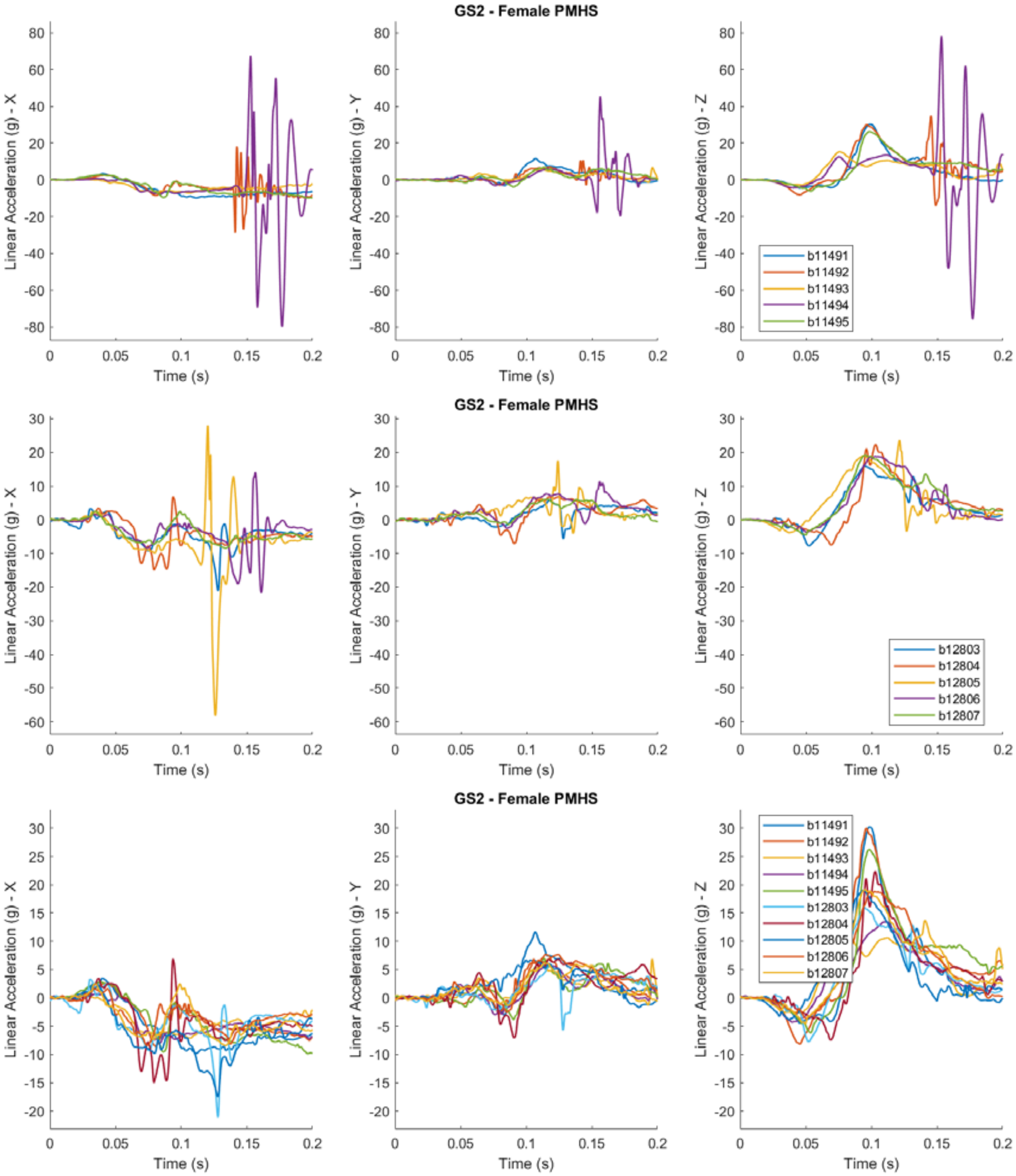

Appendix Figure CC: Original (top) and corrected (bottom) linear acceleration traces for Gold Standard 2 female PMHS kinematics. Corrected signals: b11492 (0.13 s to 0.23 s), b11494 (0.1375 s to 0.23 s), b12805 (0.114 s to 0.1501 s), and b12806 (0.135 s to 0.2 s).

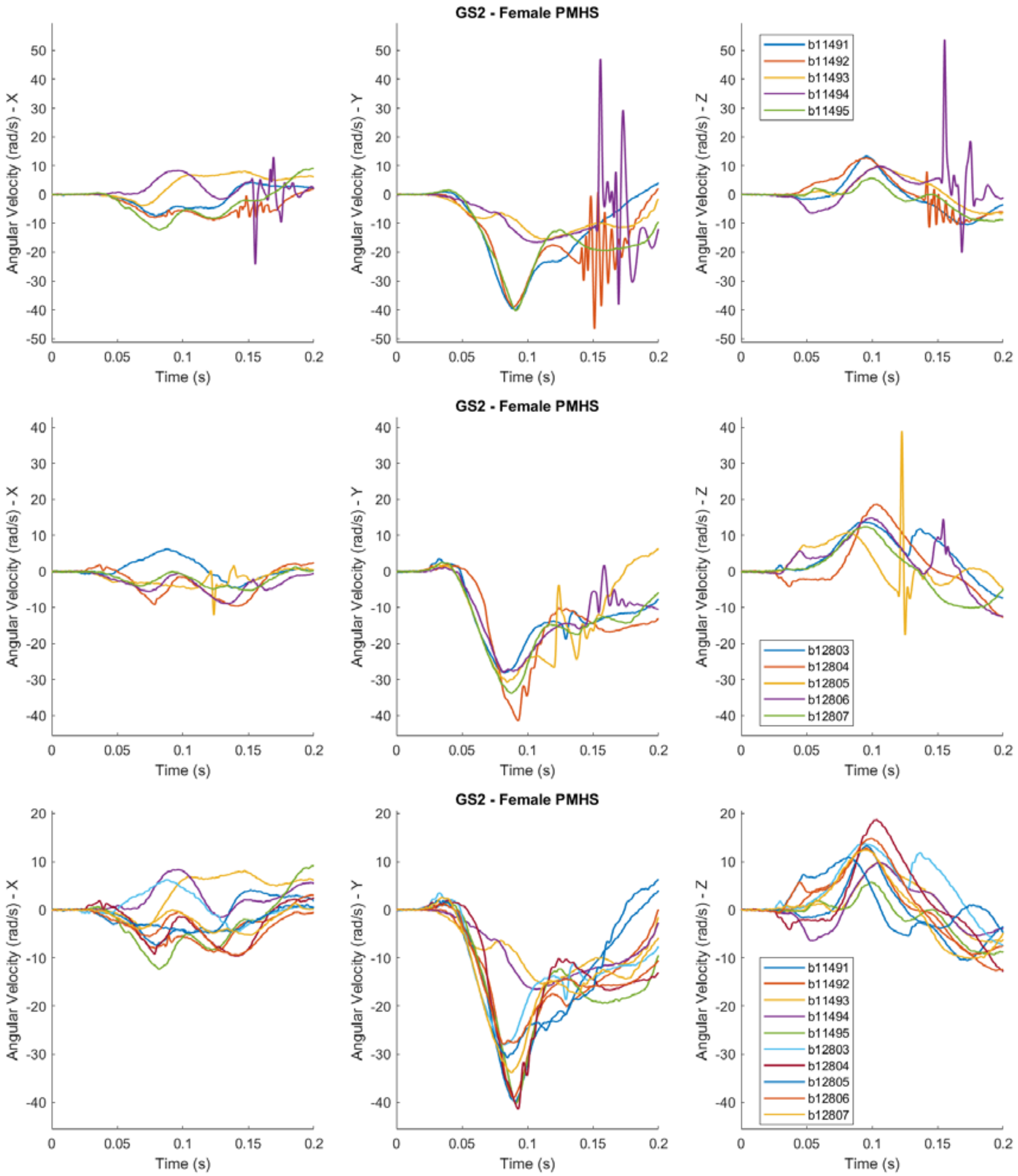

Appendix Figure DD: Original (top) and corrected (bottom) angular velocity traces for Gold Standard 2 female PMHS kinematics. Corrected signals: b11492 (0.13 s to 0.23 s), b11494 (0.1375 s to 0.23 s), b12805 (0.114 s to 0.1501 s), and b12806 (0.135 s to 0.2 s).

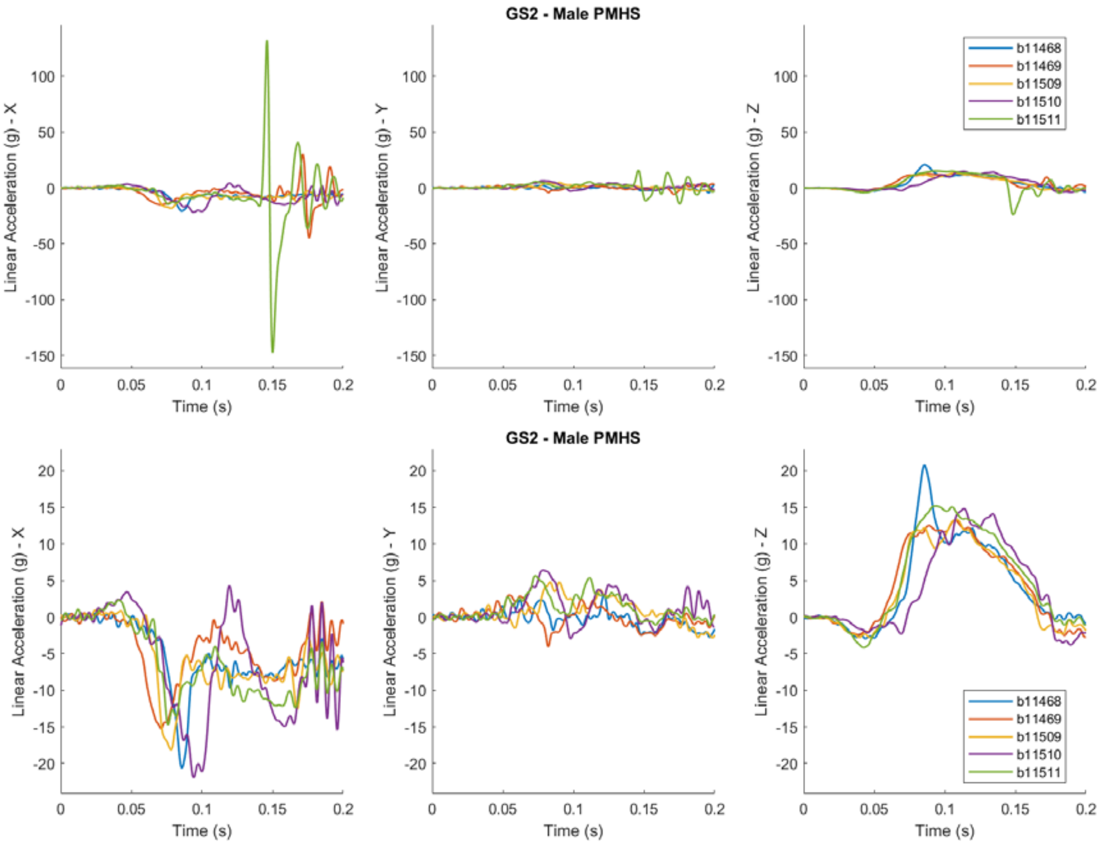

Appendix Figure EE: Original (top) and corrected (bottom) linear acceleration traces for Gold Standard 2 male PMHS kinematics. Corrected signals: b11469 (0.143 s to 0.215 s), b11511 (0.135 s to 0.22 s).

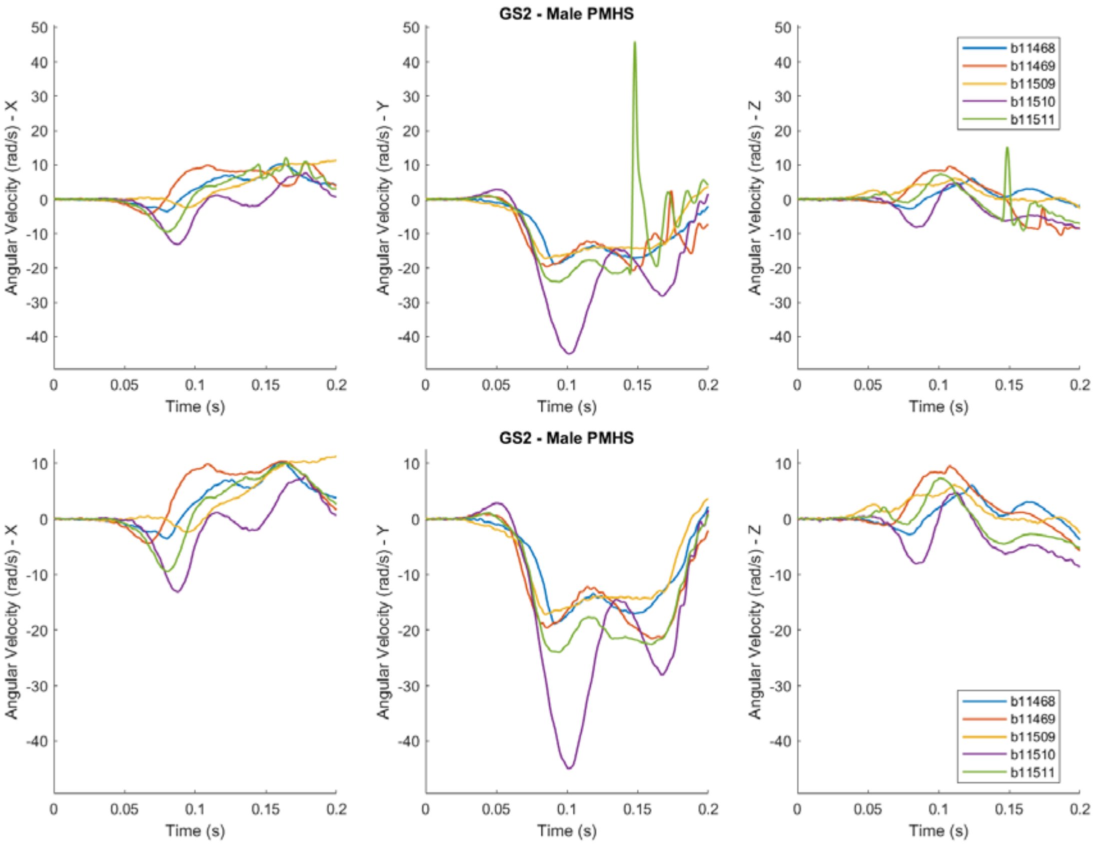

Appendix Figure FF: Original (top) and corrected (bottom) angular velocity traces for Gold Standard 2 male PMHS kinematics. Corrected signals: b11469 (0.143 s to 0.215 s), b11511 (0.135 s to 0.22 s), b11468 (0.18 s to 0.257 s), and b11510 (0.229 s to 0.3 s).

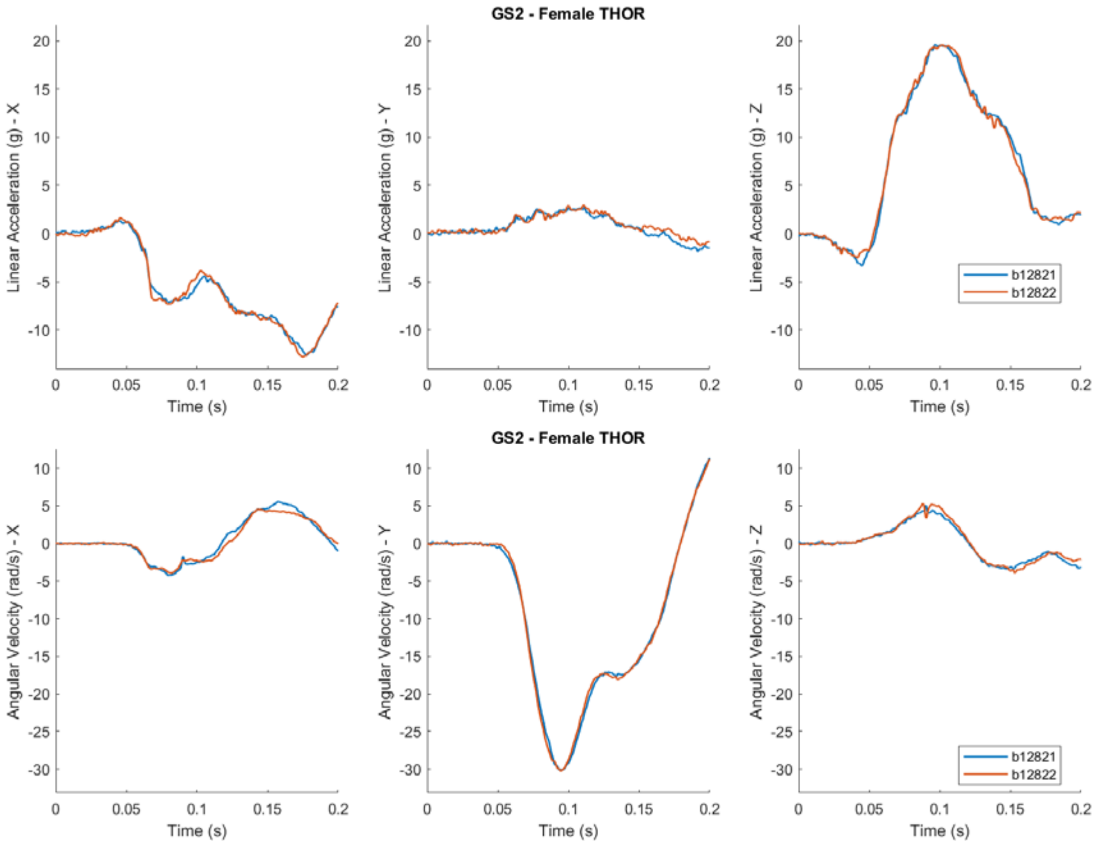

Appendix Figure GG: Original linear acceleration (top) and angular velocity (bottom) traces for Gold Standard 2 female THOR kinematics.

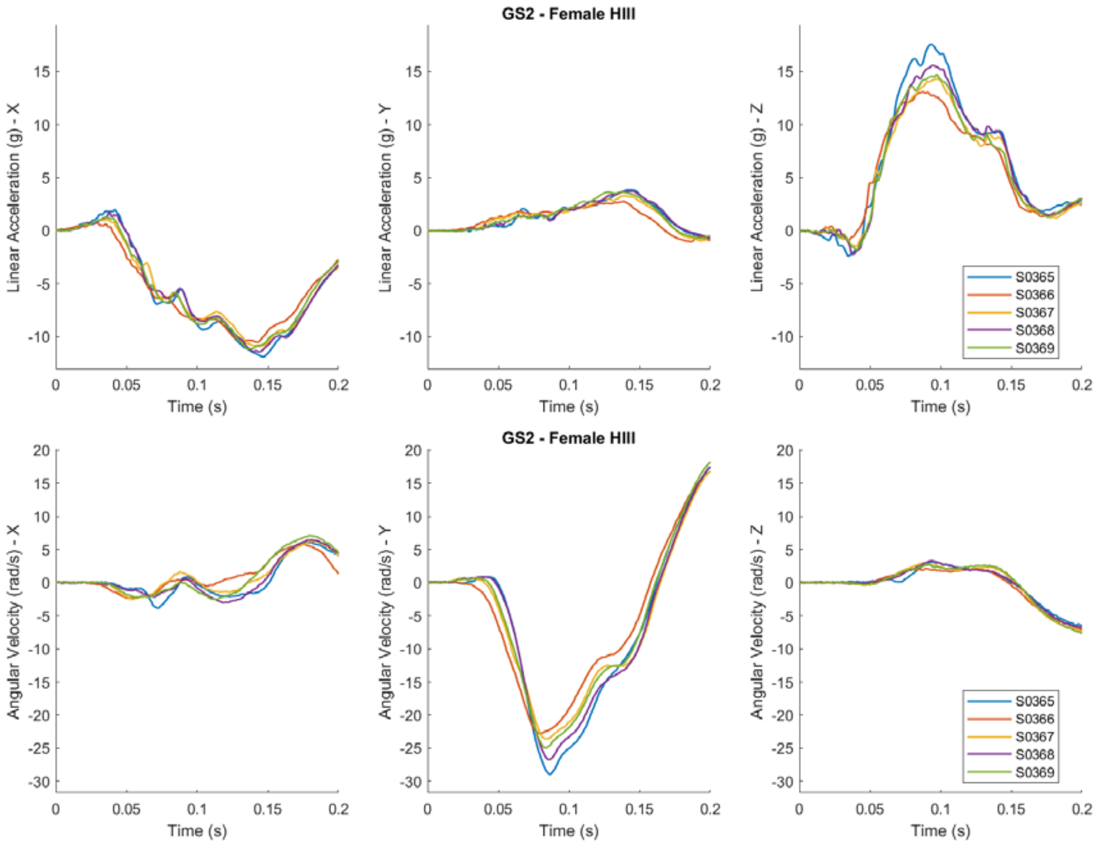

Appendix Figure HH: Original linear acceleration (top) and angular velocity (bottom) traces for Gold Standard 2 female HIII kinematics.

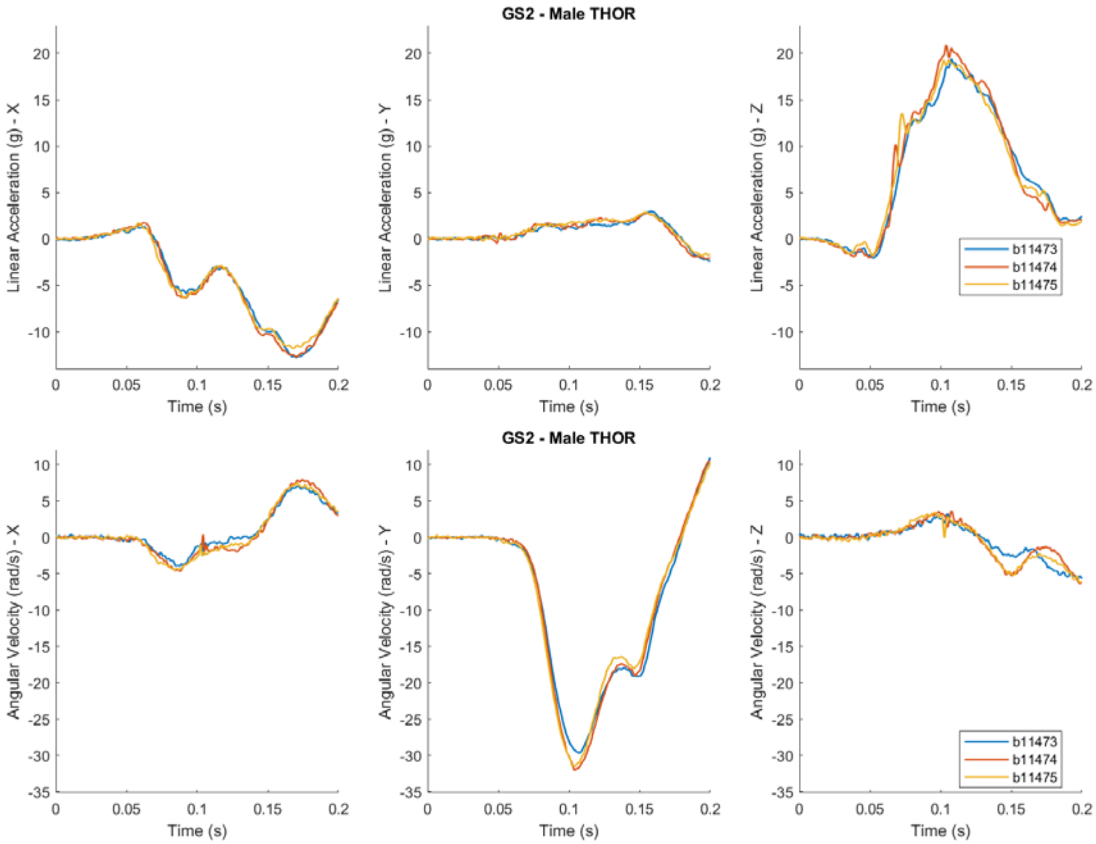

Appendix Figure II: Original linear acceleration (top) and angular velocity (bottom) traces for Gold Standard 2 male THOR kinematics.

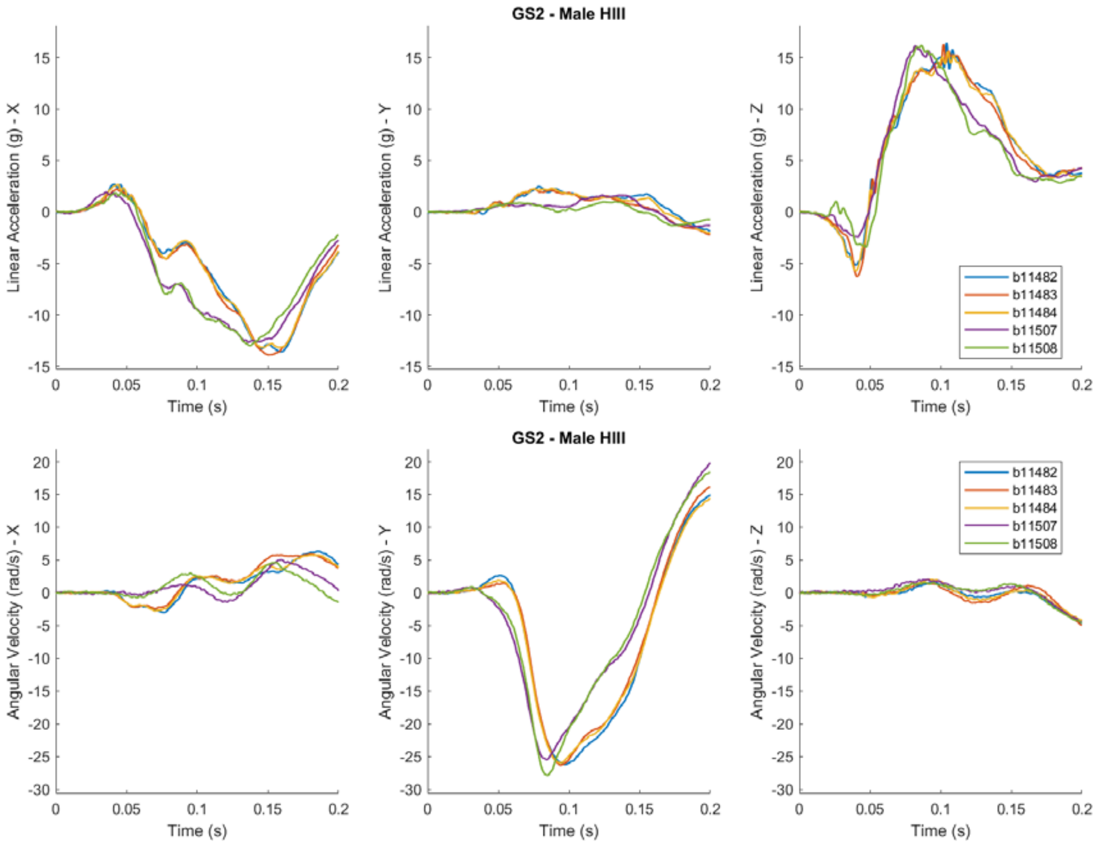

Appendix Figure JJ: Original linear acceleration (top) and angular velocity (bottom) traces for Gold Standard 2 male HIII kinematics.

C.1.2 Gold Standard 3 Traces

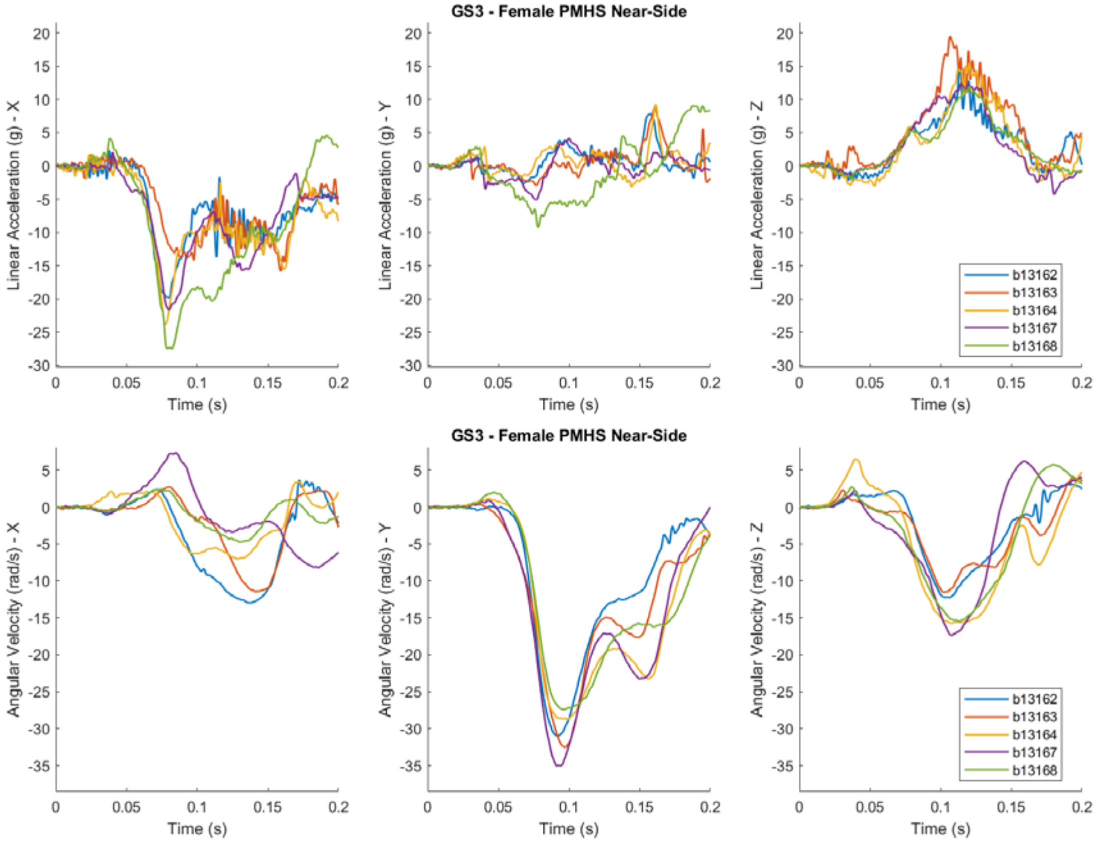

Appendix Figure KK: Original linear acceleration (top) and angular velocity (bottom) traces for Gold Standard 3 female PMHS kinematics.

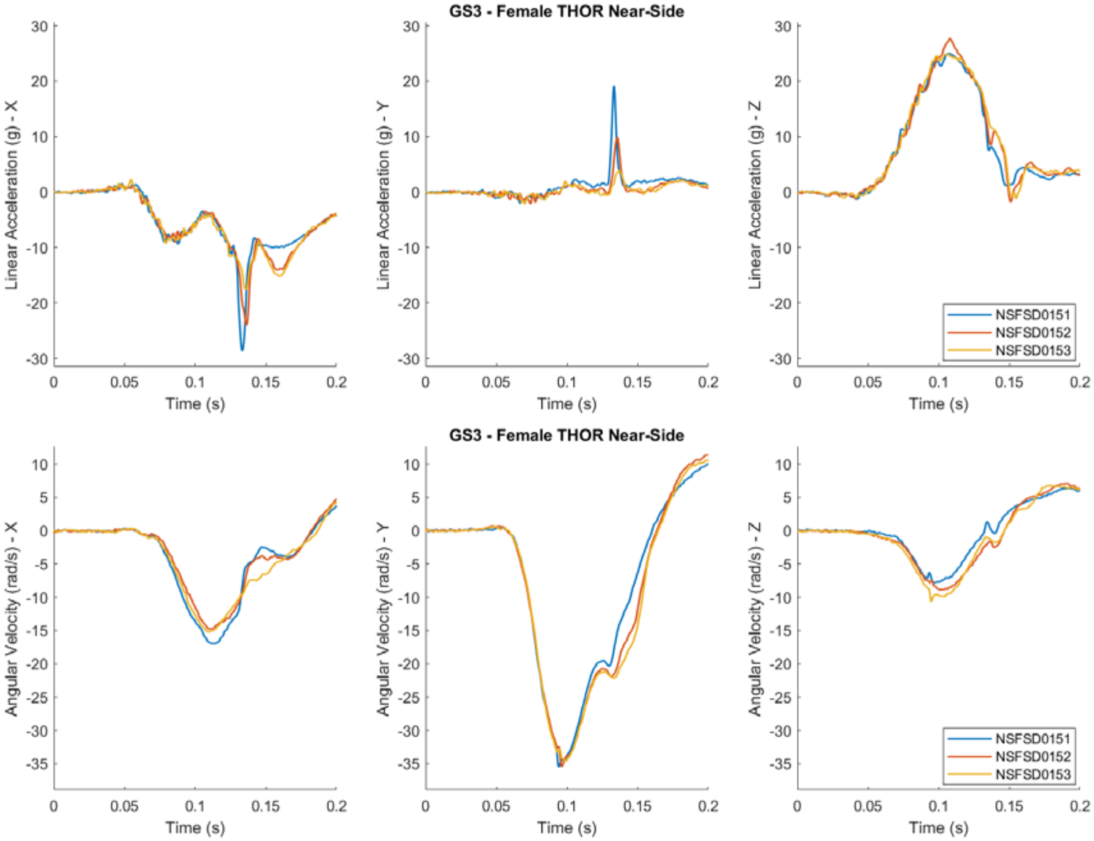

Appendix Figure LL: Original linear acceleration (top) and angular velocity (bottom) traces for Gold Standard 3 female THOR kinematics.

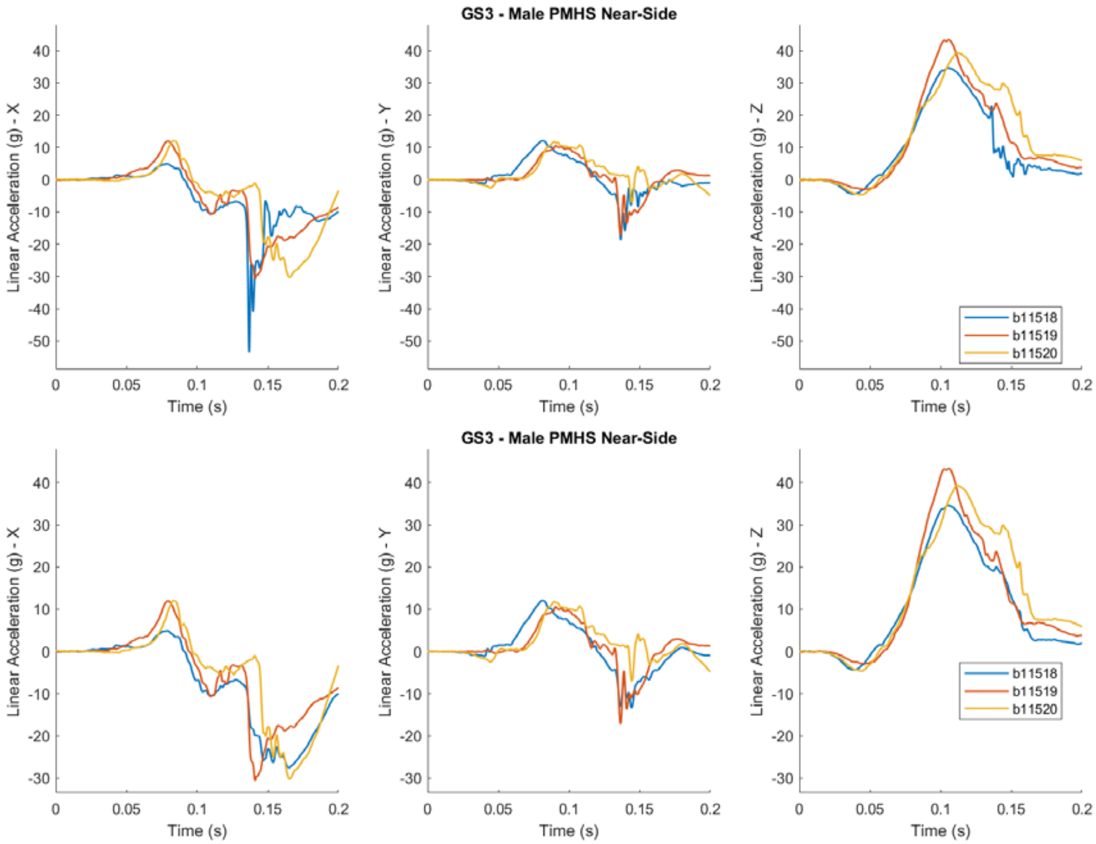

Appendix Figure MM: Original (top) and corrected (bottom) linear acceleration traces for Gold Standard 3 male PMHS kinematics. Corrected signals: b11518 (0.1324 s to 0.196 s)

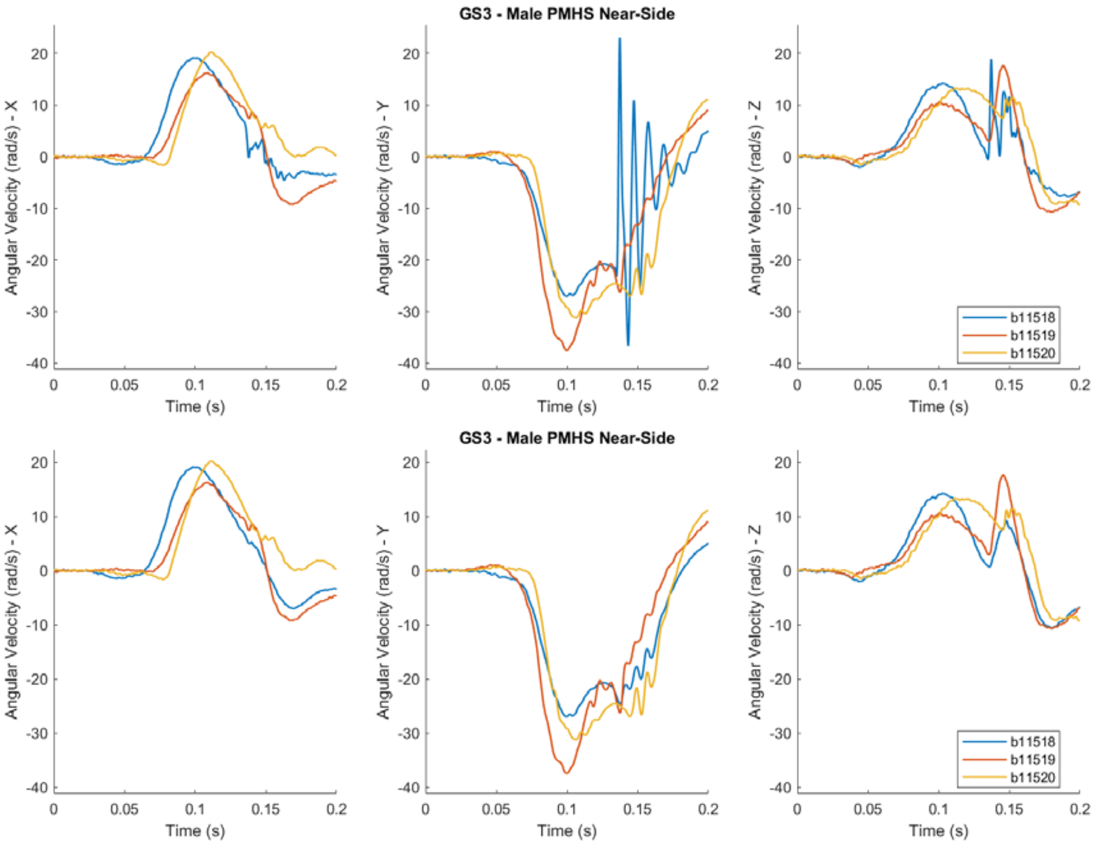

Appendix Figure NN: Original (top) and corrected (bottom) angular velocity traces for Gold Standard 3 male PMHS kinematics. Corrected signals: b11518 (0.1324 s to 0.196 s)

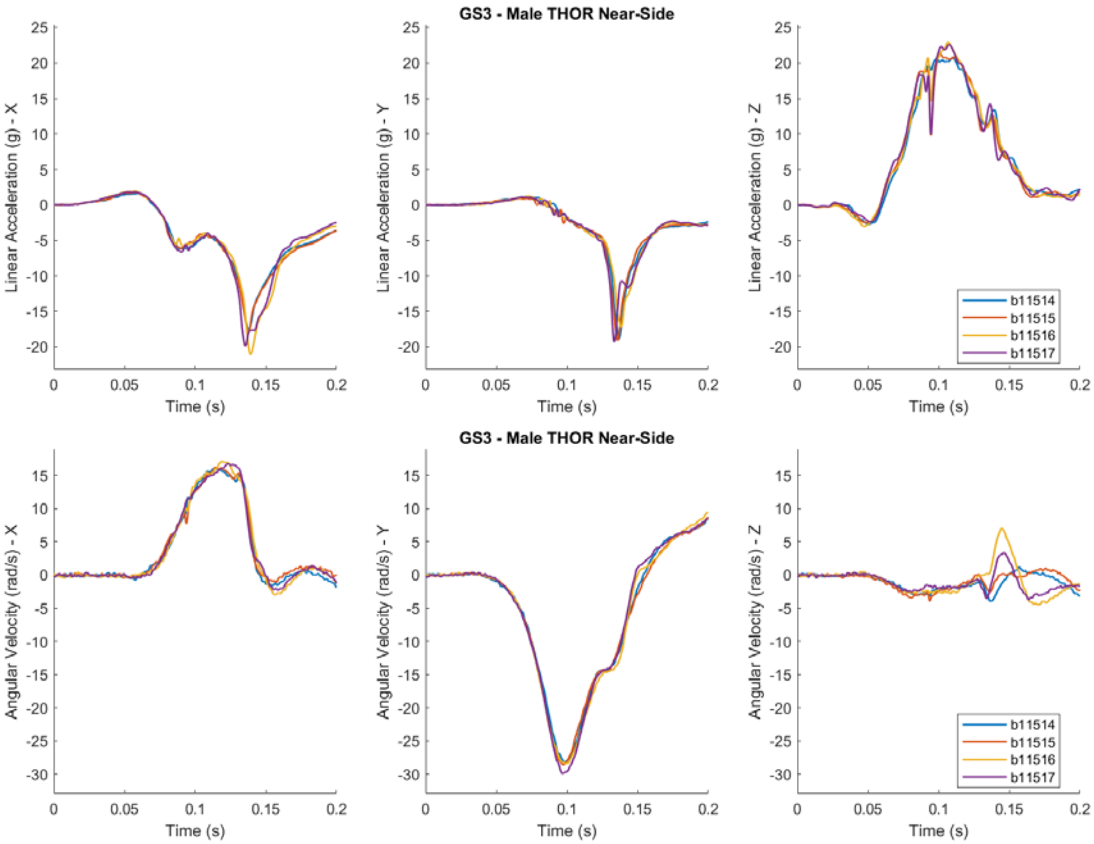

Appendix Figure OO: Original linear acceleration (top) and angular velocity (bottom) traces for Gold Standard 3 male THOR kinematics.

C.1.3 Recline 25° – 32 kph

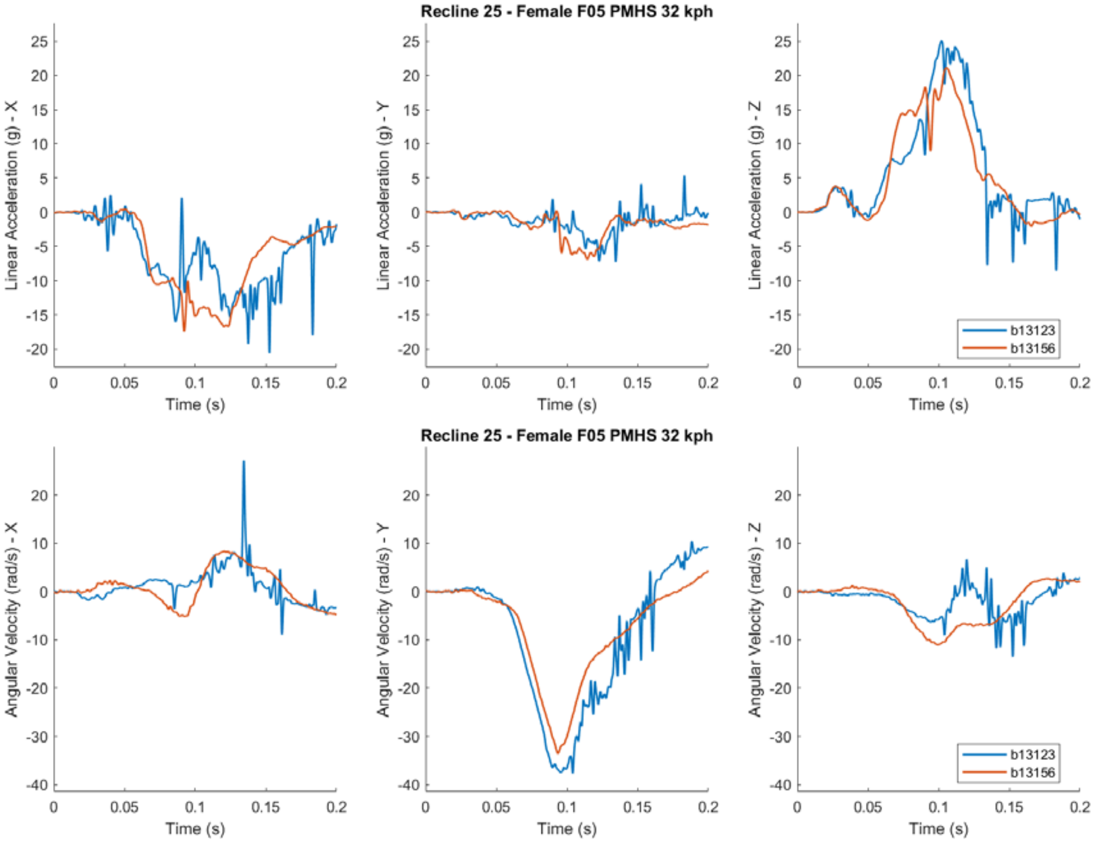

Appendix Figure PP: Original linear acceleration (top) and angular velocity (bottom) traces for Recline 25 degrees at 32 kph for female PMHS kinematics.

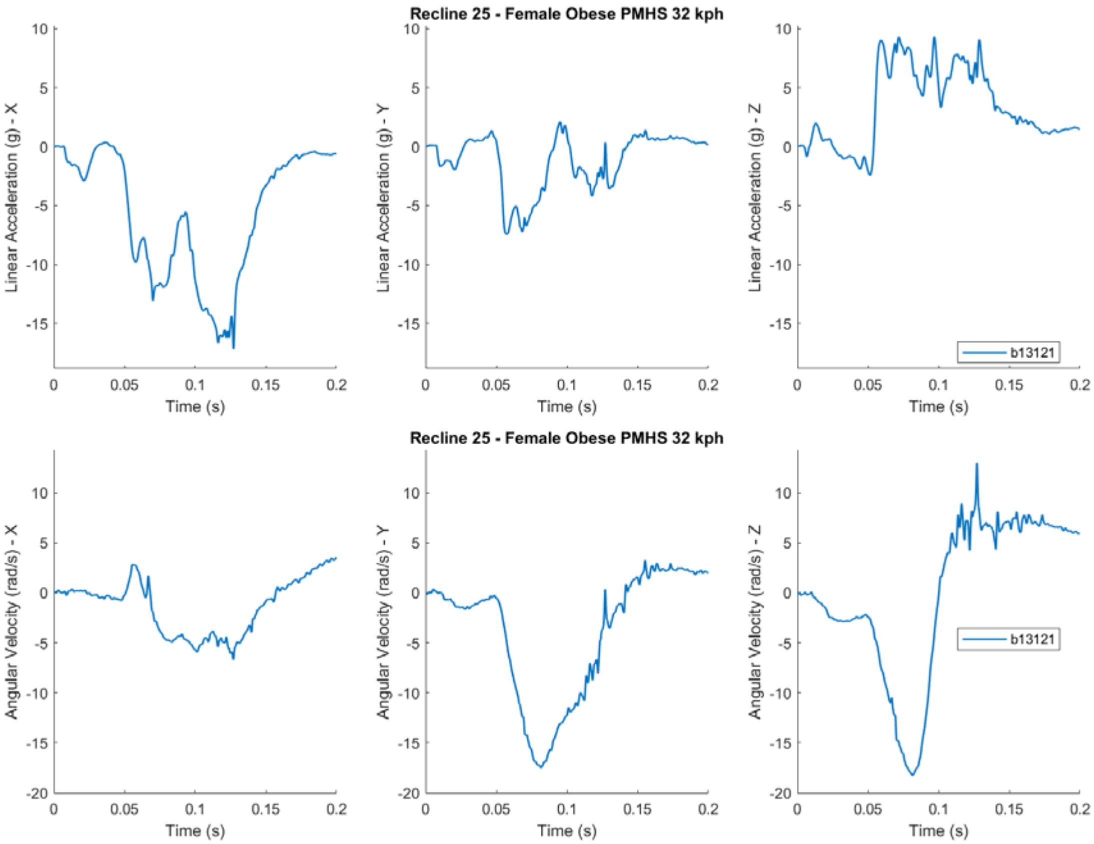

Appendix Figure QQ: Original linear acceleration (top) and angular velocity (bottom) traces for Recline 25 degrees at 32 kph for obese female PMHS kinematics.

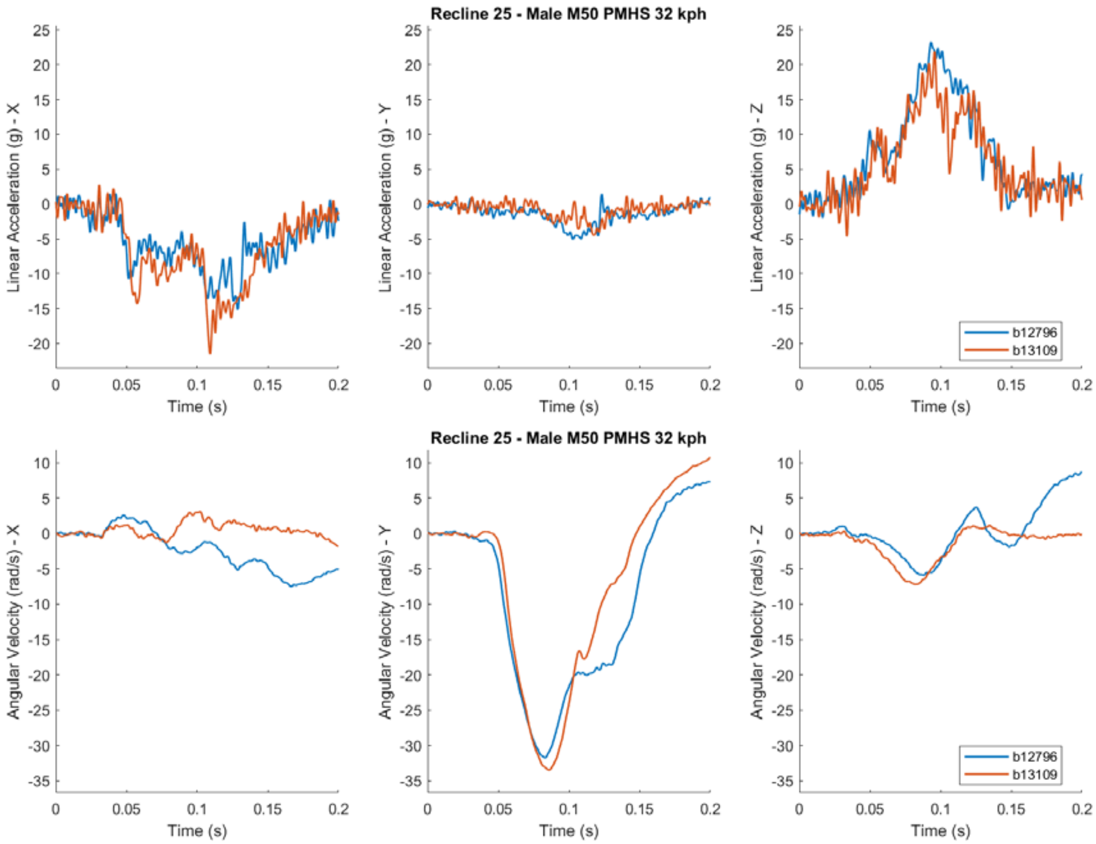

Appendix Figure RR: Original linear acceleration (top) and angular velocity (bottom) traces for Recline 25 degrees at 32 kph for male PMHS kinematics.

C.1.4 Recline 45° – 15 kph

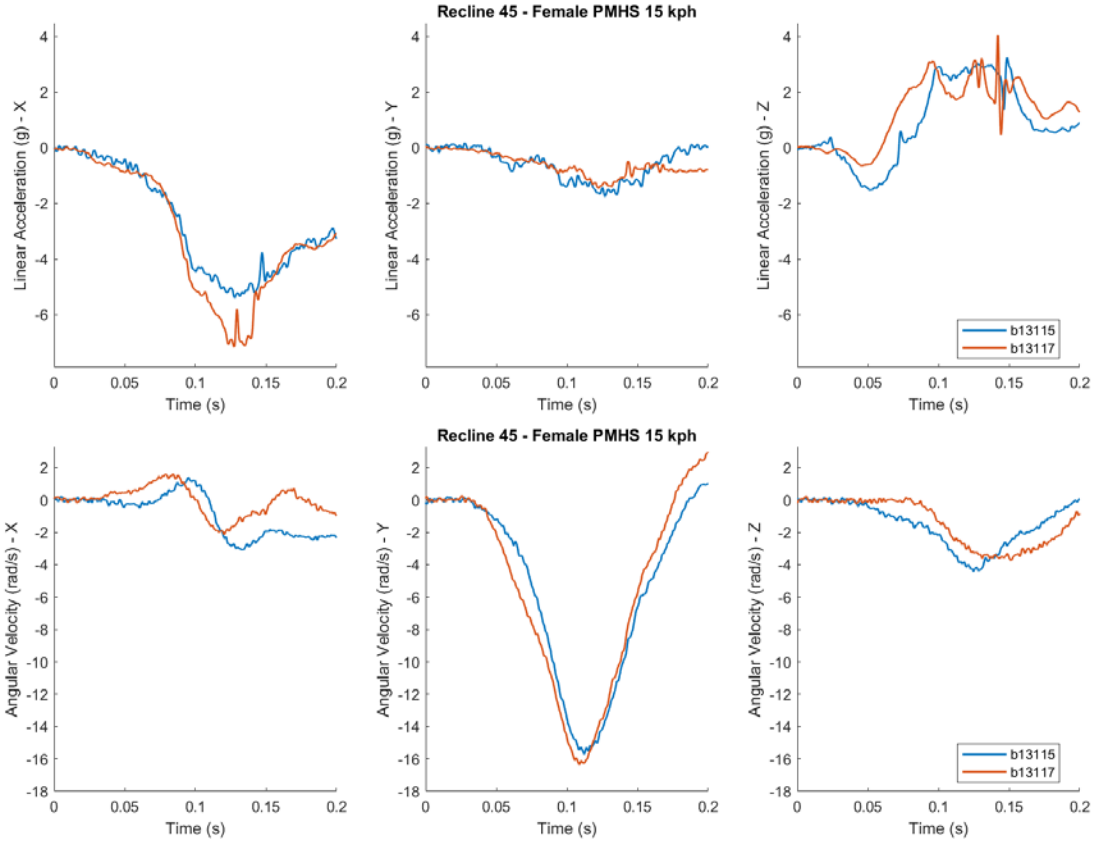

Appendix Figure SS: Original linear acceleration (top) and angular velocity (bottom) traces for Recline 45 degrees at 15 kph for female PMHS kinematics.

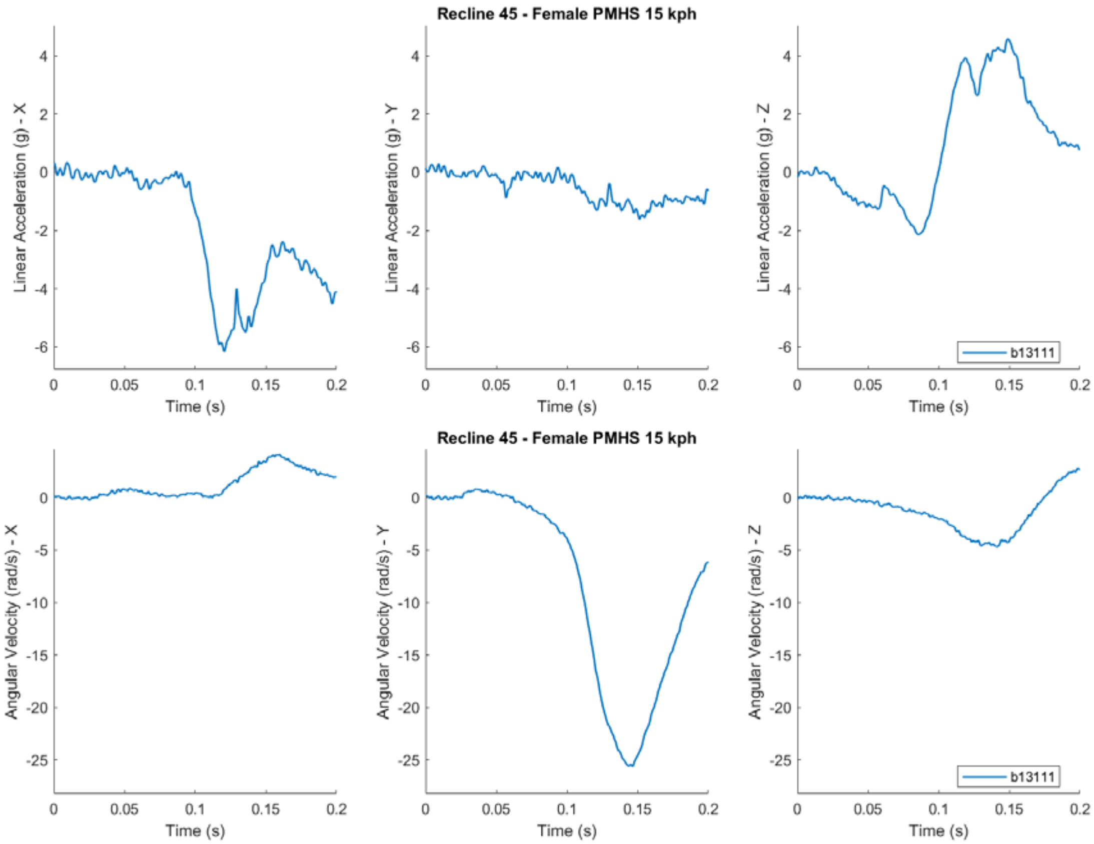

Appendix Figure TT: Original linear acceleration (top) and angular velocity (bottom) traces for Recline 45 degrees at 15 kph for obese female PMHS kinematics.

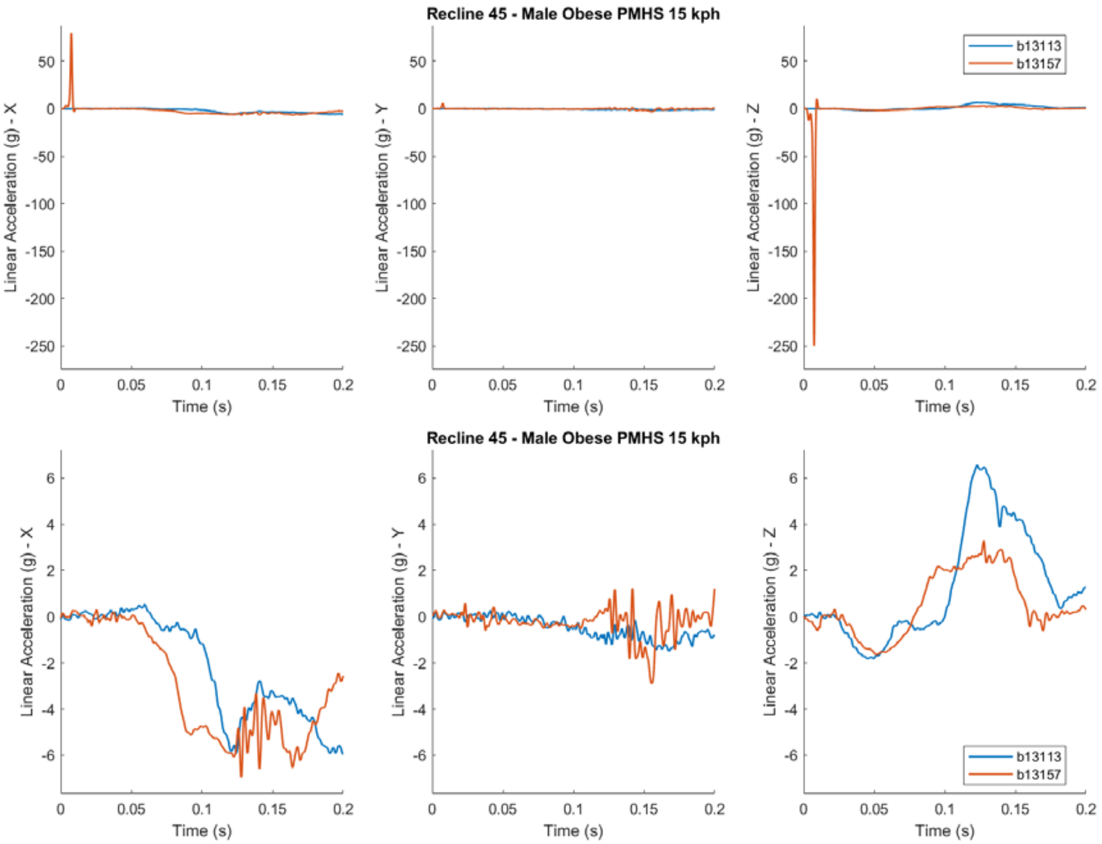

Appendix Figure UU: Original (top) and corrected (bottom) linear acceleration traces for Recline 45 degrees at 15 kph for male obese PMHS kinematics. Corrected signal: b13157 (0 s to 0.011 s)

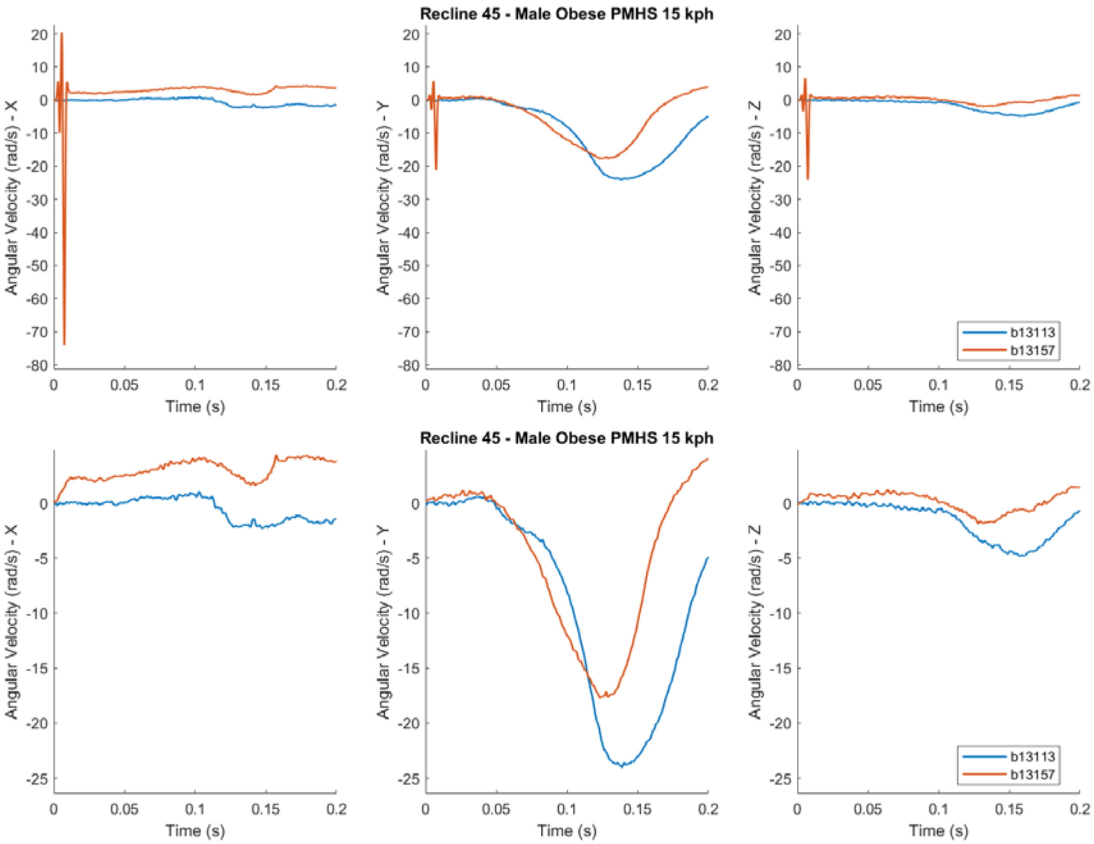

Appendix Figure VV: Original (top) and corrected (bottom) angular velocity traces for Recline 45 degrees at 15 kph for male obese PMHS kinematics. Corrected signal: b13157 (0 s to 0.011 s)

C.1.5 Recline 45° – 32 kph

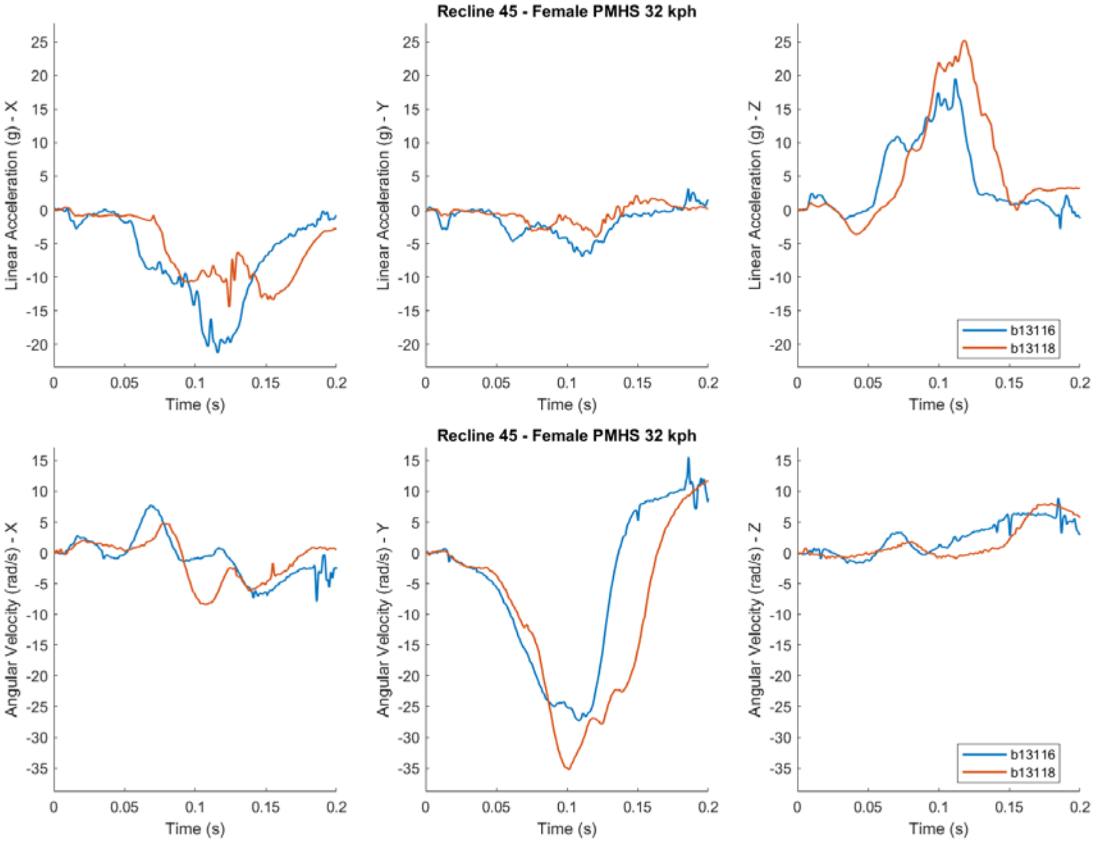

Appendix Figure WW: Original linear acceleration (top) and angular velocity (bottom) traces for Recline 45 degrees at 32 kph for female PMHS kinematics. Corrected signal: b13116 (0.182 s to 0.2)

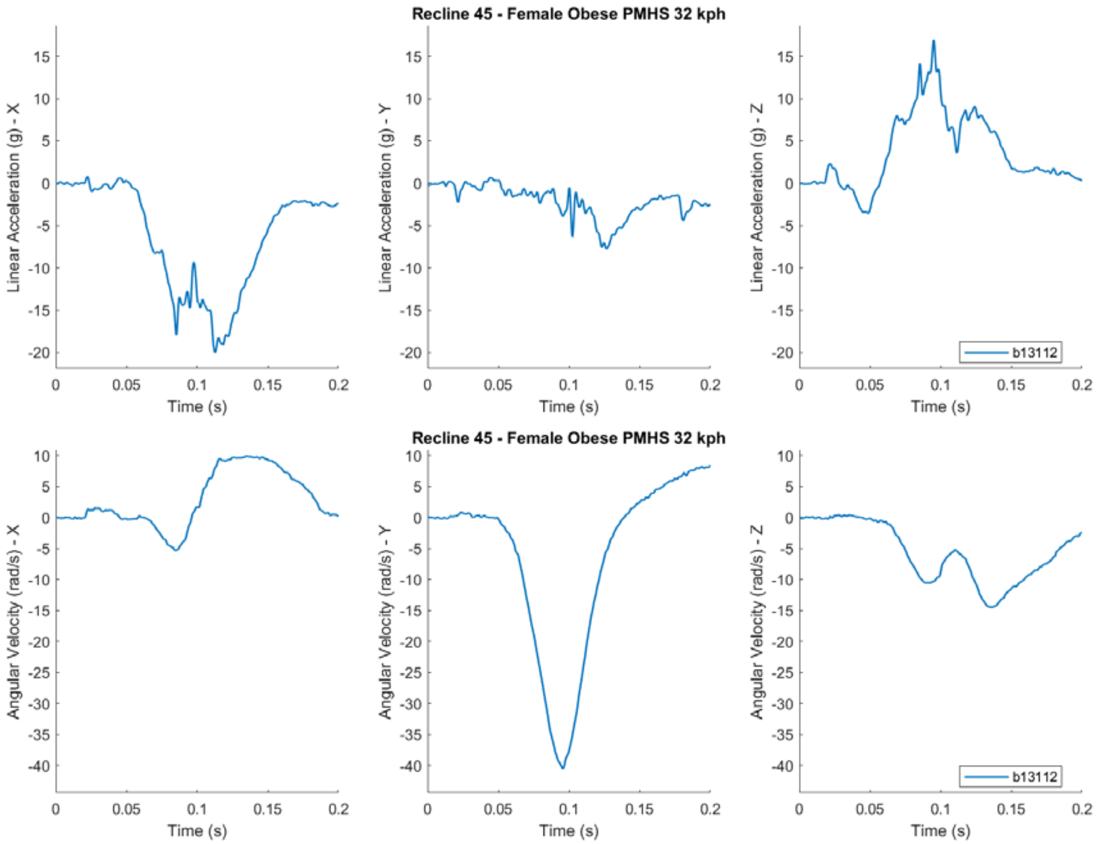

Appendix Figure XX: Original linear acceleration (top) and angular velocity (bottom) traces for Recline 45 degrees at 32 kph for obese female PMHS kinematics.

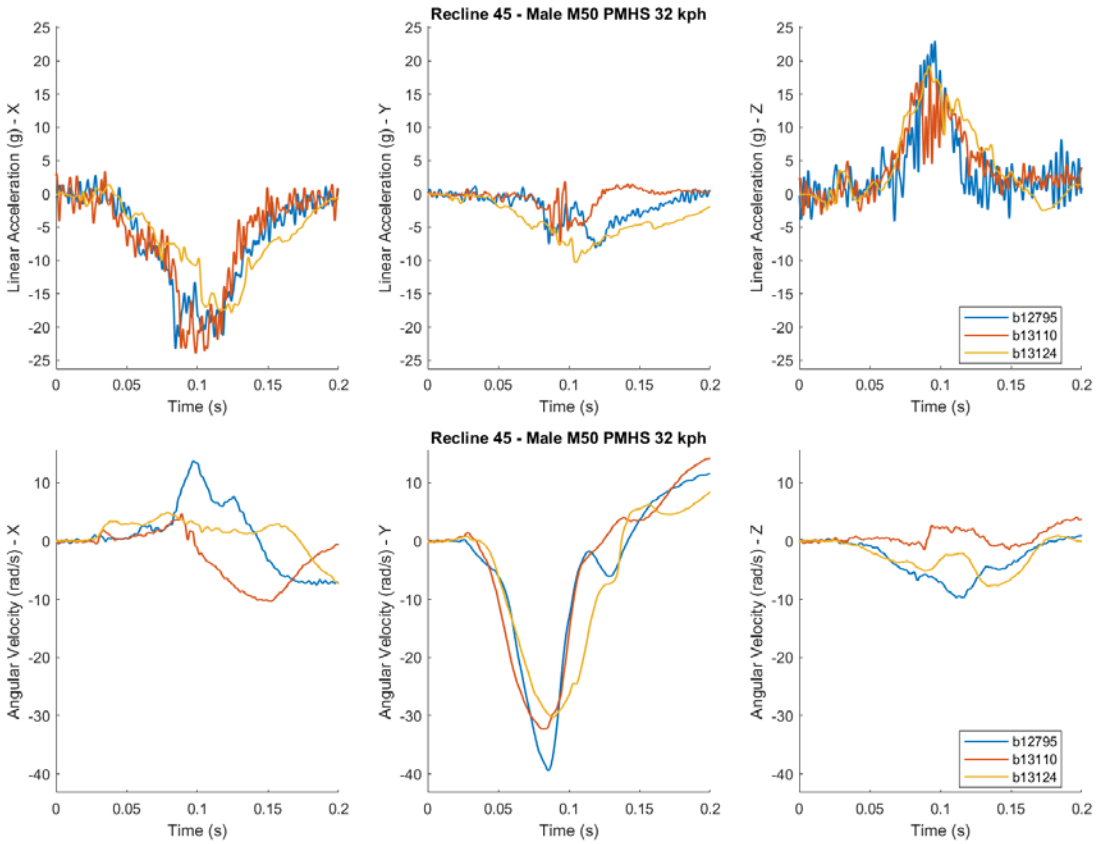

Appendix Figure YY: Original linear acceleration (top) and angular velocity (bottom) traces for Recline 45 degrees at 32 kph for male PMHS kinematics.

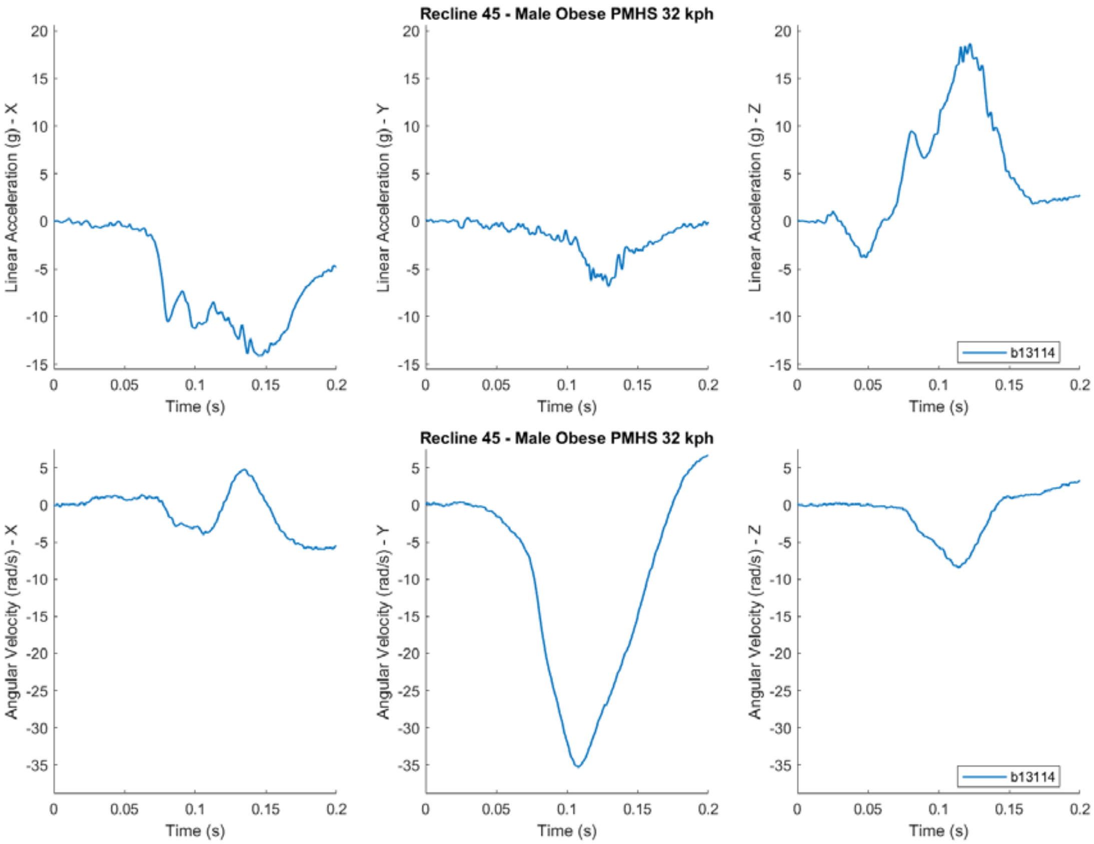

Appendix Figure ZZ: Original linear acceleration (top) and angular velocity (bottom) traces for Recline 45 degrees at 32 kph for obese male PMHS kinematics.

C.2 Head Kinematics Additional Information

Appendix Table K: Information for each of the head kinematics used in the head kinematics chapter.

Crash Condition	Source	Source Number	Surrogate	Delta V (kph)	Sex	Anthropometry
GS2	UVA	b11468	PMHS	30	M	M50
	UVA	b11469	PMHS	30	M	M50
	UVA	b11473	THOR	30	M	M50
	UVA	b11474	THOR	30	M	M50
	UVA	b11484	HIII	30	M	M50
	UVA	b11491	PMHS	30	F	F05
	UVA	b11492	PMHS	30	F	F05
	UVA	b11493	PMHS	30	F	F05
	UVA	b11494	PMHS	30	F	F05
	UVA	b11495	PMHS	30	F	F05
	UVA	b11508	HIII	30	M	M50
	UVA	b11509	PMHS	30	M	M50
	UVA	b11510	PMHS	30	M	M50

	UVA	b11511	PMHS	30	M	M50
	UVA	b12803	PMHS	30	F	F05
	UVA	b12804	PMHS	30	F	F05
	UVA	b12805	PMHS	30	F	F05
	UVA	b12806	PMHS	30	F	F05
	UVA	b12807	PMHS	30	F	F05
	UVA	b12821	THOR	30	F	F05
	UVA	b12822	THOR	30	F	F05
	UVA	S0365	HIII	30	F	F05
	UVA	S0366	HIII	30	F	F05
GS3	UVA	b11518	PMHS	30	M	M50
	UVA	b11519	PMHS	30	M	M50
	UVA	b11520	PMHS	30	M	M50
	MCW	b13162	PMHS	30	F	F05
	MCW	b13163	PMHS	30	F	F05
	MCW	b13164	PMHS	30	F	F05
	MCW	b13167	PMHS	30	F	F05
	MCW	b13168	PMHS	30	F	F05
	UVA	b11514	THOR	30	M	M50
	UVA	b11517	THOR	30	M	M50
	MCW	NSFSD0151	THOR	30	F	F05
	MCW	NSFSD0153	THOR	30	F	F05
Recline25 32kph	UMTRI	b12796	PMHS	32	M	M50
	UMTRI	b13109	PMHS	32	M	M50
	MCW	b13121	PMHS	32	F	Obese
	MCW	b13156	PMHS	32	F	F05
Recline45 15kph	MCW	b13111	PMHS	15	F	Obese
	MCW	b13113	PMHS	15	M	Obese
	MCW	b13115	PMHS	15	F	F05
	MCW	b13117	PMHS	15	F	F05
	MCW	b13157	PMHS	15	M	Obese
Recline45 32kph	UMTRI	b12795	PMHS	32	M	M50
	UMTRI	b13110	PMHS	32	M	M50
	MCW	b13112	PMHS	32	F	Obese
	MCW	b13114	PMHS	32	M	Obese
	MCW	b13116	PMHS	32	F	F05
	MCW	b13118	PMHS	32	F	F05
	UMTRI	b13124	PMHS	32	M	M50

C.3 Statistical Methods

The equations for the multivariate Bayesian linear mixed model to determine the effect of sex, BMI, and surrogate type on each of the head kinematic features, accounting for a random study effect.

$$Y_{ij}^{ACC\,X} = \left(\beta_0^{ACC\,X} + u_{j0}^{ACC\,X}\right) + \beta_1^{ACC\,X}\left(BMI_{ij}\right) + \beta_2^{ACC\,X}\left(Sex_{ij}\right) + \beta_3^{ACC\,X}\left(Surrogate_{ij}\right) + \epsilon_{ij}^{ACC\,X}$$

$$Y_{ij}^{ACC\,Y} = \left(\beta_0^{ACC\,Y} + u_{j0}^{ACC\,Y}\right) + \beta_1^{ACC\,Y}\left(BMI_{ij}\right) + \beta_2^{ACC\,Y}\left(Sex_{ij}\right) + \beta_3^{ACC\,Y}\left(Surrogate_{ij}\right) + \epsilon_{ij}^{ACC\,Y}$$

$$Y_{ij}^{ACC\,Z} = \left(\beta_0^{ACC\,Z} + u_{j0}^{ACC\,Z}\right) + \beta_1^{ACC\,Z}\left(BMI_{ij}\right) + \beta_2^{ACC\,Z}\left(Sex_{ij}\right) + \beta_3^{ACC\,Z}\left(Surrogate_{ij}\right) + \epsilon_{\mathrm{ij}}^{ACC\,Z}$$

$$Y_{ij}^{ACC} = \left(\beta_0^{ACC} + u_{j0}^{ACC}\right) + \beta_1^{ACC}\left(BMI_{ij}\right) + \beta_2^{ACC}\left(Sex_{ij}\right) + \beta_3^{ACC}\left(Surrogate_{ij}\right) + \epsilon_{\mathrm{ij}}^{ACC}$$

$$Y_{ij}^{ARS\,X} = \left(\beta_0^{ARS\,X} + u_{j0}^{ARS\,X}\right) + \beta_1^{ARS\,X}\left(BMI_{ij}\right) + \beta_2^{ARS\,X}\left(Sex_{ij}\right) + \beta_3^{ARS\,X}\left(Surrogate_{ij}\right) + \epsilon_{\mathrm{ij}}^{ARS\,X}$$

$$Y_{ij}^{ARS\,Y} = \left(\beta_0^{ARS\,Y} + u_{j0}^{ARS\,Y}\right) + \beta_1^{ARS\,Y}\left(BMI_{ij}\right) + \beta_2^{ARS\,Y}\left(Sex_{ij}\right) + \beta_3^{ARS\,Y}\left(Surrogate_{ij}\right) + \epsilon_{\mathrm{ij}}^{ARS\,Y}$$

$$Y_{ij}^{ARS\,Z} = \left(\beta_0^{ARS\,Z} + u_{j0}^{ARS\,Z}\right) + \beta_1^{ARS\,Z}\left(BMI_{ij}\right) + \beta_2^{ARS\,Z}\left(Sex_{ij}\right) + \beta_3^{ARS\,Z}\left(Surrogate_{ij}\right) + \epsilon_{\mathrm{ij}}^{ARS\,Z}$$

$$Y_{ij}^{ARS} = \left(\beta_0^{ARS} + u_{j0}^{ARS}\right) + \beta_1^{ARS}\left(BMI_{ij}\right) + \beta_2^{ARS}\left(Sex_{ij}\right) + \beta_3^{ARS}\left(Surrogate_{ij}\right) + \epsilon_{\mathrm{ij}}^{ARS}$$

$$\begin{aligned} Y_{ij}^{Alpha\,X} = {} & \left(\beta_0^{Alpha\,X} + u_{j0}^{Alpha\,X}\right) + \beta_1^{Alpha\,X}\left(BMI_{ij}\right) + \beta_2^{Alpha\,X}\left(Sex_{ij}\right) + \beta_3^{Alpha\,X}\left(Surrogate_{ij}\right) \\ & + \epsilon_{\mathrm{ij}}^{Alpha\,X} \end{aligned}$$

$$\begin{aligned} Y_{ij}^{Alpha\,Y} = {} & \left(\beta_0^{Alpha\,Y} + u_{j0}^{Alpha\,Y}\right) + \beta_1^{Alpha\,Y}\left(BMI_{ij}\right) + \beta_2^{Alpha\,Y}\left(Sex_{ij}\right) + \beta_3^{Alpha\,Y}\left(Surrogate_{ij}\right) \\ & + \epsilon_{\mathrm{ij}}^{Alpha\,Y} \end{aligned}$$

$$\begin{aligned} Y_{ij}^{Alpha\,Z} = {} & \left(\beta_0^{Alpha\,Z} + u_{j0}^{Alpha\,Z}\right) + \beta_1^{Alpha\,Z}\left(BMI_{ij}\right) + \beta_2^{Alpha\,Z}\left(Sex_{ij}\right) + \beta_3^{Alpha\,Z}\left(Surrogate_{ij}\right) \\ & + \epsilon_{\mathrm{ij}}^{Alpha\,Z} \end{aligned}$$

$$Y_{ij}^{Alpha} = \left(\beta_0^{Alpha} + u_{j0}^{Alpha}\right) + \beta_1^{Alpha}\left(BMI_{ij}\right) + \beta_2^{Alpha}\left(Sex_{ij}\right) + \beta_3^{Alpha}\left(Surrogate_{ij}\right) + \epsilon_{\mathrm{ij}}^{Alpha}$$

$$Y_{ij}^{BrIC} = \left(\beta_0^{BrIC} + u_{j0}^{BrIC}\right) + \beta_1^{BrIC}\left(BMI_{ij}\right) + \beta_2^{BrIC}\left(Sex_{ij}\right) + \beta_3^{BrIC}\left(Surrogate_{ij}\right) + \epsilon_{\mathrm{ij}}^{BrIC}$$

$$Y_{ij}^{UBrIC} = \left(\beta_0^{UBrIC} + u_{j0}^{UBrIC}\right) + \beta_1^{UBrIC}\left(BMI_{ij}\right) + \beta_2^{UBrIC}\left(Sex_{ij}\right) + \beta_3^{UBrIC}\left(Surrogate_{ij}\right) + \epsilon_{\mathrm{ij}}^{UBrIC}$$

$$\begin{aligned} Y_{ij}^{DAMAGE} = {} & \left(\beta_0^{DAMAGE} + u_{j0}^{DAMAGE}\right) + \beta_1^{DAMAGE}\left(BMI_{ij}\right) + \beta_2^{DAMAGE}\left(Sex_{ij}\right) + \beta_3^{DAMAGE}\left(Surrogate_{ij}\right) \\ & + \epsilon_{\mathrm{ij}}^{DAMAGE} \end{aligned}$$

The equations for the multivariate Bayesian linear mixed model to predict deformation metrics based on independent head kinematic features, BMI, sex, and surrogate type accounting for a random study effect.

$$\begin{aligned} Y_{ij}^{MPS-95} = {} & \left(\beta_0^{MPS-95} + u_{j0}^{MPS-95}\right) + \beta_1^{MPS-95}\left(BMI_{ij}\right) + \beta_2^{MPS-95}\left(Sex_{ij}\right) + \beta_3^{MPS-95}(Surrogate) \\ & + \beta_4^{MPS-95}\left(ACC\,X_{ij}\right) + \beta_5^{MPS-95}\left(ACC\,Y_{ij}\right) + \beta_6^{MPS-95}\left(ACC\,Z_{ij}\right) \\ & + \beta_7^{MPS-95}\left(ACC_{ij}\right) + \beta_8^{MPS-95}\left(ARS\,X_{ij}\right) + \beta_9^{MPS-95}\left(ARS\,Y_{ij}\right) + \beta_{10}^{MPS-95}\left(ARS\,Z_{ij}\right) \\ & + \beta_{11}^{MPS-95}\left(ARS_{ij}\right) + \beta_{12}^{MPS-95}\left(Alpha\,X_{ij}\right) + \beta_{13}^{MPS-95}\left(Alpha\,Y_{ij}\right) \\ & + \beta_{14}^{MPS-95}\left(Alpha\,Z_{ij}\right) + \beta_{15}^{MPS-95}\left(Alpha_{ij}\right) + \beta_{16}^{MPS-95}\left(BrIC_{ij}\right) + \beta_{17}^{MPS-95}\left(UBrIC_{ij}\right) \\ & + \beta_{18}^{MPS-95}\left(DAMAGE_{ij}\right) + \epsilon_{\mathrm{ij}}^{MPS-95} \end{aligned}$$

$$\begin{aligned}Y_{ij}^{MPSR-95} = {} & \left(\beta_0^{MPSR-95} + u_{j0}^{MPSR-95}\right) + \beta_1^{MPSR-95}\left(BMI_{ij}\right) + \beta_2^{MPSR-95}\left(Sex_{ij}\right) \\ & + \beta_3^{MPSR-95}(Surrogate) + \beta_4^{MPSR-95}\left(ACC\ X_{ij}\right) + \beta_5^{MPSR-95}\left(ACC\ Y_{ij}\right) \\ & + \beta_6^{MPSR-95}\left(ACC\ Z_{ij}\right) + \beta_7^{MPSR-95}\left(ACC_{ij}\right) + \beta_8^{MPSR-95}\left(ARS\ X_{ij}\right) \\ & + \beta_9^{MPSR-95}\left(ARS\ Y_{ij}\right) + \beta_{10}^{MPSR-95}\left(ARS\ Z_{ij}\right) + \beta_{11}^{MPSR-95}\left(ARS_{ij}\right) \\ & + \beta_{12}^{MPSR-95}\left(Alpha\ X_{ij}\right) + \beta_{13}^{MPSR-95}\left(Alpha\ Y_{ij}\right) + \beta_{14}^{MPSR-95}\left(Alpha\ Z_{ij}\right) \\ & + \beta_{15}^{MPSR-95}\left(Alpha_{ij}\right) + \beta_{16}^{MPSR-95}\left(BrIC_{ij}\right) + \beta_{17}^{MPSR-95}\left(UBrIC_{ij}\right) \\ & + \beta_{18}^{MPSR-95}\left(DAMAGE_{ij}\right) + \epsilon_{\mathrm{ij}}^{MPSR-95}\end{aligned}$$

$$\begin{aligned}Y_{ij}^{MPSxMPSR-95} = {} & \left(\beta_0^{MPSxMPSR-95} + u_{j0}^{MPSxMPSR-95}\right) + \beta_1^{MPSxMPSR-95}\left(BMI_{ij}\right) + \beta_2^{MPSxMPSR-95}\left(Sex_{ij}\right) \\ & + \beta_3^{MPSxMPSR-95}(Surrogate) + \beta_4^{MPSxMPSR-95}\left(ACC\ X_{ij}\right) + \beta_5^{MPSxMPSR-95}\left(ACC\ Y_{ij}\right) \\ & + \beta_6^{MPSxMPSR-95}\left(ACC\ Z_{ij}\right) + \beta_7^{MPSxMPSR-95}\left(ACC_{ij}\right) + \beta_8^{MPSxMPSR-95}\left(ARS\ X_{ij}\right) \\ & + \beta_9^{MPSxMPSR-95}\left(ARS\ Y_{ij}\right) + \beta_{10}^{MPSxMPSR-95}\left(ARS\ Z_{ij}\right) + \beta_{11}^{MPSxMPSR-95}\left(ARS_{ij}\right) \\ & + \beta_{12}^{MPSxMPSR-95}\left(Alpha\ X_{ij}\right) + \beta_{13}^{MPSxMPSR-95}\left(Alpha\ Y_{ij}\right) \\ & + \beta_{14}^{MPSxMPSR-95}\left(Alpha\ Z_{ij}\right) + \beta_{15}^{MPSxMPSR-95}\left(Alpha_{ij}\right) + \beta_{16}^{MPSxMPSR-95}\left(BrIC_{ij}\right) \\ & + \beta_{17}^{MPSxMPSR-95}\left(UBrIC_{ij}\right) + \beta_{18}^{MPSxMPSR-95}\left(DAMAGE_{ij}\right) + \epsilon_{\mathrm{ij}}^{MPSxMPSR-95}\end{aligned}$$

$$\begin{aligned}Y_{ij}^{CSDM-25} = {} & \left(\beta_0^{CSDM-25} + u_{j0}^{CSDM-25}\right) + \beta_1^{CSDM-25}\left(BMI_{ij}\right) + \beta_2^{CSDM-25}\left(Sex_{ij}\right) \\ & + \beta_3^{CSDM-25}(Surrogate) + \beta_4^{CSDM-25}\left(ACC\ X_{ij}\right) + \beta_5^{CSDM-25}\left(ACC\ Y_{ij}\right) \\ & + \beta_6^{CSDM-25}\left(ACC\ Z_{ij}\right) + \beta_7^{CSDM-25}\left(ACC_{ij}\right) + \beta_8^{CSDM-25}\left(ARS\ X_{ij}\right) \\ & + \beta_9^{CSDM-25}\left(ARS\ Y_{ij}\right) + \beta_{10}^{CSDM-25}\left(ARS\ Z_{ij}\right) + \beta_{11}^{CSDM-25}\left(ARS_{ij}\right) \\ & + \beta_{12}^{CSDM-25}\left(Alpha\ X_{ij}\right) + \beta_{13}^{CSDM-25}\left(Alpha\ Y_{ij}\right) + \beta_{14}^{CSDM-25}\left(Alpha\ Z_{ij}\right) \\ & + \beta_{15}^{CSDM-25}\left(Alpha_{ij}\right) + \beta_{16}^{CSDM-25}\left(BrIC_{ij}\right) + \beta_{17}^{CSDM-25}\left(UBrIC_{ij}\right) \\ & + \beta_{18}^{CSDM-25}\left(DAMAGE_{ij}\right) + \epsilon_{\mathrm{ij}}^{CSDM-25}\end{aligned}$$

C.4 Statistical Model Results

Appendix Table L: Estimated coefficients for the population-level effects of the multivariate Bayesian linear mixed model and the 95% credible interval (CrI) for the estimated parameter included in square brackets for e head kinematic biomechanical features. Bolded coefficients are significant based on the CrI. Positive sex, surrogate, and BMI coefficients imply male, cadaver, obese response was greater.

	Intercept	Sex	Surrogate	BMI
Peak ACC X	**13.21** [6.55, 19.54]	**3.33** [0.84, 5.67]	2.3 [-0.67, 5.22]	-3.44 [-7.89, 0.87]
Peak ACC Y	**5.80** [1.56, 9.88]	0.89 [-1.22, 2.99]	0.62 [-1.93, 3.17]	-0.85 [-4.72, 2.95]
Peak ACC Z	**17.96** [13.28, 22.52]	2.94 [-0.56, 6.46]	0.67 [-3.51, 4.90]	**-9.34** [-15.00, -3.42]
Peak ACC	**20.59** [15.06, 25.64]	**2.97** [0.27, 5.68]	2.17 [-1.13, 5.44]	**-7.74** [-12.64, -2.88]
Peak ARS X	**6.90** [2.87, 10.58]	**2.46** [0.59, 4.33]	0.77 [-1.60, 3.16]	-2.27 [-5.90, 1.24]

Peak ARS Y	**30.49** [26.44, 34.80]	-0.64 [-3.80, 2.62]	-0.20 [-3.96, 3.55]	-3.45 [-8.61, 1.61]
Peak ARS Z	**5.35** [1.27, 9.16]	**-2.75** [-4.28, -1.25]	**5.42** [3.46, 7.28]	1.58 [-1.72, 4.46]
Peak ARS	**31.12** [27.61, 34.75]	-0.91 [-3.84, 2.10]	1.14 [-2.44, 4.60]	-2.65 [-7.37, 2.05]
Peak Alpha X	**1277.62** [788.08, 1771.61]	103.52 [-273.10, 477.19]	-235.16 [-686.13, 222.50]	-83.69 [-688.01, 511.89]
Peak Alpha Y	**1423.91** [1056.58, 1800.13]	135.35 [-169.14, 435.68]	**391.96** [26.38, 754.84]	-399.16 [-883.34, 81.01]
Peak Alpha Z	**1014.73** [524.54, 1494.60]	-215.87 [-606.80, 173.12]	136.02 [-333.08, 594.25]	259.68 [-340.94, 882.45]
Peak Alpha	**1864.09** [1350.91, 2367.92]	96.46 [-316.72, 511.08]	184.32 [-314.40, 679.67]	-84.33 [-719.25, 565.45]
BrIC	**0.26** [0.22, 0.29]	-0.01 [-0.04, 0.01]	0.02 [-0.01, 0.05]	-0.01 [-0.05, 0.03]
UBrIC	**0.21** [0.18, 0.24]	0.00 [-0.02, 0.03]	0.02 [-0.01, 0.05]	-0.03 [-0.07, 0.00]
DAMAGE	**0.16** [0.12, 0.20]	0.03 [-0.02, 0.03]	0.01 [-0.01, 0.04]	-0.01 [-0.05, 0.03]

Appendix Table M: The intraclass correlations for each of the head kinematic features.

<table>
<tr><th></th><th colspan="3">X</th><th colspan="3">Y</th><th colspan="3">Z</th><th colspan="3">Peak Resultant</th></tr>
<tr><td>ACC</td><td colspan="3">0.695</td><td colspan="3">0.529</td><td colspan="3">0.066</td><td colspan="3">0.480</td></tr>
<tr><td>ARS</td><td colspan="3">0.534</td><td colspan="3">0.085</td><td colspan="3">0.682</td><td colspan="3">0.025</td></tr>
<tr><td>Alpha</td><td colspan="3">0.071</td><td colspan="3">0.037</td><td colspan="3">0.045</td><td colspan="3">0.043</td></tr>
<tr><td></td><td colspan="4">BrIC</td><td colspan="4">UBrIC</td><td colspan="4">DAMAGE</td></tr>
<tr><td>Injury Metric</td><td colspan="4">0.136</td><td colspan="4">0.051</td><td colspan="4">0.251</td></tr>
</table>

D. Final Sensitivity

D.1 Statistical Methods

The equations for the multivariate Bayesian linear mixed model to predict biomechanical factors based on age and sex.

$$Y_i^{ICV} = \left(\beta_0^{ICV}\right) + \beta_1^{ICV}(scale(Age_i)) + \beta_2^{ICV}(Sex_i) + \epsilon_{\mathrm{i}}^{ICV}$$

$$Y_i^{Rel\,WM} = \left(\beta_0^{Rel\,WM}\right) + \beta_1^{Rel\,WM}(scale(Age_i)) + \beta_2^{Rel\,WM}(Sex_i) + \epsilon_{\mathrm{i}}^{Rel\,WM}$$

$$Y_i^{Stiff} = \left(\beta_0^{Stiff}\right) + \beta_1^{Stiff}(scale(Age_i)) + \beta_2^{Stiff}(Sex_i) + \epsilon_{\mathrm{i}}^{Stiff}$$

$$Y_i^{DR} = \left(\beta_0^{ICV}\right) + \beta_1^{DR}(scale(Age_i)) + \beta_2^{DR}(Sex_i) + \epsilon_{\mathrm{i}}^{DR}$$

$$Y_i^{Stiff\,IQR} = \left(\beta_0^{Stiff\,IQR}\right) + \beta_1^{Stiff\,IQR}(scale(Age_i)) + \beta_2^{Stiff\,IQR}(Sex_i) + \epsilon_{\mathrm{i}}^{Stiff\,IQR}$$

$$Y_i^{DR\,IQR} = \left(\beta_0^{ICV}\right) + \beta_1^{DR\,IQR}(scale(Age_i)) + \beta_2^{DR\,IQR}(Sex_i) + \epsilon_{\mathrm{i}}^{DR\,IQR}$$

$$Y_i^{Quad1} = \left(\beta_0^{Quad1}\right) + \beta_1^{Quad1}(scale(Age_i)) + \beta_2^{Quad1}(Sex_i) + \epsilon_{\mathrm{i}}^{Quad1}$$

$$Y_i^{Quad2} = \left(\beta_0^{Quad2}\right) + \beta_1^{Quad2}(scale(Age_i)) + \beta_2^{Quad2}(Sex_i) + \epsilon_{\mathrm{i}}^{Quad2}$$

$$Y_i^{Quad4} = \left(\beta_0^{Quad4}\right) + \beta_1^{Quad4}(scale(Age_i)) + \beta_2^{Quad4}(Sex_i) + \epsilon_{\mathrm{i}}^{Quad4}$$

The equations for the multivariate Bayesian linear mixed model to predict deformation metrics based on independent biomechanical features, age, and sex.

$$\begin{aligned} Y_i^{MPS-95} = \left(\beta_0^{MPS-95}\right) &+ \beta_1^{MPS-95}(Age_i) + \beta_2^{MPS-95}(Sex_i) + \beta_3^{MPS-95}(ICV) + \beta_4^{MPS-95}(Rel\,WM_i) \\ &+ \beta_5^{MPS-95}(Stiff_i) + \beta_6^{MPS-95}(DR_i) + \beta_7^{MPS-95}(Stiff\,IQR_i) + \beta_8^{MPS-95}(DR\,IQR_i) \\ &+ \beta_9^{MPS-95}(Quad\,1_i) + \beta_{10}^{MPS-95}(Quad\,2_i) + \beta_{11}^{MPS-95}(Quad\,4_i) \\ &+ \beta_{12}^{MPS-95}(DAMAGE_i) + \epsilon_{\mathrm{i}}^{MPS-95} \end{aligned}$$

$$\begin{aligned} Y_i^{MPSR-95} = \left(\beta_0^{MPSR-95}\right) &+ \beta_1^{MPSR-95}(Age_i) + \beta_2^{MPSR-95}(Sex_i) + \beta_3^{MPSR-95}(ICV) \\ &+ \beta_4^{MPSR-95}(Rel\,WM_i) + \beta_5^{MPSR-95}(Stiff_i) + \beta_6^{MPSR-95}(DR_i) \\ &+ \beta_7^{MPSR-95}(Stiff\,IQR_i) + \beta_8^{MPSR-95}(DR\,IQR_i) + \beta_9^{MPSR-95}(Quad\,1_i) \\ &+ \beta_{10}^{MPSR-95}(Quad\,2_i) + \beta_{11}^{MPSR-95}(Quad\,4_i) + \beta_{12}^{MPSR-95}(DAMAGE_i) + \epsilon_{\mathrm{i}}^{MPSR-95} \end{aligned}$$

$$\begin{aligned} Y_i^{MPSxMPSR-95} = \left(\beta_0^{MPSxMPSR-95}\right) &+ \beta_1^{MPSxMPSR-95}(Age_i) + \beta_2^{MPSxMPSR-95}(Sex_i) \\ &+ \beta_3^{MPSxMPSR-95}(ICV) + \beta_4^{MPSxMPSR-95}(Rel\,WM_i) + \beta_5^{MPSxMPSR-95}(Stiff_i) \\ &+ \beta_6^{MPSxMPSR-95}(DR_i) + \beta_7^{MPSxMPSR-95}(Stiff\,IQR_i) + \beta_8^{MPSxMPSR-95}(DR\,IQR_i) \\ &+ \beta_9^{MPSxMPSR-95}(Quad\,1_i) + \beta_{10}^{MPSxMPSR-95}(Quad\,2_i) + \beta_{11}^{MPSxMPSR-95}(Quad\,4_i) \\ &+ \beta_{12}^{MPSxMPSR-95}(DAMAGE_i) + \epsilon_{\mathrm{i}}^{MPSxMPSR-95} \end{aligned}$$

$$\begin{aligned} Y_i^{CSDM-25} = {} & \left(\beta_0^{CSDM-25}\right) + \beta_1^{CSDM-25}(Age_i) + \beta_2^{CSDM-25}(Sex_i) + \beta_3^{CSDM-25}(ICV) \\ & + \beta_4^{CSDM-25}(Rel\ WM_i) + \beta_5^{CSDM-25}(Stiff_i) + \beta_6^{CSDM-25}(DR_i) \\ & + \beta_7^{CSDM-25}(Stiff\ IQR_i) + \beta_8^{CSDM-25}(DR\ IQR_i) + \beta_9^{CSDM-25}(Quad\ 1_i) \\ & + \beta_{10}^{CSDM-25}(Quad\ 2_i) + \beta_{11}^{CSDM-25}(Quad\ 4_i) + \beta_{12}^{CSDM-25}(DAMAGE_i) + \epsilon_i^{CSDM-25} \end{aligned}$$

D.2 Effect of Sex on Biomechanical Factors

Appendix Table N: Estimated coefficients for the population-level effects of the multivariate Bayesian linear mixed model with the 95% credible interval (CrI) for the estimated parameter included in square brackets for each biomechanical factor. Bolded coefficients are significant based on the CrI. Positive sex coefficients imply male response was greater.

	Intercept	Sex	Age
ICV	**1456.44** [1426.2, 1486.6]	**70.45** [27.14, 113.05]	**-39.98** [-61.33, -18.67]
Relative WM	**0.35** [0.351, 0.355]	-0.0001 [-0.003, 0.003]	**-0.002** [-0.003, -0.001]
Mean Stiffness	**2.72** [2.67, 2.77]	0.022 [-0.043, 0.090]	**-0.15** [-0.19, -0.12]
Mean DR	**0.22** [0.21, 0.22]	**-0.017** [-0.026, -0.009]	**0.027** [0.023, 0.031]
Stiffness IQR	**1.12** [1.07, 1.16]	0.0026 [-0.059, 0.064]	**-0.080** [-0.11, -0.049]
DR IQR	**0.12** [0.11, 0.12]	-0.0028 [-0.008, 0.0022]	**0.016** [0.013, 0.019]
Quad. 1 Percent	**33.17** [31.60, 34.76]	**3.15** [0.92, 5.36]	**-2.80** [-3.92, -1.69]
Quad. 2 Percent	**19.89** [18.47, 21.34]	**-3.66** [-5.69, -1.64]	**9.63** [8.61, 10.67]
Quad. 4 Percent	**12.91** [11.40, 14.42]	**-2.81** [-4.89, -0.68]	**1.43** [0.34, 2.50]

D.3 Additional Kinematic Features Estimated Parameters

Appendix Table O: Estimated coefficients for the population-level effects of the multivariate Bayesian linear mixed model and the 95% credible interval (CrI) for the estimated parameter included in square brackets for age, sex, and each biomechanical features (with peak resultant angular velocity) on the deformation metrics. Bolded coefficients are significant based on the CrI. Positive sex coefficients imply male response was greater.

	Intercept	Sex	Age	ICV	Rel. WM Volume
MPS-95	**0.215** [0.21, 0.22]	0.0014 [-0.0069, 0.0097]	0.0045 [-0.0027, 0.012]	**0.011** [0.0074, 0.015]	0.0014 [-0.0021, 0.005]

MPSR-95	**28.390** [27.00, 29.80]	0.308 [-1.90, 2.51]	0.565 [-1.40, 2.53]	**1.16** [0.13, 2.19]	0.161 [-0.83, 1.56]
MPSxMPSR-95	**4.159** [3.73, 4.59]	0.139 [-0.56, 0.84]	0.140 [-0.48, 0.76]	**0.344** [0.018, 0.67]	0.312 [-1.33, 1.96]
CSDM-25	**0.059** [0.044, 0.075]	0.0043 [-0.022, 0.030]	0.0037 [-0.018, 0.026]	0.010 [-0.002, 0.022]	0.0006 [-0.011, 0.012]

	Mean Stiffness	Mean DR	Stiffness IQR	DR IQR
MPS-95	0.0034 [-0.017, 0.023]	**-0.032** [-0.061, -0.0028]	0.0042 [-0.0054, 0.014]	0.0013 [-0.013, 0.016]
MPSR-95	1.403 [-3.65, 6.45]	-2.50 [-9.01, 4.16]	0.522 [-2.05, 3.07]	0.419 [-3.48, 4.42]
MPSxMPSR-95	0.312 [-1.33, 1.96]	-0.516 [-2.72, 1.80]	0.231 [-0.59, 1.05]	0.068 [-1.18, 1.32]
CSDM-25	0.017 [-0.045, 0.081]	-0.025 [-0.12, 0.070]	0.0077 [-0.023, 0.038]	0.0027 [-0.045, 0.049]

	Quad. 1 Percent	Quad. 2 Percent	Quad. 4 Percent	Peak ARS Res.
MPS-95	**0.016** [0.0022, 0.030]	0.020 [-0.0006, 0.039]	0.0094 [-0.0046, 0.023]	**0.076** [0.073, 0.079]
MPSR-95	2.497 [-1.12, 6.13]	1.726 [-3.22, 6.73]	0.589 [-2.911, 4.064]	**12.313** [11.44, 13.16]
MPSxMPSR-95	0.693 [-0.47, 1.84]	0.381 [-1.26, 1.99]	0.131 [-1.04, 1.25]	**2.509** [2.24, 2.78]
CSDM-25	0.027 [-0.017, 0.071]	0.024 [-0.040, 0.088]	0.0060 [-0.039, 0.050]	**0.048** [0.039, 0.058]

Appendix Table P: Estimated coefficients for the population-level effects of the multivariate Bayesian linear mixed model and the 95% credible interval (CrI) for the estimated parameter included in square brackets for age, sex, and each biomechanical features (with peak resultant angular acceleration) on the deformation metrics. Bolded coefficients are significant based on the CrI. Positive sex coefficients imply male response was greater.

	Intercept	Sex	Age	ICV	Relative WM Vol
MPS-95	**0.21** [0.21, 0.22]	0.003 [-0.012, 0.018]	0.004 [-0.009, 0.017]	**0.011** [0.004, 0.017]	0.001 [-0.005, 0.008]
MPSR-95	**28.45** [27.27, 29.63]	0.19 [-1.71, 2.09]	0.66 [-0.93, 2.44]	**1.18** [0.36, 2.00]	0.16 [-0.62, 0.94]
MPSxMPSR-95	**4.18** [3.81, 4.54]	0.095 [-0.51, 0.69]	0.17 [-0.34, 0.67]	**0.35** [0.10, 0.61]	0.03 [-0.21, 0.28]
CSDM-25	**0.06** [0.05, 0.08]	0.002 [-0.022, 0.026]	0.005 [-0.015, 0.025]	**0.011** [0.0001, 0.02]	0.001 [-0.009, 0.01]

	Mean Stiffness	Mean DR	Stiffness IQR	DR IQR

MPS-95	0.003 [-0.036, 0.043]	-0.021 [-0.080, 0.039]	0.0057 [-0.013, 0.025]	0.0013 [-0.027, 0.030]
MPSR-95	1.65 [-2.84, 6.24]	-3.27 [-9.30, 2.97]	0.34 [-1.88, 2.54]	0.46 [-3.00, 3.89]
MPSxMPSR-95	0.39 [-1.07, 0.87]	-0.83 [-2.93, 1.33]	0.16 [-0.55, 0.87]	0.08 [-1.00, 1.20]
CSDM-25	0.020 [-0.041, 0.083]	-0.041 [-0.14, 0.060]	0.005 [-0.024, 0.034]	0.0031 [-0.041, 0.048]
	Quad. 1 Percent	Quad. 2 Percent	Quad. 4 Percent	Peak Alpha Res.
MPS-95	0.016 [-0.010, 0.043]	0.012 [-0.026, 0.051]	0.0055 [-0.022, 0.032]	**0.071** [0.066, 0.076]
MPSR-95	2.69 [-0.54, 5.80]	2.33 [-2.01, 6.57]	0.92 [-2.21, 3.97]	**12.77** [12.10, 13.44]
MPSxMPSR-95	0.76 [-0.27, 1.77]	0.63 [-0.82, 2.06]	0.26 [-0.76, 1.27]	**2.73** [2.52, 2.94]
CSDM-25	0.029 [-0.014, 0.073]	0.036 [-0.029, 0.10]	0.013 [-0.033, 0.057]	**0.059** [0.051, 0.067]